A Molecular-Level Investigation of Organic Interfaces: from Friction to Biosensors

by

Anna Lio

A Thesis submitted
to the FACULTY OF ENGINEERING of the
UNIVERSITY OF GLASGOW
for the degree of
Doctor of Philosophy

ProQuest LLC.
789 East Eisenhower Parkway
P.O. Box 1346
Ann Arbor, MI 48106 – 1346

Dedicated to my mother, Antonietta
and the memory of my father,
Fausto Lio

Abstract

Scanning probe techniques (SPM) and atomic force microscopy (AFM) in particular were used to study organic structures at the atomic and molecular level. Organic interfaces are of prime importance to several technological applications, such as boundary lubrication and biosensors development. Because these applications rely on molecular-scale recognition and control a fundamental, molecular-level understanding of their structural and physical-chemical properties is indispensable.

The use of model organic systems, based on self-assembled monolayers, and atomic force microscopy is proposed to obtain a fundamental understanding of basic tribological issues. Self-assembled monolayers provide a relatively easy way to modify the chemical and physical properties of surfaces. The high pressures (MPa - GPa range) applied by the sharp tip of an atomic force microscope under single-asperity contact make this technique particularly suitable for tribology/mechanical studies at the nanometer-level. This thesis also discusses the present limitations of the technique related to the measurement of the cantilever's mechanical properties and the contact area and gives suggestions for improvement in the use of the AFM for nanotribology/nanomechanics studies. Methyl and carboxylic acid terminated thiol molecules and methyl terminated silane molecules were self-assembled on Au(111) and mica, respectively. For the first time, the relation between frictional properties and important parameters such as chain length, end group chemical functionality and head group-substrate interaction was studied. Based on the results obtained for the two types of layers and the direct comparison between thiol and silane layers with the same chain length, properties of these layers that reduce friction have been identified and a new molecular-level mechanism for energy dissipation in these layers is proposed. The resistance to wear and the pressure dependent structural and frictional properties of octadecylthiol monolayers on Au(111) were also studied. By using tips with radius in the 200-700 Å range, pressures from about 100 MPa to a few GPa were applied. The structural and frictional properties were studied as a function of the applied pressure and a new phenomenon in which the molecules are reversibly 'squeezed out' from under the tip at a well defined value of the applied pressure was observed. In relation to these tribological studies, molecular-level structural information for mica and Au(111) surfaces, thiol and silane layers has been obtained and fundamental issues related to the imaging/contrast mechanism in contact mode AFM are discussed. Furthermore, based on AFM characterization, preparation conditions for high quality silane layers are given and it is demonstrated that commonly used preparation methods and macroscopic contact

angle measurements are inadequate to this aim. Finally, the first part of this thesis is concluded by presenting the first AFM results aimed at investigating the effect of water on the adhesive properties of surfaces. Understanding how water interacts with surfactant layers, hydrophobic coatings, membranes is of crucial importance to several technologies such as paints, soaps, adhesives and polymers. Hydrophilic and hydrophobized mica surfaces were used as model systems and their adhesive properties were studied by measuring the pull-off force in approach-retract curves at values of the relative humidity from 5% to 95%. The results show that markedly different behaviors are obtained on the two types of surfaces, opening the way to a fundamental understanding of the way water interacts with surfaces and to a new use of the AFM as a sensitive hydrophilicity/hydrophobicity probe.

The second part of this thesis deals with the molecular-scale characterization of the 'blue' and 'red' forms of polydiacetylene (PDA) thin films prepared by the Langmuir-Blodgett (vertical) and Langmuir-Schaefer (horizontal) methods. These films form the basis of a novel, color-based biosensor for the detection of the influenza virus. 10, 12 pentacosadiynoic acid layers are functionalized with sialic acid, the receptor-specific ligand for the influenza virus hemagglutinin, and the polymer backbone serves as a chromophore that signals binding of the virus to the carbohydrate moiety by the PDA blue-to-red color transition. In order to fully exploit the use of ligand-functionalized PDA films as biosensors, it is necessary to understand the molecular mechanisms of the blue-to-red color transition induced by target binding (affinochromism). AFM was used to this aim since this technique is particularly suitable for investigating the structure and extent of long-range order in the side groups. In addition, since the molecular mechanisms underlying the optical transition of PDAs are not understood even for the more well-known thermochromic effect (induced by heat) and as due to prolonged exposure to UV light, detailed AFM and spectroscopic characterizations of these effects were also performed. Traditionally the color transition of PDAs has been studied by spectroscopic techniques, that is macroscopic methods. The studies presented in this thesis are the first direct evidence that the molecular level mechanisms of the blue-to-red color transition are rather different in the three cases, ranging from a partially disordered-to-ordered re-arrangement of the side chains for the thermochromic effect to 'buckling' of the polymer fibers for the affinochromic transition. Importantly, these results show that the complexity of these molecular level mechanisms is such that macroscopic measurements are necessarily inadequate.

Polydiacetylene films were used as templates of biological matrices to reproduce the unique conditions existing in Nature that lead to the co-alignment of minerals at the organic matrix and in turn to elucidate some of interactions that

may occur in living systems. Calcite crystals were grown on the PDA template and their nucleation face and orientation with respect to the organic matrix was observed to be controlled in all directions by the PDA matrix. These studies are the first reported example of total alignment of inorganic crystals at an organic interface and open the way to the use of polymerized synthetic membranes as new models for biomineralization and new crystalline materials.

The final part of this thesis discusses further biosensors applications using photolithography and silane chemistry to spatially define areas of an oxidized substrate with different chemical functionalities. An immobilization technique is proposed and preliminary results obtained on small fluorescent molecules and bovin serum albumin are presented. Prospects and limitations of the method are also discussed.

Preliminary results on the utilization of sub-micron lithography methods to define a reference system on a solid substrate for high resolution SPM organic/biological applications are presented. These efforts were made in the attempt to overcome one of the present limitations of SPM methods. In fact, to date it is difficult to image the same area of the sample after some transformation has taken place and results are often statistical averages obtained over several areas of the sample. While this approach is adequate in many SPM studies, it is inadequate in those where complex transformations take place.

In conclusion, the results presented in this thesis demonstrate the usefulness of AFM for molecular-scale characterization of the structure and physical-chemical properties of organic interfaces and open the way for new and very exciting uses of this technique in a variety of fundamental and technologically relevant studies.

Acknowledgments

First of all, I would like to thank my former supervisor Dr. P. Connolly and the Department of Electronics and Electrical Engineering of Glasgow University for giving me the opportunity to perform research for the Degree of Doctor of Philosophy. I am also deeply grateful to my present supervisors, Prof. C. D. W. Wilkinson and Dr. G. Moores, for their invaluable encouragement and support throughout this work.

I wish to extend my sincere gratitude to Dr. M. Salmeron at the Lawrence Berkeley National Laboratory (LBNL), University of California at Berkeley (USA). I will always be indebted to him for providing the opportunity to perform research in his group. Without his excellent guidance and enthusiastic support throughout my visit at LBNL, this thesis could have not been written. My thanks also go to Dr. D. H. Charych and Dr. D. F. Ogletree at LBNL. Debbey's exceptional knowledge of the chemistry of organic thin films and Frank's expertise in too many fields to mention them has been invaluable to me and has made my visit at LBNL an incredible experience.

I would especially like to acknowledge the members of the STM/AFM group and Center for Advanced Materials at LBNL with whom I have been fortunate to interact. Their help and friendship have been invaluable to me. In particular, I would like to thank the people with whom I have worked directly. These include Gang-Yu Liu, Rob Carpick, Jun Hu, Anke Reichert, Jon Nagy, Dong-June Ahn and Amir Berman. Gang-Yu first introduced me to the pressure dependent atomic force microscopy experiments on the thiol monolayers. Without Rob and Jun's help much of the friction work could have not been accomplished. To Anke I am particularly grateful for the preparation of the polydiacetylene films and the many chemistry conversations. Thanks to Jon for the synthesis of the sialic acid lipid. Dong-June and Amir introduced me to the fascinating world of mineralization.

I would like to thank all the staff at LBNL for their help and expertise. The facilities and support staff at LBNL are the best one could hope to work with.

My sincere gratitude also goes to all the technical staff at the Department of Electronics and Electrical Engineering at Glasgow University for their help and support during the time I spent there. In particular, B. Monaghan, M. Robertson and all of the Bioelectronics and Ultra-Small-Structures laboratories. My gratitude also goes to Prof. A. Curtis and Dr. B. Stothard for the fluorescence microscopy studies.

Special thanks to the friends I worked with at the National Research Council in Pisa, Italy. Among them deserve special mention Dr. C. Ascoli, Dr. C. Frediani, Prof. M. Allegrini, M. Labardi, F. Dinelli, P. Baschieri, T. Mariani. From them and with them I first learned about scanning probe microscopy.

I also wish to extend my warmest thanks to all my friends, for their help and support wherever this PhD project took me to. In particular, P. Gallo, M. Burgio, F. Giannasio, P. Mancuso, G. Gallone, A. Griffith, G. DeGasperis, B. Kardynal, N. Cameron, J. Cameron, B. Stothard, M. Holland and C. Holland. Together we shared happy times and they helped me go through difficult ones. I would also like to thank Mr. R. Hutchins and Mrs. M. McGoldrick for their warm understanding and encouragement throughout this PhD.

I am especially grateful to my wonderful husband, Brian McIntyre for all of his love, patience, help and understanding. Without his invaluable suggestions, revisions, encouragement and emotional support this thesis could have never been written. My thanks also go to Brian's family, for their love and continued support.

Finally, I am profoundly grateful to my family for all of their love and support. My parents' hard work, honesty and professional achievements have been inspirational to me. They always allowed me to work through (and around) my own challenges without ever denying their unconditional support. A special thought goes to my father, whom I wish could see this work brought to completion. I know in my heart that he would be smiling at me today. The thought of that smile has enabled me to overcome any difficulty and to bring to a close this important chapter of my life.

I acknowledge the financial support by the Commission of the European Communities and the Lawrence Berkeley National Laboratory. The work at LBNL was supported by the Director, Office of Energy Research, Office of Basic Energy Sciences, Materials Sciences division of the U.S. Department of Energy under contract No. DE-AC03-76SF00098.

Glasgow, February 1997

List of Illustrations

List of Tables

List of Abbreviations

SPM	Scanning Probe Microscopy/Microscope
AFM	Atomic Force Microscopy/Microscope
PDA	Polydiacetylene
STM	Scanning Tunneling Microscopy/Microscope
UHV	Ultra-High Vacuum
MD	Molecular Dynamics
FFM	Friction Force Microscopy/Microscope
SFA	Surface Force Apparatus
QCM	Quartz Crystal Microbalance
JKR	Johnson-Kendall-Roberts
DMT	Derjaguin-Müller-Toporov
OMCTS	Octamethylcyclo-tetrasiloxane
LB	Langmuir-Blodgett
IO	Independent Oscillator
CNR	National Research Council
LBNL	Lawrence Berkeley National Laboratory
SEM	Scanning Electron Microscopy/Microscope
SAM	Self-Assembled Monolayer
LS	Langmuir-Schaefer
FTIR	Fourier Transform Infrared Spectroscopy
AES	Auger Electron Spectroscopy
LPCVD	Low Pressure Chemical Vapor Deposition
PSM	Park Sharpened Microlever™
PBA	Parallel Beam Approximation
FCC	Face Centered Cubic
FFT	Fast Fourier Transform
NLO	Non-Linear Optics
FWHM	Full Width Half Maximum
OTS	Octadecyltrichlorosilane
XPS	X-Ray Photoelectron Spectroscopy
NEXAFS	Near Edge X-Ray Absorption Fine Structure
OTE	Octadecyltriethoxysilane
OTMS	Octanetrimethoxysilane
HTMS	Hexanetrimethoxysilane
DTS	Dodecyltriethoxysilane

PTFE	Polytetrafluoroethylene
THF	Tetrahydrofuran
RH	Relative Humidity
UV	Ultra-Violet
PCDA	Pentacosadiynoic Acid
SAc	Sialic Acid
SAc/PCDA	Sialic Acid Functionalized 10, 12 Pentacosadiynoic Acid
p-(SAc/)PCDA	Polymer (Sialic Acid Functionalized) 10, 12 Pentacosadiynoic Acid Films
m-(SAc/)PCDA	Monomer (Sialic Acid Functionalized) 10, 12 Pentacosadiynoic Acid Films
NMR	Nuclear Magnetic Resonance
MCT	Mercury-Cadmium-Telluride
ELISA	Enzyme-Linked Immunosorbent Assay
HA	Hemagglutinin
PBS	Phosphate Buffer Saline
ITO	Indium Tin Oxide
DMF	N,N Dymethylformamide
FITC	Fluorescein Isothiocyanate
HRSEM	High Resolution Scanning Electron Microscopy/Microscope
AEAPS	Aminoethyl-aminopropyltrimethoxysilane
RO	Reverse Osmosis
BSA	Bovin Serum Albumin
IB	Integrated Brightness
RMIB	Relative Mean Integrated Brightness
PMMA	Poly(methylmethacrylate)
IPA	Isopropyl alcohol
MIBK	Methylisobuthylketone
APS	Aminopropyltriethoxysilane

List of Publications and Presentations

1) A. Berman, D. J. Ahn, A. Lio, M. Salmeron, A. Reichert, D. Charych, Total Alignment of Calcite at Acidic Polydiacetylene Films: Cooperativity at the Organic-Inorganic Interface, *Science*, **269**, 515 (1995).

2) A. Lio, A. Reichert, J. O. Nagy, M. Salmeron, D. H. Charych, Atomic Force Microscope Study of Chromatic Transitions in Polydiacetylene Thin Films, *J. Vac. Sci. Technol. B*, **14**, 1481 (1996).

3) A. Lio, C. Morant, D. F. Ogletree, M. Salmeron, An Atomic Force Microscopy Study of the Pressure Dependent Structural and Frictional Properties of n-Alkanethiols on Gold, *J. Phys. Chem.*, in press.

4) A. Lio, D. H. Charych, M. Salmeron, A Comparative Atomic Force Microscopy Study of the Chain Length Dependence of the Frictional Properties of Alkylthiols on Gold and Alkylsilanes on Mica, *J. Phys. Chem.*, in press.

5) A. Lio, A. Reichert, D. J. Ahn, J. O. Nagy, M. Salmeron, D. H. Charych, Structural Study of Thermochromism in Polydiacetylene Thin Films Incorporating Carbohydrate Ligands, *Submitted for Publication to J. Am. Chem. Soc.*, 1996.

6) A. Lio, A. Reichert, A. Berman, J. O. Nagy, M. Salmeron, D. H. Charych, Preparation and Molecular Scale Characterization of Polydiacetylene Thin Films, *Submitted for Publication to Langmuir*, 1997.

7) J. Hu, A. Lio, D. H. Charych, M. Salmeron, The Interaction of Water with Bare and Silanated Mica Surfaces: an AFM Study of the Tribological and Hydrophilicity Properties, *In Preparation*.

8) A. Lio, M. Salmeron, Frictional Properties of Mercaptoalkanoic Acids Self-Assembled on Gold and Gold on Mica, *In Preparation*.

Presentations

1) An Atomic Force Microscopy (AFM) Study of the Structure and Friction of Gold and n-Alkanethiols on Gold as a Function of Load, A. Lio*, D. F. Ogletree, M. Salmeron, *The 1995 March Meeting of the American Physical Society, 20-24 March 1995, San Jose, CA, USA.*

2) Hertzian Friction, D. F. Ogletree*, A. Lio, R. W. Carpick, J. Hu, M. Salmeron, *The 1995 March Meeting of the American Physical Society, 20-24 March 1995, San Jose, CA, USA.*

3) An AFM Study of Chromatic Transitions in Polydiacetylene Thin Films, A. Lio*, A. Reichert, J. O. Nagy, M. Salmeron, D. H. Charych, *STM'95 Eighth International Conference on Scanning Tunneling Microscopy/Spectroscopy and Related Techniques, 23-28 July 1995, Snowmass Village, CO, USA.*

4) A Comparative Atomic Force Microscopy (AFM) Study of Self-Assembled Alkylthiols on Gold and Alkylsilanes on Mica, A. Lio*, D. H. Charych, D. F. Ogletree, M. Salmeron, *The 42nd National Symposium and Topical Conferences of the American Vacuum Society, 16-20 October 1995, Minneapolis, MN, USA.*

Table of Contents

Chapter 1

Introduction

The understanding of organic interfaces is crucial to many applications, from improvements in friction and lubrication to applications of biosensors in medicine, as well as improved understanding of structure and properties of organic and bio-molecules.

In order to reach these goals, a molecular level understanding of the structure and physical-chemical properties of such interfaces is indispensable. In the past ten years, with the invention of scanning probe microscopes, surface scientists have been able to study surfaces and probe processes taking place at surfaces with unprecedented resolution. In fact, not only atomic (scanning tunneling microscopy, or STM) or nearly atomic (atomic force microscopy) resolution is achieved, but the structure and properties of surfaces may also be probed locally. Unlike diffraction techniques, SPM techniques are not restricted to ordered surfaces, but can provide useful information about partially ordered interfaces and/or surfaces where different ordered structures co-exist. Moreover, unlike diffraction techniques, SPM can be used to study organic and biological surfaces in a non-destructive manner and in a variety of environments: air, UHV, controlled atmospheres and even liquids.

The aim of the work presented in this dissertation is to take advantage of SPM's capacity for providing detailed structural and frictional information to monitor model organic structures at the atomic and molecular level. While initial studies were performed by STM, AFM was used for the majority of the SPM work presented in this thesis, taking advantage of its suitability for the characterization of organic and biological interfaces.

This thesis is divided into four distinct sections: I. Motivation, theory and current progress in SPM experimental techniques and their application for friction and organic thin film research; II. Frictional studies of Au and mica substrate systems and alkylthiol and alkylsilane self-assembled monolayers; III. SPM investigations of novel polydiacetylene thermo- and affino-chromic systems; and IV. Investigations of potential bio-molecular immobilization systems and possible applications of semiconductor patterning capabilities for the creation of SPM reference systems.

In the first section, chapter 2 provides a general overview of the state of the

art for SPM theory, technique and instrumentation. Although primarily AFM results are discussed in this thesis, the STM technique is described first as it is the mother of all scanning probe techniques. Chapter 3 goes on to describe the current understanding of basic contact mechanics and frictional theories. These two chapters are tied together in Chapter 4, which describes how an experimental SPM apparatus may be used to carry out simultaneously, atomic and molecular level structural and frictional investigations. A brief description of the other experimental techniques used during this thesis work is given in Chapter 5. Chapter 6 details how the AFM cantilevers were used to provide quantified frictional information.

The second section of this thesis begins by presenting atomic level results on mica and Au(111)/mica (Chapter 7). Chapter 8 describes atomic level frictional results on thiol monolayers self-assembled on Au(111)/mica surfaces. Chapters 9 takes this a step further by investigating the mechanical and structural properties of n-octadecylthiol on Au(111) as a function of applied load. Data presented in this chapter highlights an interesting pressure dependent phenomena. Chapter 10 expands the novel frictional/structural studies by similarly characterizing self-assembled alkylsilanes on mica. Based on data from the alkylthiol and alkylsilane organic thin film systems, many interesting frictional comparisons may be made and a mechanism for friction dissipation is proposed.

The third section begins with a discussion of the preparation and characterization of polydiacetylene thin films for thermo- and affinochromic studies (Chapter 11). Chapter 12 concentrates on results from structural and spectroscopic investigations throughout the thermo-chromic process. Chapter 13 discusses mechanisms of novel chromic PDA transitions, including affinochromism upon exposure of functionalized PDA matrixes to influenza virus and structural re-orientation of the PDA matrix during mineralization. This chapter describes how polydiacetylenes matrices form the basis for a novel, colorimetric type of sensor and how synthetic organic systems can provide useful insights on how Nature's bio-mineralization works.

The fourth and final section starts by describing methods for patterning organic and biological molecules for sensors applications (Chapter 14). Chapter 15 discusses possible applications of semiconductor patterning techniques to write an SPM reference system on gold surfaces. Finally, Chapter 16 summarizes results and gives direction for future work.

Chapter 2

Scanning Probe Microscopy Techniques

2.1 Scanning Tunneling Microscopy (STM)

2.1.1 STM Fundamentals

Since its invention in 1982 by Binnig and Rhorer (1986 Nobel prize),[1] the scanning tunneling microscope (STM) has enabled researchers to make dramatic advances in many areas of surface science. Its operation is based upon the quantum effect of electron tunneling between two solids through a classically forbidden energy barrier. Its equivalent in solid state physics is the metal-insulator-metal tunnel junction; in the STM the insulator is replaced by a vacuum.

The STM probes surfaces by moving a sharp tip (often W, Pt/Ir or Pt/Rh wire) to within a few angstroms of the surface to be imaged. In this situation there is a finite probability for the electrons to tunnel through the potential barrier due to the exponential decay of their wave functions away from the metal electrode and in the vacuum. At thermal equilibrium the two tunnel currents are equal, that is the chemical potentials in both metals are equal. If a bias voltage is applied between the two electrodes, a net tunnel current can be measured. This current depends on the bias voltage applied, the width of the barrier and the work functions for the two metals. The solution of the Schrödinger equation for a simple square barrier gives the following result for the tunneling current density:[2, 3]

$$J_T = \frac{3}{2}\sqrt{2m}\left(\frac{e}{\hbar}\right)^2 \sqrt{\phi}\,\frac{V}{s}\exp(-2s\sqrt{2m\phi}\,/\,\hbar) \qquad (2.1)$$

where **m** is the electron mass, **e** the electron charge, $\hbar$ the Planck's constant divided by 2π, ϕ the metal work function, **V** the bias voltage and **s** the barrier width. Relation (2.1) is valid under the approximation of $K_BT \ll \phi$, which holds true for any metal at room temperature, and for small bias voltages V, so that $eV \ll \phi$. Hence the tunneling current density depends linearly on the bias voltage V and exponentially on the barrier width s.

It is this exponential relationship that gives rise to the high resolution of the STM. For example, for a typical work function value of 4 eV the decay length κ^{-1} is given by:

$$\kappa^{-1} = (2\sqrt{2m\phi}\,/\,\hbar)^{-1} \approx 0.5\text{Å} \qquad (2.2)$$

Therefore, if s changes 1 Å the tunnel current changes by about a factor of 10.

Normally, however, tip and sample have different work functions and the barrier is trapezoidal in shape (figure 2.1). In this case the barrier height ϕ of equation (2.1) is replaced by the average barrier height:[4]

$$\Phi = \frac{1}{2}(\phi_{tip} + \phi_{sample}) - (E - \frac{eV}{2}) \qquad (2.3)$$

for electrons tunneling into states at energy E above the sample Fermi level for negative tip bias and where ϕ_{tip} and ϕ_{sample} are the workfunctions of the tip and sample, respectively.

The theory described above is useful to understand the operating principle of the STM, but to get more realistic results the electronic structure of both the tip and substrate must be taken into account. The filled density of states for the cathode and the empty density of states for the anode have to be considered since they are directly involved in the tunneling process. Tersoff and Hamann[5, 6] first approached this problem by considering a locally spherical tip described by an s-wave function. The tunneling current is found to depend on the local density of states at the center of curvature $\mathbf{r_o}$ of the tip:

$$I_T \propto VD_t(E_F)\rho(\vec{r}_o, E_F) \qquad (2.4)$$

where V is the bias voltage, $D_t(E_F)$ is the density of states per unit volume of the tip and $\rho(\vec{r}_o, E_F)$ is the surface local density of states at the Fermi level, E_F, at the position of the tip.

Since the Tersoff and Hamann model other theories have been proposed.[7, 8] The description of these theories is beyond the scope of this thesis. It will be only mentioned that, even for 'simple' absorbates on metals, the detailed understanding of the STM images symmetry is rather complex and the nature of the tip has to be taken into account.[9, 10] Furthermore, theoretical work aimed at the understanding of the tunneling process through organic molecules deposited on solid substrates is still lacking and many fundamental questions are still to be answered. In fact, while several organic layers, such as alkylthiol monolayers on gold and polydiacetylenes on graphite, have been successfully imaged by STM, the imaging mechanism is not understood. In particular, the role of the substrate and the aliphatic chains has not been elucidated.[11]

2.1.2 STM Modes of Operation

Figure 2.2 shows a schematic of an STM. After bringing the tip close to the surface, so that electron tunneling between the two surfaces can be initiated, the tip

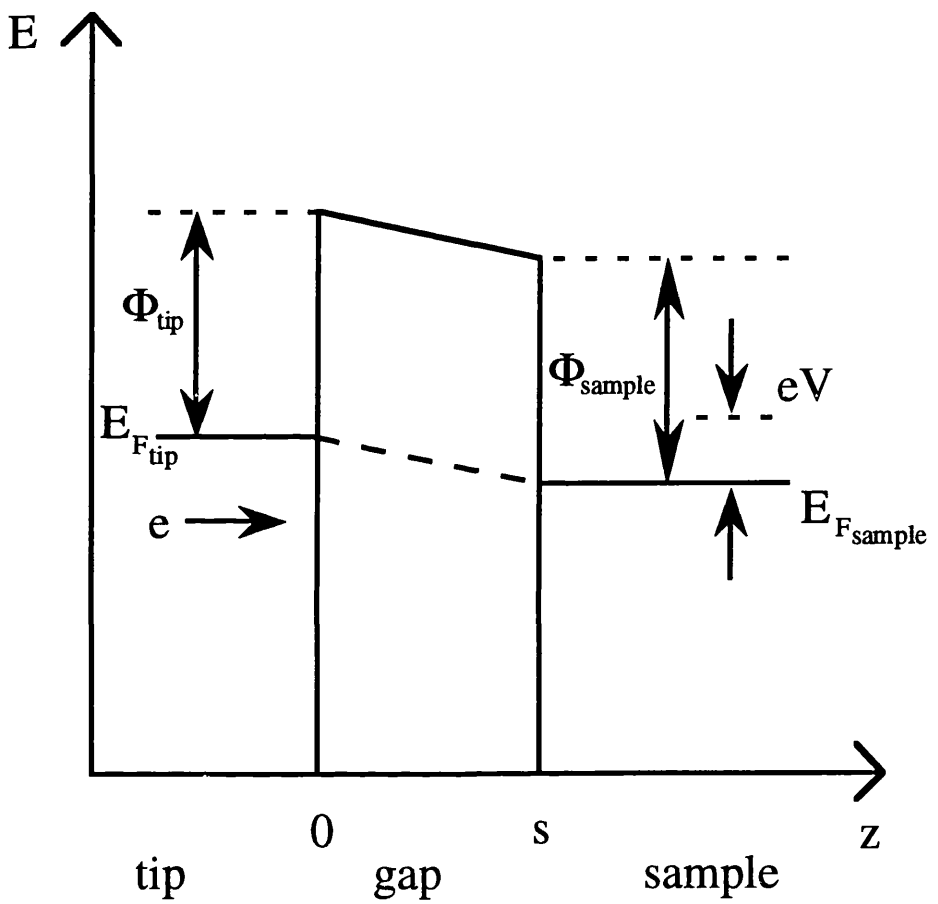

Figure 2.1. Trapezoidal potential barrier. $\Delta\Phi=\Phi_{tip} - \Phi_{sample}$.

is rastered across the surface while sensing the current.

Precise motion in three orthogonal directions with nanometric resolution is achieved by the use of piezoelectric ceramics. The piezoelectric effect is observed in crystals such as quartz and Rochelle salt, as well as in several ferroelectric ceramics, such as titanates, zirconates, stannates and mixtures of them. These ceramics are characterized by domains with electric dipoles randomly oriented. To introduce the anisotropy necessary to observe the piezoelectric effect, a strong electric field is applied at elevated temperature to the ceramic. That has the effect of aligning all the electric dipoles associated to the ceramic microcrystals along the direction of the applied electric field. Such polarization is maintained even after the electric field is turned off and for temperatures below the *Curie Point*. After the ceramic is polarized, the application of small electric fields results in a collective response of the material electric dipoles to produce an expansion in the direction of the dipoles and a contraction in the direction perpendicular to them.[12] Such ferroelectric ceramics are used in the fabrication of piezoelectric transducers for SPM applications. In the first version of the microscope[1] three rectangular transducers in a 'tripod' arrangement were used to ensure motion of the STM tip in the three orthogonal directions. Later, Binnig and Smith introduced the piezoelectric tube.[13] In this case, the outer electrode is segmented in four sectors at 90^{o}. Opposite sectors are driven by signals of the same amplitude, but opposite sign. This gives, through bending, a two-dimensional motion of the center point. Motion in the z-direction is achieved either by applying a voltage to the inner electrode, or by controlling the signals applied to the four external electrodes. The important advantages of the piezo tube compared to the 'tripod' are its small size and high resonant frequencies, which allows for higher scanning speeds. Moreover, its symmetric shape is better suited to reduce thermal drift. For these reasons the piezo tube has become the most widely used scanner in SPM systems.

By using a feedback loop, tunneling current between the tip and surface can be maintained which affords a number of modes of operation. These include *topographic* (or *constant current*), *current* (or *constant height*) and a few modulation modes, including *barrier height* (dI/dz).

Figure 2.3(a) shows the basic *topographic mode* of operation. In this mode the tunnel current is kept constant by varying the tip-sample distance (gap) as the tip scans over the surface. The height is plotted versus the tip position. The vertical resolution is often <0.1 Å while the lateral resolution is commonly about 1 Å. The topographic mode is the most widely used method of STM imaging, as it works well for samples that are not atomically flat. It was the only mode of operation used for this thesis work.

Figure 2.3(b) describes the *current mode* of imaging. In this mode, the Z

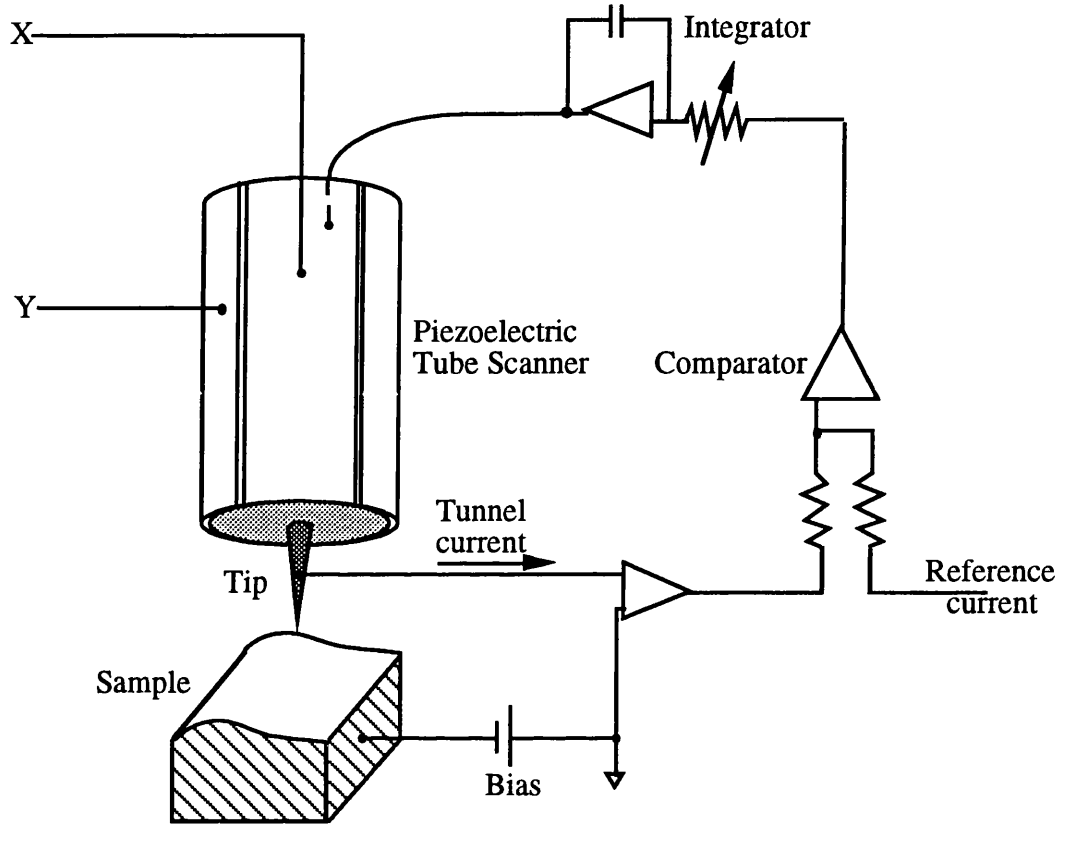

Figure 2.2. Schematic drawing of the STM setup. A piezoelectric tube supports a metallic tip, a few angstroms over the surface of the sample. Voltages applied to its electrodes cause bending and length changes of the tube that are used to scan the tip over the surface. The tunnel current between the tip and the surface is maintained by means of an electronic feedback loop.

feedback loop is slowed down such that the tip is scanned on a plane over the surface and the tunneling current is monitored. The image in this case is a function of the tunnel current and the tip position. The advantage is primarily one of speed, since only the electronics and not the Z feedback control are employed. Scan rates are commonly of the order of 1 kHz. Corresponding scan rates in topographic mode are 1 Hz. The major disadvantage of using this mode is that the surface must be atomically flat.

Binnig *et al.*[14] first demonstrated that a modulation of the gap distance will produce a component in the tunneling current proportional to the tunneling barrier height:

$$\frac{dI_T}{dZ} \propto I_T \sqrt{\phi} \qquad (2.5)$$

The barrier height ϕ is closely related to the work function of the sample. The major difference is that the work function is an averaging property of the surface, while ϕ is a local property. In the *barrier height mode,* the tip is oscillated with a sinusoidal signal as the tip moves over the surface in a topographic fashion.

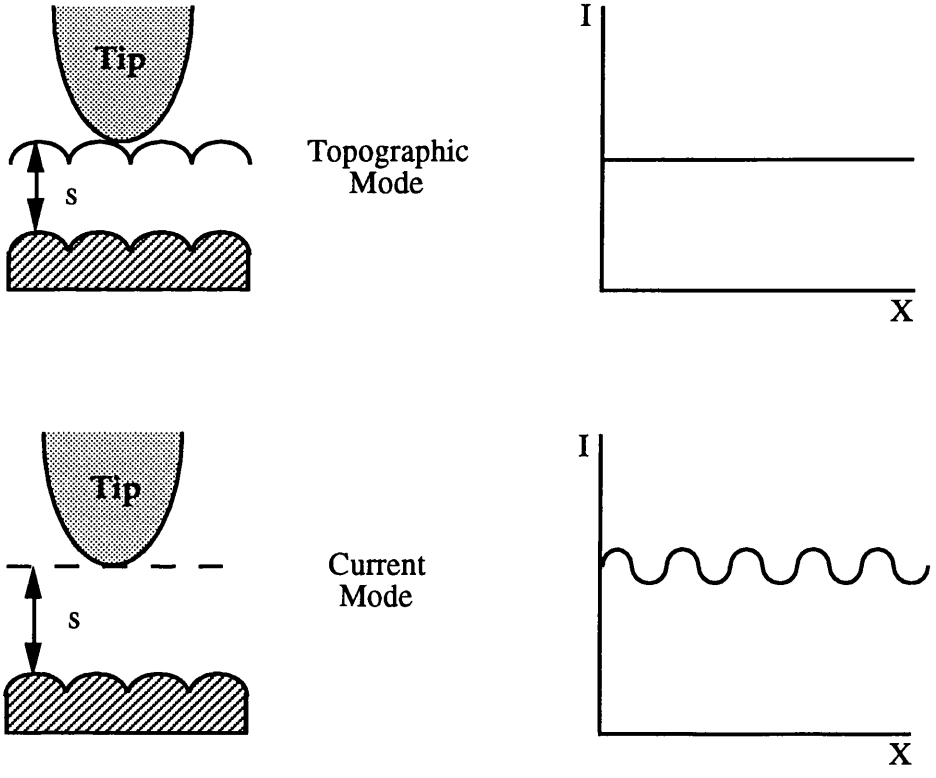

Figure 2.3. (a) Schematic representation of *topographic* (or *constant current*) *mode* of imaging. The cartoon on the left shows how the tip is moved over the surface. The graph on the right gives indication as to why this technique is termed 'constant current' imaging. (b) Schematic representation of *current* (or *constant height*) *mode*.

2.2 Atomic Force Microscopy (AFM)

2.2.1 AFM Fundamentals

The main limitation of STM is the requirement that the sample conducts. In 1986 Binnig, Quate and Gerber invented a new microscope that would overcome this limitation, the atomic force microscope (AFM).[15] Instead of measuring tunneling currents between a probe and a sample, the AFM measures forces near surfaces. The probing tip is attached to a flexible cantilever stylus. The small forces between the tip and the sample cause the cantilever to deflect. These deflections are measured with sub-angstrom sensivity by an optical or tunneling displacement detector. Images are obtained in a way similar to the STM technique, i.e. by raster scanning the tip over the sample surface and then digitizing the lever deflection or the z-movement of the piezo as a function of the lateral position x, y. Figure 2.4 shows an AFM schematic. Typical spring constants range from 0.001 to 100 N/m and motions of μm to ≈ 0.1 Å are measured by the deflection sensor. Typical forces range from 10^{-10} to 10^{-6} N. Two force regimes are possible: *non-contact* and *contact mode*. In the *non-contact mode*, with tip-sample separations of 50-1000 Å, long-range forces such as van der Waals, electrostatic, magnetic and polarization forces can be detected. When the tip and sample are 2-3 Å apart the surfaces are virtually 'in contact' and short-range ionic repulsion forces are dominant. The work presented in this thesis was carried out in *contact mode*, since it provides the highest resolution surface imaging.

An advantage of the AFM compared to other surface science techniques is that an AFM can operate in a variety of environments, including air, a controlled atmosphere, liquid, vacuum and at low temperatures. The work presented in this dissertation was performed in air, or in a controlled atmosphere.

2.2.2 The Contact Mode

As mentioned in the previous section, when the tip and the sample are in contact, strong repulsive forces act on the two surfaces.[16] These forces, or *ionic repulsion forces*, originate from the overlapping of the electron clouds of two atoms that are brought close to each other. Since, from Pauli's exclusion principle, two electrons cannot have the same quantum numbers, for the electron clouds of two atoms to overlap, electrons must go to occupy higher unoccupied energy levels. The total energy of the system is therefore increased and repulsive forces arise. Ultimately these forces determine how close two atoms can come together. These forces are very short range and increase very steeply with decreasing interatomic

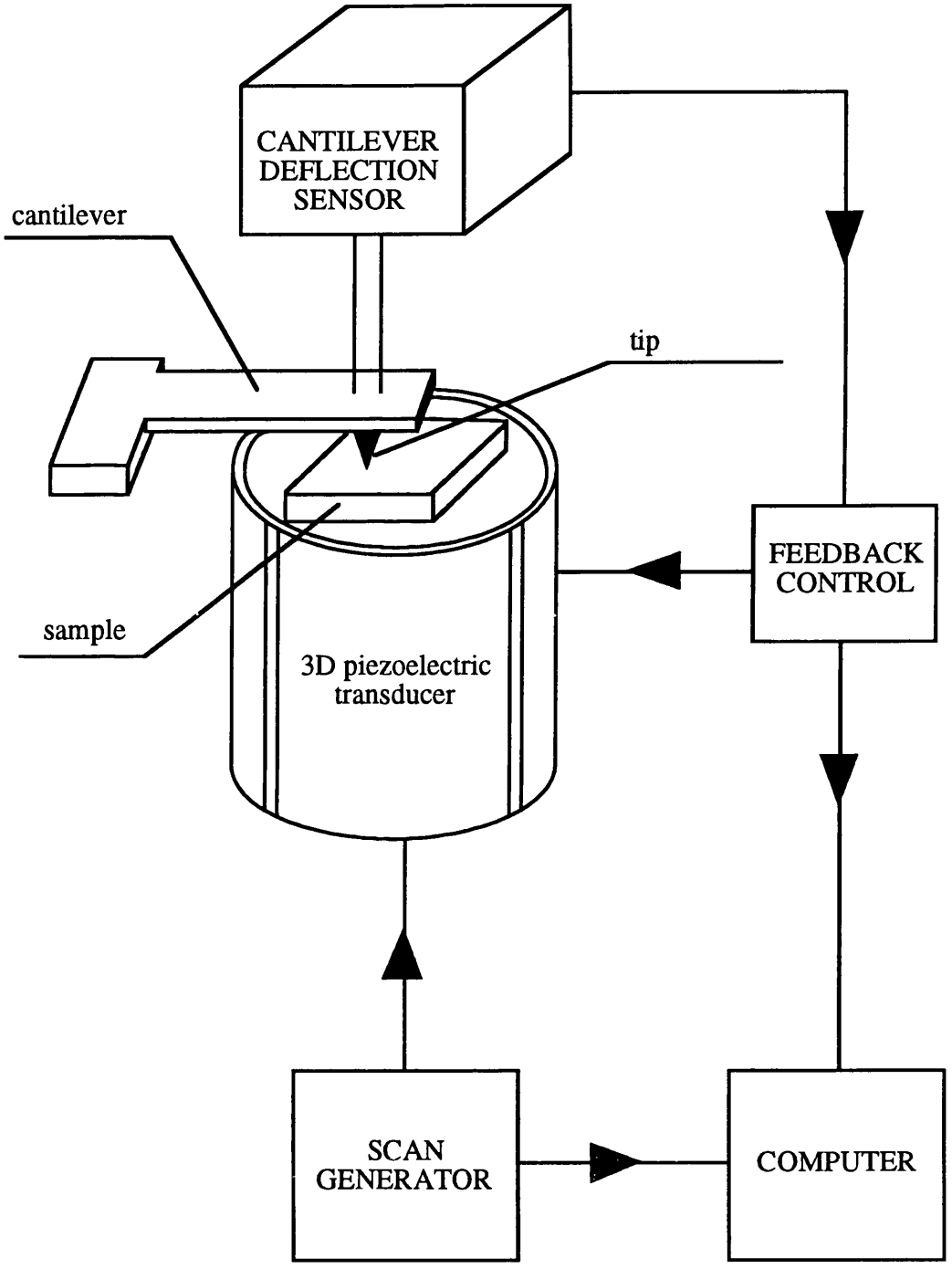

Figure 2.4. Block diagram of the AFM. Forces acting between the stylus tip and the sample surface cause small deflections of the cantilever. Deflections are measured by an optical or tunneling detector. As the tip is raster scanned across the sample, a feedback loop adjusts the sample vertical (z) position to maintain the cantilever deflection constant (*contact mode*).

distances. While there is no general equation to describe these forces, power and exponential laws have been used to model them. The phenomenological Lennard-Jones potential (figure 2.5(a)), which describes the interaction of molecules in an ideal gas, combines the attractive van der Waals and repulsive atomic potentials:

$$w(r) = 4w_o[(\sigma / r)^{12} - (\sigma / r)^6] \qquad (2.6)$$

where **r** is the intermolecular spacing. More rigorous models of repulsive forces between atoms in a gas[17] show that the repulsive force increases by a factor of up to 10^2 per angstrom as the interatomic distance decreases. It is the strong distance dependence of repulsive forces that, in a way similar to the STM, allows for high resolution in contact mode. Conversely, since longer range forces are sensed in non-contact mode, the lateral resolution that can be achieved in this mode is lower compared to contact mode. For example, attractive van der Waals forces between a sphere and a planar sample decrease as $\mathbf{r}^{-2}$,[16] which is not fast enough to allow for high lateral resolution.

In contact mode, the long range forces are still present and sum up over a large region of the tip (figure 2.5(b)).

Figure 2.6 shows the schematic of the cantilever deflection as a function of sample position (approach-retract, or force *vs.* distance curve). At large separations, the cantilever remains in its equilibrium position. When the surface is within a few hundred angstroms of the tip, an attractive van der Waals force begins to pull the cantilever toward the sample. In air, in addition to van der Waals interactions, capillary forces are also present. When the gradient of the attractive forces exceeds the force constant of the cantilever (point A in figure 2.6), the lever snaps into contact. Once the two surfaces are in contact, they move together. As the sample is pulled back from the cantilever, the two surfaces remain in contact beyond the equilibrium point B and into the attractive regime. Strong adhesive forces in vacuum and capillary force in air hold the surfaces together until point C is reached, at which point the tip pulls-off the sample. It should be remembered that the very end of the tip experiences a repulsive force whenever the tip and sample are in contact, even when the net force on the cantilever is attractive.

Van der Waals forces act on any given number of atoms and they take origin from the fact that in every atom there is an 'instantaneous' dipole moment that will act on a nearby atom to generate an induced dipole moment.[16] For distances less than 200 Å, the van der Waals potential for two atoms is of the form:

$$\mathbf{U(r)} = -C / r^6 \qquad (2.7)$$

where **C** is a constant and **r** is the interatomic distance. For separations greater than 200 Å, the potential assumes the *retarded* form:

$$\mathbf{U_r(r)} = -B / r^7 \qquad (2.8)$$

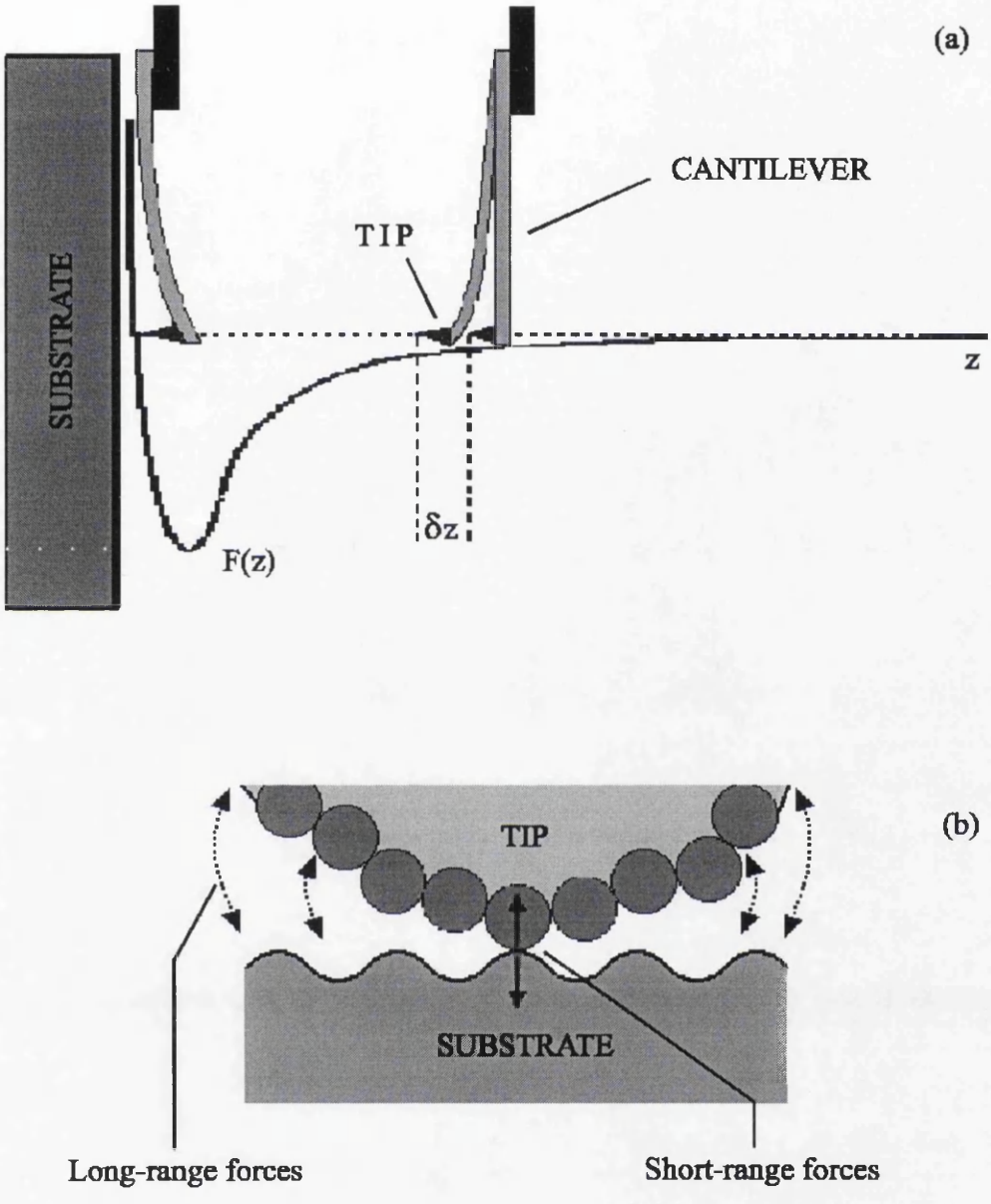

Figure 2.5. (a) Schematic diagram of the forces experienced by the tip as it approaches the substrate. In the attractive region, the forces of interaction cause a deflection of the tip toward the surface. When the tip and sample are 2-3 Å apart, the interaction is strongly repulsive. (b) Schematic diagram showing that long-range forces between the tip and sample continue to exist even after the two surfaces have come together.

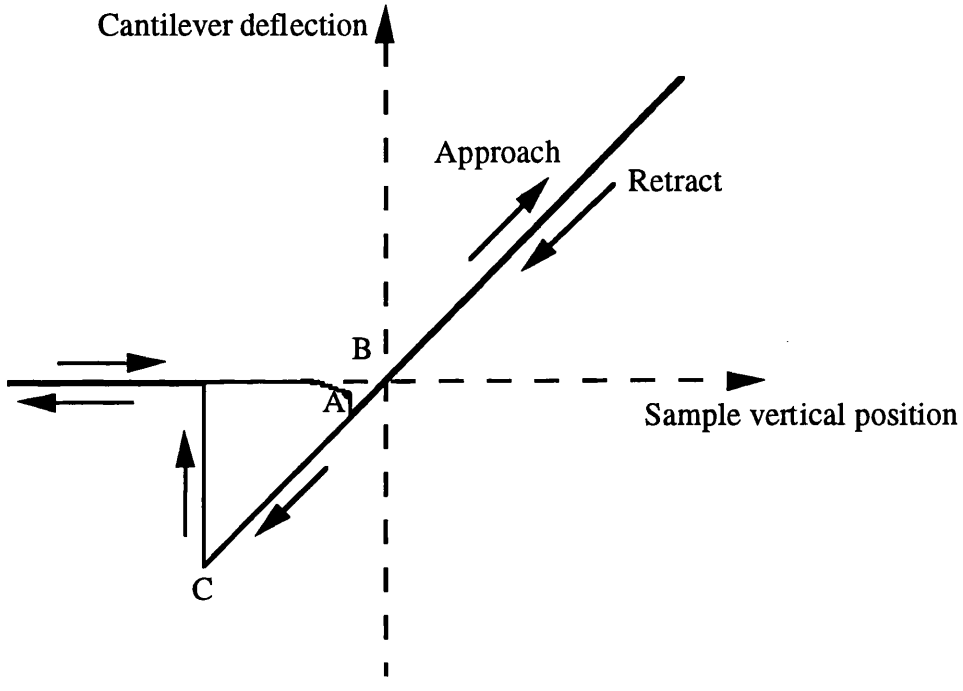

Figure 2.6. Schematic plot of cantilever deflection *vs.* sample position. As the sample approaches the cantilever, the two are pulled together by van der Waals and capillary forces. When the force gradient exceeds the cantilever force constant, the tip snaps into contact (point A). When the sample is retracted, capillary forces hold the surfaces together until point C is reached and hysteresis is observed.

For a sphere of radius R and a planar surface, the non-retarded van der Waals potential is given by

$$U(r) = -AR/6r \qquad (2.9)$$

where **A** is the Hamaker constant. Values of A range from $0.4 \cdot 10^{-19}$ to $4 \cdot 10^{-19}$ J. A rigorous description of van der Waals forces includes many-body interactions and retarded effects and is beyond the scope of this thesis.

Another force which pulls tip and surface together in air is the capillary force, which is always present under ambient conditions and arises from the formation of a meniscus on a water film between the cantilever and the sample. This meniscus strongly draws the tip towards the sample. At sufficiently high relative vapor pressures, the capillary condensate forms a ring around the contact circle. The collar shaped liquid-vapor interface is bounded by circles of radius ρ_k and its mean curvature depends on the relative humidity according to the Kelvin equation:[16]

$$\frac{1}{r_1} + \frac{1}{r_2} = \frac{\Re T \ln(p/p_s)}{\gamma V} \qquad (2.10)$$

where $\Re$ is the universal gas constant, T the absolute temperature, p/p_s the relative humidity, γ the surface tension of the liquid, V the molar volume of the liquid and r_1 and r_2 are defined in figure 2.7. The difference between the liquid and the vapor pressure is equal to the Laplace pressure:

$$P = \gamma\left(\frac{1}{r_1} + \frac{1}{r_2}\right) \qquad (2.11)$$

By the sign convention for these formulae, r_1 and r_2 are negative and positive, respectively. If r_k is defined as:

$$r_k = -r_1 \qquad (2.12)$$

and considering that for most systems, $1/\rho_k \approx 1/r_2 << 1/r_k$, the Laplace's equation (2.11) becomes:

$$P = -\gamma \frac{1}{r_k} \qquad (2.13)$$

For a sphere of radius R ($R \gg r_k$) on a planar surface and under the approximation that the minimum separation of the two surfaces, D_0, vanishes, the Laplace pressure contributes to the adhesion force with:[16]

$$F \approx 4\pi R\gamma\cos\theta \qquad (2.14)$$

where the contact angle θ is defined in figure 2.7. In the more general case, if D_0 is non zero the relation (2.14) becomes:

$$F \approx 4\pi R\gamma\cos\theta\left(1 - \frac{D_0}{2r_k\cos\theta}\right) \qquad (2.15)$$

When the two surfaces are wetted with two different contact angles the relation (2.14) becomes:

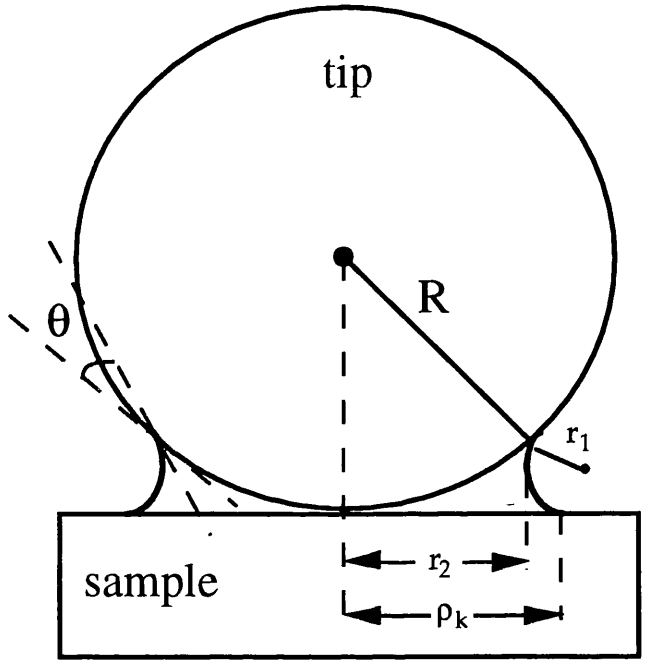

Figure 2.7. Schematic of water meniscus between a spherical tip and a planar surface.

$$F \approx 2\pi R\gamma(\cos\theta_1 + \cos\theta_2) \qquad (2.16)$$

2.2.3 Non-Contact and Tapping Modes

When the AFM is operated in *non-contact mode,*[18] the lever is vibrated at its resonant frequency. The distance to the surface is then decreased until the force gradient of the interaction modifies the stiffness of the cantilever and, as a consequence, changes its resonant frequency. A repulsive force increases the resonant frequency, while an attractive force lowers the resonant frequency. The feedback loop maintains constant either the amplitude (slope detection) or the frequency (FM-detection). In either cases profiles of *constant gradient* are measured. Force gradients between 10^{-5} and 10 N/m are measured, corresponding to forces between 10^{-13} and 10^{-7} N, at a distance of 10 nm. When the AFM is operated in non-contact mode, the probability that the tip sticks to the surface is large, therefore stiff cantilevers have to be used.

The so-called *tapping mode*[19, 20] is an hybrid form of contact and non-contact mode AFM. The cantilever vibrates at its resonant frequency. Upon approaching the sample, the tip briefly touches, or *taps*, the surface at the bottom of each swing resulting in a decrease in oscillation amplitude. The feedback keeps this decrease of amplitude at a preset value and a topographic image can be obtained. Since the restoring cantilever force has to be higher than the capillary force, stiff cantilevers (force constants between 10 and 100 N/m) and oscillation amplitudes between 30 and 100 nm need to be used. Since lateral shear forces are minimized, the technique is used for imaging soft samples, such as biological ones, to avoid the sample being swept away by the tip.[21, 22, 23] However, recently[24] it was shown that in tapping mode forces are in the same range of those applied in contact mode. For normal forces to be minimized the operating point has to be as far as possible on the low frequency side of the non-contact cantilever resonance.

2.2.4 Cantilevers

The heart of any scanning probe microscope is the tip interacting with the surface. In the case of an atomic force microscope it is mounted on a flexible cantilever. The first cantilevers used were made out either of wires or metal foils. The tips were either chemically etched in a way similar to the STM tips, or were made of little diamond fragments attached to the metal foils. Later, Albrecht *et al.* developed a method for microfabricating cantilevers with integrated tips attached to them.[25] Rectangular and V-shaped microfabricated cantilevers, made of silicon oxide or silicon nitride, are today the most widely used force sensors and are

commercially available.

In order for the cantilevers to detect small forces, their spring constant has to be as small as possible. On the other hand, for fast scan rates to be possible and vibrations effects to be minimized, the resonant frequency has to be as high as possible. Therefore, the lever's mass and consequently the lever's dimensions have to be small. Typical dimensions for microfabricated cantilevers are 100-200 μm in length, 20 μm in width and 0.5-1 μm in thickness. Typical spring constants for levers used in contact mode are in the 0.01 to 1 N/m range. If the lever is too soft it sticks to the surface and does not slide. On the other hand, in non-contact modes the lever has to be stiff enough to prevent the tip from snapping into contact with the sample. Furthermore, the mechanical Q of the lever has to be high to enable one to measure small force gradients.

While microfabrication techniques are able to provide levers with reasonably reproducible lateral dimensions, the size and exact geometry of the tip are difficult to control. Due to its crucial role in all AFM measurements, at present the tip imposes the greatest limitation on the reproducibility of AFM results.

2.2.5 Deflection Detection Methods

The deflection sensor is another important part of an AFM since it has to be sensitive enough to detect cantilever motions smaller than 0.1 Å. Furthermore, the detector should not influence the cantilever position in any way. The first detection sensor was based on electron tunneling.[14] The back side of the cantilever was coated with a conducting film and an arrangement similar to an STM was used. While the technique is very sensitive and allows distances as small as 0.01 Å to be detected, it is also very sensitive to contamination present in the tunneling gap. Such contamination can cause the tunneling tip to exert forces as large as 10^{-6} N on the cantilever.[26, 27] These forces would not have noticeable effects on rigid samples, but, since the cantilever is soft, they can cause considerable cantilever deflections. Furthermore, contamination is not stable in time, so that an unpredictable amount of noise is generated. This makes the tunneling detection method impractical for AFM operation in air.

Other deflection methods involve optical techniques. In these cases the sensor is distant from the lever and the interaction forces between the sensor and the cantilever are in most cases negligible. Optical detection systems can be classified into two types: ones using interferometry and those using optical beam deflection. In the interferometer method, an optical fiber is brought to within a few micrometers of the back of the lever to form an interference cavity. The output signal is the intensity resulting from the interference of the light beams reflected at the end of the fiber and

at the cantilever.[28, 29, 30] Sensitivity of 10^{-4} Å/(Hz)$^{1/2}$ has been reported for this method. One of the advantages of the interferometric detection method is that it can be used on curved cantilevers such as wires. This method is especially, but not exclusively, used in non-contact modes, where the AFM senses force gradients in the long range forces.

The most widely used deflection detection method is the optical lever deflection method,[31] whose principle of operation is illustrated in figure 2.8. A light beam is reflected off the back of the cantilever, which is often coated with a metal film to enhance reflection. The position of the reflected beam is monitored by a position sensitive detector. Since the detector is positioned far away from the lever, typically a few centimeters, a small variation in the cantilever deflection causes a large displacement of the beam position on the detector. Sensitivity comparable to that obtained by interferometric detection is achieved. The advantage of this method is its simplicity of implementation and that it can be easily extended to detect forces in two orthogonal directions. Using a four-quadrant photodiode, both the vertical and torsional motion of the cantilever can be detected simultaneously.[32, 33]

For the optical lever deflection method, the signal-to-noise ratio is shot-noise limited and results to be:[34]

$$\frac{S}{N} = \frac{6d\delta z}{\lambda l}\left(\frac{I_0}{2e\Delta f}\right)^{1/2} \qquad (2.17)$$

where **d** and **l** are the cantilever width and length respectively, λ the light wavelength, δz the cantilever vertical deflection, I_0 the laser power, **e** the electron charge and Δf the frequency bandwidth. For typical cantilever dimensions (d≈l/10-l/5), laser power 100 μW-1 mW and light wavelength in the red region of the optical spectrum, the minimum detectable δz is of order of 10^{-4} Å/(Hz)$^{1/2}$.

2.2.6 Contrast Mechanism in Contact Mode AFM

An understanding of the contrast mechanism in contact mode AFM is still in its infancy. Despite the early promises of 'atomic resolution', similar to that achieved in STM, to date the ability of the AFM to image single point defects, i.e. achieve 'true' atomic resolution, is still controversial. The only literature report of atomic resolution is that by Ohnesorge and Binnig.[35] The authors obtained atomic resolution images of the (1014) plane of calcite in aqueous environment at very small attractive forces, i.e. 10-40 pN, at tip-sample separations of 3-4 Å. In addition, they could image atomic-scale kinks, i.e. single point defects, at monatomic step edges. This is due to the fact that the van der Waals and capillary

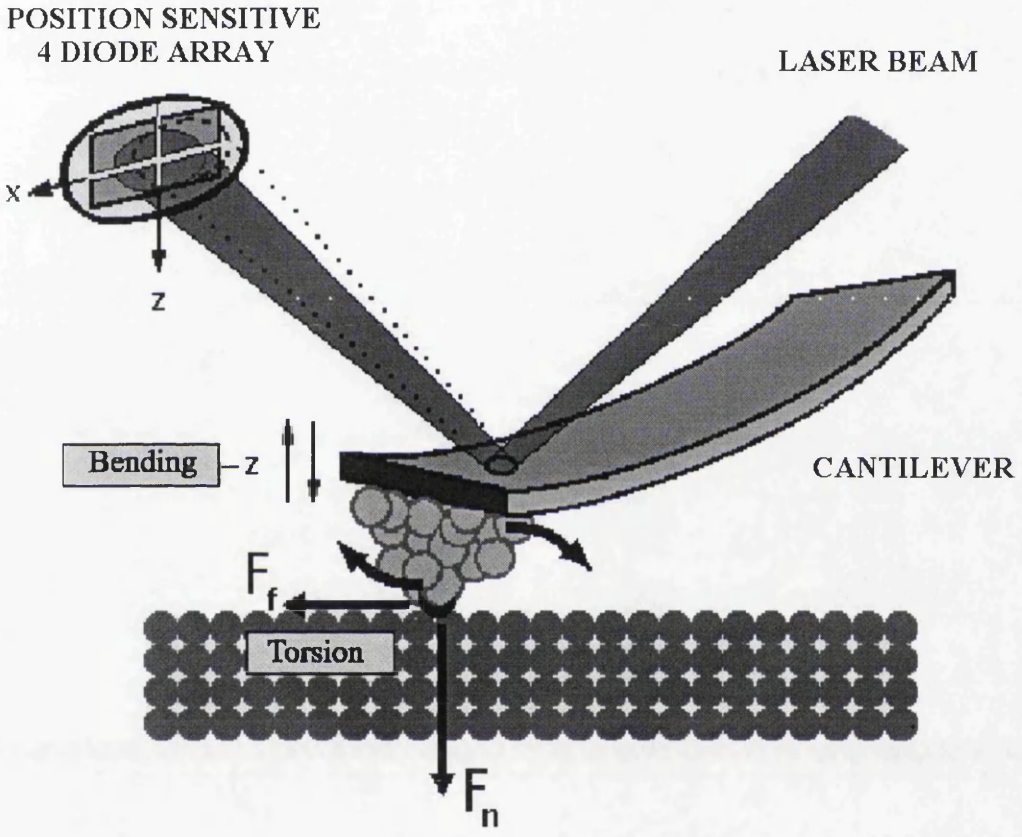

Figure 2.8. Setup of the optical lever deflection method. A laser beam is reflected off the back of the cantilever. The position of the reflected beam is measured by a four-quadrant photodiode, allowing for the simultaneous detection of the cantilever bending and torsion.

forces are greatly reduced in a liquid environment. However, such small forces are difficult to obtain in UHV or air and no conclusive AFM experiments demonstrating atomic resolution in these environments have been reported so far.

Besides the fundamental question on the highest resolution achievable in contact mode AFM, there is the need to understand the imaging/contrast mechanism that is behind the multitude of AFM images in which atomic lattices are resolved. To date such images have been obtained on a variety of surfaces, such as layered materials, ionic surfaces, metals and organic films, in UHV as well as in air and controlled atmosphere. The fact that such images are often obtained while applying forces up to a hundred nN, has raised several questions since it is impossible for a single atom to bear loads that high.[36, 37] Moreover, if the contact occurs over many atoms, what is the mechanism responsible for the lattice periodicity observed in AFM images?

The first atomic level AFM images were obtained in air by Albrecht and Quate on highly pyrolytic boron nitride.[38] In an attempt to analyze their experimental results, they applied the Gordon-Kim theory[17] to find the tip-sample separation over the boron and the nitrogen atoms at the imaging load of their experiment and assign the maxima in the AFM images. Their method, however, is not applicable if the interactions involve multiple atoms. A many-body Lennard-Jones potential was used by Gould *et al.*[39] to model the interaction of a single carbon atom with a graphite surface. By using a double-atom tip they were able to reproduce a variety of images compatible with experimental results. A molecular dynamics (MD) simulation by Abraham and Batra[40] proposed that the experimental images of graphite, such as those where only every other atom is observed,[41] could be obtained if it were a graphite 'flake', rather than a single atom at the tip, to scan the graphite surface. Such a possibility has also been suggested by Pethica for STM images of graphite[42] and by Overney *et al.*[43] for AFM imaging of layered materials. Such a 'flake' could be picked up by the tip during scanning. Its role would be to spread the applied load across a large area. If the two surfaces are in registry, the interaction is coherent and the images would reflect the translational symmetry of the surface. In the case of orientational misalignment between the 'flake' and the substrate, the corrugation would decrease.

While the above model may explain AFM images of layered materials, it is not general enough to explain lattice resolution images obtained on non-layered materials, such as ionic crystals or metals. Another model that has been suggested to explain lattice resolution images in ambient conditions considers the role of the water lubricant film present on any surface in air.[44] The authors suggest that this water film supports most of the load and that the 'atomic' resolution of AFM images is due to a single 'floating' microtip penetrating this lubricant layer. This

model, however, still does not explain lattice resolution images obtained on layered and non-layered materials in UHV. To the author's knowledge, no UHV AFM studies of metals has been reported.

Two literature reports have suggested that atomic resolution on ionic crystals could be achieved by the electrostatic forces that arise between the surface of an alkali halide and a polarizable tip and that the best conditions for atomic resolution exist when the tip scans the surface at a distance of about 3-5 Å from the surface.[45, 46]

Clearly, one of the problems in formulating a theoretical description of the contrast mechanism in AFM lies in the difficulty to account for all the forces acting on tip and sample. It was soon recognized that the geometry of the tip has a profound effect on the van der Waals forces between the two electrodes.[47, 48] As already pointed out earlier in this chapter, attractive forces play a role even when tip and sample are already 'in contact' and the interaction between the (eventual) outmost tip atom and the sample atoms is repulsive. Ciraci[49] proposes that atomic resolution can be achieved only if (i) the tip is sharp, to avoid strong long-range forces and (ii) the tip apex is atomically sharp. A multiasperity tip that is incommensurate the substrate would cause the corrugation to be washed out. It is also recognized that plastic deformation may occur at the tip apex and that in this case the force images may reflect the periodic deformation induced by the tip.

Finally, a 'Moiré pattern' mechanism has been proposed by Pethica and Sutton.[50] In this model, the measured signal, i.e. the AFM contrast, is the result of the correlation of the sample and tip lattices calculated over the contact area. If the two lattices have a simple integer ratio and the lattice is perfect, there will be a constant contrast regardless of the size of the contact region. If, however, the presence of defects or plastic deformation breaks the phase relation between the two lattices, or if the lattices are not in an integer ratio, the two signals are incoherent and the contrast is washed out. In other words, the size of the contact region would have to be smaller than the coherence length between the signals for contrast to be maintained. Then, this model implies that to obtain maximum resolution the range of the interaction, i.e. the contact area, have to be as small as possible, in agreement with other models proposed and with one's intuition. The author points out that this model does not require that the interaction mechanism be known and that most likely different mechanisms are possible for different surfaces and tips.

Further discussion on imaging mechanisms will be found in chapter 3, where the use of the AFM as a friction force microscope (FFM) will be described, and in chapter 7, where experimental results obtained on mica and gold on mica will be presented.

References

[1] G. Binnig, H. Rhorer, *Helvetica Physica Acta*, **55**, 726 (1982).

[2] R. B. Floyd, D. G. Walmsley, *J. Physics C: Solid State Physics*, **11**, 4601 (1978).

[3] J. G. Simmons, *J. Appl. Phys.*, **34**, 1793 (1963).

[4] M. C. Payne, J. C. Inkson, *Surf. Sci.*, **159**, 485 (1985).

[5] J. Tersoff, D. R. Hamann, *Phys. Rev. Lett.*, **50**, 1998 (1983).

[6] J. Tersoff, D. R. Hamann, *Phys. Rev. B*, **31**, 805 (1985).

[7] P. Sautet, C. Joachim, *Phys. Rev. B*, **38**, 12338 (1988).

[8] P. Sautet, C. Joachim, *Ultramicroscopy*, **42-44**, 115 (1992).

[9] J. C. Dunphy, D. F. Ogletree, M. B. Salmeron, P. Sautet, M.-L. Bocquet, C. Joachim, *Ultramicroscopy*, **42-44**, 490 (1992).

[10] B. J. McIntyre, P. Sautet, J. C. Dunphy, M. Salmeron, G. A. Somorjai, *J. Vac. Sci. Technol. B*, **12**, 1751 (1994).

[11] M. Salmeron, G. Neubauer, A. Folch, M. Tomitori, D. F. Ogletree, P. Sautet, *Langmuir*, **9**, 3600 (1993).

[12] D. A. Berlincourt, D. R. Curran, H. Jaffe in *Physical Acoustics: Principles and Methods*, W. P. Mason edt., vol. I-part A (Academic Press: New York, 1964).

[13] G. Binnig, D. P. E. Smith, *Rev. Sci. Instrum.*, **57**, 1688 (1986).

[14] G. Binnig, H. Rhorer, Ch. Gerber, E. Weibel, *Surf. Sci.*, **131**, L379 (1983).

[15] G. Binnig, C. F. Quate, Ch. Gerber, *Phys. Rev. Lett.*, **56**, 930 (1986).

[16] J. N. Israelachvili, *Intermolecular and Surface Forces* , 2nd edition (Academic Press:

San Diego, 1992).

[17] R. G. Gordon, Y. S. Kim, *J. Chem. Phys.*, **56**, 3122 (1972).

[18] Y. Martin, C. C. Williams, H. K. Wickramasinghe, *J. Appl. Phys.*, **61**, 4723 (1987).

[19] Q. Zhong, D. Innis, K. Kjoller, V. B. Elings, *Surf. Sci. Lett.*, **290**, L688 (1993).

[20] Digital Instruments, Santa Barbara, CA, USA.

[21] M. Radmacher, R. W. Tillmann, M. Fritz, H. E. Gaub, *Science*, **257**, 1900 (1992).

[22] R. Hoeper, R. K. Workman, D. Cheng, D. Sarid, T. Yadav, J. C. Withers, O. R. Raouf, *Surf. Sci.*, **311**, L731 (1994).

[23] K. Umemura, H. Arakawa, A. Ikai, *Jpn. J. Appl. Phys. Pt. 2*, **32**, L1711 (1993).

[24] J. P. Spatz, S. Sheiko, M. Moller, R. G. Winkler, P. Reineker, O. Marti, *Nanotechnology*, **6**, 40 (1995).

[25] T. R. Albrecht, S. Akamine, T. E. Carver, C. F. Quate, *J. Vac. Sci. Technol. A*, **8**, 3386 (1990).

[26] U. Dürig, J. K. Gimzewski, D. W. Pohl, *Phys. Rev. Lett.*, **57**, 2403 (1986).

[27] M. Salmeron, D. F. Ogletree, C. Ocal, H. C. Wang, G. Neubauer, W. Kolbe, G. Meyers, *J. Vac. Sci. Technol. B*, **9**, 1347 (1991).

[28] R. Erlandsson, G. Hadziioannou, C. M. Mate, G. M. McClelland, S. Chiang, *J. Vac. Sci. Technol. A*, **6**, 266 (1988).

[29] D. Rugar, H. J. Mamin, R. Erlandsson, J. E. Stern, B. D. Terris, *Rev. Sci. Instrum.*, **59**, 2337 (1988).

[30] D. Rugar, H. J. Mamin, P. Günther, *Appl. Phys. Lett.*, **55**, 2588 (1989).

[31] S. Alexander, L. Hellemans, O. Marti, J. Schneir, V. Elings, P. K. Hansma, M.

Longmire, J. Gurley, *J. Appl. Phys.*, **65**, 164 (1988).

[32] O. Marti, J. Colchero, J. Mlynek, *Nanotechnology*, **1**, 141 (1990).

[33] G. Meyer, N. M. Amer, *Appl. Phys. Lett.*, **57**, 2089 (1990).

[34] M. Allegrini, E. Arpa, C. Ascoli, P. Baschieri, F. Dinelli, C. Frediani, M. Labardi, A. Lio, T. Mariani, L. Vanni, *Rivista del Nuovo Cimento D- Condensed Matter*, **15**, 279 (1993).

[35] F. Ohnesorge, G. Binnig, *Science*, **260**, 1451 (1993).

[36] F. F. Abraham, I. P. Batra, S. Ciraci, *Phys. Rev. Lett.*, **60**, 1314 (1988).

[37] W. Zhong, G. Overney, D. Tománek, *Europhys. Lett.*, **15**, 49 (1991).

[38] T. R. Albrecht, C. F. Quate, *J. Appl. Phys.*, **62**, 2599 (1987).

[39] S. A. C. Gould, H.-J. Butt, P. K. Hansma, *Proceedings of the STM90/NANO I Conference, Baltimore, MA (USA)*, July 23-27 1990.

[40] F. F. Abraham, I. P. Batra, *Surf. Sci.*, **209**, L125 (1989).

[41] E. Meyer, H. Heinzelmann, P. Grütter, Th. Jung, Th. Weisskopf, H. R. Hidber, R. Lapka, H. Rudin, H.-J. Güntherodt, *J. Microscopy*, **152**, 269 (1988).

[42] J. B. Pethica, *Phys. Rev. Lett.*, **57**, 3235 (1987).

[43] G. Overney, D. Tománek, W. Zhong, Z. Sun, H. Miyazaki, S. D. Mahanti, H.-J. Güntherodt, *J. Phys.: Cond. Matter*, **4**, 4232 (1992).

[44] H. J. Mamin, E. Ganz, D. W. Abraham, R. E. Thomson, J. Clarke, *Phys. Rev. B*, **34**, 9015 (1986).

[45] F. J. Giessibl, *Phys. Rev. B*, **45**, 13815 (1992).

[46] A. L. Shluger, A. L. Rohl, D. H. Gay, R. T. Williams, *J. Phys.: Condens. Matter*, **6**, 1825 (1994).

[47] S. Ciraci in *Basic Concepts and Applications of Scanning Tunneling Microscopy and Related Techniques*, J. Behm, H. Rhorer, N. Garcia edts. (Kluwer Academic Publishers: Dordrecht, 1990).

[48] S. Ciraci, E. Tekman, A. Baratoff, I. P. Batra, *Phys. Rev. B*, **46**, 10411 (1992).

[49] S. Ciraci in *Forces in Scanning Probe Methods*, NATO ASI Series E: Applied Sciences, vol. 286 (Kluwer Academic Publishers: Dordrecht, 1995).

[50] J. B. Pethica, A. P. Sutton in *Forces in Scanning Probe Methods*, NATO ASI Series E: Applied Sciences, vol. 286 (Kluwer Academic Publishers: Dordrecht, 1995).

Chapter 3

An Introduction to Friction

3.1 Introduction

Friction, wear and adhesion are everyday phenomena of significant economical importance since they are responsible for energy and material losses of great magnitude. For centuries, the science of tribology has received the most attention from mechanical engineers aiming to improve the efficiency and precision of mechanical devices. It was known since the fifteenth century to Leonardo da Vinci that a force is necessary to move a body placed in contact on another. Based on empirical observations, in the late seventeenth century the French scientist Amontons and a century later the French engineer Coulomb came to the conclusion that sliding between two bodies in contact occurs when the tangential force reaches a value proportional to the normal load acting between them. This is expressed by the Amontons' law as:[1, 2]

$$F = \mu L \qquad (3.1)$$

where F is the frictional force and L the normal load. Furthermore, the constant of proportionality μ, the friction coefficient, does not depend on the apparent contact area, depends only weakly on the surface roughness and is constant for a given pair of materials. The mechanism of friction was thought to originate from the force necessary to slide one surface's asperities over the other's. However, this process is conservative in energy and therefore the dissipative nature of friction could not be explained. Three centuries later the mechanisms of energy dissipation involved in friction processes still have not been fully explained.

It was later recognized, first by Desagulier in the eighteenth century, but more formally only in this century, that adhesive forces existing between bodies in contact contribute to frictional forces. In the words of Tabor and Bowden[3] "Friction is the force required to shear intermetallic junctions plus the force required to plow the surface of the softer metal by the asperities on the harder surface", thus friction can be seen as the sum of two independent terms, an adhesive one and a ploughing one. While their observations were based on experiments performed on metallic samples, the model can be generalized. They also recognized that, due to surface roughness, the real area of contact is in general much smaller than the geometrical or apparent

contact area (figure 3.1) and is the important parameter in frictional processes.

In the adhesive model they first proposed, the frictional force is proportional to the real contact area, not the load:

$$F = \tau A \qquad (3.2)$$

where F is the frictional force, τ the shear stress and A the contact area.

In the case of plastic contact, Amontons' law is recovered easily. In fact, the contact area is in this case given by:

$$A = L/Y \qquad (3.3)$$

where Y is the yield strength. Inserting relation (3.3) in (3.2) gives back Amontons' law.

In the case of rough surfaces, asperities are distributed in height and it has been shown that the total contact area is proportional to the total applied load.[4] In fact, when two surfaces first come into contact, only few asperities touch. As the load increases the number of asperities in contact and the real contact area increase. It is the height distribution of the asperities that makes the total contact area proportional to the total load. It is then clear that, as far as the contact between macroscopic bodies occurs through many asperities or in the plastic regime, a relation between the frictional force and the normal load equivalent to Amontons' law will be observed.

Therefore, it would be desirable to eliminate the asperities. Furthermore, it is now well understood that friction, adhesion, lubrication are all phenomena that are controlled by processes taking place at the atomic and molecular scale. Therefore, techniques that can probe mechanics at such small scales are necessary. Still the main difficulty in investigating frictional processes lies in the fact that they take place at the buried interface at a time scale ranging from nano to microseconds. For that, new techniques that are capable of investigating the buried interface at those time scales are needed. Finally, theories that can address the mechanisms of energy dissipation have to be developed. In fact, although it has been known for a long time that frictional energy dissipates as heat, neither the macroscopic nor the microscopic mechanisms have been fully elucidated.

Still, it should not be forgotten that tribology remains primarily the domain of engineers and that its goal is most often to reduce friction and limit wear. Therefore, substantial studies should be devoted to the understanding of lubrication mechanisms. For a long time it has been known that reduced adhesion and friction are experienced by two metals whose surfaces are contaminated by preventing metal-metal contacts.[3] Often a lubricant layer of some sort is used in order to reduce friction and avoid damage of two shearing surfaces. Nevertheless, the mechanisms of liquid and boundary lubrication[5] are still poorly understood. It will probably take many years before some of the ideas and innovative concepts now

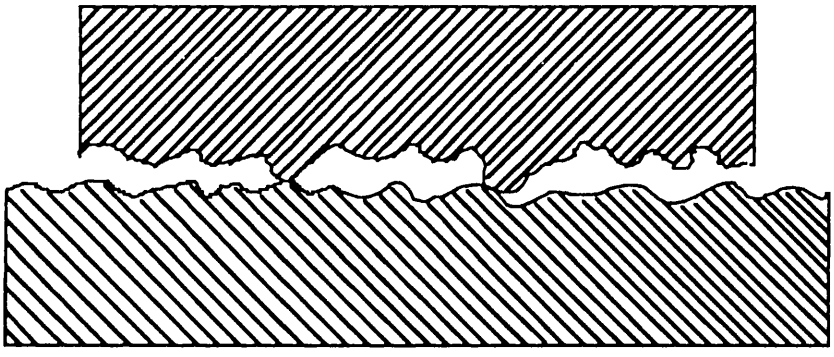

Figure 3.1. Schematic representation of two macroscopic surfaces in contact. Contact occurs only at a few asperities, so that the real contact area is much smaller than the apparent area of contact.

being elucidated by surface scientists, chemists and physicists will make their way in the technological world of tribology, but the potential for that to happen has never been greater.

Several techniques and molecular modelling schemes have been developed in the past several years that are enabling scientists to take a new look at frictional processes. Fifty years ago, scientists and engineers could only rely on optical microscopy and later on electron microscopy. Today, very high resolution techniques such as the surface force apparatus (SFA), the quartz crystal microbalance (QCM) and scanning probe microscopies are available. In addition, theorists are now able to perform sophisticated computer calculations and simulations that offer the possibility to study the atomic scale processes taking place at the sliding interface.

Before reviewing some of the experimental techniques mentioned above and the present understanding of energy dissipation mechanisms, the theoretical background necessary to the understanding of adhesion of solids in elastic conditions will be described.

3.2 The Models of Contact Mechanics

The field of contact mechanics was developed to describe the elastic contact between bodies. The first model that satisfactorily analyzed the stresses generated when two elastic bodies come into contact was introduced in 1882 by Hertz.[6] His theory was prompted by studies of optical interference in the gap between two glass lenses and the concern that the pattern of interference fringes could be influenced by elastic deformation of the lenses.

Contact mechanics theories predict the shape of the area of contact between two bodies and how it grows in size with increasing load.[7] Furthermore, the magnitude and distribution of surface tractions (normal and tangential) are also computed. Most contact mechanics models assume that the contact area is small compared to the dimensions of each body (non-conforming surfaces). In this way, the stresses can be considered localized to regions close to the contact area and independent of the stresses in the bulk of the bodies. Moreover, the stresses are calculated by considering each body as a semi-infinite elastic solid bounded by a plane, i.e. an elastic half-space and the deformations are assumed to be sufficiently small. In this way, the boundary conditions are simplified and the linear theory of elasticity can be used. The elastic equations are written for the components of the

stress and strain and the normal and tangential displacements of any point from the undisturbed position under the specified boundary conditions are found. The models that will be described here also have a circular contact area (the bodies are solids of revolution) with both the normal and tangential loading being rotationally symmetrical about the normal direction z.

3.2.1 The Hertz Theory

In the Hertz theory, the bodies in contact are assumed frictionless, so that only normal tractions are to be considered. In addition, each surface is considered topographically smooth on both the micro and macro scale. Given two solids of revolution of radii $\mathbf{R_1}$ and $\mathbf{R_2}$ (relative radius of curvature $R=(1/R_1 + 1/R_2)^{-1}$), Young's moduli E_1 and E_2 and Poisson's ratios ν_1 and ν_2, a circular contact area of radius **a**, the Hertz theory results are:

Contact radius
$$a = \left(\frac{3LR}{4E^*}\right)^{1/3} \tag{3.4}$$

Compression
$$\delta = \frac{a^2}{R} = \left(\frac{9L^2}{16RE^{*2}}\right)^{1/3} \tag{3.5}$$

Maximum Pressure
$$P_o = \frac{3L}{2\pi a^2} = \left(\frac{6LE^{*2}}{\pi^3 R^2}\right)^{1/3} \tag{3.6}$$

where **L** is the total normal load compressing the solids and **E*** is the reduced elastic modulus defined by:

$$\frac{1}{E^*} = \frac{1-\nu_1^2}{E_1} + \frac{1-\nu_2^2}{E_2} \tag{3.7}$$

The stresses predicted by the Hertz theory are compressive except that at the very edge of the contact, where the radial stress is tensile.

3.2.2 The JKR and DMT Theories

The Hertz theory predicts the relationship between the applied load and the contact radius in the absence of adhesive interactions. This assumption stood up for almost a century due to the experimental observation that the contact area between two solids (except that for very soft metals) falls to zero when the load is removed and no tensile force is required to separate them. However, as two ideal

surfaces are approached, they will first experience an attractive force, come into contact and then start to repel each other. In the ideal case, the variation of force per unit area as a function of separation can be derived from the Lennard-Jones potential. The potential and force profiles are shown in figure 3.2 (a) and (b) (in figure 3.2(b) the repulsive forces are positive). As two bodies are approached they will jump into contact as a result of an instability occurring at a certain distance z_A. As they are retracted there will be a jump-out from z_0 to z_R. Therefore, a tensile force, the adhesion force, is necessary to separate the surfaces. The adhesion force represents the limit of stability of a system and depends on the stiffness of the measuring apparatus. In many cases, however, the work $\bar{\gamma}$ necessary to separate the surfaces from $z=z_0$ to $z=\infty$ and not the force is measured. The reason why this force is not usually observed is due to the roughness of surfaces for which the asperity height is usually higher than the range of such forces.

The effect of adhesive forces on the contact problem was first described in 1971 by Johnson, Kendall and Roberts in the theory now known as JKR theory.[8] The problem was solved in the case of smooth, non-conforming surfaces which make contact over a circular area of radius **a**. The results of this theory are the following:

(i) the contact area is larger than that in the Hertz theory,

(ii) the contact area remains finite until a critical negative pull-off force is reached.

The dependence of the contact radius on the load **L**, the pull-off force (force of adhesion) $\mathbf{L_c}$, the contact radius at pull-off $\mathbf{a_c}$, the deformation δ are determined:

Contact radius

$$a^3 = \frac{3}{4}\frac{R}{E^*}\left(L + 3\pi R\bar{\gamma} + \sqrt{6\pi R\bar{\gamma}L + (3\pi R\bar{\gamma})^2} \right) \qquad (3.8)$$

Pull-off force

$$L_c = -\frac{3}{2}\pi R\bar{\gamma} \qquad (3.9)$$

Contact radius at pull-off

$$a_c = \left(\frac{9}{8}\frac{\pi\bar{\gamma}R^2}{E^*} \right)^{1/3} \qquad (3.10)$$

Deformation

$$\delta = \frac{a^2}{R} - \left(\frac{2\pi\bar{\gamma}}{E^*} \right)^{1/2} a^{1/2} \qquad (3.11)$$

where **R** and **E*** have been defined in the previous section.

Relation (3.8) can be re-written in an implicit form as:

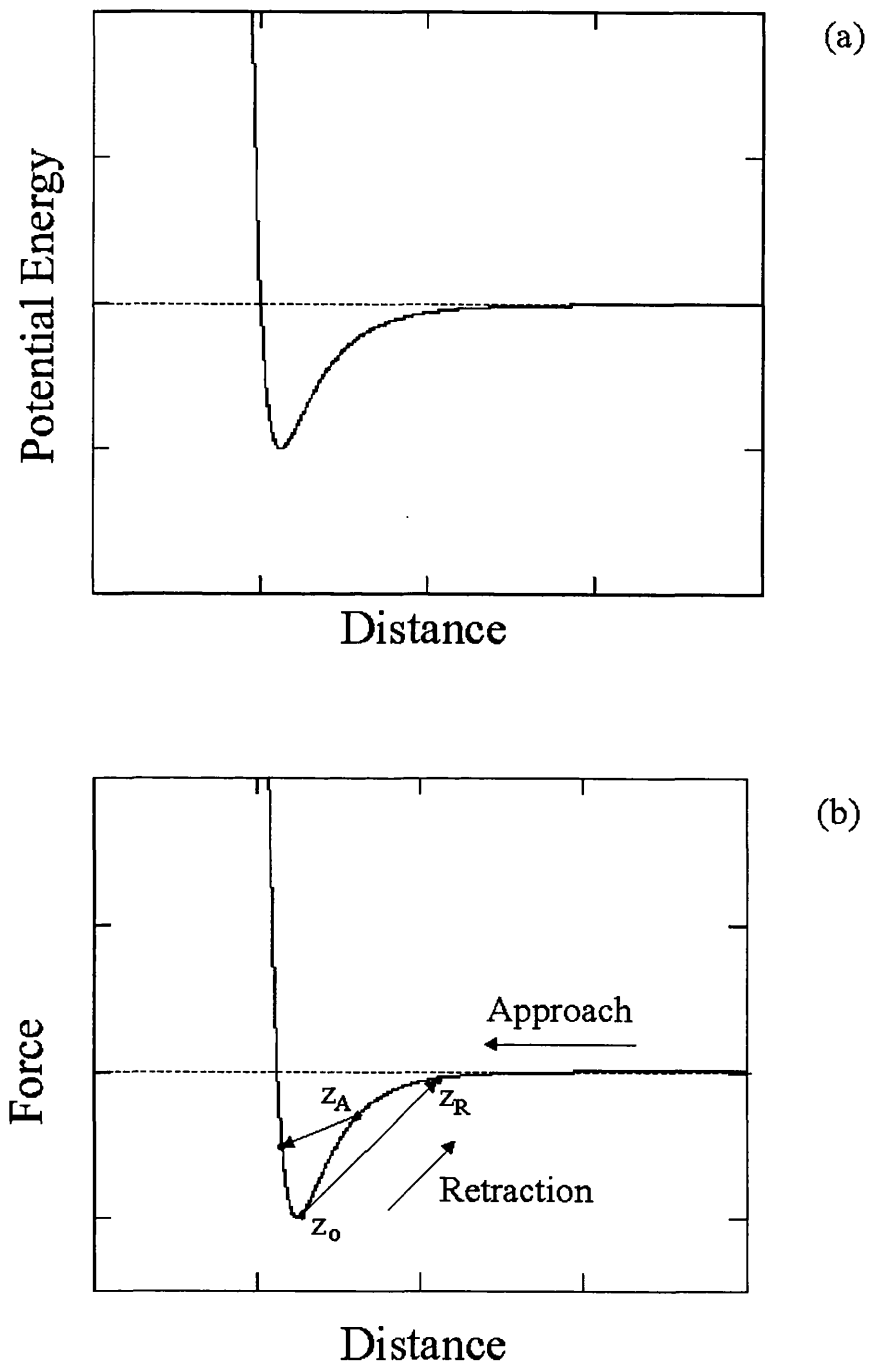

Figure 3.2. (a) Lennard-Jones potential and (b) corresponding force-distance profile. The repulsive forces are shown as positive. On approach, an instability occurs for $z=z_A$. On separation, another instability occurs when the surfaces jump apart from z_o to z_R.

$$L = \frac{4}{3} E^* \frac{a^3}{R} - (8\pi\bar{\gamma}E^*)^{1/2} a^{3/2} \qquad (3.12)$$

The first term in (3.12) is the Hertz term described in the previous section (see equation (3.4)), while the second term is due to the force of adhesion. The Hertz case is recovered by setting $\bar{\gamma}$=0. The curves corresponding to the Hertz and JKR models are shown in figure 3.3. If the load and the contact radius are normalized to L_c and a_c respectively, relation (3.12) assumes the non-dimensional form:

$$-\frac{L}{L_c} = \left[\left(\frac{a}{a_c} \right)^3 - \left(\frac{a}{a_c} \right)^{3/2} \right] \qquad (3.13)$$

The JKR theory predicts infinite stresses at the edge of the contact. In reality, the stresses will be finite. Furthermore, adhesion forces are zero outside of the contact area. Clearly this assumption is not realistic, however, as far as the elastic displacements are large compared to the range of action of the surface forces, the JKR theory gives a good description of the effects of adhesive forces on the deformation of elastic bodies in contact.

By predicting that the contact area is non-zero at pull-off, the JKR theory predicts a non-null value of the frictional force, if the Bowden and Tabor model of adhesive friction (equation 3.3) is valid.

The JKR theory is not the only description of bodies in adhesive contact, but is rather the limiting case of a continuous regime of contact mechanics. The JKR regime is most appropriate when softer materials with strong short-range adhesion are in elastic contact. Contact between stiff materials with long-range attraction are better described by the Derjaguin-Müller-Toporov (DMT) theory.[9] In this model, molecular forces act in a ring-shaped zone of non-contact adhesion, but are assumed not to be able to change the profile outside the contact area from the Hertzian profile. Therefore, the DMT model is equivalent to the Hertz one where the external load is replaced by the sum of the external load and adhesion. The pull-off force predicted by the DMT theory is given by:

$$L_c = -2\pi\bar{\gamma}R \qquad (3.14)$$

and, unlike in the JKR case, is reached at zero contact radius. That in turn implies that the frictional force at pull-off is zero, after equation (3.3).

In the DMT theory there is no stress singularity at the edge. However, the main drawback of this model is the neglect of the deformation due to attractive forces close to the edge of the contact. In 1980 Müller *et al.* [10] presented a self-consistent numerical calculation and abandoned the hypothesis that adhesion forces do not change the Hertzian profile. The result is a continuous transition from the DMT to

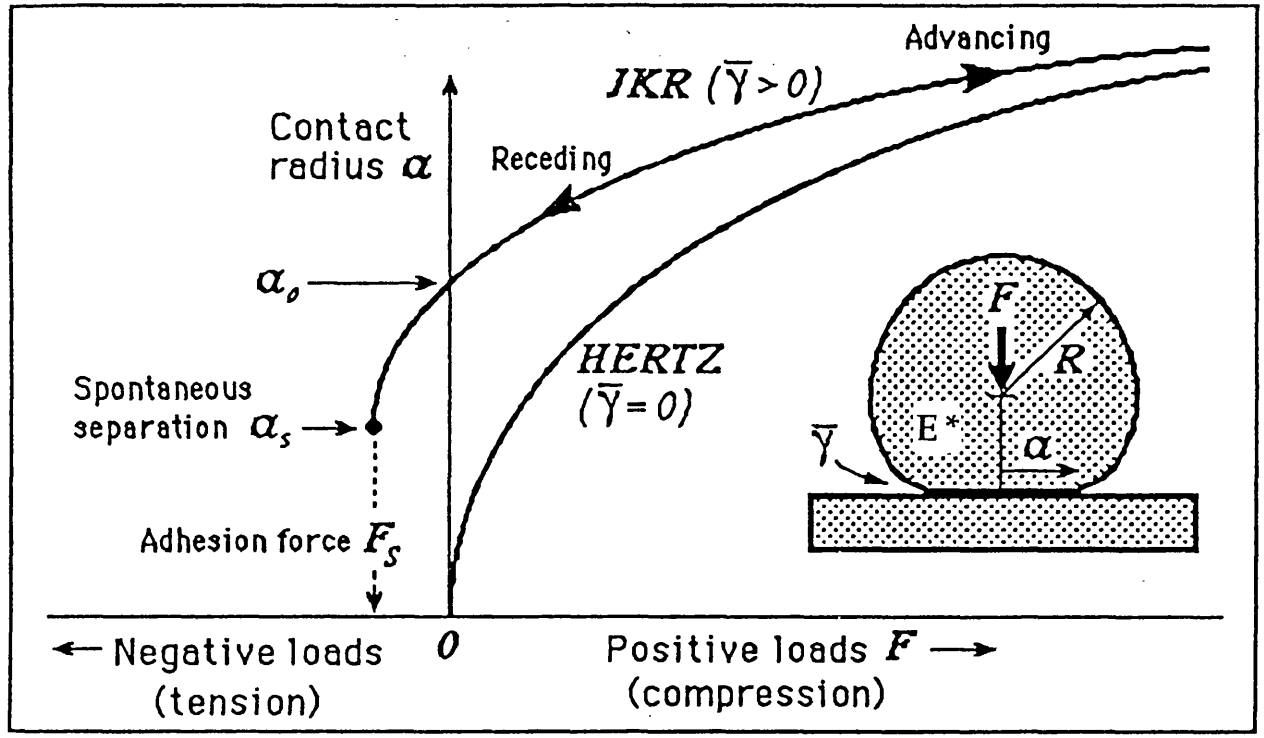

Figure 3.3. Contact radius *vs.* load of non-adhesive Hertzian contact and adhesive JKR contact under ideal conditions (from reference 22).

the JKR theory when the parameter μ, defined below, increases:

$$\mu = \left(\frac{R\bar{\gamma}^2}{E^{*2} z_o^3} \right)^{1/3} \tag{3.15}$$

where z_0 is the equilibrium separation of the surfaces, i.e. the effective range of adhesion. To be firmly in the JKR limit, μ should be about 5 or greater, whereas $\mu<0.1$ implies the DMT limit. Values in between correspond to a 'transition region' where the area-load relation is complicated to evaluate.

3.2.3 The Hertz Problem in the Presence of Capillary Condensation

The theories of contact elasticity described in the previous two sections do not include contributions to the force of adhesion from capillary condensation. A generalization of the Hertz problem to include capillary forces has been proposed by Fogden and White.[11] The treatment is similar to the DMT theory, that is the addition of capillary condensation is viewed as introduction of pressure outside the contact region. The Hertz problem was extended by taking the contact angle θ equal to zero, so that the normal component of the liquid-vapor surface tension stress is not present.

In a way similar to the DMT model, no analytical solution exists. However, two asymptotic behaviors can be derived for large and small values of the fundamental parameter of the theory **k** defined below:

$$k = \left(\frac{\pi}{2} \right)^{1/2} \frac{r_k^{3/2} E^*}{\gamma_{LV} R^{1/2}} \tag{3.16}$$

where γ_{LV} is the liquid-vapor surface tension. Hard spheres in contact in vapor near saturation favor large k values. Small k systems are characterized by larger, softer sphere and vapor pressures closer to the value marking the onset of capillary condensation. For large k values the generalized Hertz theory gives the following results:

Load
$$L = \frac{4}{3} \frac{a^3}{R} E^* - 4\pi\gamma_{LV} R \tag{3.17}$$

Contact radius at pull-off
$$a_c = 0 \tag{3.18}$$

Pull-off force
$$L_c = -4\pi R\gamma_{LV} \tag{3.19}$$

The relation (3.17) has the same mathematical form as the DMT theory, where

the first term is the Hertz load-contact radius relation and the force of adhesion is replaced by the capillary force. As for the DMT model, the contact radius at pull-off is zero.

The small k generalized Hertz load-contact radius curve can be written as:

$$-\frac{L}{L_c}=\left[\left(\frac{a}{a_c}\right)^3-\left(\frac{a}{a_c}\right)^{3/2}\right] \tag{3.20}$$

where $\mathbf{a_c}$ is the contact radius at pull-off:

$$a_c=\left(\frac{9}{4}\frac{\pi\gamma_{LV}R^2}{E^*}\right)^{1/3} \tag{3.21}$$

and $\mathbf{L_c}$ is the pull-off force:

$$L_c=-3\pi R\gamma_{LV} \tag{3.22}$$

Relations (3.20)-(3.22) have the same mathematical form as the JKR relations (3.13), (3.10) and (3.9). The two are distinguishable only by the values predicted for the contact radius at pull-off and the pull-off force. For high humidity, i.e. $p/p_{sat}\rightarrow 1$, r_k becomes increasingly large and so does k. Therefore, the dominant contribution to the force of adhesion is expected to come from capillary condensation. The large k asymptotic relations (3.17)-(3.19) were observed to be in agreement with experimental results on mica in the range $0.7<p<1$.[12] However, in only one case was the adhesion force measured to be an increasing function of the relative vapor pressure. In other cases, the adhesion force was found to decrease with increasing relative humidity and the generalized Hertz description of contact was found appropriate only near saturation. In the case of low to moderate values of the relative humidity the difficulty comes from the assumption that a stable liquid bridge still forms. Even if such bridge exists, the bulk thermodynamic principles upon which the authors based their treatment of capillary condensation are expected to break down for $p/p_{sat}\rightarrow 0$.

3.3 The Surface Force Apparatus and the Quartz Crystal Microbalance

In the surface force apparatus,[13, 14] the problem of multiasperity contact is avoided by using atomically flat mica surfaces. In this instrument two freshly cleaved mica sheets are fashioned into a cylindrical shape and oriented with their axes perpendicular to create a contact area of several μm^2. A spring attached to one

of the cylinders allows the detection of forces as low as 10 nN. The distance is monitored with accuracy of 1 Å usually using optical interferometry, although capacitance methods have also been developed more recently.[15]

Adhesion behavior is examined in contact radius *vs.* load curves during loading-unloading cycles and in pull-off measurements; friction is measured during sliding.[16] Importantly, the validity of the JKR theory has been observed in several SFA experiments.[17, 18, 19, 20]

Important SFA results include the dependence of the adhesion force between two mica surfaces in water on their angular misorientation. In this case the authors found that adhesion is enhanced when the surfaces are perfectly aligned.[21]

Several SFA studies have also been performed on surfactant monolayers deposited on mica. Depending on the state of the monolayers, i.e. crystalline, liquid or amorphous, different adhesion and friction behaviors were observed. A hysteretic behavior was observed for the contact radius and adhesion energy (as defined by the JKR theory) during loading-unloading cycles for amorphous-like layers compared to crystalline-like and liquid-like layers.[22] Furthermore, the frictional behavior for each monolayer was observed to be related to the adhesion hysteresis rather than to adhesion per se.[23] These results were interpreted based on the amount of interdigitation and molecular re-arrangements that occur when bringing two surfaces together. No interdigitation and/or molecular re-arrangements occur when two solid-like surfaces are brought into contact, which brings no hysteresis. A little hysteresis is found for liquid-like surfaces, since although interdigitation occurs the relaxation time is faster than the loading-unloading cycle time. The largest hysteresis is observed for amorphous layers due to interdigitation and slow relaxation times. Values of the adhesion energy were also found to be affected by the time the two surfaces were kept into contact, as well as the temperature and their exposure to organic vapors.

The SFA has also been used to study the static and dynamic properties of liquids confined between two mica surfaces. In the case of cyclohexane and octamethylcyclo-tetrasiloxane (OMCTS), as the separation between the two surfaces is reduced the liquid becomes first much more viscous and then undergoes a transition into a solid-like phase.[24] The forces measured exhibit an exponentially decaying oscillatory behavior, varying from attraction to repulsion. The adhesion between surfaces across such films is quantized, depending on the number of layers between the surfaces. In addition to supporting a finite normal stress it can also support a finite shear stress. 'Stick-slip' behavior was also observed and the frictional force is seen to increase in a quantized way as the number of liquid layers decreases. The measured shear stress is found to be constant as far as the number of liquid layers does not change and is observed to decrease in a quantized way,

once again in relation to the number of liquid layers trapped between the surfaces. In contrast, irregularly shaped molecules are found to give very low friction and show no stick-slip behavior.

'Stick-slip' friction is a commonly observed phenomenon, in which an increasing lateral force on an object produces no motion (stick) until the object suddenly leaps forward (slips) before coming to rest again. This behavior can occur when the force required to initiate sliding from zero velocity (the static friction) is greater than the force required to maintain sliding at a non-zero velocity (the kinetic friction). The static friction can be higher because slow processes as chemical reactions have more time to occur at a static interface than at a moving one. In other experiments performed on OMCTS molecules, no 'stick-slip' behavior was observed.[25] No critical shear stress was found to exist at moderate pressures but rather a viscous response, that is shear motion occurred even in response to a very small shear force. As the pressure increased, the liquid film was seen to undergo an apparent 'freezing' of the liquid film. At that point the viscous response disappeared and a critical shear stress was observed.

In quartz crystal microbalance experiments as developed by Krim,[26, 27] films of gases are condensed onto surfaces to thicknesses up to several monolayers. The thickness of the film is determined with a quartz crystal microbalance. The shifts in the vibrational amplitude caused by gas adsorption are monitored with sub-angstrom resolution. These shifts are due to shear forces between the condensing film and the oscillating surface. Furthermore, from these shifts the 'slip time' can be determined with sub-nanosecond accuracy. For the length and time scales involved the QCM experiments are unique in the field of tribology. With this technique energy dissipation and its mechanisms can be studied. The results are so far consistent with a frictional force proportional to the sliding velocity and theoretical models have been proposed to explain the observed behaviors, as described in the next section.

3.4 Friction and Energy Dissipation

Discussion of energy dissipation during friction processes have continued for the past 300 years. While it has been known for centuries that most frictional energy dissipates as heat, neither the macroscopic nor the microscopic mechanisms of energy dissipation have been fully elucidated. Modern experimental techniques and computer technology have opened the possibility to understand the microscopic

mechanisms of friction.

Different energy dissipation modes have been proposed for different experimental conditions and sliding interfaces. In the case of the SFA experiments, for example, described in the previous section three models have been proposed to account for energy dissipation of the sliding monolayers. The first two, by Sokoloff[28, 29, 30] and Robbins[31] postulate that phonons carry away the energy. The two authors used a simple analytical model and molecular dynamics simulations, respectively and their findings are in excellent agreement with the QCM results reported by Krim and co-workers. A third model by Persson[32, 33] proposes that energy is dissipated by electron-hole scattering. This model assumes that electrons in the metal substrates experience a drag force equal in magnitude to the force required to slide the adsorbed film. Predictions by this model of different slip times for C_2H_4 and C_2H_6 films have been confirmed by QCM experiments.[34] Thus it appears that both phonon and electron mechanisms contribute to energy dissipation in metals.

Molecular dynamics simulations of friction have produced several interesting results. These simulations use more realistic interaction potentials than analytical models and can account for effects of temperature and sliding velocity. Moreover, video animations of the simulations allow one to visualize the trajectories of the atoms. Therefore, it is possible to 'look' at what happens at the buried interface during sliding. Early MD studies depicted wear and transfer of material in the sliding contact.[35, 36] More recently studies of wearless friction, where no atoms were transferred at the interface, were reported. In one of these reports friction between two monolayers of alkane chains was studied as a function of temperature and sliding velocity.[37] At low temperatures (20 K), friction exhibits a stick-slip behavior and the energy dissipation is found to be associated with vibrating and twisting modes for strong interface interaction, while no heat flow is measured for weak interactions. As the temperature increases so does friction and video animations depict very complex dissipation modes. Torsional modes, that were 'frozen' at low temperatures, become excited and energy is transferred to the lattice vibrations in the substrate. As the temperature increases further, molecules start hopping from one surface to the other without introducing strain and friction is reduced. In addition friction was seen to increase with increasing sliding velocity.

Interesting results were also obtained by Harrison *et al.*[38, 39, 40] on the frictional behavior of H- and ($H+C_xH_y$)- terminated diamond (111) surfaces placed in sliding contact. For H-terminated surfaces different friction was observed when sliding along two different crystallographic directions that could account for the well-known frictional anisotropy of diamond single crystals. A temperature dependence similar to that described above for alkane chains was also observed.

When hydrogen atoms are substituted by CH_3 groups an increase in friction is observed at low loads, due to the excitation of turnstile motions, while a reduction in friction compared to the hydrogen case is found at high loads, due to the fact that the larger methyl groups can keep the surfaces further apart. When larger hydrocarbons are used, friction is reduced at high loads due to their increased flexibility and consequent ability to detour around high potential energy barriers.

Tupper and Brenner performed MD simulations of friction for n-hexadecylthiol monolayers on Au(111).[41] In these simulations the thiol molecules, chemisorbed on a Au(111) surface, are compressed with an infinite sheet of gold atoms identical to the substrate. The load is found to vary with a period equal to the periodicity of the gold atoms in the compressing surface in the direction of sliding and to be independent of chain packing. The shear stress is seen to oscillate with the same periodicity and in phase with load, bringing a friction coefficient that is independent of load. Out of phase oscillations are found for the average tilt angle of the molecules, suggesting that energy dissipates through a change in tilt angle caused by adhesion of the head groups to the sliding surface and does not depend on the packing of the chains.

3.5 The AFM as a Tribology Tool

3.5.1 Atomic-Scale Stick-Slip

Atomic and molecular lattices are resolved by AFM on a variety of surfaces and for certain ranges of loads even after repeated scanning of the tip over the same region of the surface. These AFM images demonstrate that the tip must be sliding across the surface with no wear and represent the most direct evidence to date that wearless sliding is possible.

As it will be shown in chapter 7, many AFM images show features that are the result of the forces parallel to the surfaces and frictional forces in particular.

The first AFM studies of frictional forces at atomic-level resolution were reported by Mate *et al.* and Erlandsson *et al.* for tungsten wires sliding on graphite[42] and mica[43] surfaces in air. This work used an AFM based on optical interferometry in which the sample and tip are in a horizontal orientation. Two fiber optics detect bending and torsion of the tungsten wire separately. Figure 3.4 shows the pattern of the frictional force measured by the authors in reference 43 on a mica surface. The lateral force signal was seen to vary in a stick-slip pattern, that exhibits the periodicity of the sample surface (lattice constant=5.2 Å). The stick-slip observed

in these experiments appears very much like that observed in SFA experiments, however its origin is not the velocity dependence of the frictional force, but its dependence on position. The following phenomenological model was introduced by the authors. Since the surface features are encountered at a frequency smaller than the lever's resonant frequency (few tens to few hundred Hz *vs.* few tens to few hundred kHz), the tip always comes to an instantaneous mechanical equilibrium in response to the force of the lever and sample. Considering displacements only along the scanning direction x, the total force on the tip can be written as a function of the tip position x_t and the sample position x_s:

$$F = -k_l x_t + F_s(x_t - x_s) \qquad (3.23)$$

where the first term represents the force exerted by the cantilever on the tip (Hooke's law) and F_s is the tip-sample force that depends only on the relative position of the tip and sample, x_t-x_s. In the regions where $\frac{dF}{dx_t} > 0$, i.e. F_s' is larger than k_l, the tip is not at a stable equilibrium. If the tip finds such regions it will slip until it finds a region where $\frac{dF}{dx_t} < 0$. If F_s' is always less than k_l there is no slipping. Such change from discontinuous to continuous behavior was observed on graphite.[42] The linear regions seen at the beginning of each scan in figure 3.4 correspond to the tip and sample moving together (static friction). When the restoring force from the cantilever is high enough to overcome the static friction the tip starts sliding in a stick-slip pattern.

Fujisawa *et al.* investigated the stick-slip motion between silicon nitride tips and layered materials, such as mica and MoS_2.[44, 45] By using soft cantilevers (k=0.02 N/m)[44] and scanning across the lever major axis (X scan) they observed a stick-slip pattern for the lateral force signal and a square wave behavior for the topography. In addition, the two signals were synchronized with each other. When scanning along the lever axis (Y scan) the topographic signal showed a stick-slip pattern, while the lateral force exhibited a square wave behavior. Figure 3.5 schematically illustrates their results, assuming that the x direction is perfectly aligned with one of the substrate's crystallographic directions. By using a stiffer lever (k=0.75 N/m)[45] the topographic signal from an X scan showed no atomic-scale corrugation. The authors concluded that both signals, the topographic and lateral force one, are affected by the stick-slip motion. To explain the observed behavior, the authors propose a two-dimensional stick-slip motion model, where the stick points have the same periodicity of the lattice (figure 3.5(c)). The motion of the tip along the fast scan direction (that is, x in a X scan and y during a Y scan) is stick-slip like, as observed by Mate *et al.*[42, 43] The motion across the fast scan direction (that is y during a X scan and x during a Y scan) is a zig-zag walk: the tip

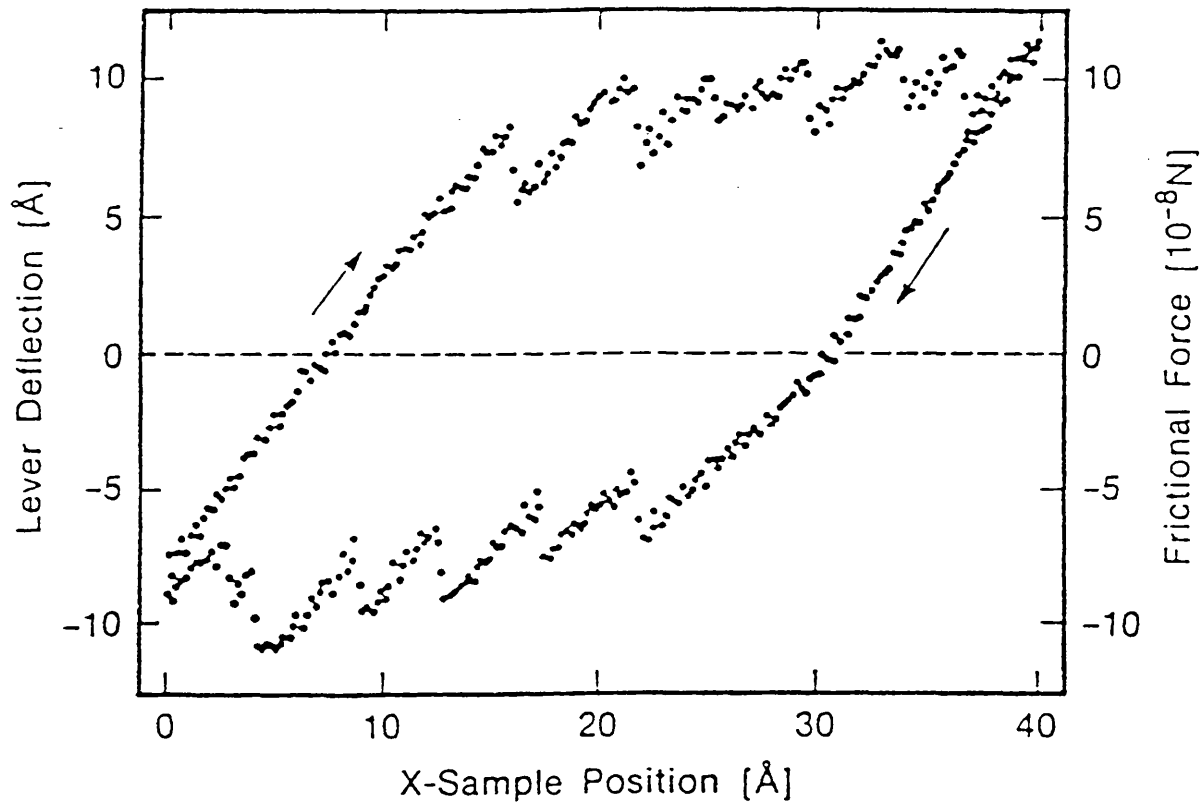

Figure 3.4. Atomic scale 'stick-slip' of a tungsten tip on a mica surface in air (from reference 43).

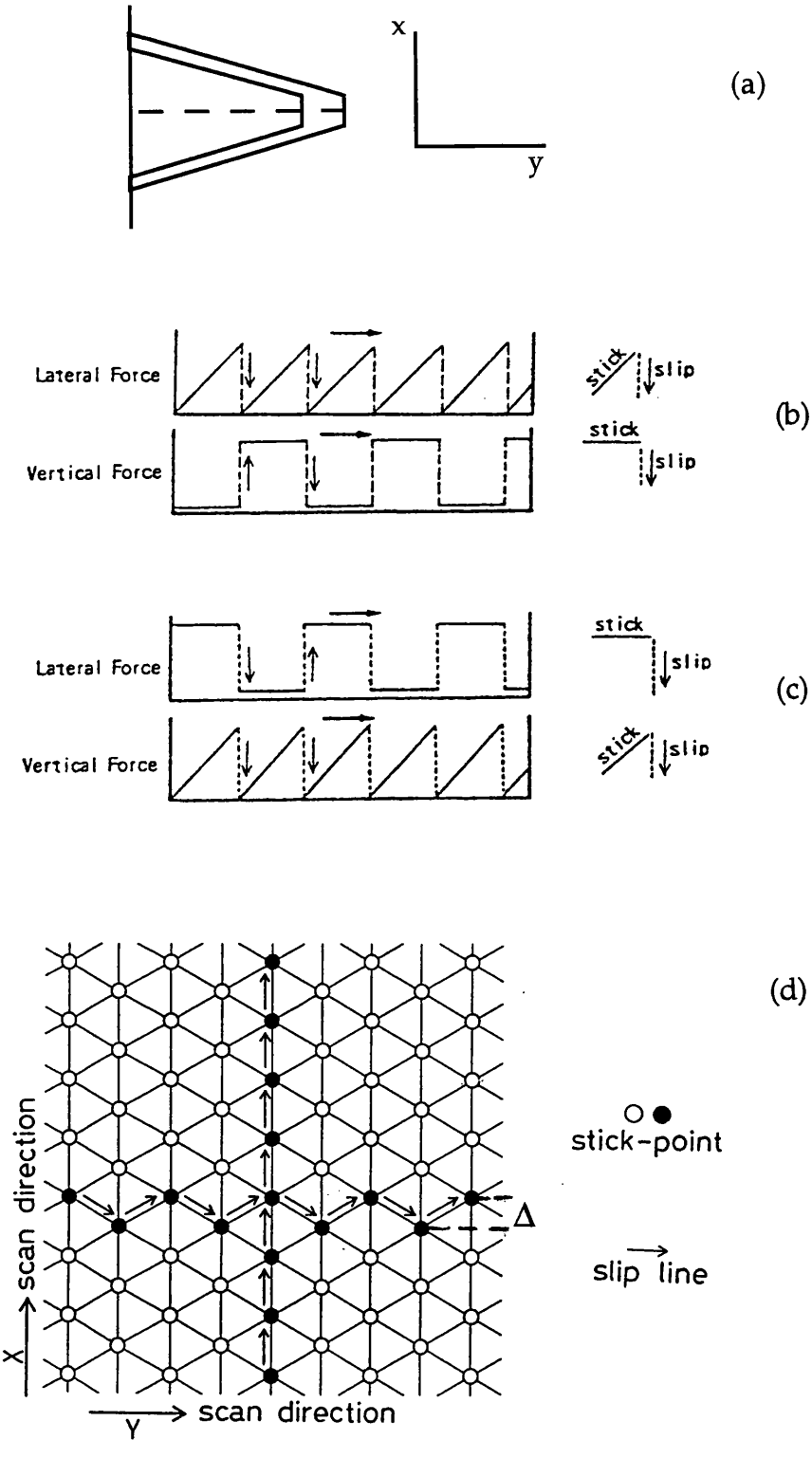

Figure 3.5. (a) Schematic drawing of a V-shaped cantilever and definition of the x and y directions. (b) Schematic representation of the behavior of the lateral and vertical force during an X-scan and (c) a Y-Scan. The arrows represent the scan direction. (d) The two-dimensional stick-slip model for a hexagonal unit cell. (Adapted from references 44 and 45).

stops during the stick event and it moves of a distance Δ during the slip event. If the scan direction is not parallel to one of the substrate's crystallographic direction, the period and amplitude of the 2D-stick slip will be irregular.[45] Importantly, as the authors point out, these results are consistent with the 'topography' signal be due to the y component of the frictional force acting on the cantilever and therefore does not reflect the sample atomic corrugation. Therefore, the AFM appears to work as a two-dimensional frictional-force microscope. Further discussion on the role of the forces acting along the lever major axis will be found in chapters 6 and 7.

3.5.2 Models of Wearless Friction

A few simplified models have been reported in literature to explain mechanisms of wearless friction. The model introduced by McClelland and Cohen[46] used an approach similar to that used a long time ago by Tomlinson.[47] Figure 3.6 shows a schematic of two atomically smooth surfaces in contact. Each solid is assumed to be bound together by strong intra-solid bonds, but that the inter-solid interaction across the interface is weak, consisting only of van der Waals interactions. When the lower solid A in figure 3.6 slides over the upper solid B, the interaction is not strong enough to break bonds within the solid, but it can in principle move the atoms within the solid, generating phonons and dissipating energy.

To understand how energy can be dissipated for this type of interface, the independent oscillator (IO) model is used. In this simplified model, solid A of figure 3.6(a) is replaced by a single row of atoms anchored to a rigid handle, while solid B is replaced by non-interacting atoms bound as damped harmonic oscillator to the B handle (figure 3.6(b)). The IO model makes the assumption that the handles are kept at zero absolute temperature. Because of the periodicity of solid A, the sliding behavior can be analyzed by following the motion of atom B_o across one atomic spacing. Atom B_o experiences forces from the spring above and the atoms below; the corresponding potentials are V_{BB} and V_{AB}, respectively. As substrate A moves, the combined potential V_s changes. The changing potential and trajectories of atom B_O are shown in figure 3.7 (a)-(e). The sketches on the left and right are relative to 'strong' and 'weak' V_{AB} interactions, respectively. In a 'strong' potential, the atom is first repelled; then beyond half an atomic spacing, it snaps back, the atomic equivalent of stick-slip. The snap back can be understood in terms of the evolving shape of the potential V_s and the fact that in an adiabatic process, such as the ones described here, an atom must always sit at a minimum. The transition from (d) to (e) in figure 3.7 is irreversible and the energy put into straining the spring is converted into vibrational motion which dissipates into the substrate as heat. This

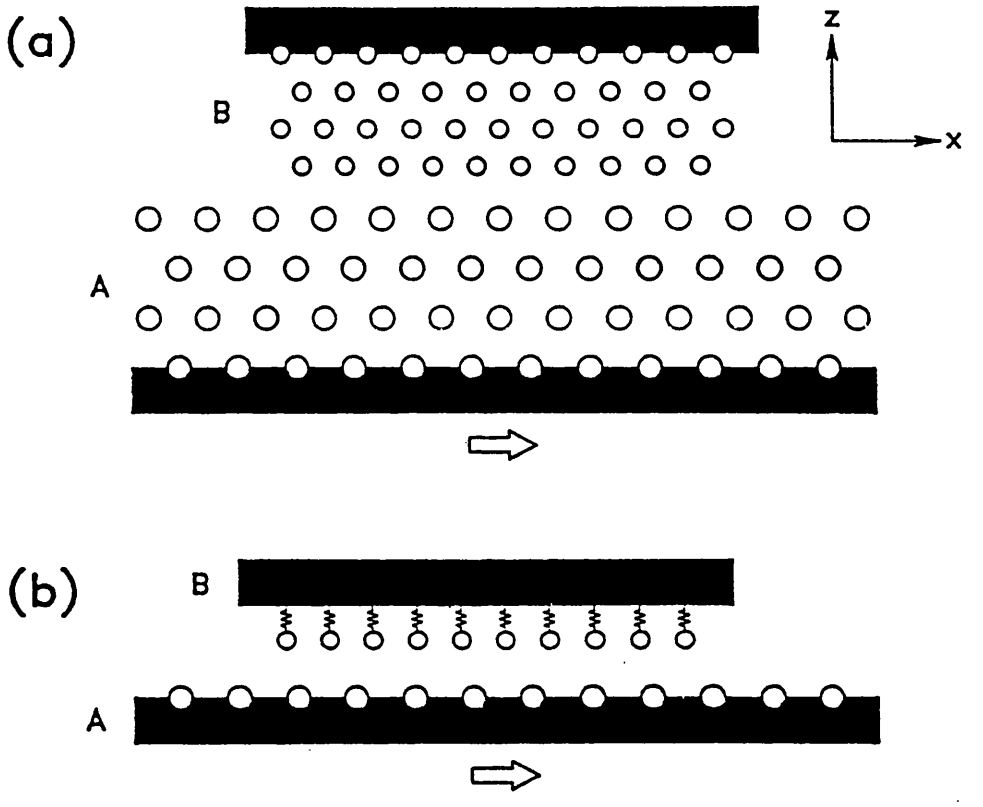

Figure 3.6. (a) Schematic representation of two atomically smooth surfaces in contact. (b) Independent oscillator model. The arrows represent the sliding direction. (From reference 46).

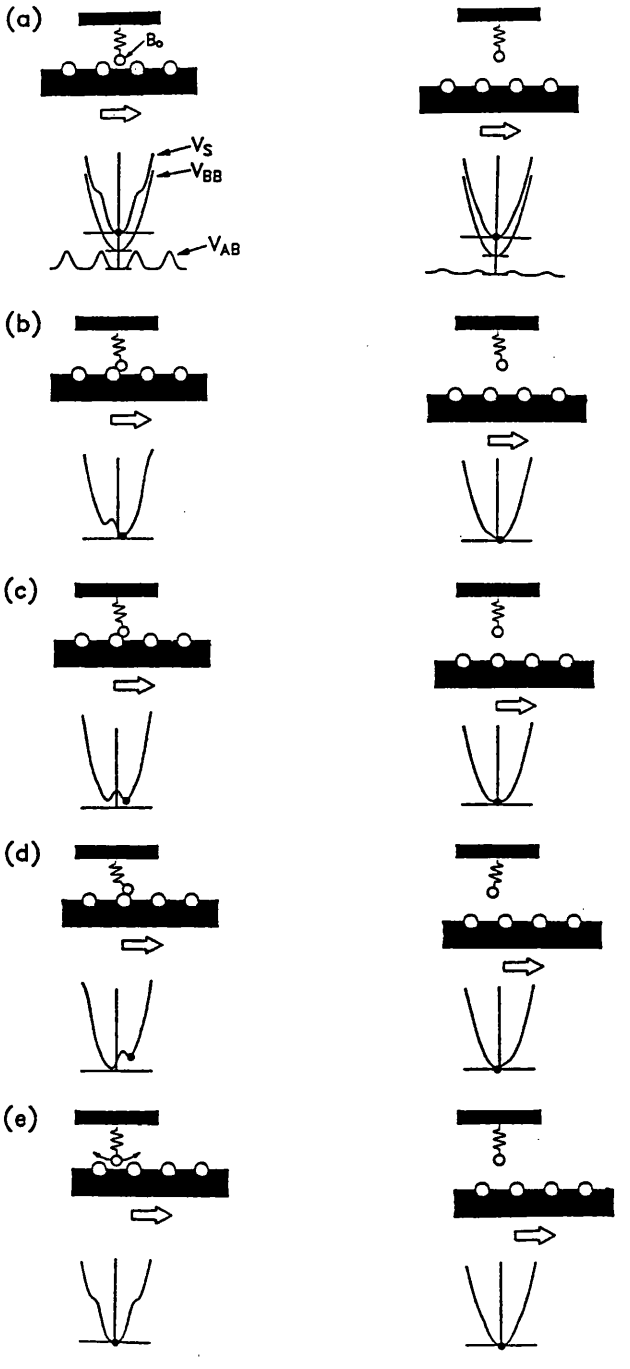

Figure 3.7. Motion of an atom B_0 of B (see figure 3.6) in the IO model. Left and right columns diagram strong and weak interactions, respectively. The top panels diagram the relevant potentials, while the subsequent panels illustrate the response of B_0 (represented by a black dot on V_s) to sliding of A. (From reference 46).

instability can be avoided by using a 'weak' interaction potential (right schetches in figure 3.7). The atoms move smoothly through a repulsive then attractive force field and the system remains in equilibrium throughout the cycle, so that no energy is dissipated and friction is zero.

Another model, that describes conditions associated with frictionless sliding, is due to Tománek *et al.*[48] Their model accounts for the elasticity of the FFM and find that friction depends not only on the properties of the surfaces in contact and the applied load, but also on the spring constant of the lever. For hard springs, a reduction of friction is predicted, while maximum friction is yielded by soft springs. Moreover, the 'friction coefficient' μ=Friction/Load is found to depend on the applied load, that is there is no friction coefficient!

A different model was proposed by Colchero *et al.*,[49] who noted that the conclusion reached by the model described above that hard springs do not dissipate energy is counterintuitive. The model they propose takes into account the local elasticity of tip and sample and finds that the softest spring in the system (the cantilever and the local tip-sample deformation) determines the elastic behavior of the system. When an unstable point is reached, the potential energy is transformed into kinetic energy of the two springs in a way that depends on the relative strength of the two springs and with most energy released into the softest spring. The energy released into the cantilever can be damped by air or internal friction in the cantilever, while the energy stored in the tip-sample deformation is carried away by phonons. Pethica and Sutton[50] also note that the latter process is dissipative only if the strains involved in the slipping region are greater than those associated with phonon displacements and if group of atoms are coherently involved in the slip event. Both of these conditions seem to be fulfilled in the case of AFM experiments.

3.5.3 Nanomechanics Studies by AFM

Much work has been done since the first realization that an AFM can also work as a friction force microscope. The advantage of using the FFM for frictional studies is that the contact is reduced to a single asperity. However, there are also some limitations, since in most AFM studies the contact area is not directly known[51] and the tip geometry is difficult to control. Therefore, at present the technique cannot provide absolute numbers and relative measurements conducted with one tip are more meaningful.

At a low resolution, the FFM technique is used in the characterization of surfaces where different materials or chemical functionalities co-exist. Although at present it is not understood how frictional properties are affected by factors such as the molecule chain length, chemical identity of the terminal group and

order/disorder within the layer, the technique has been found to be able to discriminate, for example, between different terminal groups such as methyl and carboxylic acid,[52] fluorocarbon from hydrocarbon regions in phase-separated Langmuir-Blodgett (LB) monolayers on silicon[53] and patterned on a quartz substrate,[54] MoS_2 layers deposited on mica and alumina,[55] AgBr films deposited on NaCl single crystals.[56] It is important to note that characterizations of the kind described above are possible only if the sample preparation results in 'large enough' flat areas having different frictional properties. In fact, when imaging at low resolution, the lateral force images show two components, as schematically shown in figure 3.8. When the tip scans across a step, the contact area is changed, which in turn causes a change in the lateral force. In addition, attractive forces, such as van der Waals and capillary forces change too. A larger attractive force, for example, will have to be compensated by a larger repulsive force causing an increase in the contact area. The change in the lateral force depends on the scanning direction and a contrast reversal is observed in the lateral force images.[57] On the flat terraces of figure 3.8, the lateral force is proportional to the frictional force, i.e. there is no topographic component. If the terraces are smaller than the tip size, the tip will be unable to resolve the frictional contrast between two adjacent terraces.

A number of friction *vs.* load studies have been reported on carbon surfaces,[57] bare and lubricated silicon oxide surfaces,[58] MoS_2 on mica and alumina,[55] ionic crystals,[59] bare and silanated mica surfaces.[60, 61] In particular, Hu *et al.* showed that a mica surface can be used as a reference substrate in friction studies, since the dependence of the frictional force with applied load was found to be quite reproducible for different samples, tip radii, scanning speed and crystallographic direction.[60] Of particular relevance are the studies performed in UHV by Carpick *et al.* on freshly cleaved mica.[62, 63] By performing experiments in a clean (i.e. free of contamination and in absence of capillary forces) environment, the authors observed, for the first time by AFM, that the frictional force varies with load in proportion to the contact area, as predicted by the JKR theory (see section 3.2.2).

During this thesis work particular attention was given to the study of frictional properties of self-assembled monolayers, as a function of their chain length, chemical identity of their end-group and head group-substrate interaction. These experiments will be described in detail in chapters 8, 9 and 10 and are the first systematic investigations of this kind. Based on these AFM studies a mechanism of energy dissipation is suggested for these layers.

In addition to allow friction studies in the wearless regime, the AFM tip can be used to investigate the nanometer-scale mechanical response of surfaces to high applied pressures. In fact, in a typical AFM experiment forces of the order of a

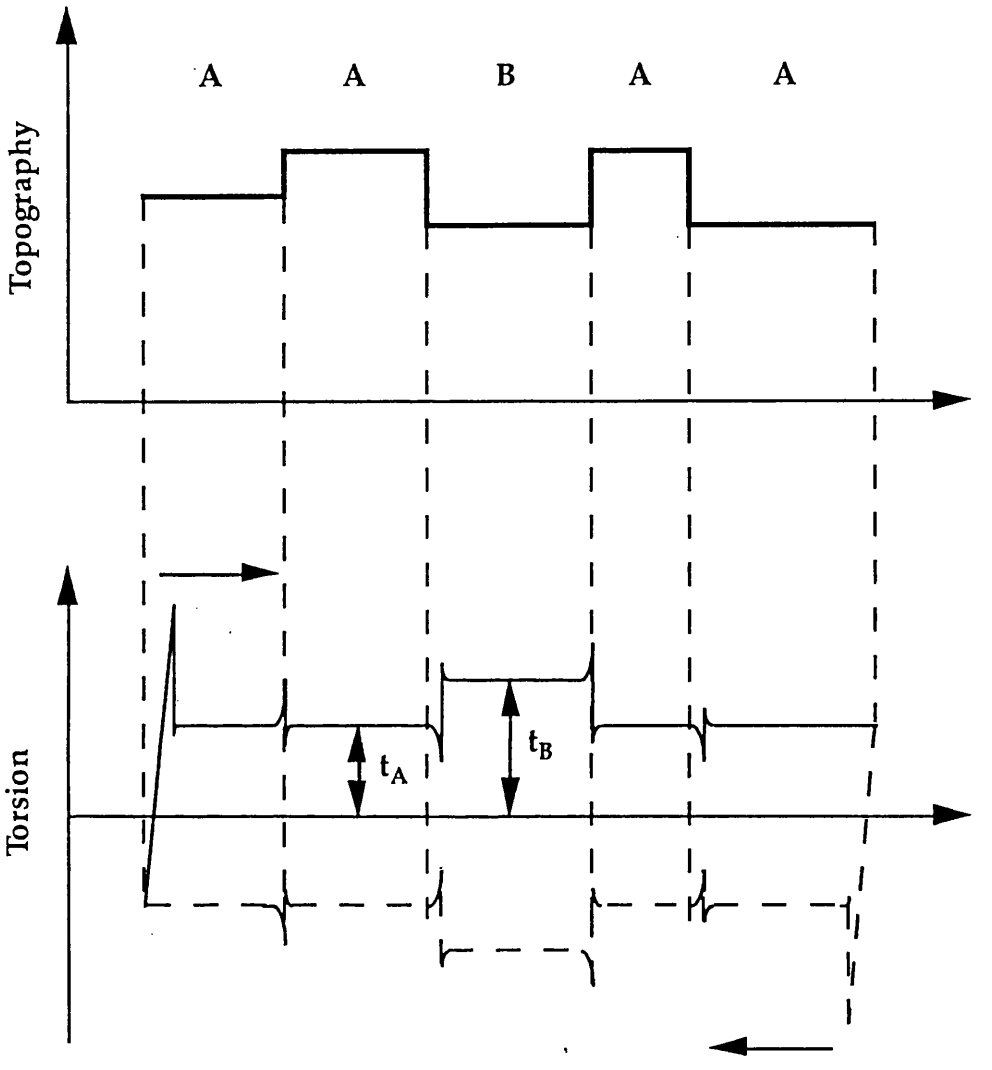

Figure 3.8. Schematic diagram of the topographic signal (top) and lateral force 'friction loop' (bottom) measured on a stepped surface. Two different materials, A and B, are present on the substrate (top). The cantilever twists of different angles, t_A and t_B, on regions A and B, respectively and a contrast is visible in the lateral force images. An increase/decrease is seen in the lateral force signal as the tip scans across a step (bottom). The arrows indicate the scan direction.

few nN are applied to nm-sized contact areas causing pressures in the GPa-regime. These pressures are similar to those involved in macroscopic experiments.

Nanoindentation tests are of particular interest to the magnetic media disks industry where films that ensure low wear under repeated shearing conditions are needed. In these studies, a hard tip, typically diamond, is pushed into the substrate to create an indentation and the microhardness is measured.[64, 65]

Apart from the above technological applications, the high pressures applied by the AFM tip can be used to test the resistance to wear of a variety of materials,[60, 66, 67, 68] including organic layers,[69, 70, 71, 72] and as a 'nanomachining' tool.[73, 74, 75] During the course of this project, novel AFM experiments, aimed at investigating the structure and mechanical properties of self-assembled monolayers under high applied pressures, were performed. These results are reported in chapter 9.

3.6 Summary

The complicated role in tribology of multiasperity contact highlights the crucial importance of doing experiments where asperities are either absent or well-defined. In this respect, the SFA and the AFM techniques for the first time offer the possibility to study the wearless regime of friction at the atomic level. Bowden and Tabor early recognized that adhesion can contribute to friction, independently of the contribution from the ploughing of surface asperities. To date AFM images represent the most direct evidence that wearless sliding is possible. In addition, the QCM technique uniquely allows one to perform friction experiments at the nanoscale level and at time scales in the nanosecond range. The use of these techniques is helping scientists to identify new modes of energy dissipation and theorists are in turn using the new results to progress in the understanding of the mechanisms of energy dissipation at the microscopic level.

A new relationship between adhesion and friction has been discovered by SFA experiments of surfactant monolayers. Friction was found to correlate not with the adhesion but with the adhesion hysteresis and this is related to the extent of interpenetration and entanglement of the molecules across the sliding interface.

The present understanding is that friction is increased by many factors, such as strong interfacial interactions, defects at the interface, crystal alignment and commensurability, thermal activation of energy-dissipating modes such as torsional and rotational ones in alkane chains. The size and shape of molecules can also

influence frictional behavior, with small molecules being able to follow low-friction trajectories not available to larger ones and conversely large molecules may reduce friction if they have enough flexibility and are able to spread across the surface.

AFM and FFM are providing new ways to investigate the fundamental laws of friction as well as new mechanisms of energy dissipation. The high pressures applied in most AFM experiments makes the AFM tip a suitable tool to investigate the mechanical response of a variety of surfaces to very high pressures.

References

[1] D. Dowson, *History of Tribology*, (Longman, London, 1979).

[2] *Fundamentals of Friction: Macroscopic and Microscopic Processes*, I. L. Singer, H. M. Pollock edts., NATO ASI Series (Kluwer Academic Publishers: Dordrecht, 1992).

[3] F. P. Bowden, D. Tabor, *Friction and Lubrication of Solids*, (Oxford University Press, 1964).

[4] J. A. Greenwood, J. H. Tripp, *Proc. Roy. Soc. A*, **295**, 300 (1966).

[5] The regime of boundary lubrication corresponds to surfaces separated by at most few layers of lubrication molecules.

[6] H. Hertz, *J. Reine Angew. Math.*, **92**, 156 (1882).

[7] K. L. Johnson, *Contact Mechanics* (Cambridge University Press, 1985).

[8] K. L. Johnson, K. Kendall, A. D. Roberts, *Proc. Roy. Soc. London A*, **312**, 301 (1971).

[9] B. V. Derjaguin, V. M. Müller, Y. P. Toporov, *J. Colloid Interface Sci.*, **53**, 314 (1975).

[10] V. M. Müller, V. S. Yushenko, B. V. Derjaguin, *J. Colloid Interface Sci.*, **77**, 91 (1980).

[11] A. Fogden, L. R. White, *J. Colloid. Inter. Sci.*, **138**, 414 (1990).

[12] H. K. Christenson, *J. Colloid Inter. Sci.*, **121**, 170 (1988).

[13] D. Tabor, R. H. S. Winterton, *Proc. Roy. Soc. London A*, **312**, 435 (1969).

[14] J. N. Israelachvili, D. Tabor, *Proc. Roy. Soc. London A*, **331**, 19 (1972).

[15] P. Frantz, N. Agrait, M. Salmeron, *Langmuir*, **12**, 3289 (1996).

[16] J. N. Israelachvili, P. M. McGuiggan, A. M. Homola, *Science*, **240**, 189 (1988).

[17] Y. L. Chen, C. A. Helm, J. N. Israelachvili, *J. Phys. Chem.*, **95**, 10736 (1991).

[18] R. G. Horn, J. N. Israelachvili, F. J. Pribac, *J. Colloid Interface Sci.*, **78**, 260 (1987).

[19] J. N. Israelachvili, D. Tabor, *Wear*, **24**, 386 (1973).

[20] B. J. Briscoe, D. C. Evans, *Proc. Roy. Soc. London A*, **380**, 389 (1982).

[21] P. M. McGuiggan, J. N. Israelachvili, *Chem. Phys. Lett.*, **146**, 469 (1988).

[22] J. N. Israelachvili in *Fundamentals of Friction: Macroscopic and Microscopic Processes*, I. L. Singer, H. M. Pollock edts., NATO ASI Series (Kluwer Academic Publishers: Dordrecht, 1992).

[23] H. Hoshizawa, Y. L. Chen, J. N. Israelachvili, *J. Phys. Chem.*, **97**, 4128 (1993).

[24] D. Y. C. Chan, R. G. Horn, *J. Chem. Phys.*, **83**, 5311 (1985).

[25] J. Van Alsten, S. Granick, *Phys. Rev. Lett.*, **61**, 2570 (1988).

[26] J. Krim, A. Widom, *Phys. Rev. B*, **38**, 12184 (1988).

[27] J. Krim, D. H. Chiarello, *Phys. Rev. Lett.*, **66**, 181 (1991).

[28] J. B. Sokoloff, *Phys. Rev. B*, **42**, 760 (1990).

[29] J. B. Sokoloff, *Wear*, **167**, 59 (1993).

[30] J. B. Sokoloff, *Thin Solid Films*, **206**, 208 (1991).

[31] M. Cieplak, E. Smith, M. O. Robbins, *Science*, **265**, 1209 (1994).

[32] B. N. J. Persson, *Phys. Rev. B*, **44**, 3277 (1991).

[33] B. N. J. Perrson, D. Schumaker, A. Otto, *Chem. Phys. Lett.*, **78**, 204 (1991).

[34] C. Mak, C. Daly, J. Krim, *Thin Solid Films*, **253**, 190 (1994).

[35] U. Landman, W. D. Luedtke, E. M. Ringer in *Fundamentals of Friction*, I. L. Singer, H. M. Pollock edts. (Kluwer Academic Publishers: Dordrecht, 1992).

[36] J. Belak, I. F. Stowers, in *Fundamentals of Friction*, I. L. Singer, H. M. Pollock edts. (Kluwer Academic Publishers: Dordrecht, 1992).

[37] J. N. Glosli, G. M. McClelland, *Phys. Rev. Lett.*, **70**, 1960 (1993).

[38] J. A. Harrison, C. T. White, R. J. Colton, D. W. Brenner, *Phys. Rev. B*, **46**, 9700 (1992).

[39] J. A. Harrison, R. J. Colton, C. T. White, D. W. Brenner, *Wear*, **168**, 127 (1993).

[40] J. A. Harrison, C. T. White, R. J. Colton, D. W. Brenner, *J. Phys. Chem.*, **97**, 6573 (1993).

[41] K. J. Tupper, D. W. Brenner, *Thin Solid Films*, **253**, 185 (1994).

[42] C. M. Mate, G. M. McClelland, R. Erlandsson, S. Chiang, *Phys. Rev. Lett.*, **59**, 1942 (1987).

[43] R. Erlandsson, G. Hadziioannou, C. M. Mate, G. M. McClelland, S. Chiang, *J. Chem. Phys.*, **89**, 5190 (1988).

[44] S. Fujisawa, Y. Sugawara, S. Ito, S. Mishima, T. Okada, S. Morita, *Nanotechnology*, **4**, 138 (1993).

[45] S. Fujisawa, E. Kishi, Y. Sugawara, S. Morita, *Jpn. J. Appl. Phys.*, **33**, 3752 (1994).

[46] G. M. McClelland, S. R. Cohen in *Chemistry and Physics of Solid Surfaces (vol. 8)*, R. Vancelow, R. Howe edts. (Springer Series in Surface Sciences, 1990).

[47] G. A. Tomlinson, *Phil. Mag. Series*, **7**, 905 (1929).

[48] D. Tománek, W. Zhong, H. Thomas, *Europhys. Lett.*, **15**, 887 (1991).

[49] J. Colchero, O. Marti, J. Mlynek in *Forces in Scanning Probe Methods*, NATO ASI

Series E: Applied Sciences, vol. 286 (Kluwer Academic Publishers: Dordrecht, 1995).

[50] J. B. Pethica, A. P. Sutton in *Forces in Scanning Probe Methods*, NATO ASI Series E: Applied Sciences, vol. 286 (Kluwer Academic Publishers: Dordrecht, 1995).

[51] To the author's knowledge, measurements of the contact area are performed only by Pethica and co-workers by measuring the surface stiffness. See S. P. Jarvis, A. Oral, T. P. Weihs, J. B. Pethica, *Rev. Sci. Instrum.*, **64**, 3520 (1993).

[52] A. Kumar, H. A. Biebuyck, G. M. Whitesides, *Langmuir*, **10**, 1498 (1994).

[53] R. M. Overney, E. Meyer, J. Frommer, H.-J. Güntherodt, M. Fujihira, H. Takano, Y. Gotoh, *Langmuir*, **10**, 1281 (1994).

[54] M. Fujihira, Y. Morita, *J. Vac. Sci. Technol. B*, **12**, 1609 (1994).

[55] A. Schumacher, N. Kruse, R. Prins, E. Meyer, R. Lüthi, L. Howald, H.-J. Güntherodt, L. Scandella, *J. Vac. Sci. Technol. B*, **14**, 1264 (1996).

[56] L. Howald, R. Lüthi, E. Meyer, G. Gerth, H. Rudin, H.-J. Güntherodt, *J. Vac. Sci. Technol. B*, **12**, 2227 (1994).

[57] C. M. Mate, *Wear*, **168**, 17 (1993).

[58] M. Binggeli, C. M. Mate, *Appl. Phys. Lett.*, **65**, 415 (1994).

[59] R. Lüthi, E. Meyer, M. Bammerlin, L. Howald, H. Haefke, T. Lehmann, *J. Vac. Sci. Technol. B*, **14**, 1280 (1996).

[60] J. Hu, X.-D. Xiao, D. F. Ogletree, M. Salmeron, *Surf. Sci.*, **327**, 358 (1995).

[61] X.-D. Xiao, J. Hu, D. H. Charych, M. Salmeron, *Langmuir*, **12**, 325 (1996).

[62] R. W. Carpick, A. Agrait, D. F. Ogletree, M. Salmeron, *J. Vac. Sci. Technol. B*, **14**, 1289 (1996).

[63] R. W. Carpick, A. Agrait, D. F. Ogletree, M. Salmeron, *Langmuir*, **12**, 3334

(1996).

[64] D. B. Bogy, *J. Tribology-Transactions of the ASME*, **114**, 493 (1992).

[65] B. Bushan, V. N. Koinkar, *Appl. Phys. Lett.*, **64**, 1653 (1994).

[66] S. R. Cohen, G. Neubauer, G. M. McClelland, *J. Vac. Sci. Technol. A*, **8**, 3449 (1990).

[67] M. Salmeron, A. Folch, G. Neubauer, M. Tomitori, D. F. Ogletree, W. Kolbe, *Langmuir*, **8**, 2832 (1992).

[68] A. B. Mann, J. B. Pethica, *Langmuir*, **12**, 4583 (1996).

[69] G. S. Blackman, C. M. Mate, M. R. Philpott, *Vacuum*, **41**, 1283 (1990).

[70] M. Salmeron, G. Neubauer, A. Folch, M. Tomitori, D. F. Ogletree, P. Sautet, *Langmuir*, **9**, 3600 (1993).

[71] X.-D. Xiao, G.-Y. Liu, D. H. Charych, M. Salmeron, *Langmuir*, **11**, 1600 (1995).

[72] T. P. Weihs, Z. Nawaz, S. P. Jarvis, J. B. Pethica, *Appl. Phys. Lett.*, **59**, 3536 (1992).

[73] T. Jung, H. Hug, A. Moser, U. Schwarz, D. Brodbeck, R. Hofer, *Ultramicroscopy*, **42-44**, 1446 (1992).

[74] M. Fujihira, H. Takano, *J. Vac. Sci. Technol. B*, **12**, 1860 (1994).

[75] Th. Schimmel, R. Kemnitzer, J. Küppers, Ch. Kloc, M. Lux-Steiner in *Forces in Scanning Probe Methods*, NATO ASI Series E: Applied Sciences, vol. 286 (Kluwer Academic Publishers: Dordrecht, 1995).

Chapter 4

SPM Instruments and Experimental Methods

4.1 Introduction

In this chapter a description of the scanning probe microscopy experimental systems used for this thesis work is given. STM studies were performed at the Department of Electronics and Electrical Engineering at the University of Glasgow (UK), while AFM experiments were initially performed at the National Research Council (CNR) in Pisa (Italy) and later at Lawrence Berkeley National Laboratory (LBNL) at the University of California at Berkeley (USA).

The scanning tunneling microscope used at Glasgow University, was a commercially available instrument (W. A. Technology, Cambridge, UK). The author was responsible for its operation and maintenance for good part of the period spent in Glasgow. The AFM used in Pisa was a home built apparatus, construction of which was in part work of the author's Laurea degree thesis (Physics Department, University of Pisa, October 1991). Two microscopes were used at LBNL, a commercially available instrument (Autoprobe™, Park Scientific Instruments, Sunnyvale, CA, USA) and a home-built machine. Complete mechanical and electronic maintenance on the home-built AFM was performed by the author during the whole period of time spent in Berkeley.

In this chapter, brief descriptions will be given for the STM, AFM (Pisa) and commercial AFM (Berkeley), while greater details of modes of operation and experimental methods will be given for the home-built AFM used at LBNL. The greatest part of the AFM studies presented in this thesis was conducted with the latter machine.

4.2 Berkeley's Home-Built AFM

4.2.1 The Apparatus

The cross-sectional view of the home-built AFM employed at LBNL is shown in figure 4.1.[1] Its design is very simple and similar to that of other scanning force microscopes.[2, 3] It employs a microfabricated cantilever with an integrated tip and an optical lever to detect the cantilever motion. The sample is mounted on the end of a piezoelectric tube scanner and is magnetically clamped. The piezotube is segmented with 8 electrodes, which provides motion in three orthogonal directions. Four segments are used for the x and y scan (1 μm scan range) and the other four give the offset in the x and y directions (1.5 μm offset range). The inner electrode is used for motion in the vertical (z) direction. The x fast scan direction is perpendicular to the cantilever long axis, while the y slow scan direction is along the cantilever long axis. In some cases the scan was rotated by 90^{o}, i.e. scanning was carried out parallel to the lever long axis.

Light from a laser diode[4] is focused on the end of the cantilever and reflected onto a 4-segment photodiode.[5] The cantilever motion is sensed by combining, via addition and subtraction, the photocurrents from the 4 segments in pairs in such a way as to detect the optical beam deflection in two orthogonal directions. One direction corresponds to motion of the cantilever normal to the sample surface ('A-B' signal) and the other to twisting of the cantilever ('1-2' signal). The schematic of such detection scheme is shown in figure 4.2.

The AFM electronics is a home-built unit consisting of an 'AFM amplifier', scan and offset generators and feedback unit. The 4 photocurrents are pre-amplified and then combined to provide the 'A-B', '1-2' and total reflected laser intensity (A+B ≡ 1+2) into the 'AFM amplifier' unit (figure 4.2). The same electronics, except for the 'AFM amplifier' box, is also used on all the other SPM systems at the STM/AFM lab at LBNL. The electronics is interfaced to an IBM compatible PC and software, written by Dr. D. F. Ogletree of the STM/AFM group at LBNL, provides control of the scan generator and feedback unit. The same software also enables one to analyze and process SPM data.

During operation the AFM head is suspended through 3 elastic bands from a small stainless steel frame. This system has proven to be very effective in damping low-frequency noise, that can greatly affects AFM and other SPM imaging.[6] The AFM head is also enclosed into a chamber that provides sound insulation and that can be filled with any gas.

View of the tip-sample area through an optical microscope is used to carry out the coarse, initial approach of the tip to the sample by three screws located

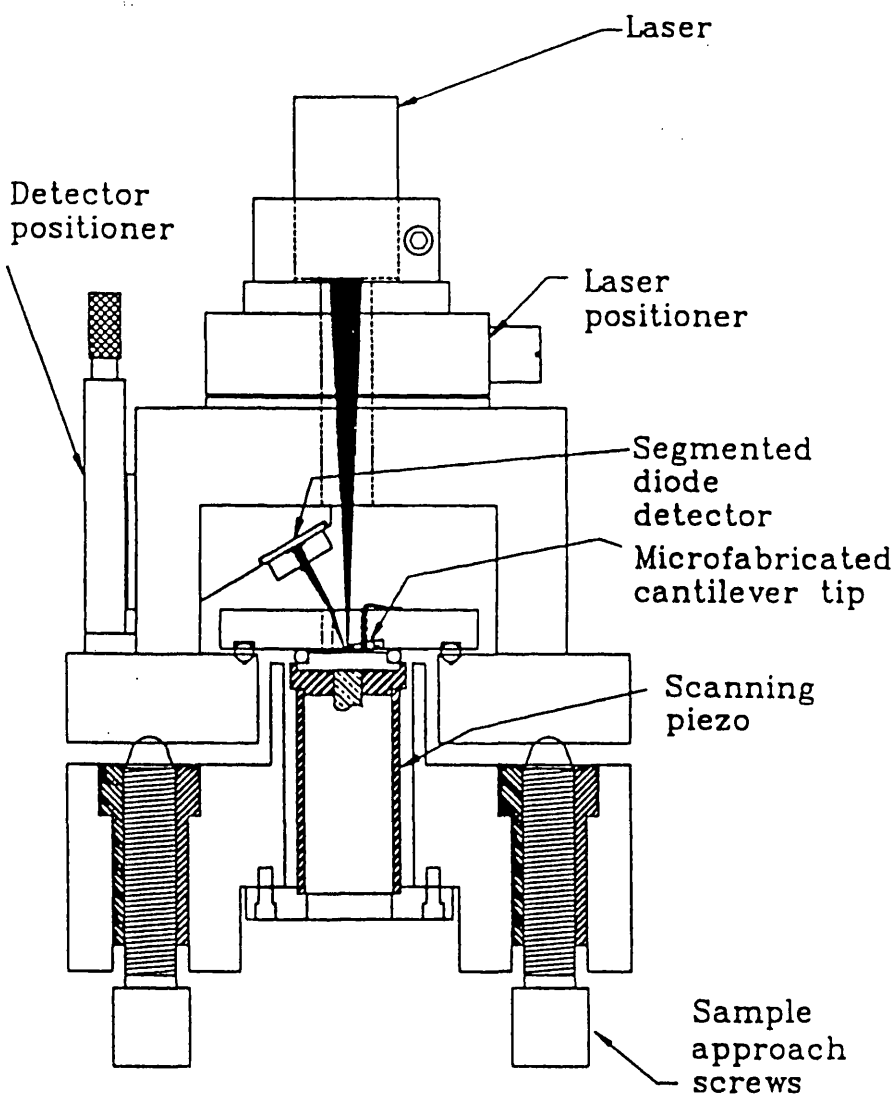

Figure 4.1. Cross-sectional view of the home-built AFM used at LBNL.

under the AFM head.

Gold-coated silicon nitride cantilevers, commercially available from Digital Instruments and Park Scientific Instruments, were used.

4.2.2 Operating Modes

As schematically shown in figure 4.2, the normal deflection of the cantilever (and the externally applied load F_{ext}) is proportional to the difference between the light intensities measured by the top and bottom sectors of the photodiode. The cantilever twisting in the x direction is proportional to the difference between the photo-currents detected by the left and right sectors of the photodiode. This signal ('1-2' signal) is used for friction images.

When the lever undergoes large z displacements, a change in the '1-2' signal is often observed. This can be due to mis-alignment of the optical components, a rotation of the photodiode, or a displacement of the tip from the lever axis. Such coupling is a source of error in friction measurements made at different loads. This problem is avoided in this system by electronically decoupling the '1-2' signal from the 'A-B' one. To do so, a small percentage of the 'A-B' signal is subtracted or added to the '1-2' signal so that the latter is constant during approach-retract curves. Since the '1-2' signals are much smaller than the 'A-B' signals (25 to 40 times for the levers used for this thesis work), it was not necessary to also decouple 'A-B' by electronically rotating the quadrant photodiode output.

Data are acquired simultaneously for both signals in the forward (+x) and backward (-x) scan directions so that a set of four images is obtained for each scan. A +x/-x pair of scan lines of the frictional force images gives a 'friction loop'. To eliminate any offset in the lateral force signal, half the width of the friction loop is used as a measure of friction.

For the work reported in this thesis, the microscope is operated in two different modes, *topographic* and *variable load mode*. In the *topographic*, or *constant deflection mode*, the 'A-B' signal (and the external load F_{ext}) is kept constant by a feedback loop. The feedback 'error' signal gives the surface topography. Simultaneous images show the variations in the lateral force. Typical scan rates used go from about 1 kHz (large scan areas and non-flat topography) to up to 10 kHz (atomic lattice resolution images).

When the microscope is operated in the *variable load mode*, the feedback is disabled and the normal load is changed after each scan line by moving the sample up or down. The y scan range is set to zero. Schematic of this mode of operation is shown in figure 4.3. In this case, the y axis in the AFM image represents the sample vertical displacement z and hence the normal force applied between

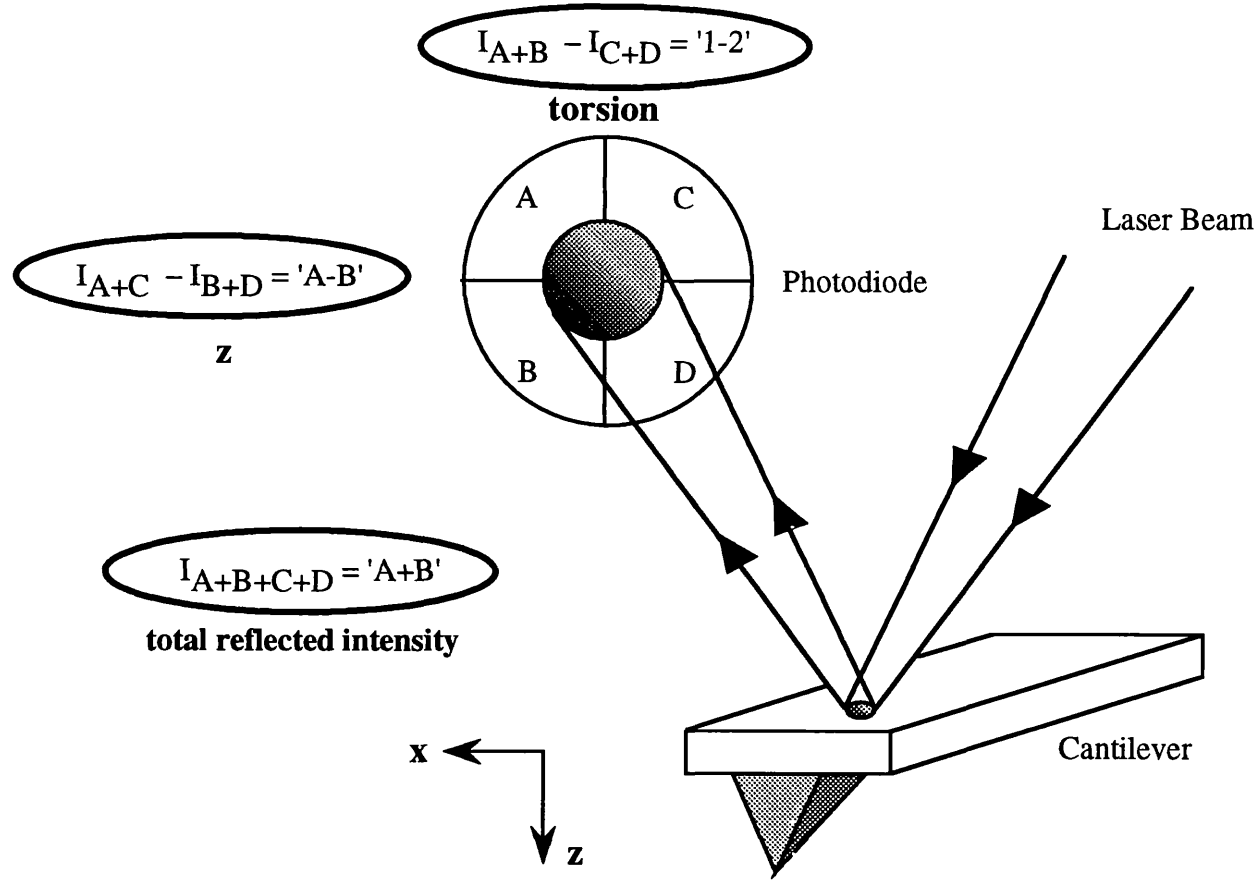

Figure 4.2. Principle of simultaneous measurement of normal and lateral forces. The difference between the intensities of the upper and lower sectors of the photodiode is proportional to the z-bending of the cantilever. The difference between the intensities of the left and rights sectors is proportional to the torsion of the lever.

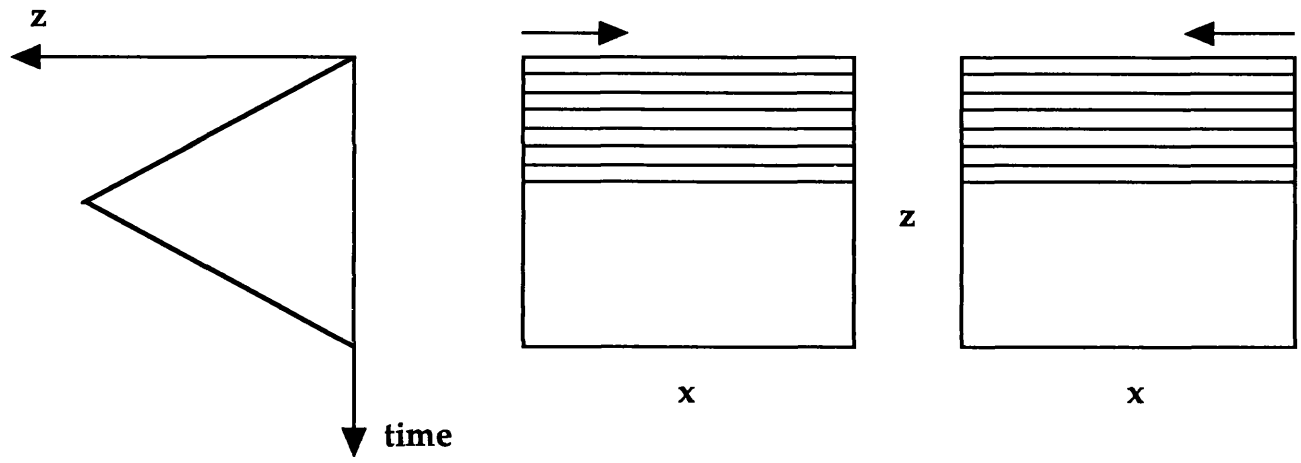

Figure 4.3. Schematic of *variable load mode* of operation. The normal force between the tip and sample is changed after each scan line by applying a voltage step to the piezo z electrode. In this case the axis in AFM images represent the sample horizontal (x) and vertical (z) displacements.

tip and sample. The 'A-B' and the '1-2' signals are acquired simultaneously. The 'A-B' data for each x scan line are averaged together and the result is plotted versus sample vertical displacement z (figure 4.4). The '1-2' image for the backward -x direction is subtracted from that corresponding to the forward +x direction and then all the data points along each horizontal line are averaged together. The edges of the images corresponding to static friction effects are always excluded from the average. The '1-2' data so obtained are then plotted versus the 'A-B' signal (load or F_{ext}). For the majority of experiments reported in this thesis, variable load mode curves were taken by first increasing and then decreasing the normal load. Occasionally, the sequence was reversed. If friction is plotted versus the applied z piezo voltage, V_z, rather than lever deflection, the plot is significantly distorted by piezo hysteresis and creep, as shown in figure 4.5. The hysteresis visible in figure 4.5 (a) and 4.5 (b) is due to the response of the piezoelectric transducer to the applied voltage. In fact, after the tip makes contact with the surface, the 'A-B' signal is proportional to the nominal z piezo displacement, while the actual z displacement is not proportional to the applied voltage because of piezo hysteresis and creep. When the frictional force is plotted directly *vs.* the 'A-B' voltage the hysteresis disappears, as shown in figure 4.5 (c).

4.2.3 Instrumental Calibration

In order to perform quantitative AFM studies, it is necessary to know the normal and lateral force constants of the cantilever, the sensitivity of the optical detection and the shape of the tip. Ideally this calibration should be performed *in situ.* In this work such calibrations were not available, so the quantitative data presented throughout this thesis is based on estimated calibrations.

The AFM tip radius **R** was estimated from the apparent width **w** of monatomic steps of height **h** by using the formula:

$$\mathbf{R=w^2/2h} \qquad (4.1)$$

The formula is derived from simple geometrical considerations as shown in figure 4.6. More details on the two types of tips used and their radii will be given in chapter 6 and 7.

The piezo scanner lateral sensitivity was calibrated from lattice-resolution images of mica and Au(111), as discussed in detail in chapter 7. The optical deflection sensitivity relative to bending, S_z, was determined from the slope of the 'A-B' versus piezo voltage V_z curves, i.e. approach-retract curves. Since the measured slope is affected by piezo hysteresis and creep, the average between the slope of the approach and retract branches was taken. When the microscope is operated in *variable load mode,* the approach-retract curves taken as described in

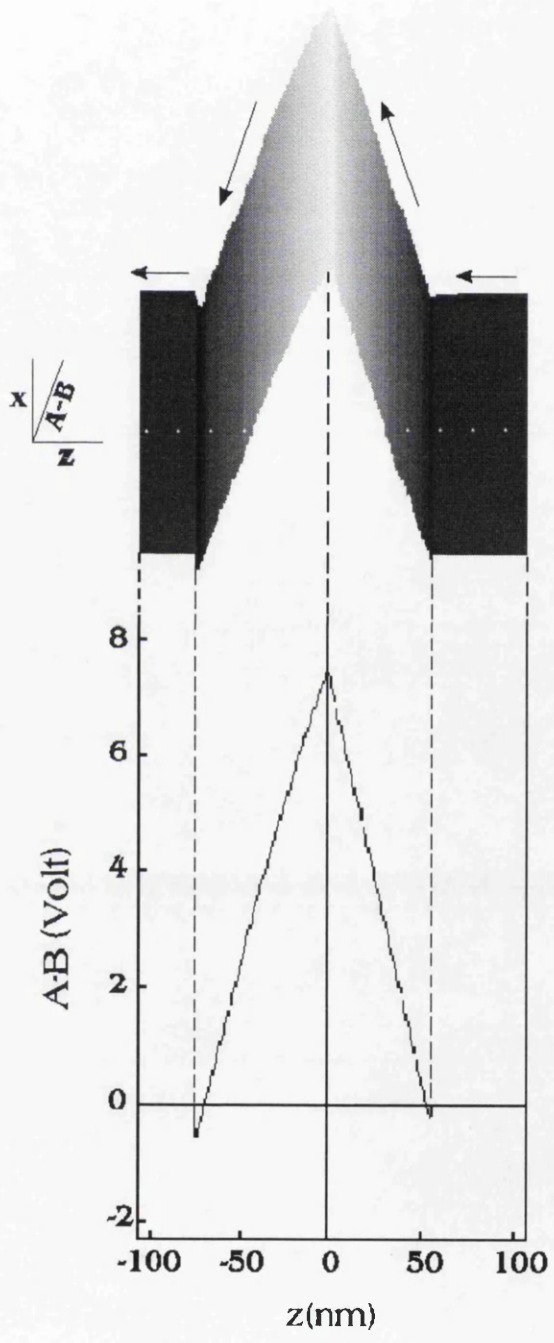

Figure 4.4. (top) 3-D plot of the lever bending image ('A-B' signal) obtained on a self-assembled monolayer of octadecylthiol on Au(111) in *variable load mode*. All the data points along each x scan line are averaged together and the 'A-B' data is then plotted as a function of sample vertical displacement z to give an approach-retract curve (bottom).

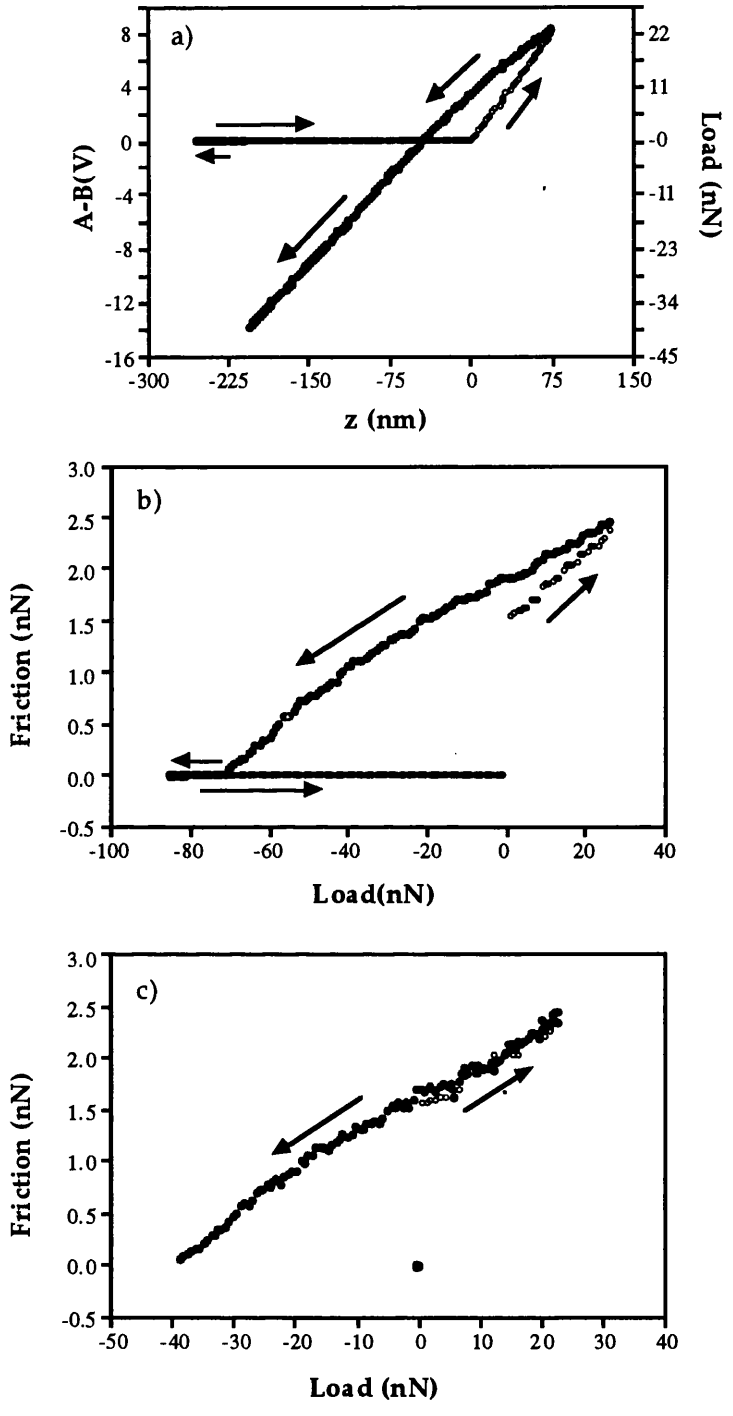

Figure 4.5. Lever deflection signal *vs.* piezo nominal displacement (applied voltage) approach-retract curve (a), friction *vs.* nominal displacement (b) and friction *vs.* 'A-B' signal (c) curves obtained on a mica surface. The values relative to approach and retract branches are shown as open and filled circles, respectively. Load is the externally applied force and negative loads correspond to the tip being pulled off the surface. The hysteresis visible in (a) and (b) is due to the response of the piezoelectric transducer to the applied voltage. In (c) the hysteresis has disappeared. The 'A-B' signal is proportional to the piezo z displacement, while the actual z displacement is not proportional to the applied voltage due to piezo hysteresis and creep.

section 4.2.2 lead to a slightly different calibration. Since the acquisition rate is slower for these curves than for normal approach-retract curves (25-40 Hz compared to 500 Hz-1kHz), the piezo hysteretic response and creep produce the observed difference. Therefore, in this mode the averaged slope of the approach and retract branches of a series of faster and slower approach-retract curves is used for calibrating the bending signal. The small-signal z piezo calibration was determined from monatomic step heights on Au(111) and from single-layer steps on mica, artificially generated by wearing the surface, as it will be described in chapter 7. The lever displacement ('A-B' voltage) was converted to load using cantilever force constants estimated from a continuum elasticity model after measuring the levers critical dimensions by SEM.[7, 8] Details of the method are given in chapter 6. The lateral optical deflection sensitivity was assumed equal to the normal deflection sensitivity, and the force calibration was derived from an estimate of the relative deflection due to bending and twisting of the cantilever.

The values for forces quoted throughout this thesis are necessarily approximate due to the calibration methods used here, however they are probably correct within a factor of two.

4.3 Berkeley's Commercial AFM System

The second AFM used in Berkeley was an AutoProbe™ LS system available from Park Scientific Instruments. The vibration isolation system for this microscope combines the manufacturer provided suspension system with a home-made one. The whole head is suspended with bungee cords from a metallic frame, which rests in sand. This home-made vibration isolation system is used in other SPM systems at LBNL and has proven to be very effective.

The microscope head schematic is shown in figure 4.7.[9] The scanner is a piezoelectric tube positioned under the sample. The scan range is 80 μm. The cantilever position is fixed. Pre-mounted Si Ultralevers™ cantilevers (Park Scientific Instruments, Sunnyvale, CA, USA) are used with this system.

The x and y stage is controlled by two stepper motors and can be moved by 12 mm and 37 mm in the x and y direction, respectively. The sample-tip approach is automatic and controlled by three stepper motors. An optical microscope and high-resolution CCD camera help one to position the tip in a desired location on the sample.

The microscope is operated in contact mode under ambient conditions and

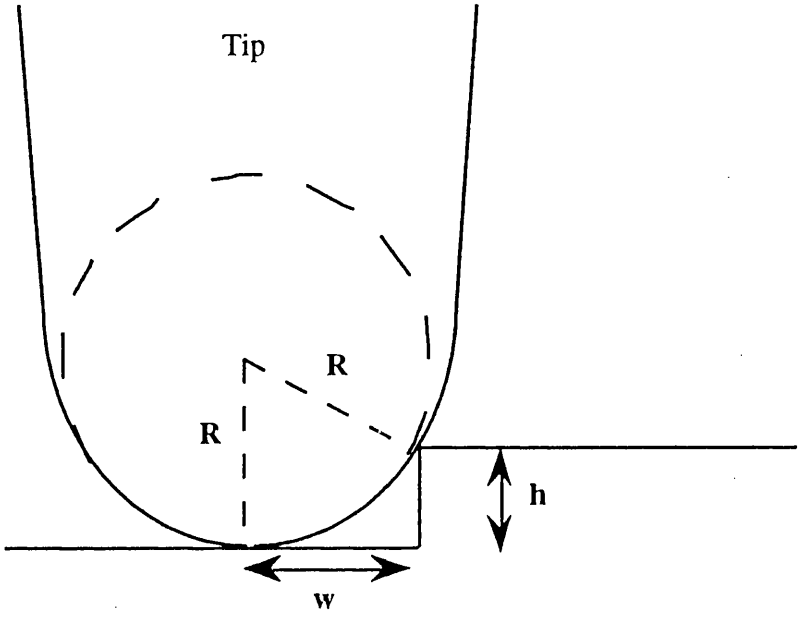

$$R^2 = w^2 + (R-h)^2$$

$$R = (w^2/2h) + h/2 \approx w^2/2h$$

Figure 4.6. Evaluation of AFM tip radius, **R**, from measured atomic step height, **h**, and apparent step width, **w**. The tip apex is approximated to a perfect sphere of radius **R**.

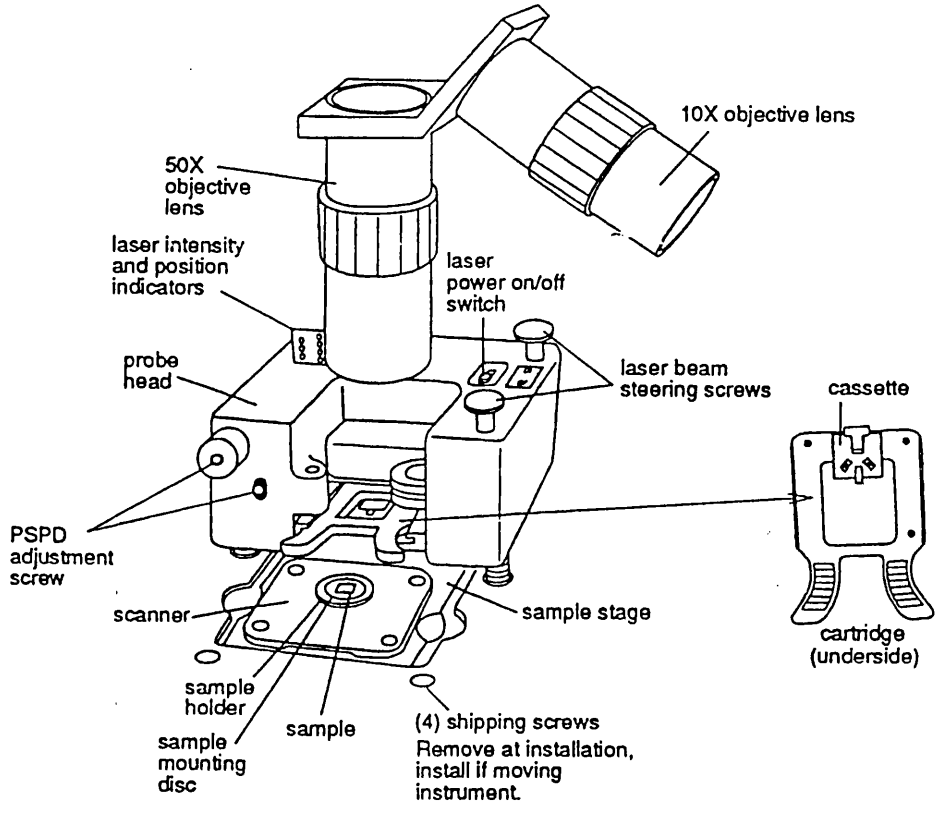

Figure 4.7. Schematic of the head of an AutoProbe™ LS AFM system (from reference 9).

only the forward topographic image can be acquired, i.e. the bending signal only is detected by a two-quadrant photodiode.

4.4 Pisa's AFM System

This scanning force microscope operates in contact mode under ambient conditions. Its schematic diagram is showed in figure 4.8.[10] The microscope is mounted on a vibration damping table and is contained in an aluminum box for the screening of acoustic and electrical noises. The sample is mounted on an xyz piezo transducer (Staveley Sensors Inc., USA), which has a maximum x and y scan range of 28 μm. The coarse approach of the sample to the tip is made by means of two micrometers connected by a reduction lever. The cantilever is always in a fixed position to allow deflections to be detected by the optical lever technique. The light source is a laser beam from a 5 mW laser diode.[11] A four-segment photodiode is used for detection of the normal bending and lateral twisting of the cantilever. Commercially available silicon nitride cantilevers (Park Scientific Instruments, Sunnyvale, CA, USA) were used. Uncoated cantilevers were used in Pisa to avoid thermal effects due to the laser light (note that this laser power is 20 times higher than the one used in Berkeley for the same type of laser diode).[12]

The electronics is a home-built, hardware controlled unit. Images are displayed in real time on the monitor of an IBM compatible PC using a grey-level representation and can then be treated for the subtraction of a sloping plane, filtering, contrast enhancement.

The microscope described above is actually a combined AFM/STM system. In the STM mode the cantilever is replaced by a sharp metal tip facing the sample. A switchable logarithmic amplifier included in the control unit allows for the linearization of the tunnel current.[10]

4.4 Glasgow's Commercial STM

The scanning tunneling microscope used in Glasgow is commercially available from W. A. Technology Ltd., Cambridge (UK). It operates in air. The microscope is placed on a vibration-damping table and during operation is enclosed in a thick, wooden box which interior walls are coated with sound-absorbing foam. This

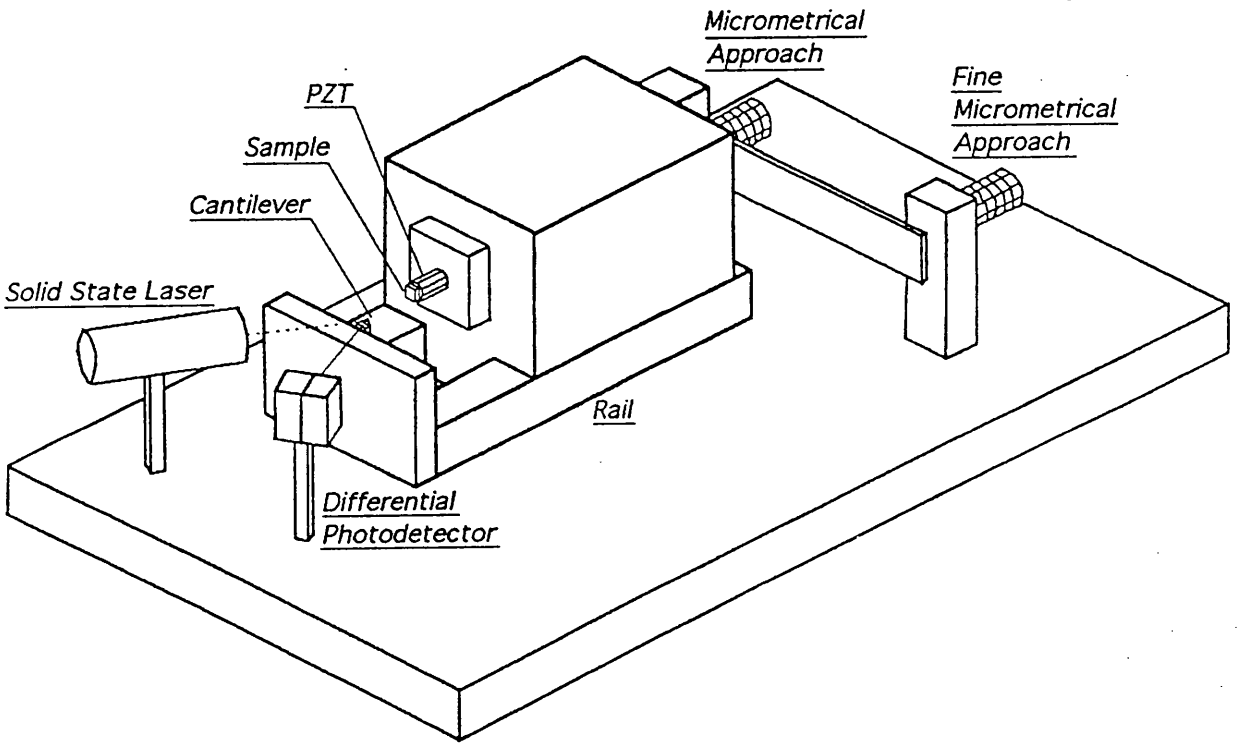

Figure 4.8. Schematic drawing of the head of the AFM apparatus used at the CNR, Italy.

insulation system was implemented during the second year of this project in order to improve the performance of this microscope.

Tip and sample are housed in a rigid stainless-steel frame (figure 4.9).[13] Two internal anti-vibration stacks, consisting of flat rectangular metal plates resting freely on separators of Viton synthetic rubber, are present for high frequency isolation. A binocular microscope allows for viewing of the tip-sample gap. A coarse and a fine control of the gap distance are possible. The coarse control moves the specimen, the fine one moves the tip. Fine movements of the tip in x, y, z are provided by a piezotube transducer. No coarse motion in x and y is possible.

The electronic control unit is provided by the company. It can be operated manually from the front panel of the control unit itself or controlled from an IBM compatible PC. Forward and reversed x and y scans are possible and the maximum scan area is 504 nm x 504 nm. The maximum number of image points per line and number of lines is 256.

Images are displayed in real-time on the PC monitor and on a grey-scale monitor. The software, provided from the company, also allows for image and data processing.

Initially, W tips were used as probes. These tips were electropolished from a tungsten wire (ϕ = 0.5 mm) in a 2M KOH solution at 9 V dc, without any further treatment. However, during the first year of this project, it was recognized that the oxide layer present on the surface of W tips made imaging unstable and unusually high bias voltages (1-2 Volts) were necessary to make the tunnel gap stable. Indeed, an electrochemistry study of the electropolishing process showed anodic oxidation of W occurring in KOH solution.[14] In view of those results, W tips were replaced by commercially available Pt/Ir tips (Materials Analytical Services, NC, USA).

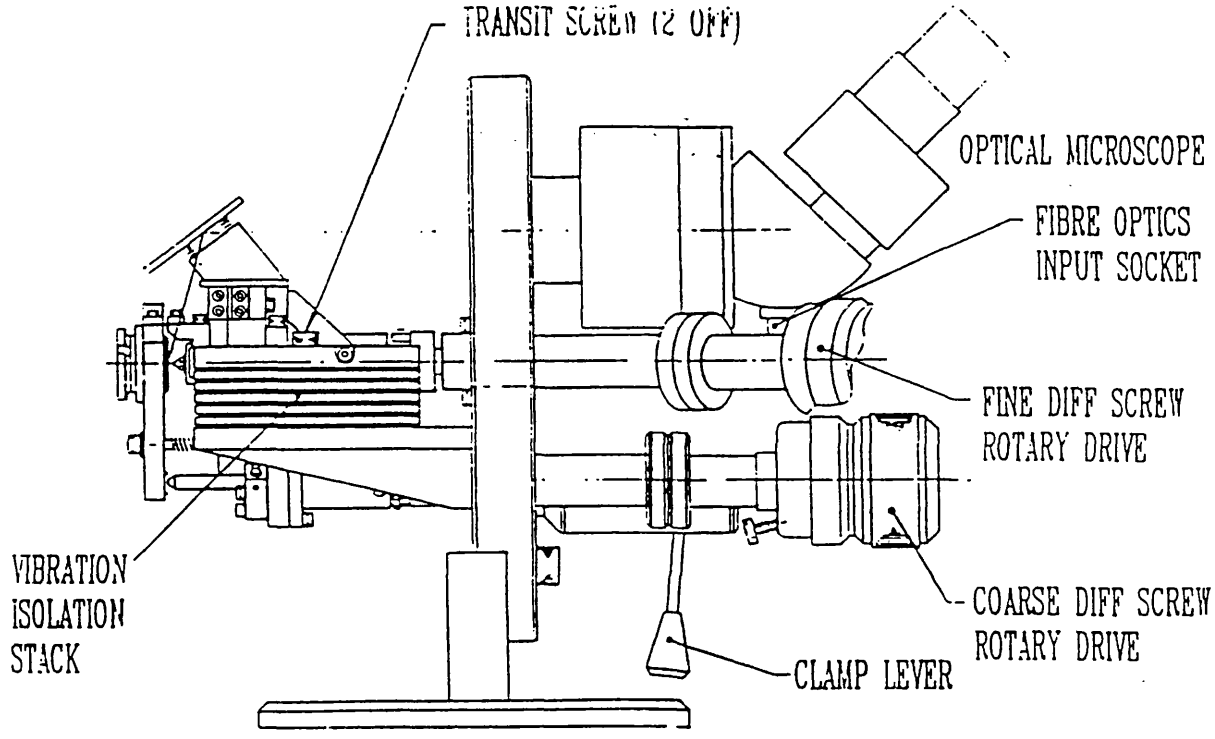

Figure 4.9. Cross-sectional view of the W. A. Technology STM system used at Glasgow University (from reference 13).

References

[1] W. F. Kolbe, D. F. Ogletree, M. B. Salmeron, *Ultramicroscopy*, **42-44**, 1113 (1992).

[2] G. Meyer, N. M. Amer, *Appl. Phys. Lett.*, **53**, 1045 (1988).

[3] S. Alexander, L. Hellemans, O. Marti, J. Schneir, V. Elings, P. K. Hansma, *J. Appl. Phys.*, **65**, 164 (1989).

[4] Toshiba TOLD 9211 laser diode (670 nm wavelength, operated at 250 μW).

[5] PIN-SPOT4D segmented diode from United Detector Technology, Hawthorne, CA, USA.

[6] A. Lio, *Laurea Degree Thesis* (Physics Department, University of Pisa, October 1991).

[7] D. F. Ogletree, Personal Communication.

[8] D. F. Ogletree, R. W. Carpick, M. Salmeron, *Rev. Sci. Instrum.*, **67**, 3298 (1996).

[9] *Autoprobe™ User's Manual*, Park Scientific Instruments, Sunnyvale, CA, USA.

[10] M. Allegrini, E. Arpa, C. Ascoli, P. Baschieri, F. Dinelli, C. Frediani, M. Labardi, A. Lio, T. Mariani, L. Vanni, *Rivista del Nuovo Cimento D- Condensed Matter*, **15**, 279 (1993).

[11] Toshiba TOLD 9211.

[12] M. Allegrini, C. Ascoli, P. Baschieri, F. Dinelli, C. Frediani, A. Lio, T. Mariani, *Ultramicroscopy*, **42-44**, 371 (1992).

[13] *STM User's Manual*, W. A. Technology Ltd., Cambridge, UK.

[14] A. Lio, *I Year PhD Report*, Department of Electronics and Electrical Engineering, Glasgow University, February 1993.

Chapter 5

Other Experimental Methods

5.1 Introduction

This chapter briefly describes the experimental methods, other than SPM, used during this thesis work. The chapter is divided into 3 sections. The first section gives an account of the self-assembly and Langmuir-Blodgett techniques used for the preparation of thin organic films. The second section describes surface analysis techniques: contact angle measurements, fluorescence microscopy, Fourier transform infrared spectroscopy, scanning electron microscopy, x-ray diffraction and Auger electron spectroscopy. The third section gives an account of photolithography and electron-beam lithography methods.

5.2 Preparation Methods of Organic Thin Films

Two methods are commonly used to prepare organic thin films, the self-assembly and the Langmuir-Blodgett techniques.

5.2.1. Self-Assembly

Molecules with a hydrophobic part and a polar group can *spontaneously* adsorb from a solution onto an appropriate substrate in contact with the solution,[1] as schematically shown in figure 5.1(a).

To date several classes of molecules have been self-assembled, such as silanes on hydroxilated surfaces; alkanethiols on gold, silver and copper; alcohols and amines on platinum and carboxylic acids on aluminum oxide and silver.

Figure 5.1(b) shows a molecule schematic. The head-group is the surface active part responsible for chemisorption on the substrate. Once the molecules have adsorbed and the molecules are close enough together, the van der Waals interactions between the alkyl chains are the driving force for the formation of 'ordered' and 'close-packed' assemblies. It should be noted that the term 'close-

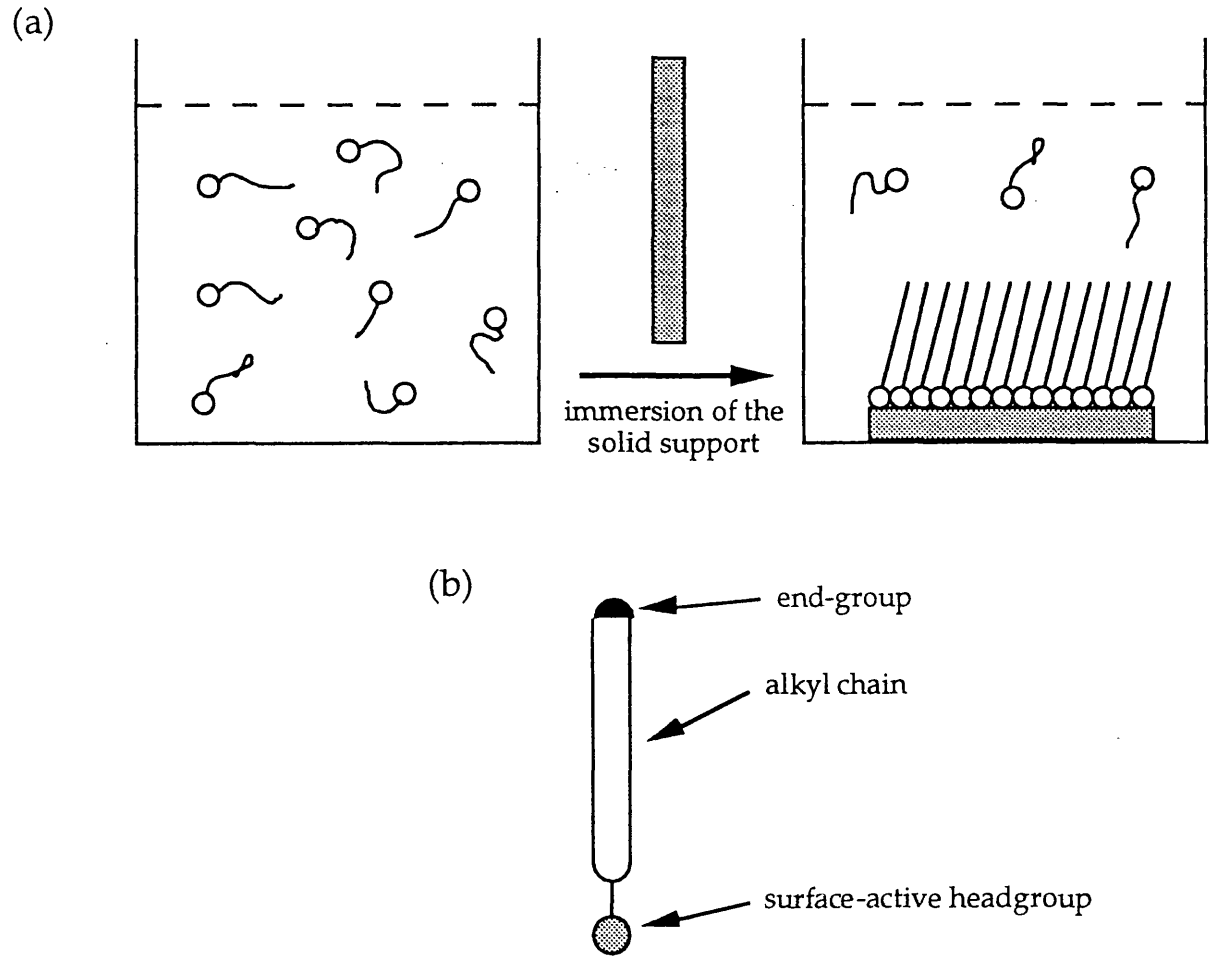

Figure 5.1. (a) Schematic view of the self-assembly process. (b) Schematic representation of a surfactant molecule.

packed' is associated in this contest with the density of crystalline polyethylene and does not mean that self-assembled monolayers (SAMs) are pinhole- and defect-free. In addition, the term 'ordered' does not necessarily imply long-range, crystalline-like order. As it will be shown in this thesis, alkylsilane SAMs only show short-range order as opposed to the long-range order of long chain alkylthiols on gold.

5.2.2 Langmuir-Blodgett Technique

In a Langmuir-Blodgett experiment,[2, 3, 4] molecules that are hydrophilic at one end and hydrophobic at the other (amphiphiles) are spread at the air-water interface of a trough by dropping a solution of the material in a volatile solvent on the water surface. The solvent evaporates and the molecules remaining at the surface are packed by applying an appropriate surface pressure, π. The molecules are then transferred to a solid substrate by vertically dipping it into the water while keeping the molecular density at the interface constant. A schematic of this method is shown in figure 5.2(a)-(c). The molecules in the trough are compressed by moving barriers, while the surface pressure is measured as a function of molecular area (surface pressure-molecular area, π-A, isotherm) (figure 5.2(d)).[5] As the molecules are spread, they are far apart forming a 'two-dimensional gas'. In this case the surface pressure is low. As the barrier moves, the distance between the molecules decreases and the surface pressure increases. In some cases, such as that of stearic acid, a phase transition is observed to the 'liquid-expanded phase'. In this phase the area per molecule is still large and *gauche* conformations can be found in the molecules. As the barrier compresses the film even further, there is another transition to the 'solid state', or 'liquid-condensed phase'. In this phase the molecules are closely packed and uniformly oriented. If the pressure in increased further, a decrease ('collapse') in the pressure is observed. When the collapse occurs, molecules are forced out of the monolayer to form agglomerates. The collapse pressure is a function of several variables, such as pH of the subphase, temperature, speed by which the barrier is moved.

Another way of depositing layers on solid substrate is by the Langmuir-Schaefer, or horizontal lifting technique.[6] In this method the substrate is horizontally touched to the water surface, that is parallel to it. When the sample is lifted from the water surface, the monolayer is transferred keeping, in theory, the same molecular direction. This method is particularly useful for the deposition of rigid films, i.e. films that are in the two-dimensional solid phase in the π-A isotherm. In particular, the method is suitable for transferring monolayers of polymeric amphiphiles due to their high viscosity.

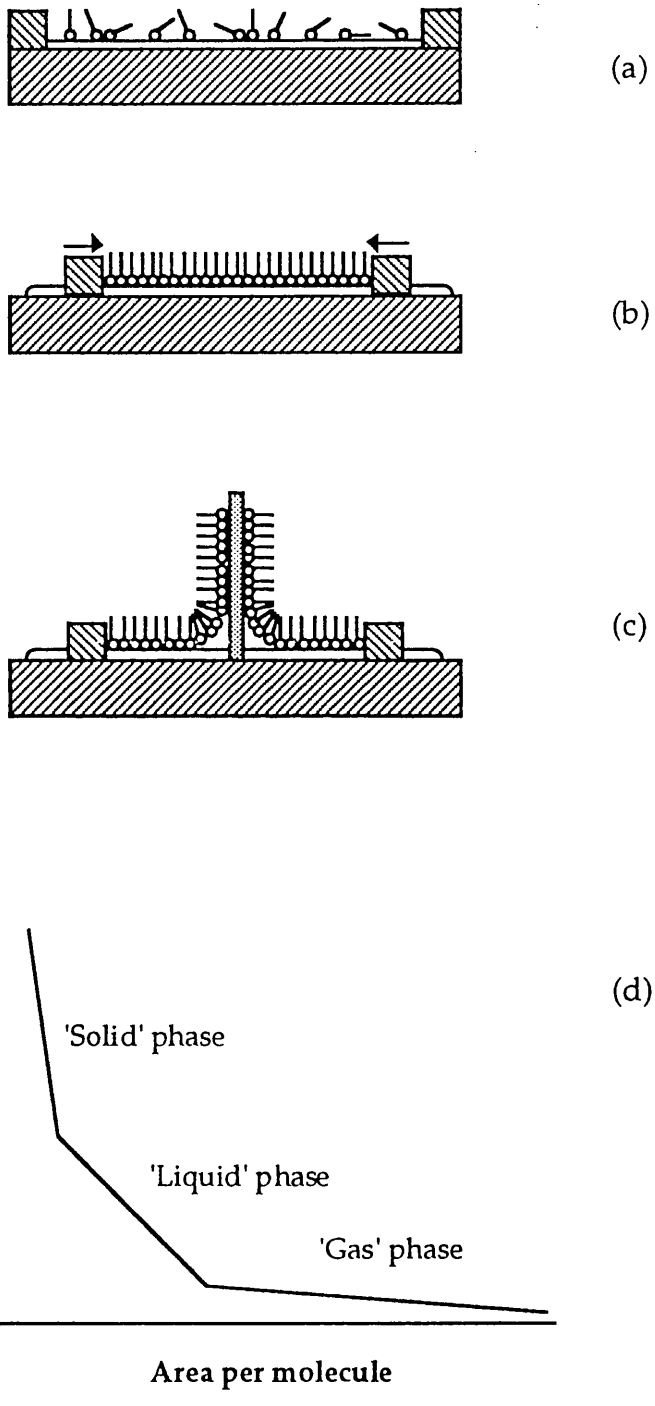

Figure 5.2. (a)-(c) Schematic representation of the Langmuir-Blodgett process. A monolayer of molecules in a two-dimensional 'gas phase' (a) and in the 'solid phase' (b). (c) Deposition of a compressed monolayer from the air-water interface to a vertical plate. (d) Generalized π-A isotherm for a long-chain surfactant.

5.3 Analysis of Surface Properties

5.3.1 Contact Angle Measurements

The quality of monolayer and multilayers films is commonly estimated from wetting measurements. This is due to the fact that the shape of a drop on a solid surface is affected by the free energy of this surface. When a liquid does not wet a surface completely, it forms an angle θ, the contact angle with the surface (figure 5.3). The contact angle of a drop on an ideal solid surface is the result of the balance between the cohesive forces in the liquid and the adhesive forces between the solid and the liquid, as expressed by the Young equation:[7]

$$\gamma_{LV} \cos(\theta) = \gamma_{SV} - \gamma_{SL} \qquad (5.1)$$

where γ_{LV}, γ_{SV} and γ_{SL} are the liquid-vapor, solid-vapor and solid-liquid interfacial energies, respectively. When the attraction between the surface and the liquid is strong, the drop spreads out and the contact angle is measured to be a small number, typically 5-10^{o} (figure 5.3 (a)). In the case where the interaction of the liquid with itself and the environment out-weighs the attraction of the liquid for the surface, the water beads up on the surface (figure 5.3(b)) and the contact angle rises.

The most common method of measuring contact angles is to measure θ directly for a drop of liquid resting on a flat surface using a contact angle telegoniometer.

Despite the relatively simplicity of contact angle measurements, their interpretation in terms of microscopic properties can be very difficult due to the fact that real surfaces are not flat and homogeneous, but rather rough and inhomogeneous. An example of misleading contact angle results will be given in chapter 10, in the case of self-assembled alkylsilanes on mica.

5.3.2 Fluorescence Microscopy

Some substances when irradiated with light of a certain wavelength, partly absorb it and partly re-emit it as light of longer wavelength. If the light is re-emitted almost instantaneously after the excitation, the process is called fluorescence.[8] The process is summarized in figure 5.4.

The characteristic spectra of fluorescence are the excitation and the emission spectra. The first one is a plot of the total intensity of fluorescence versus the excitation wavelength, while the second is a plot of the relative intensity of fluorescence *vs.* wavelength.

The basic principles of fluorescence microscopy are those of optical microscopy. However, a fluorescence microscope includes special parts respect to a

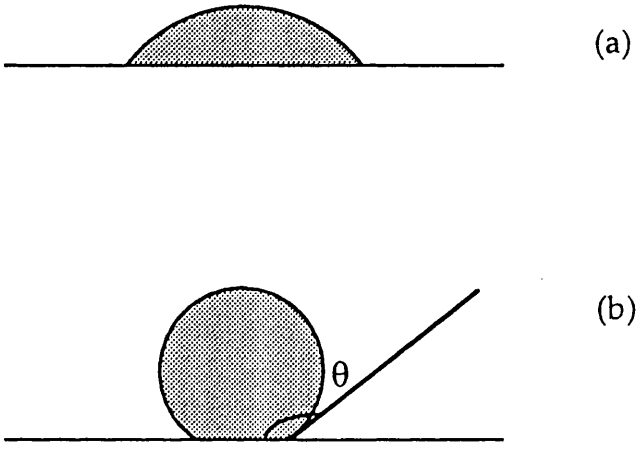

Figure 5.3. A liquid drop on a solid surface. (a) The drop spreads out on a hydrophilic surface, while (b) it beads up on a hydrophobic substrate.

conventional optical microscope. One of the most commonly used arrangements is shown in figure 5.5. The excitation filter, normally a band-pass filter, is used to select the wavelength needed to excite fluorescence. The barrier filter, a long-pass or band-pass filter, prevents the excitation light to reach the eyepiece. This is quite important since fluorescent light is normally very weak. Ideally, the excitation filter should have 100% transmission at the absorption peak of the fluorophore and 0% at fluorescence wavelengths. Viceversa for the barrier filter. Finally, the dichroic mirror reflects the excitation wavelengths and transmits the fluorescence ones.

5.3.3 Fourier Transform Infrared Spectroscopy

The basic principle of Fourier transform infrared spectroscopy (FTIR) is common to all infrared spectroscopies, i.e. infrared radiation is used to excite vibrational levels in molecules spectra.[9] An FTIR spectrometer basically consists of two parts: a) a Michelson interferometer and b) a computer for data acquisition and analysis. The light from an infrared source is first splitted in two parts, made to interfere and finally recombined in the interferometer. It is then directed to the sample and focused on an infrared detector (figure 5.6). A laser beam with the same optical path as the infrared beam is used to reference the position of the moving mirror in the Michelson interferometer and give the sampling signal for data collection. The detector signal is recorded as a function of the path difference between the two parts of the infrared beam in the interferometer. The signal is then Fourier transformed, which gives the output signal as a function of frequency.

In absorption and reflection infrared spectroscopy the radiation is passed through (or reflected from) the sample, which can be held anywhere between the source and the detector. The transmittance of the sample is calculated by taking the ratio of the energy transmitted through the sample at each frequency in the spectrum to the energy at the detector. The reflectance is equal to the energy reflected off the sample to the energy reflected off a specular reflector.

5.3.4 Scanning Electron Microscopy

In a scanning electron microscope (SEM)[10] a beam of electrons with energies up to 30 or 40 keV is focused at the surface of the specimen and raster scanned across it. When the primary electron beam strikes the surface a number of phenomena occur, as schematically shown in figure 5.7. Each of them can be used to provide a particular information about the specimen. *Secondary electrons* are low energy (few tens of eV) electrons that originate from the collision of the high energy electrons of either the primary beam or the backscattered electrons with the sample

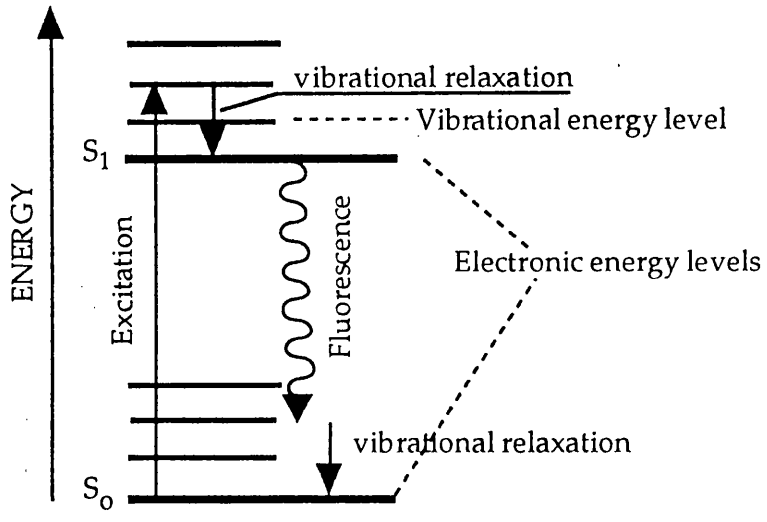

Figure 5.4. An electron is excited from the ground level S_0 to an excited energy level S_1 through absorption of a photon. The molecule may then return to the ground state by emission of a photon. If the lifetime of the excited state is between 1 and 10 ns, the re-emission of light is called fluorescence.

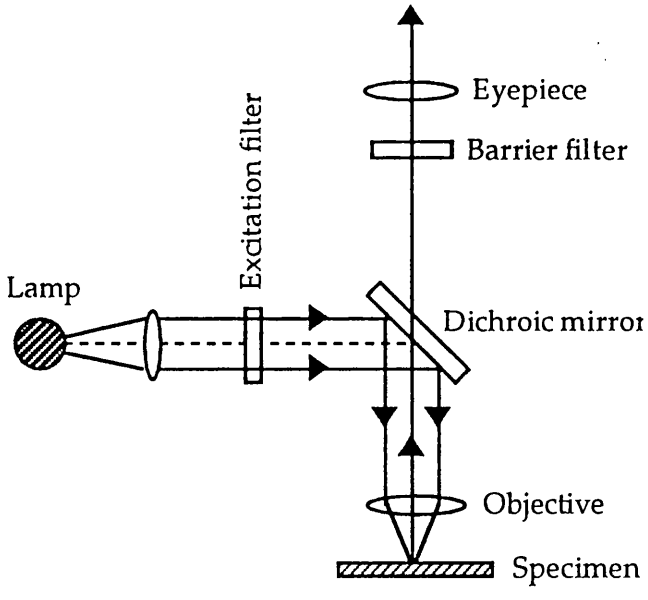

Figure 5.5. Schematic diagram of an epi-fluorescence microscope.

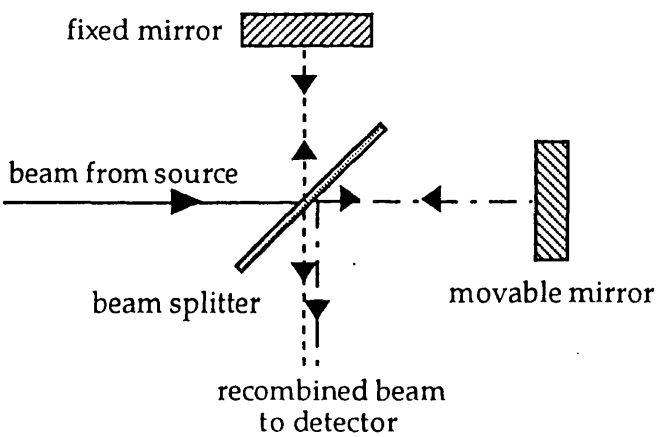

Figure 5.6. Schematic diagram of the Michelson interferometer.

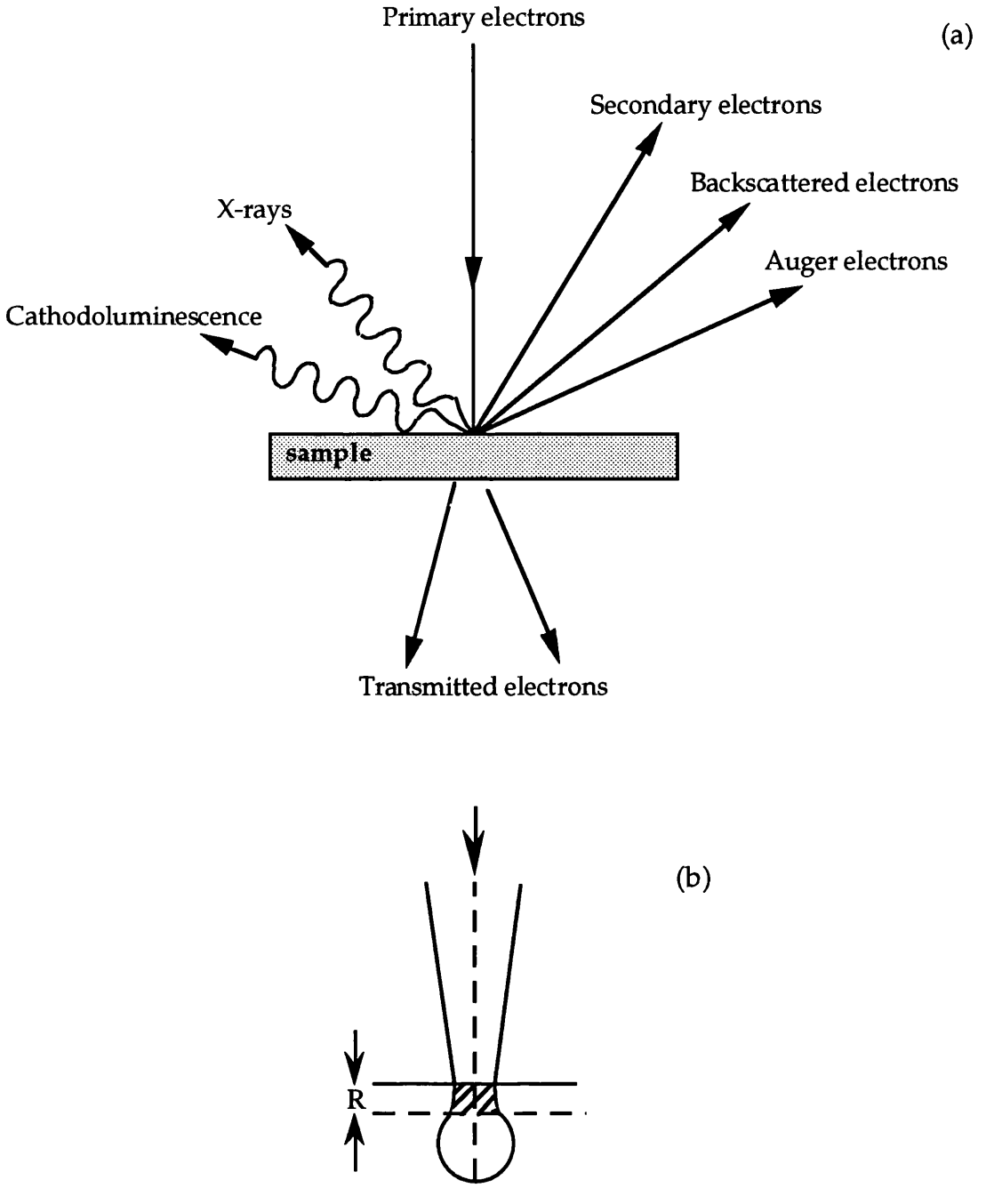

Figure 5.7. (a) Photon and charged particle emission phenomena that take place at an electron bombarded surface. (b) Secondary electrons are created in a large 'droplet' inside the specimen, but only those released in the shaded area will escape to form the secondary electron yield. (Adapted from reference 10).

atoms. *Backscattered electrons* are thought to be primary beam electrons that are scattered back after colliding with the specimen atoms. Their energies range from the full primary beam energy to the secondary electrons energy. The total secondary electron yield, δ, is defined as the number of electrons emitted per incident primary electron. The intensity of both secondary and backscattered electrons is very sensitive to the angle at which the primary beam strikes the surface, i.e. to the surface topography. Both types of electrons can be used for SEM imaging.

5.3.5 X-Ray Diffraction

When an element is bombarded by electrons of enough energy, a core level is ionized creating a vacancy. This vacancy can be filled by an electron from one of the higher energy levels. The energy difference between the two levels is radiated as a photon of x-ray radiation. Each atom species is therefore characterized by a specific x-ray emission spectrum. Theses lines are superimposed on a background continuum (*white radiation*), which is only determined by the maximum energy used to excite the x-rays.

According to the Bragg's law, given an incident beam of x-rays (or electrons) on a crystal there will be a strong reflected intensity only for incident angles θ that satisfy the following relation:

$$2d\sin\theta = n\lambda \qquad (5.2)$$

where **d** is the separation between the atomic planes, λ is the x-radiation wavelength and n is an integer. Every crystalline solid contains a number of crystallographic directions identified by their Miller Indices. Each of these directions gives rise to diffraction at particular angles. Therefore, by changing the incident angle the various crystal lattice planes can be identified.

5.3.6 Auger Electron Spectroscopy

The Auger electron is the result of a secondary process following the ionization of a core level in a surface atom by a 2-3 keV electron beam. To fill the vacancy created in the ionization process, the atom may decay to a lower energy state releasing the energy difference between the two states. This energy can then ionize an even more outer electron, i.e. the Auger electron. When the Auger transitions occur within a few angstroms of the surface, the Auger electrons may be ejected from the surface without loss of energy. The energy and shape of the Auger peaks in the secondary electron energy distribution can be used to identify the composition of the solid surface.[11]

An Auger electron spectroscope (AES) consists of an ultrahigh vacuum system, an electron gun for specimen excitation, and an energy analyzer for

detection of Auger electron peaks in the total secondary electron energy distribution, N(E). Because the Auger peaks are superimposed on a rather large background, the derivative of N(E) with respect to energy, dN(E)/dE is detected. The peak-to-peak magnitude of an Auger peak is directly related to the surface concentration of the element which produces the Auger electrons. Quantitative analysis may be accomplished by comparing the peak heights obtained from an unknown specimen with those from pure elemental standards or from compounds of known composition.

5.4 Lithography Methods

5.4.1 Photolithography

Patterns can be defined onto a substrate using lithography. In the photolithography process,[12] a pattern is created in a mask. This mask is then pressed against, or held in very close proximity to, a substrate that has been coated with a light-sensitive polymer, the resist. UV light (λ<450 nm) passing through the transparent regions of the mask, will expose corresponding areas of the resist, causing a change in the polymeric material, so that it can be dissolved selectively by a chemical developer (positive resist). The open regions in the resist define areas of access to the substrate for subsequent processing, such as metallization, etching, etc. When the width of the lines in the mask is comparable to the wavelength of the light used for exposure, diffraction effects from the mask openings and reflection effects between the upper and lower surfaces of the resist degrade the quality of the image created on the sample. Linewidth of 0.75 μm can be achieved using thin layers of resist and projection photolithography, in which the mask forms the object in an optical system that projects an image onto the resist-coated substrate.

5.4.2 Electron-Beam Lithography

In electron-beam lithography,[13] a focussed electron beam is deflected over a surface in a controlled way under computer control. The electron beam exposes the resist where it strikes and locally changes the characteristic of the resist so that subsequent development can remove the exposed areas of the resist (positive resist). This resist pattern constitutes a mask in direct contact with the substrate and it can be used for any other subsequent pattern definition process.

The resolution of e-beam lithography is limited by the electron beam size and scattering from the lateral secondary electrons which lead to the 'proximity' effect. To date the smallest feature defined by e-beam lithography is ≈2 nm.[14]

References

[1] A. Ulman, *Introduction to Ultrathin Organic Films: from Langmuir-Blodgett to Self-Assembly* (Academic Press: San Diego, 1991).

[2] I. Langmuir, *J. Am. Chem. Soc.*, **39**, 1848 (1917).

[3] K. A. Blodgett, *J. Am. Chem. Soc.*, **57**, 1007 (1935).

[4] K. A. Blodgett, *Phys. Rev.*, **51**, 964 (1937).

[5] G. L. Gaines Jr., *Insoluble Monolayers at Liquid-Gas Interfaces*, (Interscience: New York, 1966).

[6] I. Langmuir, V. J. Schaefer, *J. Am. Chem. Soc.*, **57**, 1007 (1938).

[7] J. N. Israelachvili, *Intermolecular and Surface Forces*, 2nd edition (Academic Press: San Diego, 1992).

[8] F. W. D. Rost, *Fluorescence Microscopy*, vol. I (Cambridge University Press: Cambridge, 1992).

[9] P. R. Griffiths, J. A. de Haseth, *Fourier Transform Infrared Spectroscopy* (Wiley: New York, 1986).

[10] I. M. Watt, *Principles and Practice of Electron Microscopy*, (Cambridge University Press: Cambridge, 1985).

[11] D. Briggs, M. P. Seah, *Practical Surface Analysis by Auger and X-Ray Photoelectron Spectroscopy*, (Wiley: New York, 1983).

[12] W. M. Moreau, *Semiconductor Lithography: Principles, Practices and Materials*, (Plenum Press: London, 1988).

[13] G. R. Brewer in *Electron-Beam Technology in Microelectronic Fabrication*, G. R. Brewer edt. (Academic Press: New York, 1980).

[14] M. Mochel, C. Humphreys, J. Eades, J. Mochel, A. Petturd, *Appl. Phys. Lett.*, **42**, 38 (1983).

Chapter 6

AFM Cantilevers

6.1 Introduction

Since the introduction by Albrecht *et al.* in 1989[1] most AFMs, either home-built or commercially available, employ microfabricated cantilevers. As introduced in section 2.5, they offer many advantages over electropolished metal wires or other home made force sensors, as they are available in a range of force constants, are relatively easy to use and their tips are relatively sharp and durable. On the other hand, their small size makes it difficult to characterize their mechanical properties. Although the determination of their normal and lateral force constants is critical to quantitative AFM force measurements, at present this issue still remains a great experimental difficulty. A few methods for the experimental determination of the normal force constant have been reported in the literature. Cleveland *et al.*[2] measured the shift in resonant frequency for loaded levers; Jaschke and Butt[3] used the thermal vibrations of free levers, while Li *et al.*[4] deflected the AFM lever with a larger lever of known spring constant. For the lateral force constant at present no *in-situ* experimental method for its determination has been proposed. A method recently developed by Ogletree *et al.* allows one to determine experimentally the response of a cantilever to lateral forces in terms of its normal force response.[5] According to this method, quantitative friction measurements can be made if the normal force constant is known. By using a faceted $SrTiO_3$ (305) surface,[6] the authors can also determine the tip shape. However, due to the limited size of the crystal facets, this procedure is useful for tip radii $\approx$ 500 nm or less.

Calculations of cantilever force constants are also difficult since they depend on knowledge of the levers' dimensions, that can be controlled only to a certain extent. Most levers are made of Si, SiO_x or silicon nitride. Silicon nitride for cantilevers is fabricated by the low-pressure chemical deposition (LPCVD) method without *in-situ* measurement of its mechanical properties. The films are unlikely to have a stochiometric composition, i.e. to be Si_3N_4 and the composition is also expected to change from one batch to another. Furthermore, levers are often metallized on one side to increase optical reflectivity and the metal layer must be taken into consideration when calculating the lever force constants.

In addition to difficulties in the determination of the lever spring constants, uncertainty also arises from the fact that both the absolute values and the ratio of the normal and lateral force sensitivity depend on the precise alignment of the laser beam with respect to the cantilever. Clearly, *in-situ* and routine experimental determination of force constants for each lever used is desirable, since irregularities and defects can significantly change the mechanical response even of levers that are part of the same fabrication batch.

Quantitative force measurements are still difficult at present. In the case of friction studies, especially great care has to be used when comparing experiments performed on different surfaces. Relative measurements performed with the same lever, with unchanged laser beam alignment, are more meaningful at present.

In this chapter, the cantilevers used for the AFM work carried out at LBNL will be described and estimates for their force constants and normal to lateral sensitivity ratio will be given.

6.2 SEM and AES Characterization of Microfabricated Cantilevers

All levers used for this thesis work are made either of silicon nitride or silicon and are commercially available from Digital Instruments (Santa Barbara, CA, USA) and Park Scientific Instruments (Sunnyvale, CA, USA).

Two shapes of levers are commonly made by manufacturers, a rectangular and a V-shaped (or triangular) one. The V-shaped levers are less prone than the rectangular ones to twisting as they jump in and out of contact with the surface. Cantilevers are mounted on a small chip and sharp square-pyramidal tips are fabricated at the other end. In most cases several levers of different size and geometry are made on the same chip, so that a wide range of force constants is available. A schematic of the arrangement of the levers on a chip is shown in figure 6.1 for the Park Scientific Instruments Microlevers™.

Cantilever dimensions such as length, width and thickness are usually provided by the manufacturers. However, these values are only nominal, since routine measurements are not performed by manufacturers. Furthermore, the spring constants depend critically on dimensions, such as tip size and offsets, which are not indicated. Therefore, in order to calculate, or estimate, the lever force constants it is important to measure the dimensions of the lever to a greater accuracy. For this purpose, scanning electron microscopy can be used. Typical dimensions range

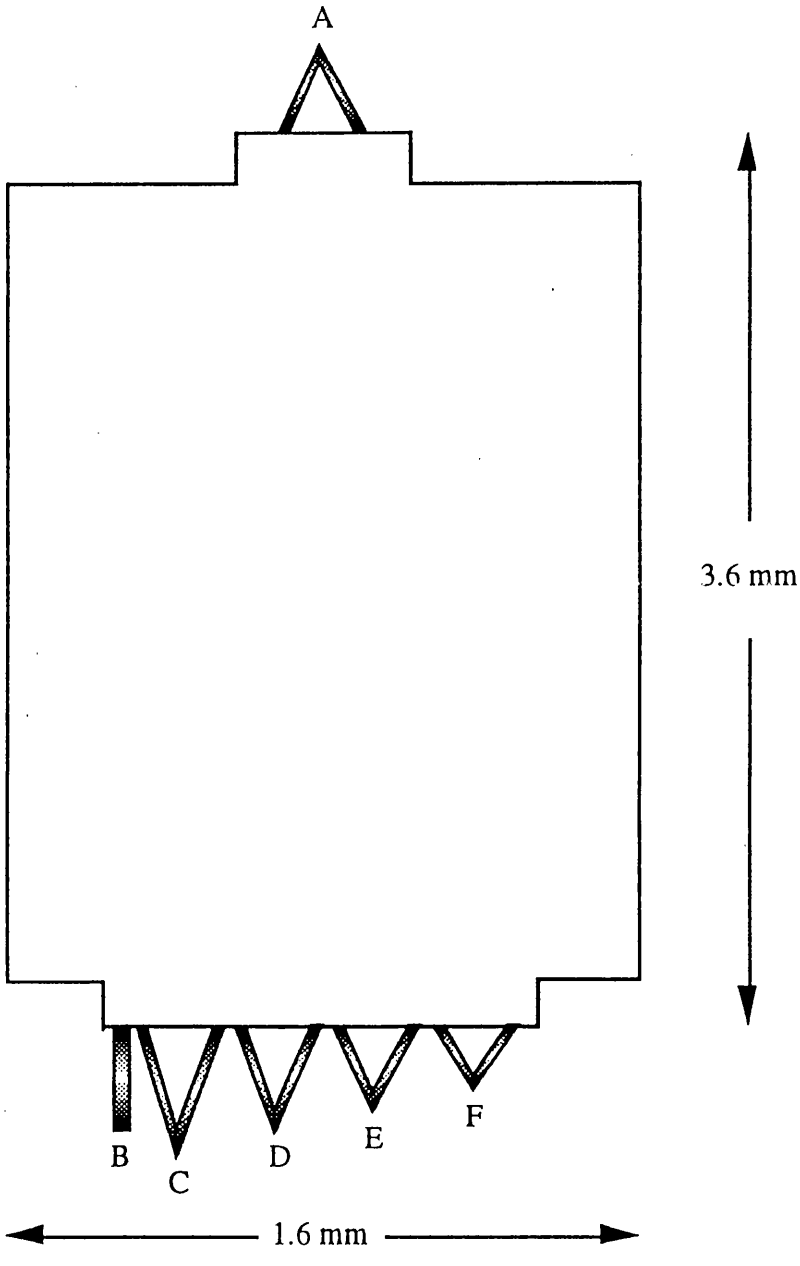

Figure 6.1. Microlever chip for silicon nitride Microlevers™. The chip holds 6 cantilevers of different sizes providing a range of force constants from 0.01 N/m (C) to 0.5 N/m (F).

from 80 to 300 μm for the length and 20-30 μm for the width, making SEM an ideal technique in this case. Since both Si and Si_xN_y are insulating, low electron beam voltages must be used in order to avoid excessive surface charging. Figure 6.2(a) and 6.2(b) show two SEM pictures of a Park Scientific Microlever™ (PSM 1) and a Digital cantilever respectively, both obtained with a Φ660 AES/SEM system. A 3 kV electron beam voltage was used. The lever thickness and tip height could not be measured with this instrument. Table 6.I shows the results of SEM measurements for a series of levers. The nominal values are also indicated. More detailed data for tips 1 (V-shaped PSM) and 4 (V-shaped Digital) of table 6.I is shown in table 6.II. All dimensions are defined in figure 6.3.

Surface elemental characterization by Auger electron spectroscopy was also performed with the same instrument on both Si and Si_xN_y cantilevers. Both types of cantilevers are usually stored in air and therefore contamination is expected to be present on their surface. Auger spectra obtained for a silicon nitride cantilever and a silicon lever are shown in figure 6.4 and 6.5, respectively. Spectra were obtained before (a) and after an Ar^+ sputtering (b) with a 1.5 kV electron beam voltage. Corresponding element concentrations are shown in tables 6.III and 6.IV. As can be seen from figures 6.4 and 6.5 and tables 6.III and 6.IV, both cantilevers show a high degree of contamination, primarily carbon and oxygen, as expected. The Ar^+ sputtering has the effect of 'cleaning' the surfaces. For the Si_xN_y levers the final composition is clearly not stochiometric, i.e. Si_3N_4. In view of the LPCVD method employed this result is not surprising.

Figure 6.2 (following two pages). Scanning electron micrographs of a silicon nitride (a) Park Scientific Microlever™ (lever F of figure 6.1) and (b) a Digital cantilever. Note the offset of the tip from the lever major axis in (a).

(a)

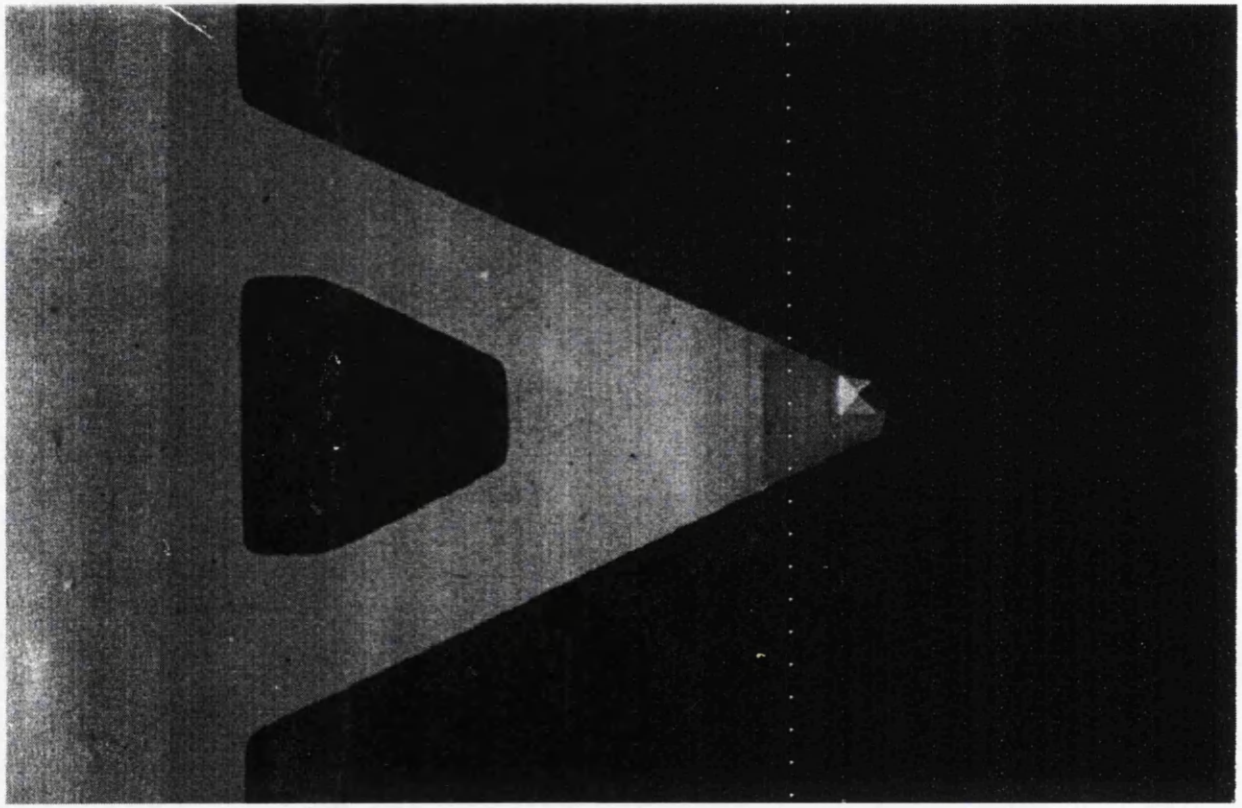

(b)

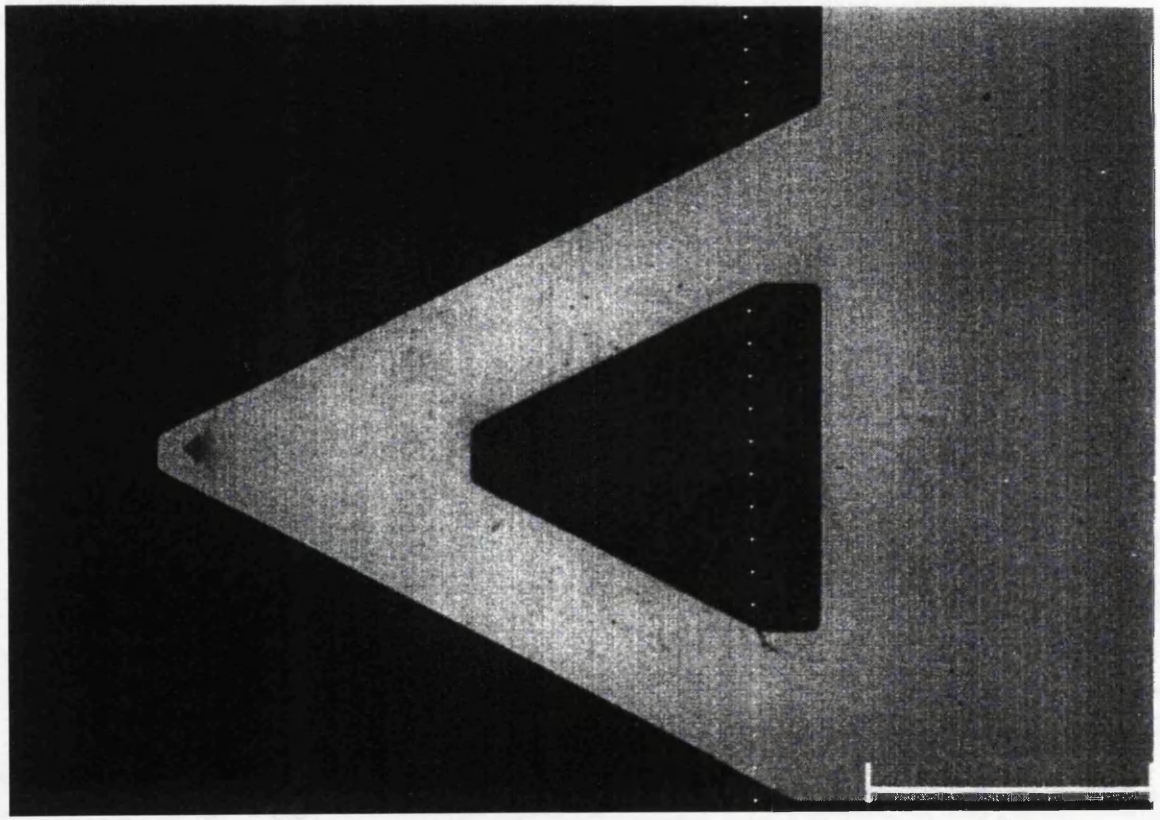

Lever	Nominal			SEM Measurement	
	L (μm)	w (μm)	t (μm)	L (μm)	w (μm)
(1) *V-shaped PSM*	85	18	0.6	83.0	18.5
(2) *V-shaped PSM*	140	18	0.6	143.9	19.2
(3) *Rectangular PSM*	200	20	0.6	215.0	19.0
(4) *V-shaped Digital*	115	21	0.6	118.6	26.3

Table 6.I. Nominal cantilevers' length (L), arm width (w) and thickness (t), as given by the manufacturers. Dimensions as determined by SEM are shown in the two farthest right columns.

Lever	L	L_1	w_{base}	w_{top}	f_1	f_2	w	w'	Θ	tip	t_x	t_y
(1) *V-shaped PSM*	83	34.5	82.4	5.0	10.8	12.7	18.5	16.8	24.9	4.6	3.1	2.1
(2) *V-shaped PSM*	143.9	87.8	144.3	5.8	11.6	20.2	19.2	17.4	25.9	5.4	3.8	2.4
(4) *V-shaped Digital*	118.6	62.2	125.7	6.2	11.0	9.9	26.3	23.4	26.7	5.1	4.6	0.5

Table 6. II. SEM measurements for cantilevers (1), (2) and (4). See figure 6.3 for the definition of quantities shown.

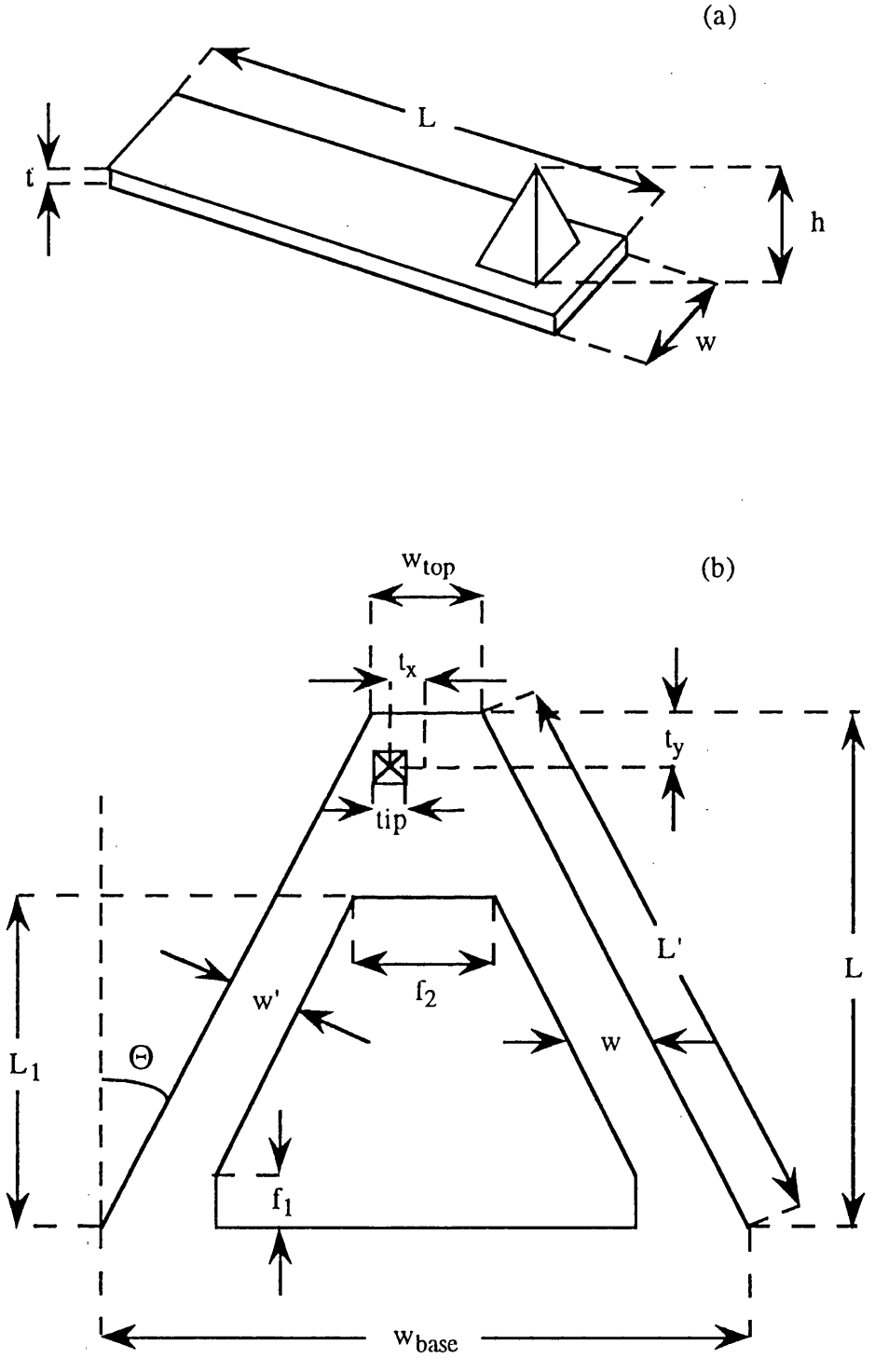

Figure 6.3. Schematic of rectangular (a), V-shaped (b) cantilevers and definition of quantities listed in tables 6.I and 6.II.

(a)

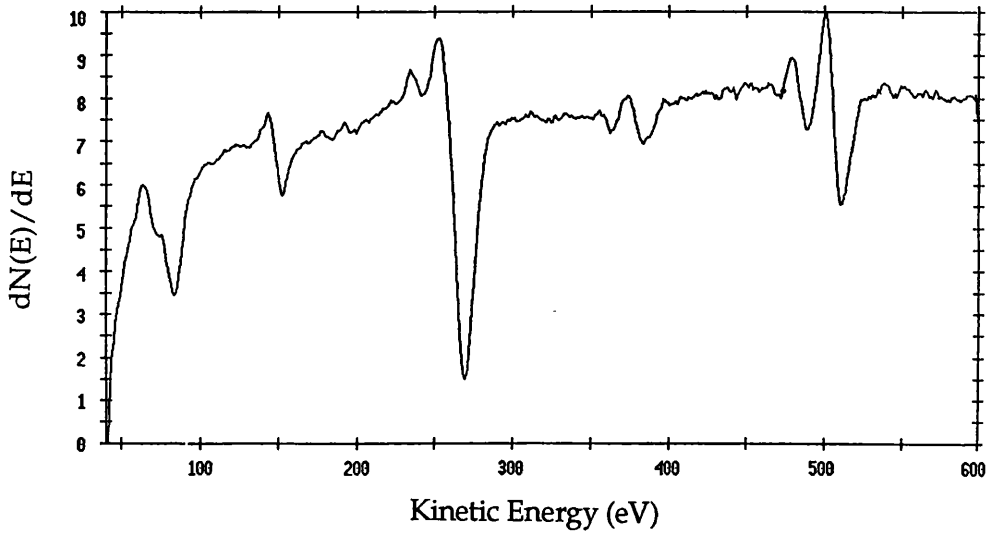

(b)

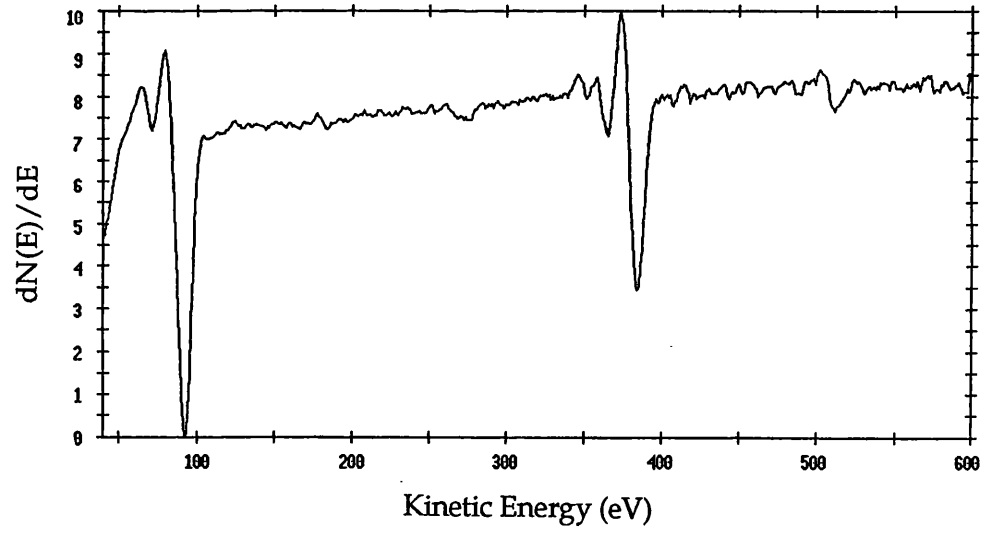

Figure 6.4. AES spectra for a silicon nitride Park Scientific Microlever™ (PSM 1) before (a) and after (b) Ar^+ sputtering. A 1.5 kV electron beam voltage was used.

(a)

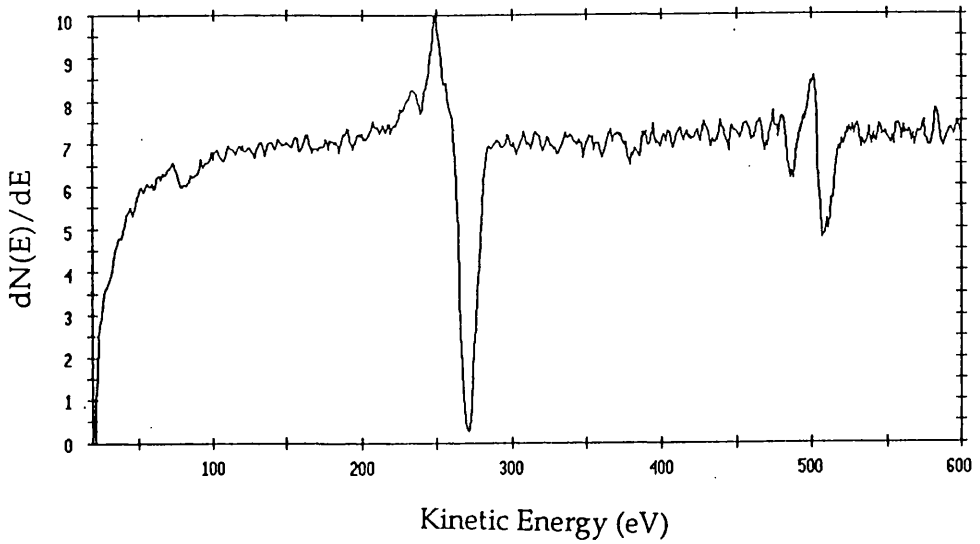

(b)

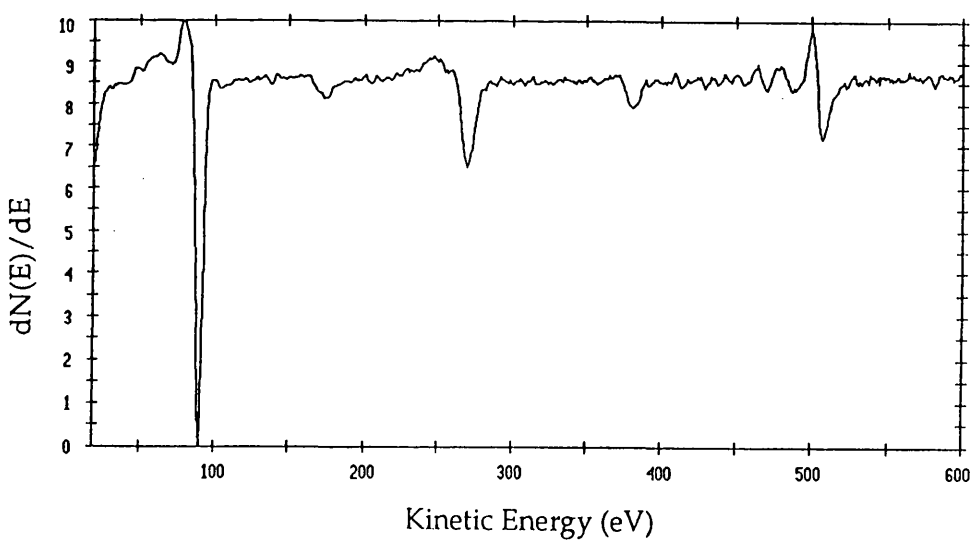

Figure 6.5. AES spectra for a silicon Park Scientific Ultralever™ before (a) and after (b) Ar^+ sputtering. A 1.5 kV electron beam voltage was used.

Before Sputtering		After Sputtering	
Element	Concentration(%)	Element	Concentration(%)
C	63.67	C	7.79
O	14.98	O	4.91
Si	11.58	Si	48.60
N	5.89	N	37.83
S	3.88		

Table 6.III. Element concentrations before and after Ar^+ sputtering for a silicon nitride cantilever (PSM 1), as determined by AES.

Before Sputtering		After Sputtering	
Element	Concentration(%)	Element	Concentration(%)
C	83.87	C	24.71
O	12.12	O	8.90
Si	4.01	Si	53.80
		N	5.22
		B	7.37

Table 6.IV. Element concentrations for a V-shaped silicon cantilever (Ultralevers™, Park Scientific Instruments, Sunnyvale, CA, USA) before and after Ar^+ sputtering, as determined by AES.

6.3 Cantilevers Resonant Frequency

When a new lever is mounted in the microscope, its resonant frequency is measured. When the lever is out of contact and far away from the sample, it oscillates at its natural resonant frequency due to thermal vibrations. In contrast, the oscillation is greatly suppressed when tip and sample are in contact.

The STM/AFM acquisition and data analysis software at LBNL enables one to measure the lever motion amplitude as a function of frequency much like a Fast Fourier Transform spectrum analyzer. The frequency bandwidth can be changed and multiple sampling performed. The maximum bandwidth is 74.5 kHz. This bandwidth enables one to measure the resonant frequency of all levers used except one (lever PSM 1 of table 6.I), that it is higher than 100 kHz. An oscilloscope was used for the frequency measurement in this case.

Table 6.V shows the nominal and experimental values of the resonant frequency for the levers introduced in table 6.I. Measurements for the two types of levers (PSM and Digital) were performed on cantilevers belonging to the same wafer.

Lever	Nominal f_R (kHz)	Measured f_R (kHz)	Δf_R (kHz)
(1) *V-shaped PSM*	120	108.3	2.7
(2) *V-shaped PSM*	38	34.5	1.1
(3) *Rectangular PSM*	15	13.5	0.4
(4) *V-shaped Digital*	40	52.2	1.6

Table 6.V. Nominal and experimentally determined values of the resonant frequency for the microcantilevers whose dimensions are given in table 6.I. The uncertainty in the measurements is the statistical standard deviation, Δf_R.

As can be seen, the values for the PSM levers are about 10% lower than the nominal ones, while the frequency for the Digital lever is about 30% higher than the value indicated by the manufacturer.

6.4 Cantilevers Spring Constants

The nominal values for normal spring constant of the triangular cantilevers provided by the manufactures usually are only a very rough estimate. In the case of rectangular levers the force constants can be calculated analytically and are given by:[7]

Bending
$$k_N = \frac{Et^3 w}{4L^3} \tag{6.1}$$

Torsion
$$k_T = \frac{Gwt^3}{3Lh^2} \tag{6.2}$$

where **E** and **G** are the cantilever's Young's and shear modulus, respectively; **L**, **w**, **t** are the cantilever length, width and thickness respectively and **h** is the tip height.

The resonant frequency can also be calculated and is given by:

$$f_R = 0.162\left(\frac{E}{\rho}\right)^{1/2} \frac{t}{L^2} \tag{6.3}$$

where ρ is the cantilever's density.

In the case of triangular levers, the nominal value of the spring constant provided by the manufacturers is calculated using a simple 'parallel beam approximation' (PBA). This approximation, first introduced by Albrecht,[1] considers a triangular lever as equivalent to two rectangular beams in parallel. According to Albrecht's method the normal spring constant $\mathbf{k_N^T}$ for a triangular lever of projected length **L'** and arm width **w'** is:

$$k_N^T = 2k_N^R \tag{6.4}$$

where $\mathbf{k_N^R}$ is the spring constant of a rectangular lever of length **L'** and width **w'**. This approximation, however, does not yield realistic results as shown by Sader.[8] In the case of plates of arbitrary shape and structure, an exact analytical solution for their static deflection does not exist. Sader *et al.*[9] calculated the normal force constant by a rigorous finite element analysis and showed that the Albrecht's approximation yields estimates that are off by about 25%. They also introduced a new PBA approximation where the V-shaped cantilever is equivalent to a rectangular beam of length L_1 and width 2w' and a triangular end piece. This method was shown to yield results that are only 2% in error of the finite element analysis results.[8]

The methods mentioned above only enable one to calculate or estimate the spring constant relative to bending. However, in addition to normal forces, forces in the x,y plane are also present. As shown in figure 6.6, forces along the x direction will cause the cantilever to twist, while forces applied along the y direction will cause the lever to 'buckle'.

The force constants used for the AFM studies performed at LBNL were estimated from a continuum elasticity model.[10, 11] Contrary to the above described methods, this model enables one to estimate force constants relative to bending, twisting and 'buckling' of the lever. Furthermore, it also takes into account the effect of the 'fillets' f_1 and f_2 in the corners of the central area cut-out of the V-shaped levers. The effects of these fillets is to increase the normal stiffness by about 10%. In this approach, for which mathematical details will be omitted here, the V-shaped lever is treated as a variable width beam. The curvature of a small solid element is proportional to the moment of the torque acting on it and inversely proportional to the product of the Young's modulus and the moment of inertia around the bending axis. The differential equations obtained for the lever curvature due to bending and twisting can be solved analytically for each section (arms and top section), they are then combined and boundary conditions applied. The angular deflections and force constants can then be obtained.

This method does not take into account the effect of the Au coating present on the back side of the cantilever. However, it has been shown that even a thin coating can dramatically change the spring constant. As described in reference 8, the coating decreases the cantilever resonant frequency and increases the spring constant as follows:

Resonant frequency

$$f' = f_o \sqrt{\frac{1}{1 + (\rho_{Au} / \rho_{cant})(t_{Au} / t_{cant})}} \qquad (6.5)$$

Normal spring constant

$$k'_N = k_N^o \left(\frac{t_{Au} + t_{cant}}{t_{cant}} \right)^3 \frac{E_e}{E_{cant}} \qquad (6.6)$$

with

$$E_e = \frac{E_{Au} t_{Au} + E_{cant} t_{cant}}{t_{Au} + t_{cant}} \qquad (6.7)$$

where f', k'_N and f_o, k_N^o are values for the coated and uncoated cantilevers respectively; t_{Au} and t_{cant} are the thickness of the gold coating and uncoated cantilever; E_{Au} and E_{cant} are the Young's modulus of gold and cantilever,

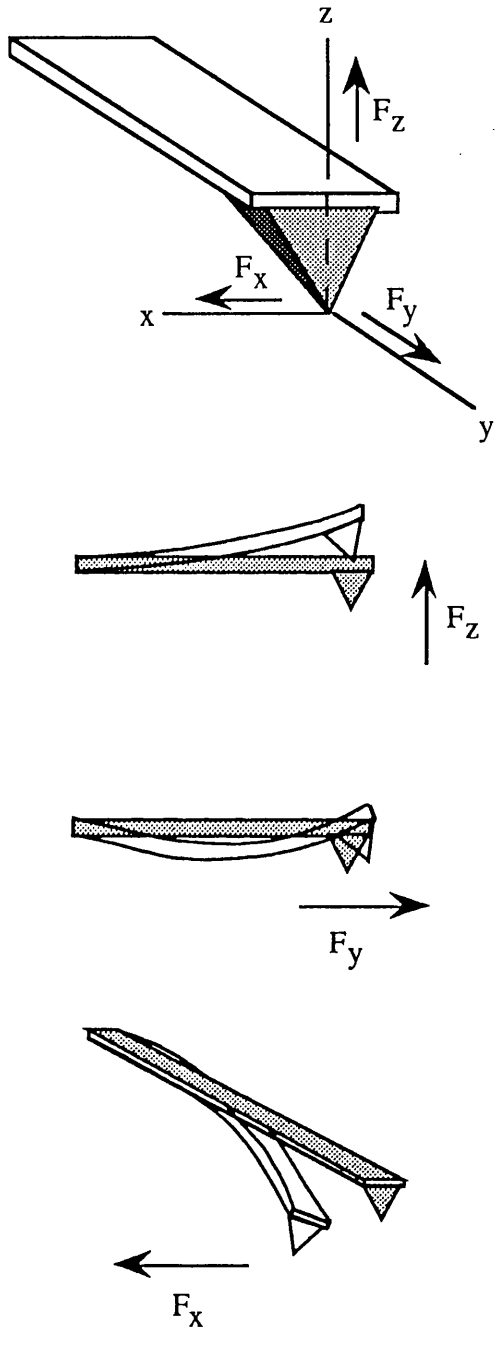

Figure 6.6. Schematic representation of the forces acting on the cantilever tip apex. F_z causes a displacement of the cantilever in the z direction; F_y induces a deflection of the cantilever without z displacement ('buckling'); F_x causes the cantilever to twist.

respectively.

In order to estimate the lever force constants, the Young's modulus, Poisson's ratio and the density of the material have to be known. All three depend critically on the preparation conditions and are not specified by manufacturers. From literature reports on Si_xN_y prepared in conditions similar to those used in the preparation of microcantilevers, a density value, $\rho_{Si_xN_y}$, of 2.8 g/cm^3 was used.[8] A value of 0.3 was taken for Si_xN_y Poisson's ratio, $\nu_{Si_xN_y}$. The Young's modulus for the PSM levers was determined from the measured value of the resonant frequency of rectangular levers by equating it to the theoretical value as given by relation (6.5), with f_0 given by relation (6.3). The values of E_{Au} and ρ_{Au} were taken from the literature (E_{Au}=78 GPa, ρ_{Au}=19.3 g/cm^3)[12] and a typical value of 20 nm was used for t_{Au}. The value so obtained for $E_{Si_xN_y}$ is 140 GPa. This value is within the range of values measured for LPCVD Si_xN_y. The same values were also used for the Digital levers.

Table 6.VI and 6.VII show the estimated angular sensitivities and force constants obtained for V-shaped levers PSM (1), PSM (2) and Digital (4) (see table 6.I for levers' dimensions). The nominal normal spring constants are also shown in table 6.VII for comparison. The estimated values of the angular sensitivities depend on the position of the laser spot on the lever, as shown in figure 6.7. The values in tables 6.VI were obtained by considering the laser beam positioned in the center of the triangular region at the end of the lever. The estimated normal spring constant (table 6.VII) for the two SPM levers are about 25% (1) and 20% (2) higher than the nominal values, while the one for the Digital lever is ~40% lower. This latter result was at first surprising, however Cleveland *et al.*[2] measurements of f_R and k_N for similar levers yielded 54 kHz and 0.36 N/m,[2] i.e. values consistent with the ones reported here. It is important to note that the AFM detects the total angular deflection, that is it cannot distinguish between contribution from normal and 'buckling' forces. Therefore, the topography corrugations will reflect both contributions. From table 6.VI values for the angular deflections due to the coupling can be estimated. Under feedback control, a 1 nN 'buckling' force causes the tip to retract or advance a distance:

$$\frac{\theta_{bk}}{\theta_{bd} k_N} \text{ (nm)} \qquad (6.8)$$

The results for levers (1), (2) and (4) give values of 0.10, 0.38 and 0.17 nm, respectively. Not surprisingly, these results indicate that the 'buckling' coupling effect becomes increasingly important with longer levers. This coupling effect should be kept in mind when analyzing AFM 'atomic' corrugations and interpreting AFM topographic images. In fact, when scanning parallel to the lever major axis, i.e. Y

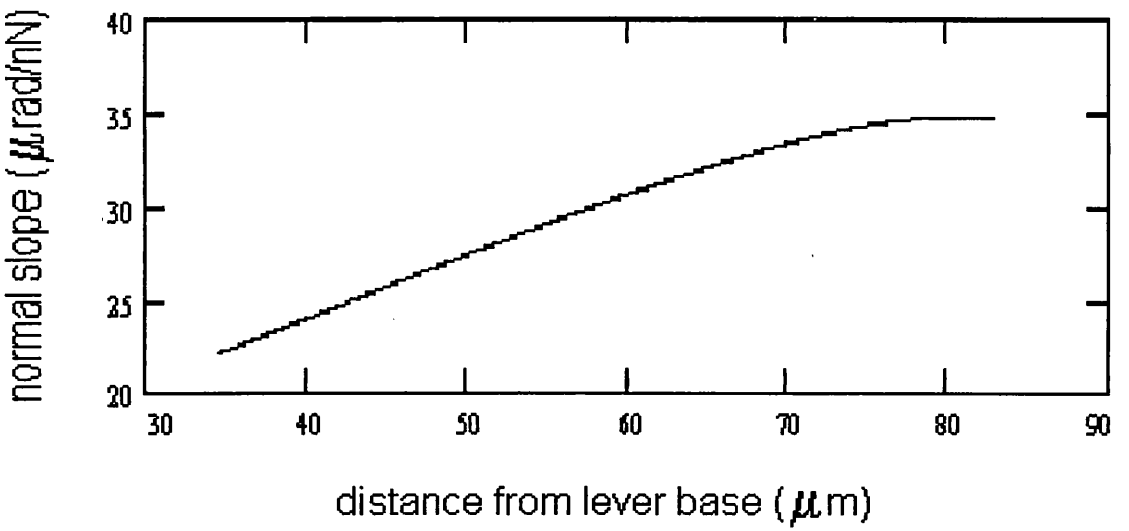

Figure 6.7. Calculated curve showing the variation in slope along the length of the triangular region at the end of a V-shaped cantilever PSM 1.

Lever	θ_{bd} (μrad/nN)	θ_t (μrad/nN)	θ_{bk} (μrad/nN)
(1) *V-shaped PSM*	30.3	1.19	1.83
(2) *V-shaped PSM*	94.0	2.6	4.0
(4) *V-shaped Digital*	40.1	1.43	2.2

Table 6.VI. Estimated angular sensitivities for bending (θ_{bd}), twisting (θ_t) and 'buckling' (θ_{bk}) for the V-shaped microcantilevers whose dimensions are given in table 6.I.

Lever	Nominal k_N (N/m)	Estimated k_N (N/m)	Estimated k_T (N/m)	Estimated k_B (N/m)
(1) *V-shaped PSM*	0.5	0.62	150.6	231.7
(2) *V-shaped PSM*	0.1	0.12	74.2	114.1
(4) *V-shaped Digital*	0.58	0.34	115.5	177.6

Table 6.VII. Nominal and estimated force constants for bending (k_N), torsion (k_T) and 'buckling' (k_B), for the V-shaped cantilevers characterized in these studies.

scan, with a soft lever, it is common to obtain 'atomic' corrugations of several angstroms.[13] These corrugations are inconsistent with the ideal picture of an AFM tip tracing contours of constant charge density,[14] which would lead to typical corrugations of a few tenths of an angstrom. For example, for a PSM 2 lever, a 1 nN force along the lever's major axis, would give an apparent corrugation of 3 Å. The effect becomes more important with softer levers, such as levers D and C in figure 6.1 (k^{nom}=0.03 and 0.01 N/m). Further discussion about this point will be found in chapter 7, where experimental results for mica and Au(111) films will be described.

6.5 'Calibration' of the Lateral Force Signal

As already said in chapter 4, no experimental calibration method for the lateral force signal was available when the friction *vs.* load experiments described in this thesis were performed. Therefore, only relative measurements performed with the same lever are to be considered meaningful.

An estimated 'calibration' of the lateral force signal can be obtained from the continuum elasticity model described in the previous section. The detector angular sensitivities are defined by:

Bending
$$S_{bd} = \frac{\theta_{bd}}{V_{ab}} \tag{6.9}$$

Torsion
$$S_t = \frac{\theta_t}{V_{12}} \tag{6.10}$$

where $\mathbf{V_{ab}}$ and $\mathbf{V_{12}}$ are the 'A-B' and '1-2' signals defined in chapter 4. The detector calibration for the lateral force signal, S_L, can be expressed in terms of the calibration for the normal force signal, S_N as following:

$$S_L = \frac{S_t}{S_{bd}} \frac{\theta_{bd}}{\theta_t} S_N \text{ (nN/V)} \tag{6.11}$$

If S_t/S_{bd}=1, relation (6.11) becomes

$$S_L = \frac{\theta_{bd}}{\theta_t} S_N \text{ (nN/V)} \tag{6.12}$$

where S_N can be obtained from approach-retract curves as described in

chapter 4. All frictional force values reported in this thesis are estimates obtained under the above approximations. Table 6.VIII summarizes values of θ_{bd}/θ_t for levers (1), (2) and (4).

Lever	θ_{bd}/θ_t
(1) *V-shaped PSM*	≈25.5
(2) *V-shaped PSM*	≈36
(4) *V-shaped Digital*	≈28

Table 6.VIII. Estimated relative deflection due to bending and twisting of the cantilever for V-shaped cantilevers (1), (2) and (4).

References

[1] T. R. Albrecht, S. Akamine, T. E. Carver, C. F. Quate, *J. Vac. Sci. Technol. A*, **8**, 3386 (1990).

[2] J. P. Cleveland, S. Manne, D. Bocek, P. K. Hansma, *Rev. Sci. Instrum.*, **64**, 403 (1993).

[3] M. Jaschke, H. J. Butt, *Rev. Sci. Instrum.*, **66**, 1258 (1995).

[4] Y. Q. Li, N. J. Tao, J. Pan, A. A. Garcia, S. M. Lindsay, *Langmuir*, **9**, 637 (1993).

[5] D. F. Ogletree, R. W. Carpick, M. Salmeron, *Rev. Sci. Instrum.*, **67**, 3298 (1996).

[6] S. S. Sheiko, M. Möller, E. M. C. M. Reuvekamp, H. W. Zandbergen, *Phys. Rev. B*, **48**, 5675 (1993).

[7] S. P. Timoshenko, J. N. Goodier, *Theory of Elasticity*, 3rd ed. (McGraw Hill: New York, 1987).

[8] J. E. Sader, *Rev. Sci. Instrum.*, **66**, 4583 (1995).

[9] J. E. Sader, L. White, *J. Appl. Phys.*, **74**, 1 (1993).

[10] D. F. Ogletree, Personal Communication.

[11] D. F. Ogletree, R. W. Carpick, M. Salmeron, *Rev. Sci. Instrum.*, **67**, 3298 (1996).

[12] *Goodfellow Catalog*, Goodfellow Corp., Malvern, PA, USA.

[13] H. Heinzelmann, E. Meyer, D. Brodbeck, G. Overney, H.-J. Güntherodt, *Z. Phys. B-Condensed Matter*, **88**, 321 (1992).

[14] G. Binnig, Ch. Gerber, E. Stoll, T. R. Albrecht, C. F. Quate, *Europhys. Lett.*, **3**, 1281 (1987).

Chapter 7

AFM/FFM Characterization of Mica and Au(111) on Mica

7.1 Introduction

Layered crystalline materials were among the first investigated by AFM, due to their simplicity of preparation and relative chemical inertness in air. Their cleavage planes consist of large, atomically flat surfaces that are ideal for AFM investigations. Often their crystal structure is also independently known by diffraction techniques and therefore they can be used to test and calibrate the microscope at the 'atomic' level. The first 'atomic lattice resolution' images on an insulator were obtained by Albrecht and Quate on highly pyrolytic boron nitride.[1, 2] Since then several inorganic materials, such as graphite[3, 4, 5] transition metal dichalcogenides[6, 7] and alkali halides (non-layered) [8, 9, 10] have been investigated.

Mica has been studied by AFM by several groups[11, 12, 13] and is often used for the x,y calibration of the instrument. Figure 7.1 shows its crystalline structure.[14] Micas are layered aluminosilicate minerals, consisting of negatively charged 2:1 layers separated by inter-layer alkali cations (figure 7.1(a)). A 2:1 layer contains two tetrahedral sheets and one octahedral sheet. Each tetrahedral sheet is of composition T_2O_5 (T=tetrahedral cation) and within each sheet individual tetrahedra are linked with neighboring tetrahedra by sharing three corners each to form an hexagonal unit mesh pattern of the sort illustrated in figure 7.1(b). The 2:1 layers must superimpose so that the hexagonal rings of adjacent basal surfaces line up and enclose the interlayer cation. The tetrahedral cations are normally Si, Al, Fe^{2+} and Fe^{3+}, while octahedral cations are usually Mg, Al, Fe^{2+} and Fe^{3+}. The interlayer cation is normally K, occasionally Na. The formula for muscovite mica can be written as $KAl_2(AlSi_3)O_{10}(OH)_2$.

Among metal films, Au(111) mica films on mica have received the greatest attention since these films are used for the self-assembly of alkylthiol molecules. Figure 7.2 shows the fcc lattice of a Au(111) surface. During this PhD project, both mica and Au(111)/mica surfaces were used for the self-assembly of molecules and therefore a thorough characterization of these substrates was performed. Furthermore, both surfaces were used to calibrate the piezo scanner of the Berkeley's

home-built AFM, in the three orthogonal directions.

7.2 Experimental Section

Muscovite mica samples (various sources) were cleaved by using a sharp knife and immediately mounted in the AFM for imaging.

Gold samples were prepared by resistive evaporation (Denton Vacuum evaporator model DV-502A, NJ, USA) onto freshly cleaved mica. The mica substrates were heated in vacuum (typical base pressure: 10^{-6} bar) to 250 °C by using two quartz lamps positioned close to a stainless steel sample holder. Samples were heated at the set temperature for two to three hours to allow for equilibration of the temperature across the substrates. Gold was deposited at a rate of 2-3 Å/sec while still heating the mica substrates, with the rate of deposition monitored by a 6 MHz gold coated quartz crystal (Sycon Instruments, Inc., NY, USA). Typical film thickness was 1500-2000 Å. After evaporation, the substrates were cooled down radiatively to less than 60 °C in vacuum, removed from the evaporator and stored in Fluoroware™ containers in a desiccator.

7.3 Topographic Mode Images of Mica

Figure 7.3 shows topographic and lateral force images (a, b, e, f) obtained on freshly cleaved mica with a sharpened lever of nominal force constant 0.1 N/m at 1 nN. The 2D Fast Fourier power spectra are also shown (c, d, g, h). The lateral force images are raw data, a background subtraction was performed on the topographic images. The hexagonal periodicity of the SiO_4 units of the cleavage plane is clearly revealed (lattice constant = 5.2 Å) in all four images shown, in agreement with previous AFM reports.[11, 12, 13] The bands observed in all images at the beginning of each scan line correspond to static friction effects. When the scan is initiated, the tip and the surface move together until the force exerted by the lever on the tip is high enough to overcome the static frictional force and the tip can slide across the surface. The observed contrast reversal for the forward and backward lateral force images corresponds to the 'friction loop' as described in chapter 3. Figure 7.4 shows a friction loop obtained on a mica surface. The periodicity of the mica unit cell is reflected in the lateral force signal, which exhibits a 'stick-slip'

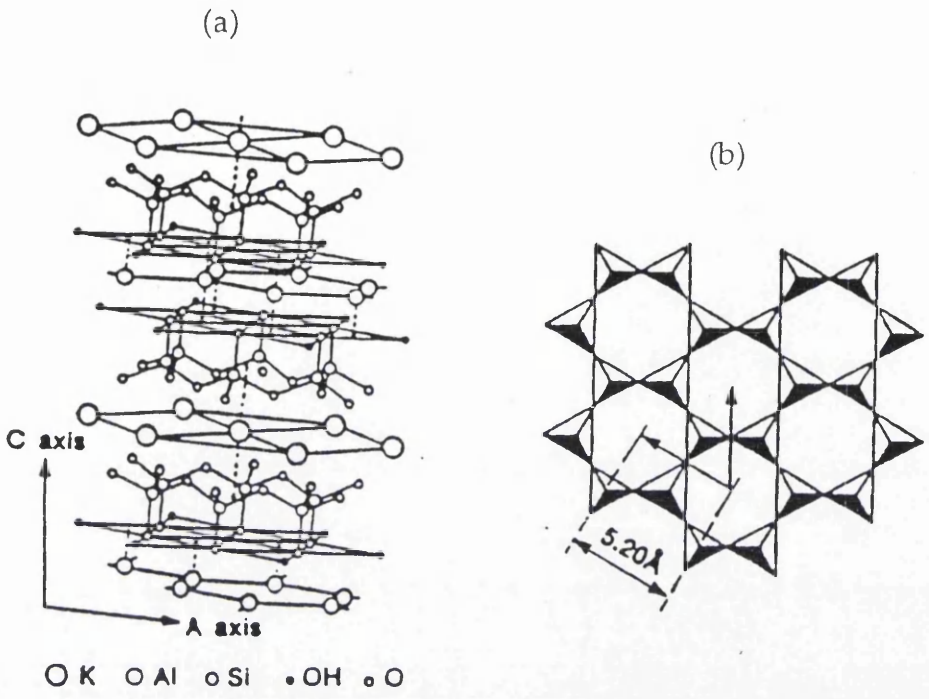

Figure 7.1. The Muscovite mica structure. (a) The cleavage plane is defined by the potassium layer sandwiched between the two hexagonal sheets of SiO_4 tetrahedra. (b) Top view of the hexagonal layer of SiO_4 units. The periodicity observed in AFM images is indicated.

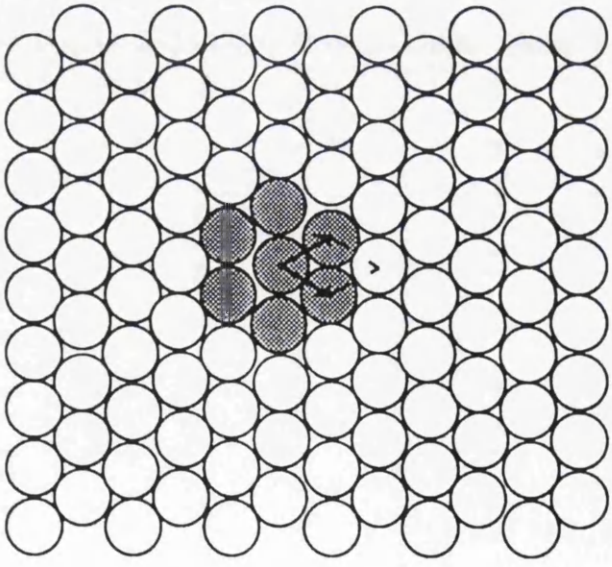

Figure 7.2. Atomic arrangement and real-space unit cell for Au(111) surfaces. The lattice constant is 2.88 Å.

Figure 7.3 (following page). Topographic (a, b) and simultaneous lateral force (e and f) images of a freshly cleaved muscovite mica surface. 2D Fast Fourier power spectra are also shown (c, d, g and h). Images were obtained with a PSM 2 lever, k^{nom}=0.1 N/m. Static friction effects are visible at the beginning of each scan line in both topographic and friction images. The unit cell is hexagonal with lattice constant, as measured from both real-space images and 2D-FFT spectra, of 5.3 ± 0.5 Å. This value closely corresponds to the periodicity of the SiO_4 units of the mica cleavage plane. Scale bars=10 Å. The arrows indicate the scan direction.

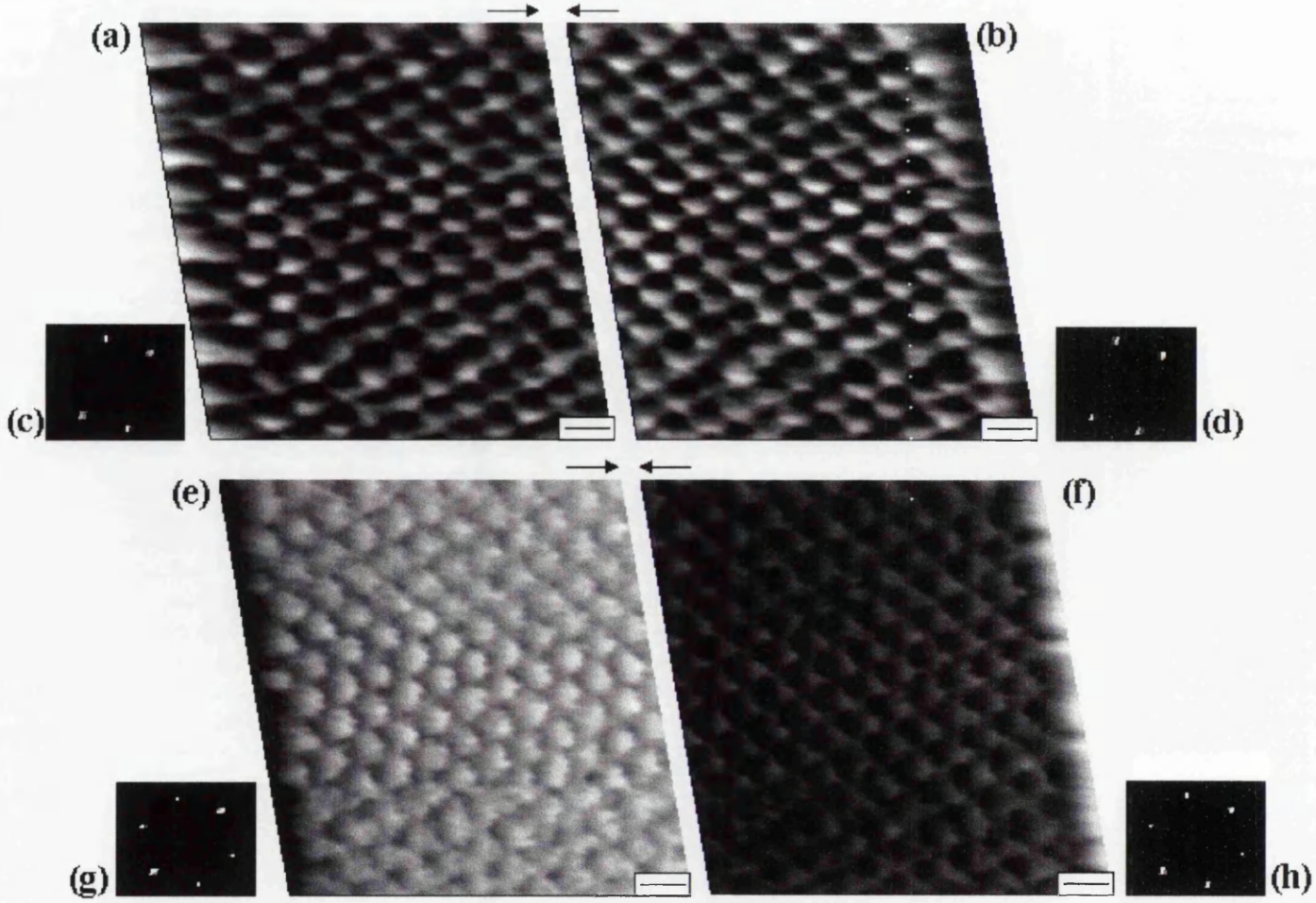
(a)
(b)
(c)
(d)
(e)
(f)
(g)
(h)

behavior. Its origin is the dependence of the frictional force on position and can be thought as being similar to the pulling of a stick across the bars of a fence. As the sample moves, the tip is in a stable position as long as the forces of the lever and sample on the tip balance. Therefore the modulation in the frictional force increases and the tip 'sticks'. When the derivative of the frictional force equals the spring constant, the tip 'slips' until it finds a new stable position.

When imaging mica, or other layered materials, it is not uncommon to obtain highly distorted AFM images as those shown in figure 7.5 (a) and (b). The apparent size of the unit cell in figure 7.5(a) is 7 and 8.2 Å in the x and y directions, respectively. The apparent unit cell area is more than twice the value of the undistorted cell. A reversal of contrast was also observed when reversing the scan direction. This type of images is probably due to the AFM tip dragging a mica flake as it slides across the surface.[15] In fact, after taking a large scan the images recovered, as shown in figure 7.5 (c) and (d). Despite the fact that mica and other layered materials are widely used for piezo calibration purposes, these results demonstrate that extreme care has to be taken since in many cases distorted images cannot be readily recognized.

7.4 Topographic Mode Images of Au(111) on Mica

Figure 7.6 (a) and (c) show two AFM images of evaporated Au(111) films on mica. The morphology is that of polycrystalline films with islands 1000-2000 Å in size. A light shade illumination was used in figures 7.6 (b) and (d) to enhance the contrast. Several monatomic steps are revealed on the islands of the film shown in figure 7.6 (a) and (b). In the case of figure 7.6 (c) and (d) instead, the majority of islands appeared to be atomically flat. Figure 7.7 shows a series of Au(111) monatomic steps (step height=2.44 Å) as imaged by a sharpened (a) and a conventional pyramidal tip (b), respectively. These steps, or other steps of known height, can be used to calibrate the piezo tube in the vertical direction. However, in many cases the measured height of small steps, such as those in figure 7.7, can be affected by the often necessary background subtraction of the data. In fact, while a background correction is generally performed before image acquisition, generally residual correction is necessary on the image itself. In the case of step bunching, as often observed on these Au(111) surfaces, the correction can become critical and a substantial error can derive in the z calibration. Therefore, mica monatomic steps (step height=10 Å), artificially created by scratching the surface of mica with sharp

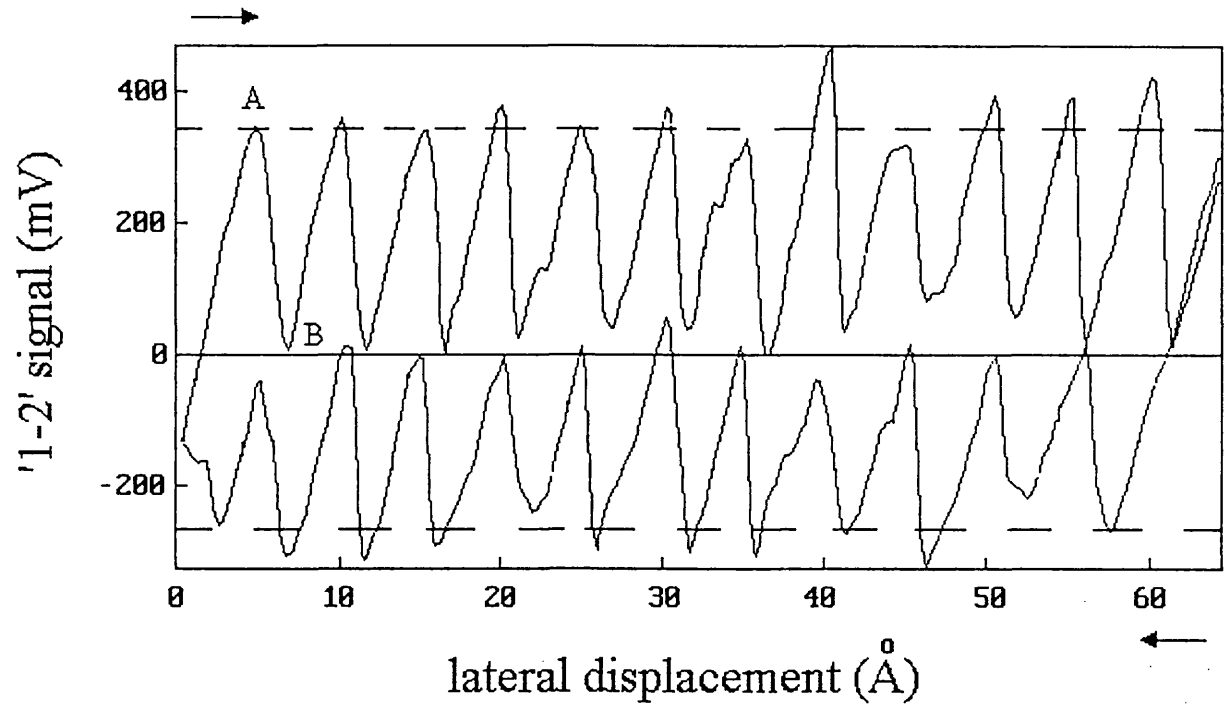

Figure 7.4. "Friction loop' at a constant applied load for a mica surface. The tip initially sticks to the surface until some critical lateral force is achieved (point A). At this point, the tip slips and sticks again (point B). This behavior is repeated upon reversal of the scan direction. The frictional force signal, shown as uncalibrated '1-2' signal, has the periodicity of the surface atomic lattice.

Figure 7.5 (following page). Distorted topographic images of mica. The effect is most likely due to a mica flake being dragged across the surface. After scanning a large area, the images recovered their hexagonal symmetry, as shown in (c) and (d). Images were acquired with a PSM 2 lever (k^{nom}=0.1 N/m) at 1 nN load. Scale bars= 10 Å.

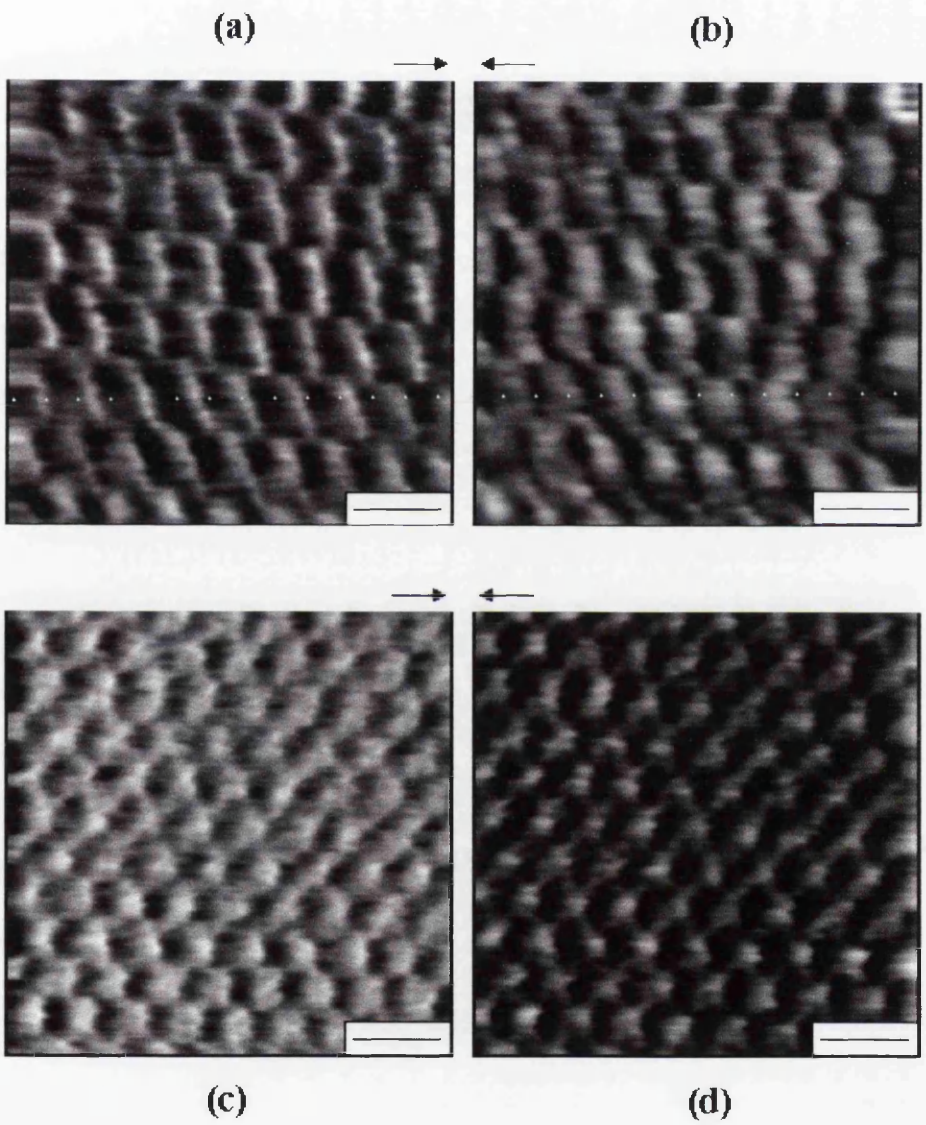
(a)
(b)
(c)
(d)

Figure 7.6 (following page). Topographic images (a and c) of two Au(111) films deposited on mica. A light shade illumination is used in (b) and (d) to enhance contrast. Several monatomic steps can be identified on the islands of the film shown in (a) and (b), while many islands in (c) and (d) appear atomically flat. Scale bars= 1000 Å (a and b), 2000 Å (c and d).

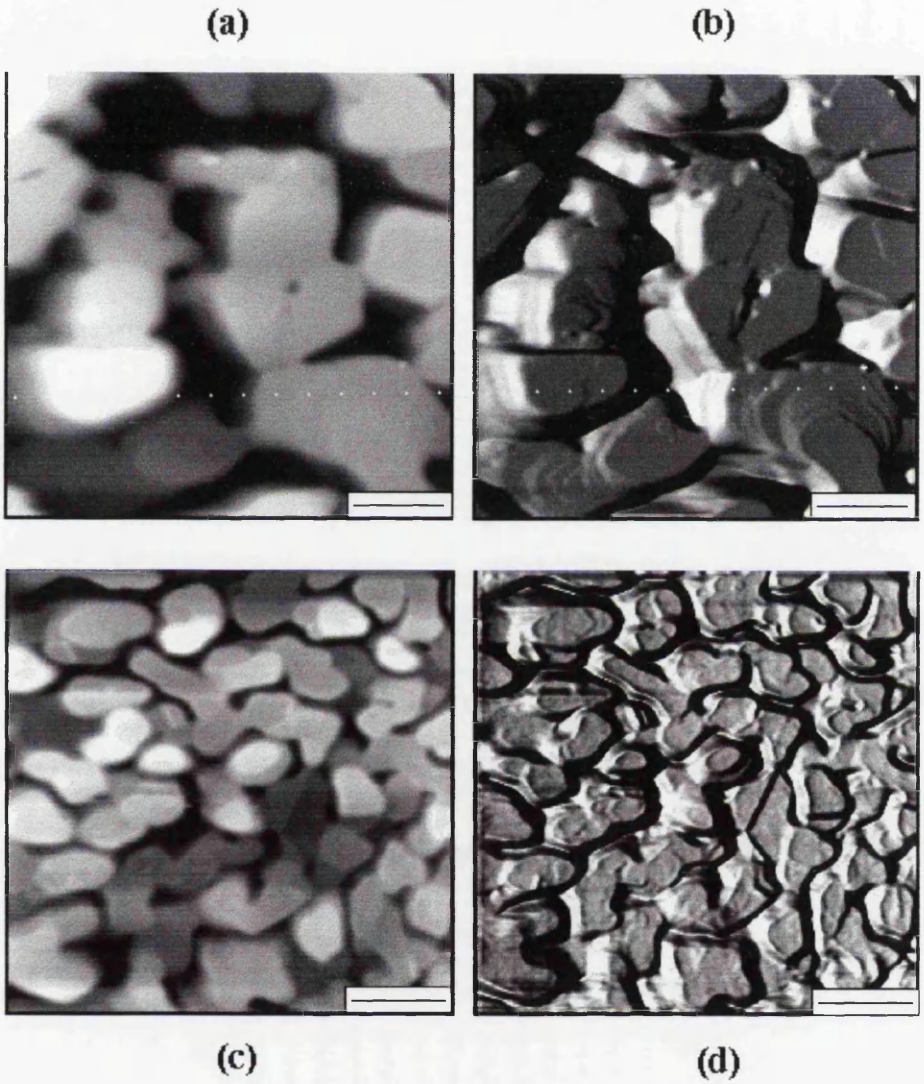
(a)
(b)
(c)
(d)

tips were also used for the z calibration. These experiments will be described in section 7.5.

The images shown in figure 7.7 demonstrate the effect that the tip radius can have on AFM imaging of steps or other 3D-structures. The sharpened tips, which are found to have a 200-400 Å radius of curvature, can resolve the topography of the stepped surface in figure 7.7(a) much more sharply than the pyramidal tip used for figure 7.7(b). The step profile in figure 7.7(b) is clearly the result of the convolution of the tip and surface profile. Typical radii of curvature for pyramidal tips were found to be in the 400-1000 Å range.

Atomic lattice resolution images of Au(111) on mica are shown in figure 7.8. A hexagonal 1x1 pattern is resolved in both topographic and lateral force images and the lattice constant is measured to be 2.9 ± 0.2 Å. This distance corresponds to the nearest-neighbor distance for Au(111) (see figure 7.1). Static friction effects are again visible at the beginning of each scan line and a stick-slip behavior with the periodicity of the 1x1 lattice is seen for the lateral force signal. Figure 7.9 shows a friction loop obtained on a Au(111) surface. Similarly to figure 7.4, the lateral force signal has the periodicity of the surface.

7.5 Layer-by-Layer Scratching of a Mica Surface

Repeated scanning of mica can result in the tip wearing out the surface. The load at which damage occurs depends on the tip radius and it is of the order of 10-20 nN for sharpened tips with typical tip radii of 200-400 Å. Since mica is a layered material, successive layers of material can be worn out by continuing to scan at the same or increasing load. The damage occurrence is usually characterized by the loss of atomic lattice resolution. An example of a damaged mica surface is shown in figure 7.10 where a hole approximately 250 Å wide, i.e. the size of the scan, was formed (figure 7.10(a)). The line cursor profile across the hole in (a) is shown in (b) and a step about 10 Å high, corresponding to a single mica atomic layer, is measured. These artificially created steps were used together with Au(111) steps for the calibration of the piezo scanner in the vertical direction.

During this procedure the tip is sometimes blunted, as indicated by the fact that a higher value of the load is required to continue scratching the surface.

Figure 7.7 (following page). Au (111) monatomic steps as imaged by a sharpened (a) and a conventional pyramidal tip (b), respectively. Line profiles are shown to the right of the images. The narrow steps profile is well resolved by the sharp tip, while the profile measured by the pyramidal tip is the result of the convolution of tip shape and surface topography. The tip used in (a) yielded a tip radius of ≈ 300 Å.

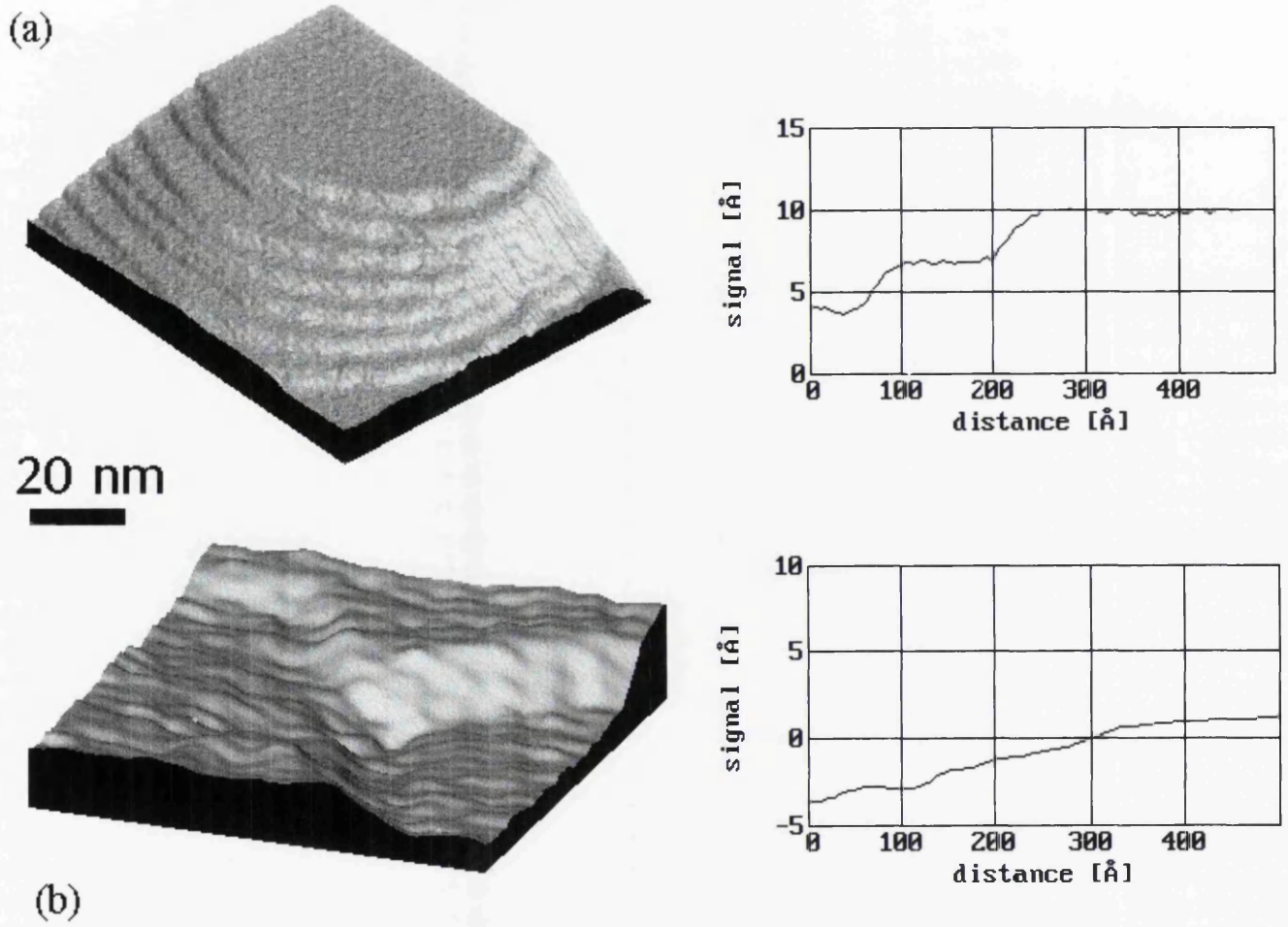
(a)
20 nm
(b)
signal [Å]
15
10
5
0
0
100
200
300
400
distance [Å]
signal [Å]
10
5
0
-5
0
100
200
300
400
distance [Å]

Figure 7.8 (following page). Topographic (a, b) and simultaneous lateral force (e, f) images of a freshly evaporated Au(111) film on mica. 2D Fast Fourier power spectra are also shown (c, d, g and h). Images were obtained with a pyramidal tip, k^{nom}=0.58 N/m. Static friction effects are visible at the beginning of each scan line in both topographic and friction images. A hexagonal unit cell with lattice constant 2.9 ± 0.5 Å is observed. This value closely corresponds to the 1x1 periodicity of a Au(111) surface. Scale bars=10 Å.

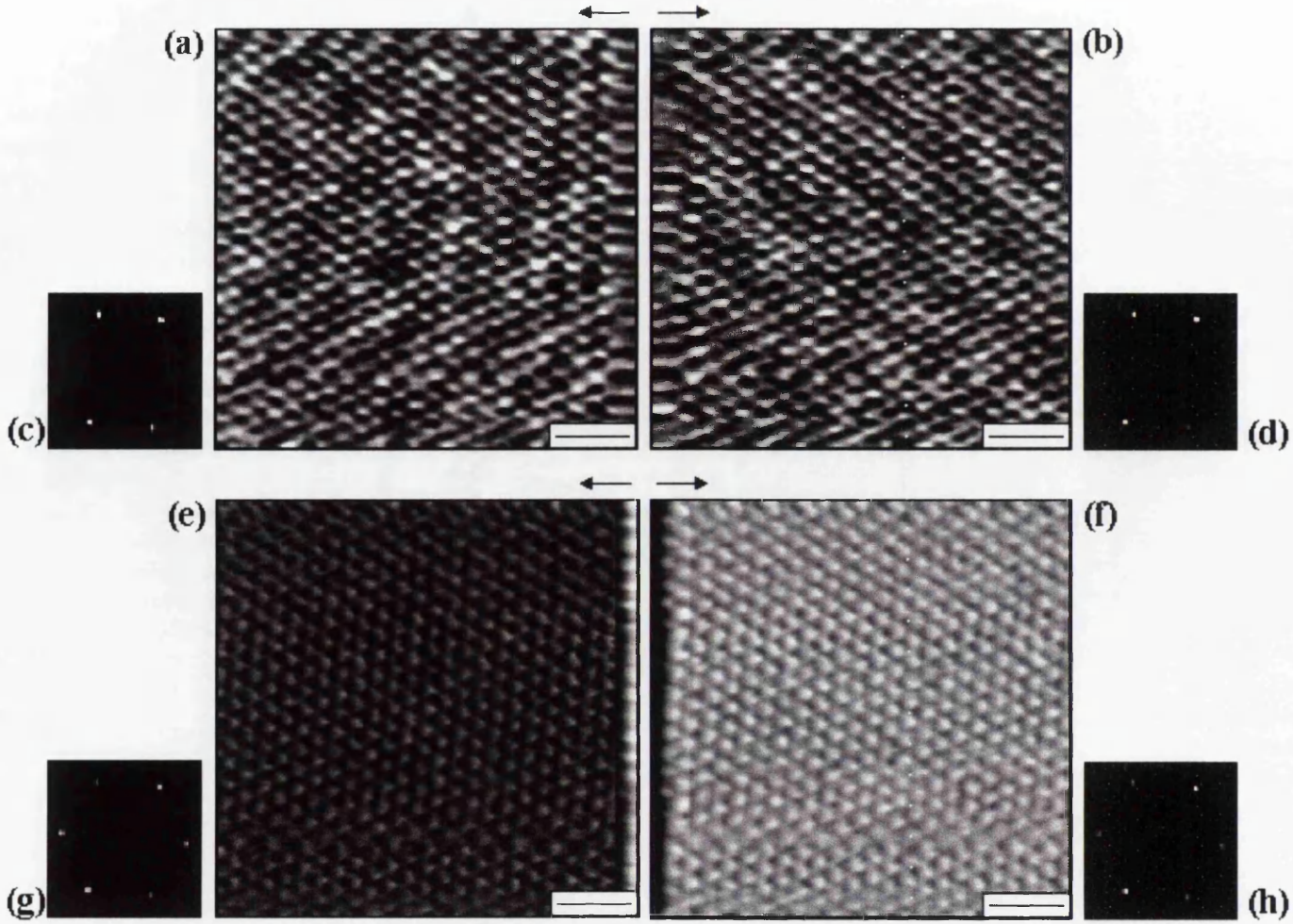
(a)
(b)
(c)
(d)
(e)
(f)
(g)
(h)

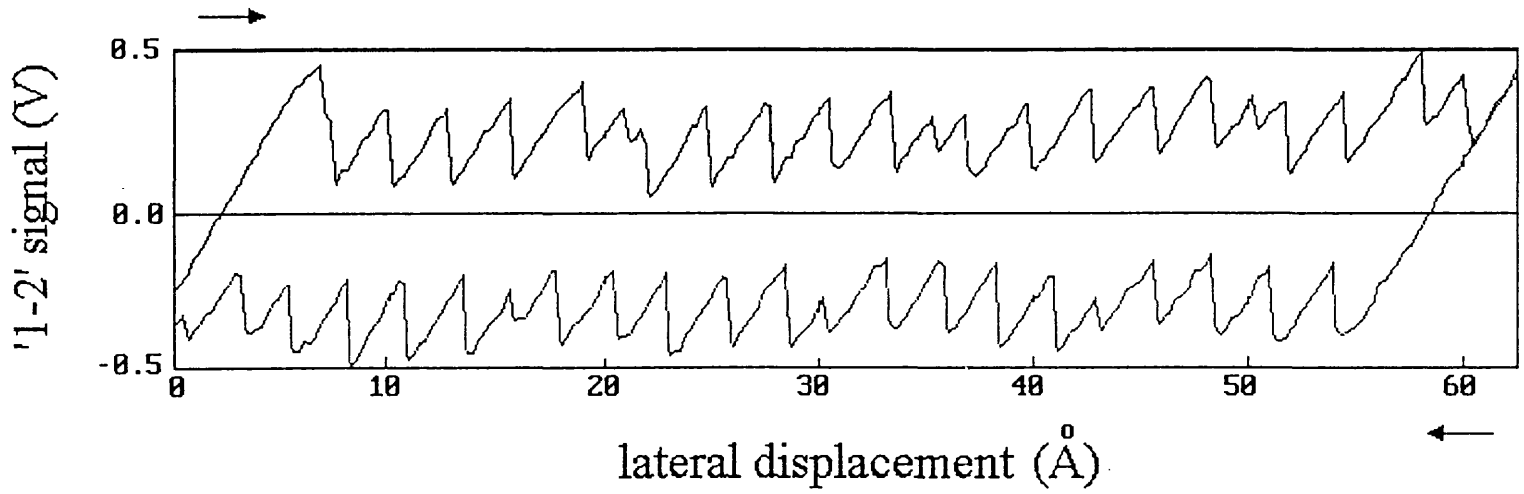

Figure 7.9. 'Friction loop' at a constant applied load for a Au(111) surface. The behavior is similar to that described in figure 7.4. In this case, however, the '1-2' signal has the periodicity of the Au(111) surface.

Figure 7.10 (following page). Topographic image showing the wear of mica. The hole was created by repeatedly scanning over a 250 x 250 $Å^2$ area of the surface with a sharp tip (k^{nom}=0.5 N/m) at about 10 nN. The hole, 10 Å deep (b), was formed after the 11th scan. From the measured step widths (≈ 50 Å and ≈ 70 Å), a tip radius of 150 Å to 250 Å is estimated. The asymmetric line profile shown in (b) is probably the result of an asymmetric tip. Scale bar=500 Å.

(a)

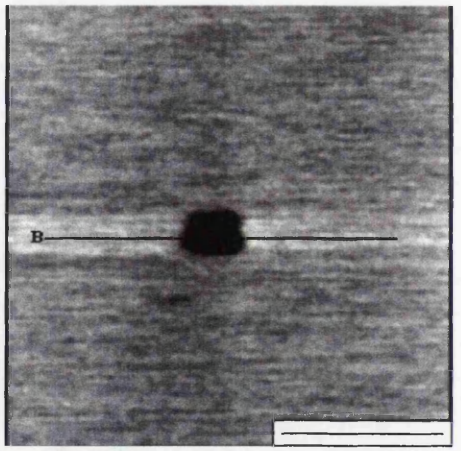

(b)

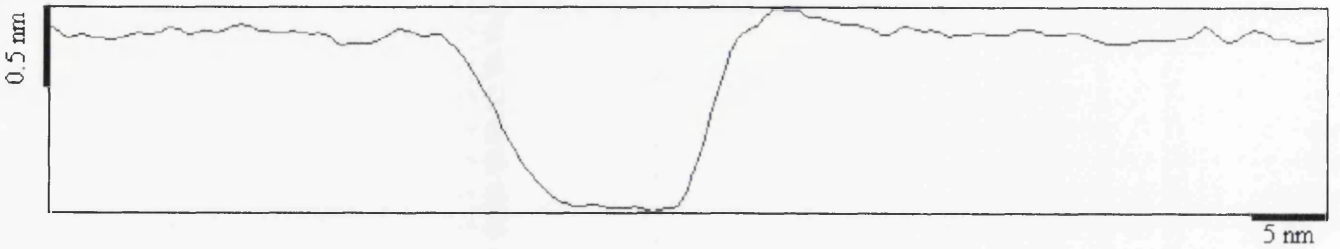

7.6 'Atomic Lattice' Resolution

Atomic-level topographic and lateral force images, such as those shown in figure 7.3 and 7.8, were routinely obtained with both conventional, i.e. 'blunt', and sharpened, i.e. 'sharp', pyramidal silicon nitride tips. AFM/FFM images of mica and Au(111) appear to reproduce well the atomic periodicity of the two surfaces and, as the majority of AFM images reported in literature, show a 'perfect' lattice. In addition, atomic lattice resolution images can be obtained for a wide range of loads, up to several tens of nN, depending on the tip radius and surface. As already discussed in chapter 2, this observation prompts questions on the contrast and imaging mechanisms responsible for such images, since it is not possible for a single atom to bear these loads. On the other hand, if many tip atoms are in contact with the surface it is hard to explain the routine observation of atomic lattice resolution. In this case, the AFM image would still be periodic since the surface has translational symmetry. The observed image would then be a complex superposition of several 'single-atom' images. This would not be a simple addition since the relative loads on the different contact atoms and the elastic normal and lateral deformations of tip and surface would change as the tip moved across the unit cell, and each contributing tip atom might not be in contact with the surface throughout the unit cell. Clearly with a multi-tip model, as the one just described, the appearance of the AFM images should vary significantly from tip to tip and day to day. The topographic image corrugation should also decrease as the load increases and a larger number of tip atoms comes into contact with the surface. A second multi-tip model is possible where the atoms do not contribute equally. Perhaps a relatively large number of 'secondary' atoms helps bear the load, while the contrast variation across the unit cell is controlled by only one or two 'primary' atoms.

Further questions arise when the 'atomic' corrugation in topographic images, such as those shown in figure 7.3 and 7.8, is measured. The 'atomic' corrugation in the topographic images of mica (figure 7.3 (a) and (b)) is measured to be ≈3 Å, while that for Au(111) (figure 7.8 (a) and (b)) is ≈1 Å. As observed in chapter 6, these corrugations are not consistent with the AFM tip tracing contours of constant charge density. It is possible to think that the apparent corrugation may increase if the compliance of the surface varies across the unit cell. Consider, for example, the case of a Au(111) surface and assume that one 'primary' atom is responsible for the contrast. Then it may happen that, when the tip atom is on top of a surface atom, that is pushed down into the surface. As the tip atom moves onto a bridge or hollow site where two or three gold atoms share the load, the surface will not be

indented as much. In this way the AFM topographic images would be a convolution of the atomic corrugation and compliance of the surface and the maxima of the images would not necessarily correspond to the atomic positions.

Another model that would explain lattice resolution images such as those shown in this chapter, is that of the 2D stick-slip motion introduced by S. Fujisawa *et al.* and discussed in chapter 3.[16, 17] In this model, the topographic signal is due to the component of the frictional force across the fast scan direction. As the tip scans the surface and 'hops' from one stick site to the next, it also moves perpendicular to the scan direction of a distance Δ (see figure 3.5). As observed by S. Fujisawa and co-workers, the amplitude of the 'topographic' signal may correspond to the width of the zig-zag walk taken by the tip. In the case of mica, such width is ≈2.6 Å, while for a Au(111) surface is ≈1.45 Å, if the scan direction is perfectly aligned with one of the rows of the sample atoms. In practice, the topography signal due to the tip 'meandering' between the stick sites will be irregular since the scan direction will not be exactly along one row of stick sites. The values of the 'atomic' corrugation for the images of figure 7.3 and 7.8 seem to be roughly consistent with this picture. One further observation can be made from the 2D-FFT spectra of the topographic images in figure 7.3 and 7.8. The two spots closest to the horizontal direction are missing, or more generally are very weak. The other two sets of spots correspond to dragging the tip across rows of atoms, where there is a strong stick-slip, while horizontal (or nearly horizontal) spots are due to the tip moving along (or almost along) the rows of atoms, like in an atomic 'ditch'. The tip occasionally hops from one row to the next, but this is less regular and less frequent, so that the corresponding spots in the 2D-FFT spectra are weaker.

Clearly, the conclusion that the 2D stick-slip motion is the mechanism responsible for the contrast observed in topographic images cannot be reached only from two images! In general, the corrugations measured by the author from topographic images of a variety of samples, included organic thin films, are too high to reflect real atomic corrugations. In the hope to better understand the ideas discussed in this section, further data analysis is still undergoing and further experiments are necessary. In particular, if the 2D stick-slip motion is at the origin of topographic images, then the corrugation should be independent of load (in the wearless regime). The mechanical response of the surface to the load applied seems to play a role. It is often observed that the contrast in topographic images degrades after prolonged scanning (this is especially true for organic films), while the stick-slip of the lateral force images remains unchanged. In addition, it might be interesting to investigate the role played, if any, by the tip geometry. For this task, however, the tip must be well characterized. The method introduced by Carpick *et al.*[18] is suitable to this purpose, especially if $SrTiO_3$ crystals with wider facets can

be made, so as to allow also for the characterization of 'blunt' tips.

It should be added that additional factors can contribute to the observed topographic corrugations. For example, if the lever major axis is not exactly perpendicular to the scan direction, there can be contribution from the 'buckling' of the lever, as described in chapter 6. In the home-built AFM system used at LBNL for all the high-resolution studies, the lever is kept in place by a fine spring wire and the positioning with respect to the holder is performed by eye. Therefore, it is not impossible for the lever to be slightly misoriented. Since the feedback loop does not distinguish between F_z and F_y contributions to bending (i.e. to the 'A-B' signal), contributions from 'buckling' may play a role even when performing an X scan. This effect may explain the reversal of contrast sometimes observed in topographic images (if the topographic contrast is only due to the tip moving from one stick site to the next the contrast should not depend on the scanning direction).

Finally, contributions from 'buckling' forces to the topographic signal amplitude can be quite large when scanning parallel to the lever's major axis. In this case, very large 'atomic' corrugations may be obtained by using soft levers. For example, by using soft V-shaped levers with k^{nom}=0.01 N/m, Au(111) atoms as much as 10 Å high were obtained by the author! An estimate of the 'buckling' contribution to the topographic signal can be obtained by using the method described in chapter 6, yielding a value of ≈1.3 nm/nN, consistent with the experimental data.

Further discussion on the contrast mechanism will be found in chapter 8, where studies on self-assembled monolayers of thiols on Au(111) are described.

References

[1] T. R. Albrecht, C. F. Quate, *J. Appl. Phys.*, **62**, 2599 (1987).

[2] T. R. Albrecht, C. F. Quate, *J. Vac. Sci. Technol. A*, **6**, 271 (1988).

[3] G. Binnig, C. F. Quate, Ch. Gerber, *Phys. Rev. Lett.*, **56**, 930 (1986).

[4] O. Marti, B. Drake, P. K. Hansma, *Appl. Phys. Lett.*, **51**, 484 (1987).

[5] P. J. Bryant, R. G. Miller, R. Yang, *Appl. Phys. Lett.*, **52**, 5233 (1988).

[6] E. Meyer, D. Anselmetti, R. Wiesendanger, H.-J. Güntherodt, F. Lévy, H. Berger, *Europhys. Lett.*, **9**, 695 (1990).

[7] R. D. Barrett, J. Nogami, C. F. Quate, *Appl. Phys. Lett.*, **57**, 992 (1991).

[8] E. Meyer, H.-J. Güntherodt, H. Haefke, M. Kron, *Europhys. Lett.*, **15**, 319 (1991).

[9] F. J. Giessibl, G. Binnig, *Ultramicroscopy*, **42-44**, 281 (1992).

[10] L. Howald, R. Lüthi, E. Meyer, G. Gerth, H. Haefke, R. Overney, H.-J. Güntherodt, *J. Vac. Sci. Technol. B*, **12**, 2227 (1994).

[11] R. Erlandsson, G. M. McClelland, C. M. Mate, S. Chiang, *J. Vac. Sci. Technol. A*, **6**, 266 (1988).

[12] S. Fujisawa, Y. Sugawara, S. Ito, S. Mishima, T. Okada, S. Morita, *Nanotechnology*, **4**, 138 (1993).

[13] J. Hu, X.-D. Xiao, D. F. Ogletree, M. Salmeron, *Surf. Sci.*, **327**, 358 (1995).

[14] *Micas, Reviews in Mineralogy*, S. W. Bailey edt., vol 13 (Mineralogical Society of America, Blacksburgh, VA, 1984).

[15] M. B. Salmeron in *Surface Diagnostics in Tribology: Fundamental Principles and Applications*, K. Miyoshi, Y. W. Chung edts. (World Scientific Publishing Co.:River Edge, 1993).

[16] S. Fujisawa, Y. Sugawara, S. Ito, S. Mishima, T. Okada, S. Morita, *Nanotechnology*, **4**, 138 (1993).

[17] S. Fujisawa, E. Kishi, Y. Sugawara, S. Morita, *Jpn. J. Appl. Phys.*, **33**, 3752 (1994).

[18] R. W. Carpick, N. Agrait, D. F. Ogletree, M. Salmeron, *J. Vac. Sci. Technol. B*, **14**, 1289 (1996).

Chapter 8

Structural and Frictional Studies of Self-Assembled Thiols on Au(111)

8.1 Introduction

Self-assembled monolayers and Langmuir-Blodgett films provide an important and attractive way to modify physical and chemical properties of solid surfaces. Their potential applications now extend from non-linear optics based devices[1, 2, 3, 4, 5] chemical and biological microsensors,[6, 7, 8] to microelectronics resists[9, 10, 11] and tribology applications.[12, 13, 14] Many of these applications rely on molecular-scale recognition and control, therefore a molecular-scale understanding of these systems, from their structure to their electronic and mechanical properties, is indispensable. Such fundamental knowledge will ultimately make it possible to discover new and tailor already in use systems for an even larger number of applications.

This and the next two chapters will show that organic monolayers can be used as model systems for the understanding of basic tribological issues. Ultrathin organic films, such as self-assembled and Langmuir-Blodgett monolayers, have been of great interest in recent years due to their potential use as boundary lubricants in several technological applications, such as information storage devices and micromechanical systems.[12, 13, 14, 15, 16, 17, 18, 19] Requirements for effective boundary lubrication are strong adhesion of the molecules to the substrate, reduced friction and high resistance to wear. In the case of LB films the molecules interact with the substrate through weak van der Waals and ionic forces and repeated shearing results in the molecules being worn away.[20] On the contrary, self-assembled aliphatic molecules such as alkylthiols R-$(CH_2)_{n-1}$-SH and alkylsilanes R-$(CH_2)_{n-1}$-SiX_3 (R symbolically represents the molecule's terminal group and X is either chloride or alkoxy) are covalently bonded to the substrate and therefore are better candidates as lubricants. Moreover, the possibility of changing the chain length, terminal group and cross-linking within the layer makes self-assembled monolayers attractive systems to study the nature of frictional interactions at the molecular scale. In addition, despite their technological importance for lubrication,[12-19] little is known about the structure and mechanical properties of

organic layers when subjected to externally applied normal and shear loads.

Among organic monolayers, SAMs of alkylthiols $CH_3(CH_2)_{n-1}SH$ (hereafter indicated as C_n) on Au(111) have been widely investigated in the past ten years. [21-52] They are relatively easy to prepare and give well ordered, close-packed films for n≥8. The details of the headgroup-substrate interaction are still controversial. A model derived from early diffraction and spectroscopy studies[23, 25, 29, 30] and supported by some computer calculations[50-52] predicted that, for long chain thiols, sulfur atoms would adsorb at every other three-fold hollow site on the Au(111) surface, separated by approximately 4.99 Å. The alkyl chains are depicted as being in an *all-trans* conformation, arranged in a hexagonal $\left(\sqrt{3}x\sqrt{3}\right)R30^o$ unit cell relative to the Au(111) lattice and tilted about 30° from the surface normal (figure 8.1). A "c(4x2)" superlattice (relative to the $\left(\sqrt{3}x\sqrt{3}\right)R30^o$ structure) has been observed in He diffraction, x-ray diffraction and scanning tunneling microscopy studies.[31-33, 39, 40] AFM studies have shown a hexagonal $\left(\sqrt{3}x\sqrt{3}\right)R30^o$ unit cell,[44, 45, 47] however, to the author's knowledge, the c(4x2) superstructure has never been observed by AFM. More recently, grazing incidence x-ray studies performed on C_{10} layers have suggested the presence of a disulfide bond.[33] These results are consistent with the sulfur atoms being adsorbed at both the Au hollow and bridge sites. They also indicate that the hydrocarbon chains are in a nearly hexagonal configuration, but that the S-C bond is *gauche*, in contrast with the previous model. Recent optical sum frequency generation experiments[34] showed that the arrangement of S atoms relative to the Au substrate does not have the 3-fold symmetry required by a model with all S atoms adsorbed at the Au hollow sites.

Spectroscopic and contact angle studies have shown that properties of long chain alkylthiols (n>8) on Au(111) are independent of chain length, while a certain variation exists for shorter chain.[22, 23] This has been explained by the fact that the short chains are less densely packed and/or increasingly disordered. STM studies performed in UHV have shown that, for n<6, self-assembled methyl terminated alkylthiols on Au(111) single crystals are in a 2D-liquid state when removed from solution. Through desorption of molecules, the layers evolve to an ordered phase, characterized by a lower density with respect to the longer chain case.[41] Low-energy electron diffraction studies of vapor-deposited short chains thiols (n≤10) on Au(111) single crystals found ordered structures, characterized by lower density of molecules with respect to the dense $\left(\sqrt{3}x\sqrt{3}\right)R30^o$ phase.[28] Other studies using He-diffraction had measured no diffraction peaks from layers with n=6 self-assembled on Au(111)/mica, but have recently confirmed the existence of lower density phases on layers deposited from a molecular beam onto Au(111)

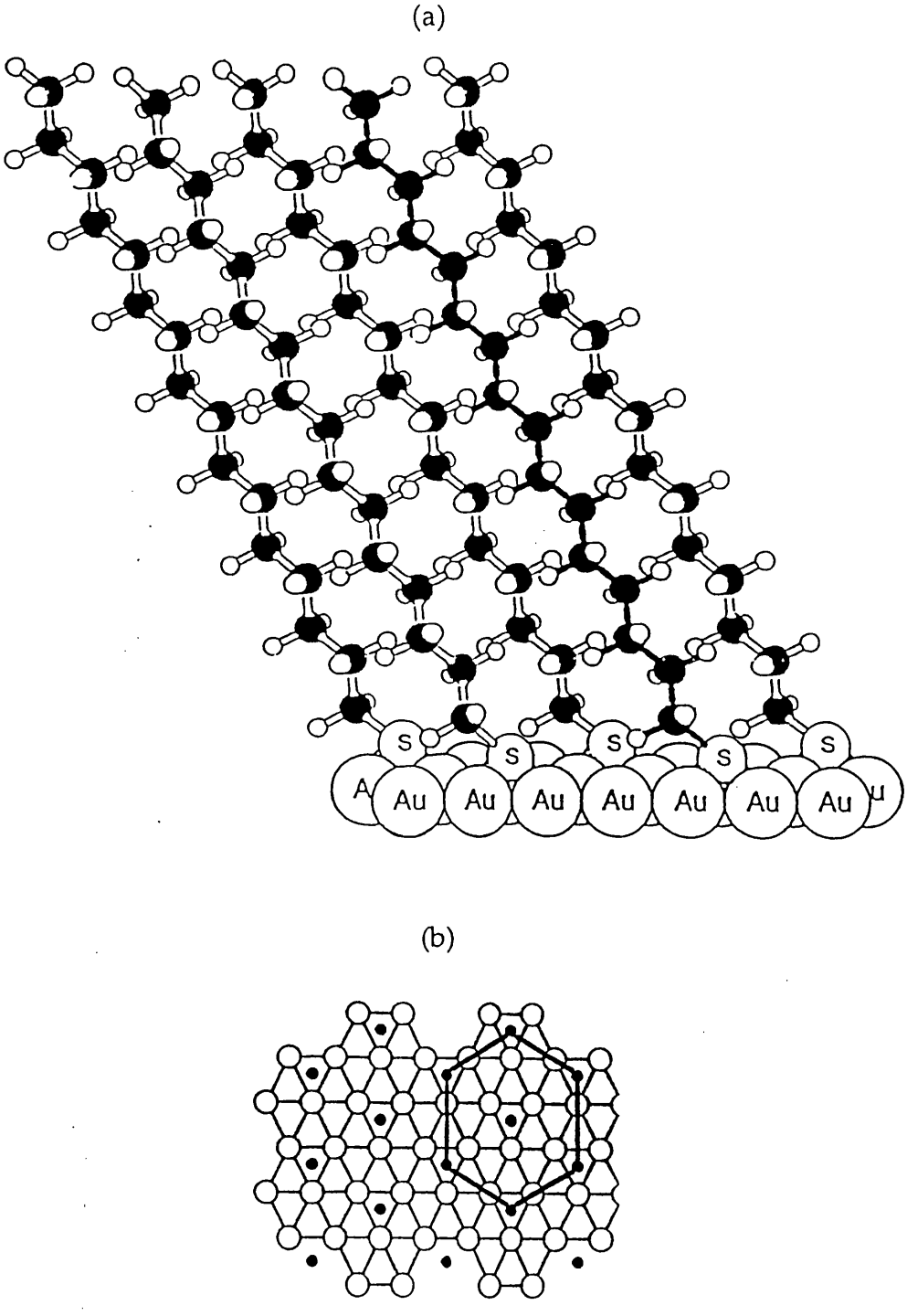

Figure 8.1. (a) Schematic of molecular packing of long chain alkylthiol molecules on Au(111) surfaces. Chains are shown in an *all-trans* conformation and tilted about 30° from the surface normal. The determination of the absorption sites for the S atoms on the Au(111) surface is still controversial. In (b) S atoms (filled circles) are located at the three-fold hollow sites and the unit cell is described as $\left(\sqrt{3}x\sqrt{3}\right)R30^{o}$ with respect to the (1x1) structure of Au(111).

single crystals.[53]

Fewer studies can be found in literature on substituted alkylthiols, i.e. terminating with a functional group other than methyl.[25, 54-56] In particular, carboxylic acid terminated chains show to have a crystalline-like packing for n=16 and a liquid-like conformation for n=11. Also, layers with n=11 are revealed to be very poor electrochemical barriers, interpreted as due to a high concentration of defects and pinholes which make the layers permeable.[54] Moreover, stronger inter-layer hydrogen-bonded and with water interactions were also found for acid layer (n=15) when compared to other hydrophilic surfaces, such as for alcohol terminated molecules.[55] Both type of surfaces, however, are completely wetted by water.

Studies in the past showed that friction of aliphatic polar compounds is a function of the chain length and terminal group.[57] Several AFM reports on the frictional properties of a different number of organic surfaces can be found in the literature.[20, 58-60] However, to the author's knowledge, no systematic study, aimed to understand how the frictional properties of organic monolayers depend on chemical identity of the end group, order within the monolayer and head-group substrate interaction, has been reported. It is important to be able to address the different factors that affect mechanical and frictional properties separately. However, it is not always possible to vary these properties one by one. For example, changing the terminal group might also change the order in the layer due to steric effects.[1] A previous study at the STM/AFM lab showed[61] that the chemical nature of the terminal group, methyl in that particular case, is not the only factor determining the frictional properties of self-assembled alkylsilane molecules on mica. In fact, the frictional forces were found to depend strongly on the chain length, yielding higher values on shorter chains. This result was interpreted as a result of decreased packing density and order for the shorter chains, which in turn means increased number of energy modes, such as kinks, defects and chains distortions, available for energy dissipation.

In this chapter, preparation, molecular structure characterization and frictional properties of methyl (CH_3) and carboxylic acid (COOH) terminated alkanethiol monolayers on Au(111) on mica will be described. In chapter 10, some of these results will be compared to those obtained on alkylsilane SAMs on mica.

8.2 Thiol Monolayers Preparation

Alkylthiols with n=18, 12, 8, 6 were purchased from Aldrich Chemical Company (Milwakee, WI, USA). Undecanethiol (n=11) was purchased from Pfaltz & Bauer (Waterbury, CT, USA). Mercaptoundecanoic acid ($COOH(CH_2)_{10}SH$) was synthesized by Mr. Larry McGhee, at the Department of Chemistry of Glasgow University according to a method described in the literature.[62]

For the preparation of the monolayers, Au(111) films on mica were prepared as described in chapter 7, removed from the vacuum evaporator and immediately immersed in 1 mM ethanolic solutions of thiols. The gold substrates were left in the solution at room temperature for at least 36 hours, then rinsed with ethanol and dried in a N_2 stream. Samples were immediately mounted into the microscope to avoid surface contamination.

8.3 Topographic Mode Images of Thiol SAMs

Figure 8.2 shows simultaneous topographic (a, b) and lateral force (e, f) images obtained on a C_{12} alkylthiol layer. As can be seen also from the 2D-FFT spectra (figure 8.2 (c), (d), (g) and (h)), a hexagonal periodicity is revealed. The lattice constant, as measured on different samples and with different tips, is 4.9±0.3 Å. This periodicity corresponds closely to the unit mesh observed for several long chain thiol monolayers by several diffraction techniques, STM and previous AFM studies. In contrast to other techniques, however, the c(4x2) superstructure is not observed. Similar results were obtained on C_{18}, C_{11} and C_8 layers. To the author's knowledge, this is the first time that it has been shown by AFM that the chains of C_{11} layers are also hexagonally packed.

But, what does the AFM tip actually image? It is known from He-diffraction studies that at room temperature the methyl termination of the alkyl chains is thermally disordered.[29] Moreover, non-linear optical (NLO) experiments have shown that C_{18} alkylsilane layers are orientationally disordered for pressures around 80 MPa, possibly due to *gauche* defects in the terminal methyl/methylene groups.[63] Since in these AFM experiments it was not possible to directly measure force and contact area, a contact mechanics model has to be used to estimate the pressure applied by the AFM tip. As described in chapter 3, a few theories are available for this purpose. The Hertz model describes the elastic deformation of solids in contact with no attractive interactions. The JKR theory includes the effect

Figure 8.2 (following page). Topographic (a, b) and simultaneous lateral force (e, f) images of a freshly prepared C_{12} alkylthiol monolayer on Au(111)/mica. 2D Fast Fourier power spectra are also shown (c, d, g and h). Images were obtained with a pyramidal tip (k^{nom}=0.58 N/m) at 0.5 nN external load. A hexagonal unit cell with lattice constant 4.9 ± 0.3 Å is measured. This value corresponds closely to the hexagonal packing of the alkyl chains, as determined by diffraction techniques, STM and previous AFM studies. Scale bars = 10 Å.

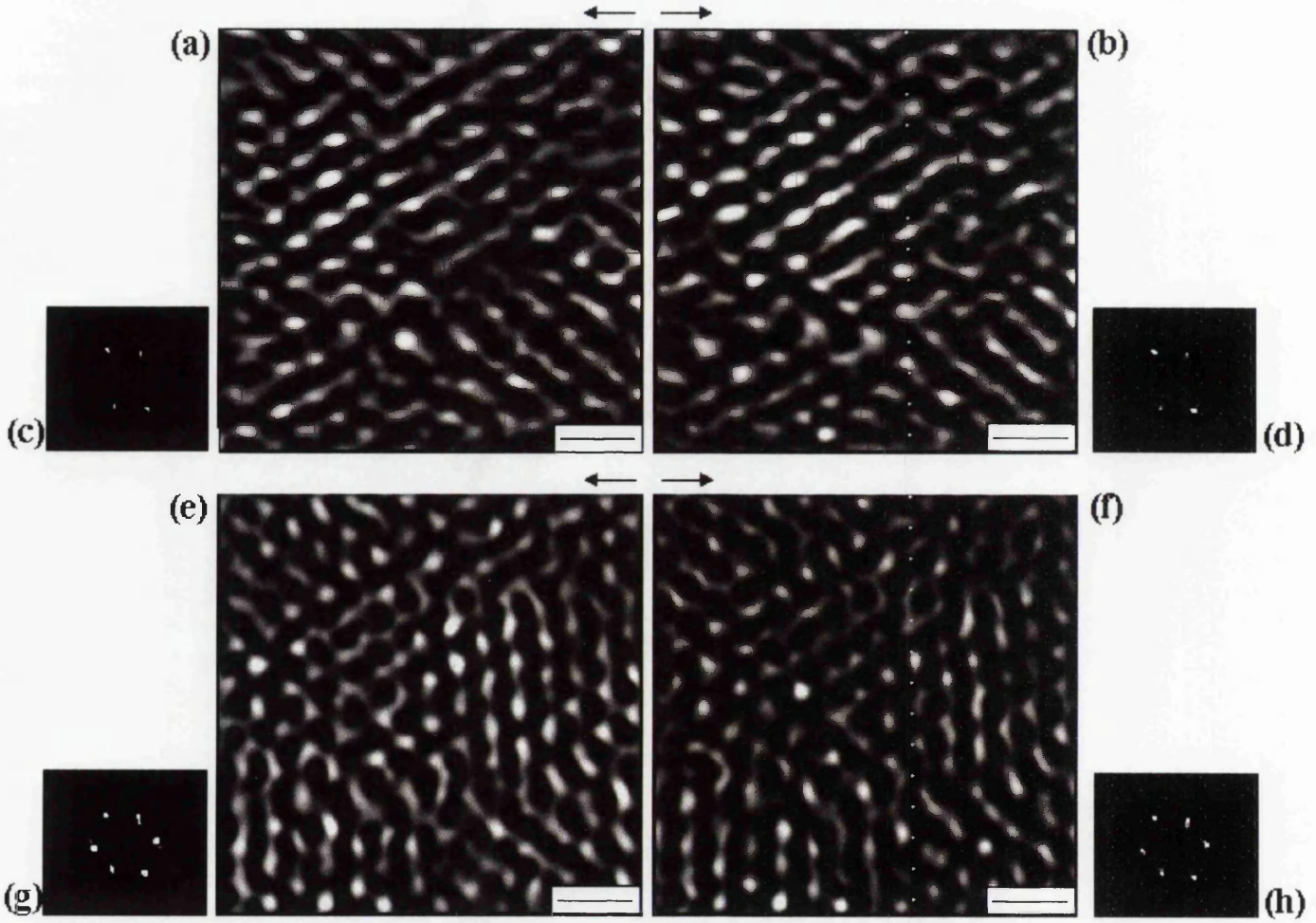
(a)
(b)
(c)
(d)
(e)
(f)
(g)
(h)

of adhesive interaction in the contact proportional to the contact area, which causes additional elastic deformation of the solids. In air, there are tip-surface forces that do not depend strongly on the contact area such as the "capillary" force, that are not taken well into account by the JKR theory.[64] If the capillary force is the dominant interaction, which is often the case for AFM in ambient laboratory conditions, it is reasonable to use a 'shifted Hertz model', with an effective load equal to the magnitude of the pull-off force added to the externally applied load. This treatment introduced by Fogden and White[65] is similar to the treatment of the van der Waals forces in the DMT theory, as described in chapter 3. In the case of figure 8.2 a tip with a radius ≈500 Å was used. The pull-off force was measured to be ≈22 nN and the images were obtained with an external load of 0.5 nN. A 'shifted' Hertz theory where the external load is substituted by the total load (external force+pull-off) gives a pressure of about 1.2 GPa. This value for the pressure is one order of magnitude larger than the values accessed in NLO experiments. It is most likely, therefore, that in the AFM experiments *gauche* defects were present at least at the methyl termination and possibly terminal methylene groups of the alkyl chains. In these conditions the AFM images taken at low loads still reflect the average long-range order of the main bodies of the alkyl chains.

The c(4x2) superlattice has been attributed to two different twists of the hydrocarbon chains about the chain axis within one single unit mesh.[29] A more recent model proposes that the c(4x2) superstructure originates from mixed bonding sites on the Au(111) surface, which in turn cause a height modulation of the hydrocarbon chains.[33] As discussed in chapters 3 and 7, the observed periodicity in AFM images is directly correlated to the periodicity in the lateral force images, where contrast is due to the stick-slip nature of friction. The observed $\left(\sqrt{3}x\sqrt{3}\right)R30^{o}$ periodicity means that the tip "sticks" once for each molecule, even though many molecules are in the contact area. In fact, the stick-slip picture implies that the relative motion between the tip and surface is concentrated in the 'slip' event: during the 'stick' period, strain builds up in the lever and surface. During the stick-slip motion there may be some bending, that will produce a contrast in the z direction. Other effects, such as lateral and normal deflection coupling, lever 'buckling' and AFM feedback response may also contribute. Within this model, it is hard to imagine that the AFM sticking would be sensitive to the subtle differences giving rise to the superlattice, even if it were not disordered due to tip-pressure effects.

AFM images obtained on C_6 layers did not reveal any long-range order (figure 8.3). These results are in apparent disagreement with some diffraction and STM studies. This might be due to the fact that the samples used in these studies were analyzed within a few hours of their preparation to avoid possible contamination in

air. STM and He-diffraction studies indicate that it takes a few days after the samples have been out of the solution for C_6 layers to re-organize. Another possible explanation is that the layer may become disordered under the pressure applied by the AFM tip. In the case of short chains, the pressure-induced terminal defects may be sufficient to completely disorder the chains, an effect that will be magnified by the reduced stability and/or packing density of the shorter molecules.

AFM images of $C_{10}COOH$ thiols did not reveal any long-range order, similarly to the C_6 layers. These results are consistent with other literature reports, which have observed a liquid-like packing for these layers.[56] The substitution of the methyl group with the larger carboxylic acid one has the effect of increasing the number of methylene units necessary to obtain crystalline-like packing as compared to unsubstituted alkylthiols.

8.4 Frictional Properties of Thiol SAMs: Chain Length Dependence

Figure 8.4 shows friction *vs.* load curves for alkylthiol monolayers (CH_3-$(CH_2)_{n-1}$-S-Au) with n = 18, 12, 11, 8 and 6. A curve taken on a freshly cleaved mica surface with the same tip is also shown as a reference. The tip used had an estimated radius of ≈500 Å and nominal force constant of 0.58 N/m. Each curve is composed of an approach and a retract branch corresponding to increasing and decreasing loads. There is a jump to contact in the approach branch that is used to define the zero load. For the lower chain lengths, there is a small amount of hysteresis, with the load branch being below the unload branch. This is most visible for the C_6 film. As can be seen, the friction curves for the C_{18}, C_{11} and C_8 layers are undistinguishable. The curve for the C_{12} layer lies below them and the frictional forces on C_6 are roughly twice as large. Furthermore, all curves lie well below the mica curve. The applied load was limited to values that did not cause any damage on any of the monolayers, as revealed by topographic scans of the areas where the curves were acquired. As it will be shown in the following two chapters, when high loads, or sharper tips, are used the layers are affected either reversibly (see chapter 9) or irreversibly[61] and the frictional forces become unstable.

Adhesion energies can, in principle, be determined from the force *vs.* distance curves. In most AFM experiments using soft levers, however, as described in chapter 2, there is an instability that causes the tip to jump into contact with the surface during approach and to abruptly pull-off during retraction. Therefore, the force

Figure 8.3 (following page). Topographic (a, b) and simultaneous lateral force (c, d) images of freshly prepared C_6 alkylthiol monolayers on Au(111)/mica. No long-range order is observed for these layers, in apparent disagreement with STM studies in UHV. Images were acquired with a pyramidal tip (k^{nom}=0.58 N/m) at 0.5 nN external load. Scale bars = 10 Å.

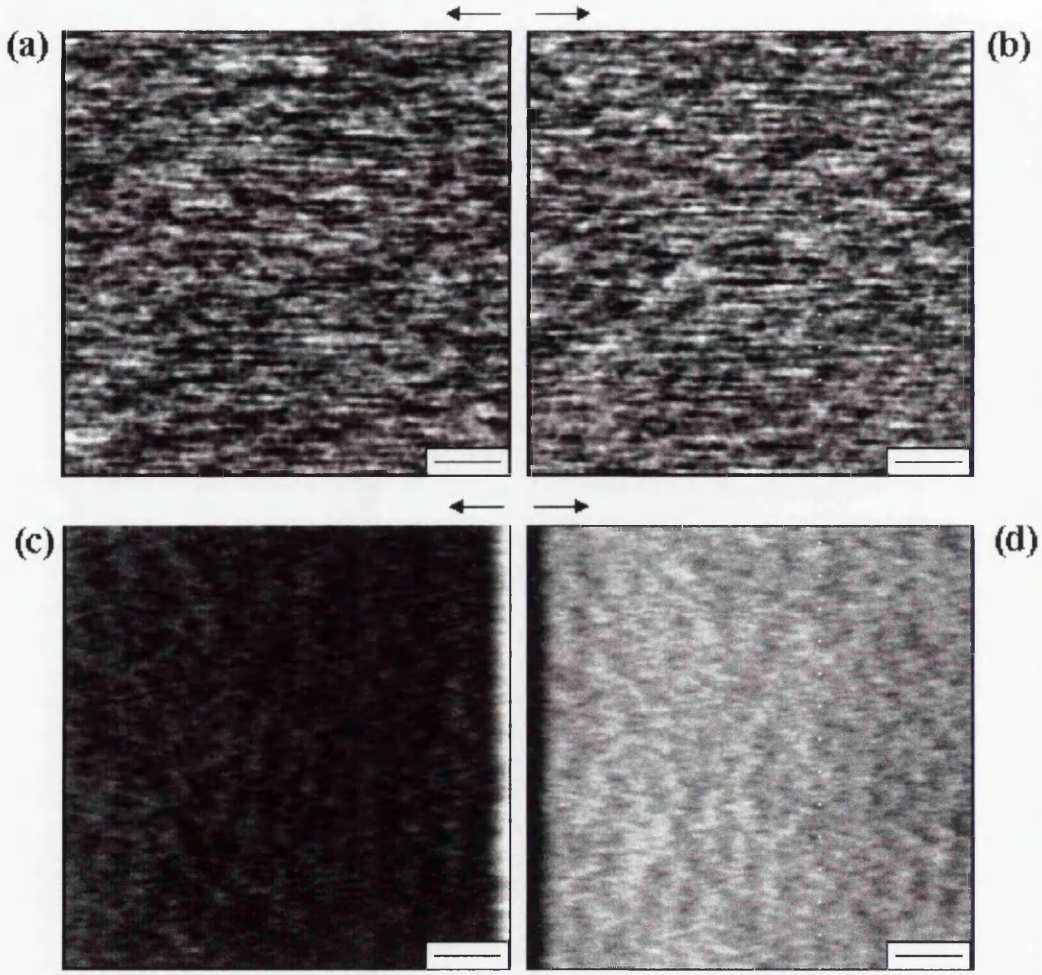
(a)
(b)
(c)
(d)

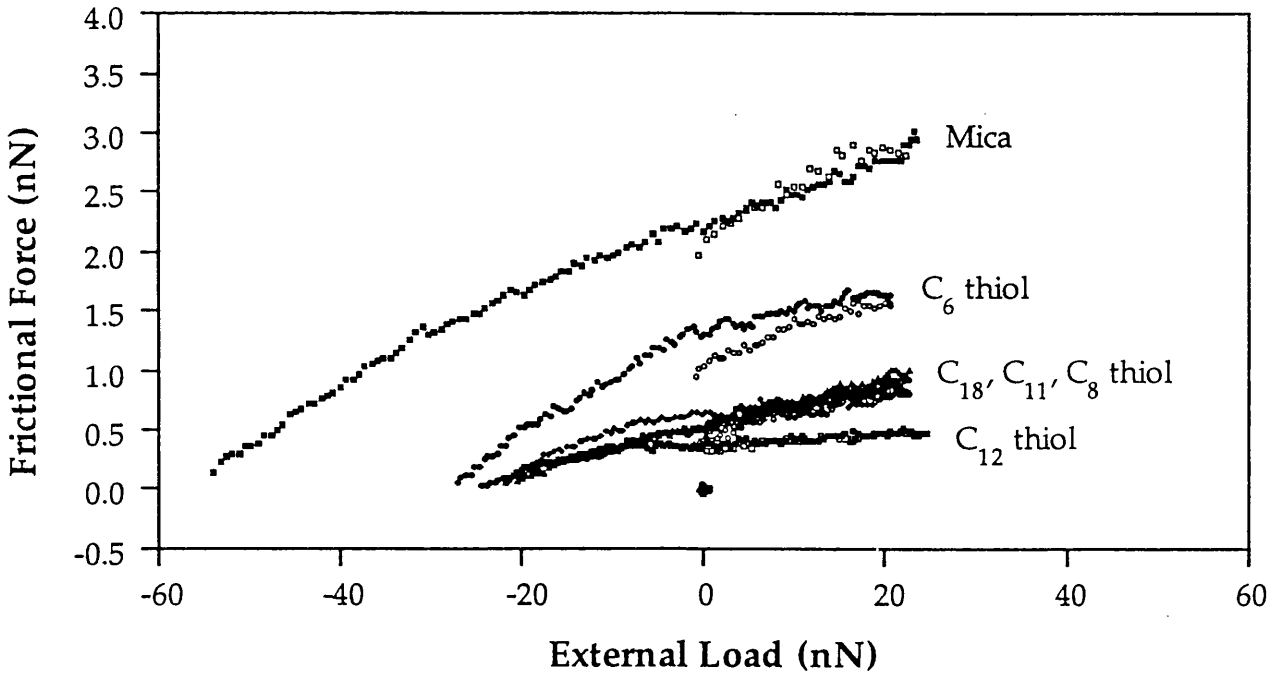

Figure 8.4. Friction *vs.* load curves obtained for C_{18}, C_{12}, C_{11}, C_8 and C_6 alkylthiol monolayers on Au(111)/mica. A curve for mica is also shown as a reference. The load was limited to values that did not cause any damage on the layers being probed. All curves were obtained with the same silicon nitride lever, with an estimated force constant of 0.34 N/m (k^{nom}=0.58 N/m). Approach and retract branches are shown as open and filled symbols, respectively.

curve cannot be determined and integrated in the important region of the surface proximity to obtain the adhesion energy. Instead, the pull-off forces are used as a measure of adhesion, an approximation that implicitly assumes that all the potential curves have the same shape. Values of the pull-off forces found in these experiments are presented in Table 8.I. These values are averages of several measurements on different areas of the samples. The pull-off forces for the C_{18}, C_{12}, C_{11} and C_8 are identical within the uncertainty, while a 20% increase is observed for the C_6 layers. The values measured on the organic layers are roughly half the values measured on mica, which is an hydrophilic surface. i.e. has a high surface energy.

An increase in pull-off force could be expected for the shorter chains due to their higher compressibility, which gives rise to a higher contact area for the same applied load. This probably explains the higher pull-off forces observed for the C_6 films. The effect of the compressibility on the pull-off force has been demonstrated by a recent study by Koleske *et al.*[66]

These results clearly demonstrate that the frictional properties of surfaces do not depend only on the chemical nature of the exposed groups, although these do determine the surface energy. Otherwise, all chain lengths should have yielded similar friction values. In order to understand these results the molecular order has to be considered. In the formation of self-assembled monolayers, the molecule-substrate and molecule-molecule interactions both play important roles, and determine the "quality" and character of the films. Inter-chains interactions are dominated by van der Waals forces. While the exact cohesive energy for these systems is difficult to compute, an approximate value of the cohesive energy per CH_2 group can be obtained by summing the interactions of each CH_2 group with the CH_2 groups in the same chain and in the neighboring ones, under the approximation of an ideally close-packed monolayer.[61] The stabilization energy provided by additional methylene groups saturates at n=8-10, at which point the energy per methylene group is ~7 kJ/mol. Thus, the invariance of structure and properties for long chain alkylthiols, as shown by different techniques, is anticipated. It also explains the similarity of frictional behavior for films, with lengths n>12.

It is proposed that the increase in friction for the short chains (n<8) is due to poor packing of the molecules. This makes possible the excitation of numerous defects and energy dissipating modes, that are sterically quenched in the densely packed films. Further discussion of this point will be found in chapter 9 and 10.

A surprising result of these studies is that the C_{12} thiol layers yield lower frictional forces than their C_{18} counterpart. The anomalous behavior of the C_{12} may be related to the purity of the chemicals employed. According to the manufacturer a small difference exist (99.4% for the C_{12} *vs.* 99.2% for the C_{18}). Although purity is

Surface	Pull-off force F_{po} (nN)	ΔF_{po} (nN)
Alkylthiols		
C_{18}	21.3	1.5
C_{12}	22.0	1.7
C_{11}	22.2	1.1
C_8	20.5	1.8
C_6	24.5	3.1
Mica	54.2	1.8

Table 8.I. Pull-off forces, F_{po}, measured from force *vs.* distance curves. ΔF_{po} is the statistical standard deviation.

an important factor that might affect the ordering and packing of the film, the observed difference is not understood at present.

8.5 Frictional Properties of Thiol SAMs: End Group Dependence

Figure 8.5 shows an example of friction *vs.* load curves obtained on a $C_{10}COOH$ sample and methyl terminated samples with equal n, C_{11} and n=6, C_6. A curve taken on a freshly cleaved mica surface is also shown as a reference. The same lever of figure 8.4 was used. As can be seen, the frictional force measured on the carboxylic terminated layers is about one order of magnitude larger than that measured on C_{11} alkylthiol layers. Moreover, it is about 6 and 3 times larger than that measured on C_6 alkylthiol films and mica, respectively. The pull-off force on $C_{10}COOH$ layers is 43 ± 2 nN. Water contact angles measurements performed on freshly prepared acidic thiol layers showed a completely wetted surface, however after storing the samples in a desiccator for three days the contact angle increased to 75.2 ± 1.7^{o}. This result is consistent with the carboxylic acid terminated thiol layers becoming contaminated in ambient conditions, as a consequence of their high surface energy. The friction measurements reported here were performed on freshly prepared, hydrophilic samples. Values for the pull-off forces measured on C_{11}, C_6 thiol monolayers and mica are reported in table 8.I. Pull-off forces measured on mica and on methyl terminated layers are approximately 25% higher and half the values for the $C_{10}COOH$ layers, respectively.

To interpret the friction results shown in figure 8.5, the surface energy and packing of the molecules have to be considered. Disordered AFM images (similar to those obtained on C_6 methyl terminated layers, figure 8.3) were obtained on these layers, consistent with diffraction techniques which have indicated a liquid-like order for these films. Similarly to the mechanism proposed for short chains thiols, the disorder/short-range order in the chains favors the creation of defects and excitation of energy modes, thus increasing friction. However, in this case a further contribution to the high measured values of the frictional force probably comes from the higher surface energy of the acidic layers compared to the hydrophobic films. The study of (ordered) films formed from longer mercaptoalkanoic acids molecules, should help one to elucidate a more precise relationship between the hydrophilicity of the surface and the frictional properties of these layers.

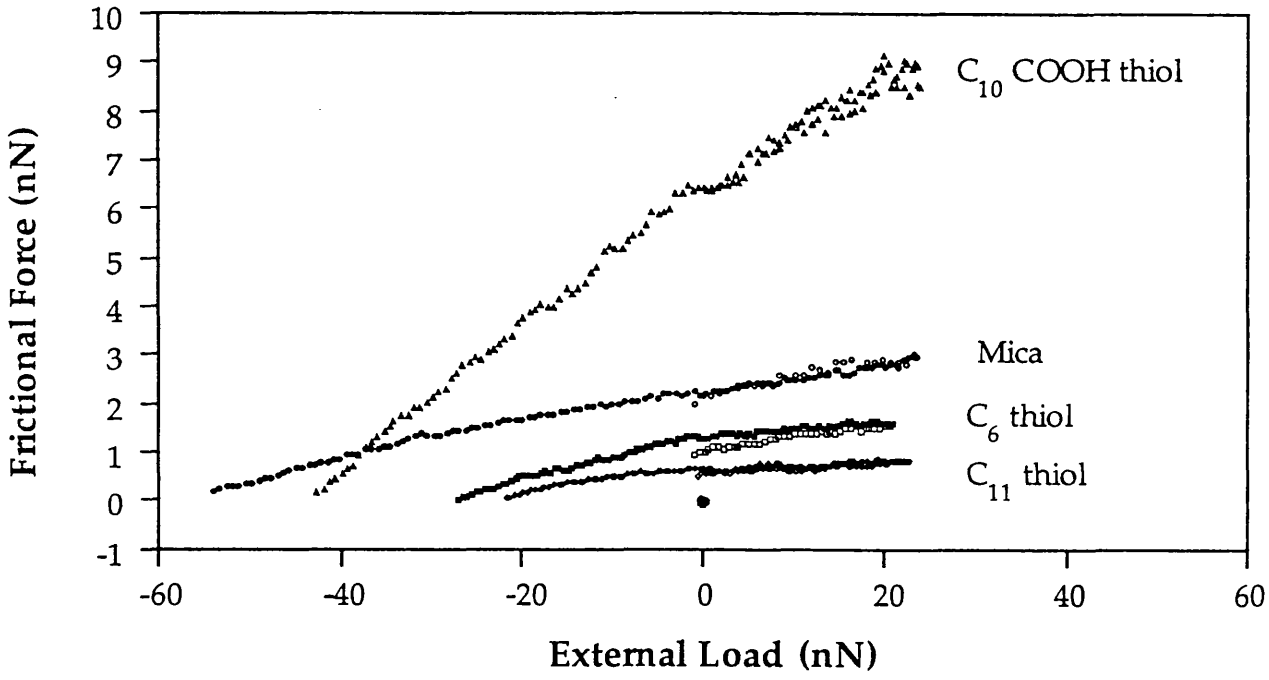

Figure 8.5. Friction *vs.* load curves obtained for $C_{10}COOH$, C_{11} and C_6 alkylthiol monolayers on Au(111)/mica. A curve for mica is also shown as a reference. The load was limited to values that did not cause any damage on the layers being probed. All curves were obtained with the same silicon nitride lever, with an estimated force constant of 0.34 N/m (k^{nom}=0.58 N/m). Approach and retract branches are shown as open and filled symbols, respectively.

8.6 Frictional Properties of Au(111) Thin Films

Figure 8.6 shows an example of a friction *vs.* load curve taken on Au(111)/mica. For comparison, curves taken with the same pyramidal tip (k^{nom}=0.58 N/m) on C_{18} thiol and mica surfaces are also shown. As can be seen, the curve for the Au(111) film lies well below the ones acquired on the C_{18} thiol layer and mica. This result was at first surprising: the alkylthiol layer acts as an 'anti-lubricant', that is it increases friction rather than reducing it. However, the result is consistent with other observations. Contact angle measurements carried out on freshly prepared Au(111)/mica films gives a value of 73 ± 2^{o}. That indicates that the surface is contaminated, most likely because of carbonaceous materials. It has been known for several years that Au surfaces are not hydrophilic in character as soon as they are exposed to ambient conditions.[67] The above value of the contact angle is about 40% lower than that measured on C_{18} thiol layers ($\approx 112^{o}$). However, the pull-off forces measured on Au(111) are usually smaller than those for C_{18} thiol films, 4 nN *vs.* 23 nN for the example shown in figure 8.6. Not surprisingly, the relative ratio is not constant when different samples are examined and different tips are used, however pull-off forces for Au(111) films are consistently lower than those measured on any of the long chain alkylthiols layers studied. Even if the gold surface is contaminated, the origin of such relation between the adhesive properties of the two surfaces is not understood at present. Importantly, topographic mode images taken on Au(111) films showed that the surface responds elastically at all applicable loads and no damage occurs even at pressures where the C_{18} thiols layers undergo important modifications (see chapter 9). At the loads and pressures investigated here (please note that a 'blunt' tip was used), C_{18} thiols layers appear undamaged, although defects and distortions are probably created in the outer portion of the layer. If the same mechanism of energy dissipation proposed in sections 8.4 and 8.5 is used here, the lower frictional forces measured on Au(111) films would seem to be consistent with the elastic properties of the surfaces. The contamination layer may be responsible for the initial increase seen in the frictional force as the tip comes into contact with the gold surface. This contamination is presumably only physisorbed onto the surface and easily displaced by the tip. Interestingly, after the removal of the contaminant layer, the frictional force shows little dependence on the applied load and a little amount of hysteresis is observed only at loads corresponding to the tip being pulled off the surface (negative loads in figure 8.6).

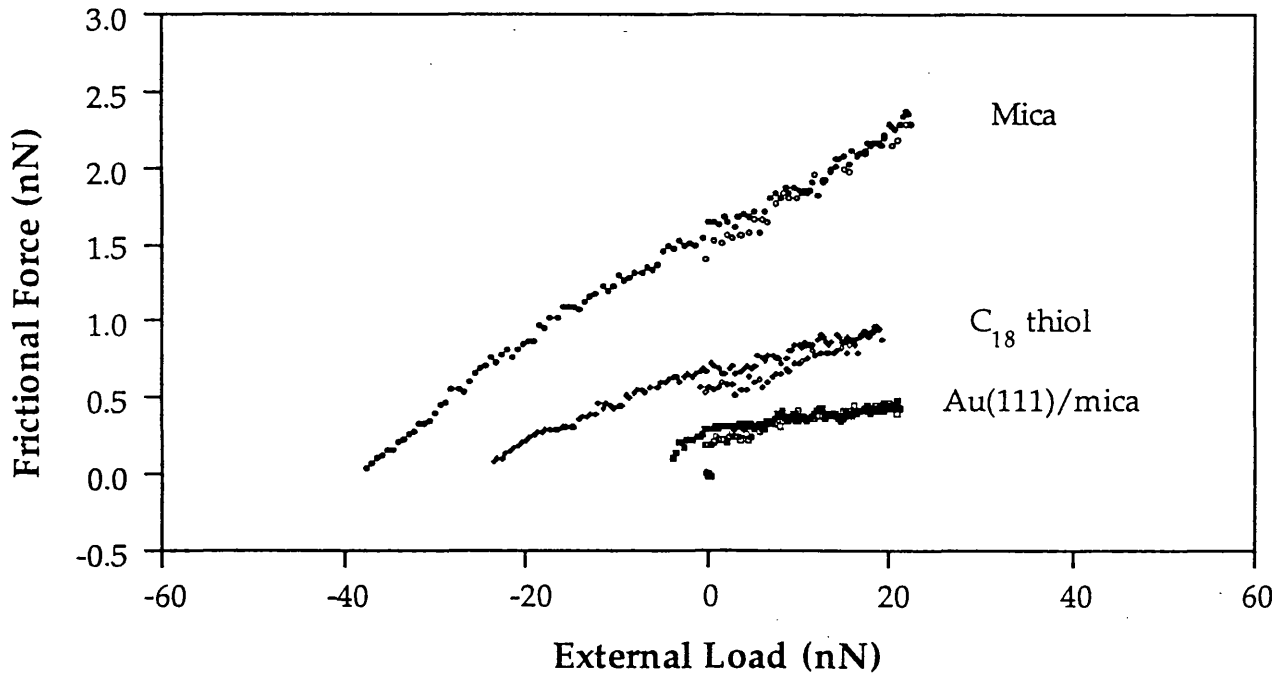

Figure 8.6. Friction *vs.* load curves obtained for Au(111)/mica and C_{18} alkylthiol monolayers on Au(111)/mica. A curve for mica is also shown as a reference. The load was limited to values that did not cause any damage on the layers being probed. All curves were obtained with the same silicon nitride lever, with an estimated force constant of 0.34 N/m (k^{nom}=0.58 N/m). Approach and retract branches are shown as open and filled symbols, respectively.

References

[1] A. Ulman, *An Introduction to Ultrathin Organic Films: from Langmuir-Blodgett to Self-Assembly*, (Academic Press, San Diego, 1991).

[2] O. A. Aksipetrov, M. M. Akmediev, E. D. Mishina, V. R. Novak, *JEPT*, **37**, 207 (1983).

[3] N. Carr, M. J. Goodwin, *Makromol. Chem. Rapid Comm.*, **8**, 487 (1987).

[4] F. Kajzar, J. Messier, *Thin Solid Films*, **132**, 11 (1985).

[5] T. Hasegawa, K. Ishikawa, T. Kanetake, T. Koda, T. Takeda, H. Kobayashi, K. Kubodera, *Chem. Phys. Lett.*, **171**, 239 (1990).

[6] S. Baker, G. G. Roberts, M. C. Petty, *Proc. IEE Part I*, **130**, 260 (1983).

[7] W. M. Reichert, C. J. Bruckner, J. Joseph, *Thins Solid Films*, **152**, 345 (1987).

[8] M. Aizawa, M. Matsuzawa, H. Shinohara, *Thin Solid Films*, **160**, 463 (1988).

[9] A. Barraud, *Thin Solid Films*, **99**, 317 (1983).

[10] S. W. J. Kuan, C. W. Frank, Y. H. Yen Lee, T. Eimori, D. R. Allee, R. F. W. Pease, R. J. Browning, *J. Vac. Sci. Technol. B*, **7**, 1745 (1989).

[11] J. Huang, D. A. Dahlgren, J. C. Hemminger, *Langmuir*, **10**, 626 (1994).

[12] F. P. Bowden, D. Tabor, *The Friction and Lubrication of Solids*, (Oxford University Press: London, 1968).

[13] T. Miyamoto, I. Sato, Y. Ando, in *Tribology and Mechanics of Magnetic Storage Systems*, B. Bushan, N. S. Eiss edts., 1988.

[14] B. Bushan, B. K. Gupta, *Handbook of Tribology: Materials, Coatings and Surface Treatments*, (McGraw-Hill: New York, 1991).

[15] M. Suzuki, Y. Saotome, M. Yanagisawa, *Thin Solid Films*, **60**, 453 (1988).

[16] E. Ando, Y. Goto, K. Morimoto, K. Ariga, Y. Okahata, *Thin Solid Films*, **180**, 287 (1989).

[17] J. Ruhe, V. J. Novotny, K. K. Kanazawa, T. Clarke, G. B. Street, *Langmuir*, **9**, 2383 (1993).

[18] H. Zarrad, P. Clechet, M. Belin, C. Martelet, N. Jaffrezic-Renault, *J. Micromech. Microeng.*, **3**, 222 (1993).

[19] B. Bhushan, V. N. Koinkar, *J. Appl. Phys.*, **75**, 5741 (1994).

[20] B. Bhushan, A. V. Kulkarni, V. N. Koinkar, M. Boehm, L. Odoni, C. Martelet, M. Belin, *Langmuir*, **11**, 3189 (1995).

[21] R. G. Nuzzo, D. L. Allara, *J. Am. Chem. Soc.*, **105**, 4481 (1983).

[22] C. D. Bain, E. B. Troughton, Y.-T. Tao, J. Evail, G. M. Whitesides, R. G. Nuzzo, *J. Am. Chem. Soc.*, **111**, 321 (1989).

[23] M. D. Porter, T. B. Bright, D. L. Allara, C. E. D. Chidsey, *J. Am. Chem. Soc.*, **109**, 3559 (1987).

[24] S. D. Evans, A. Ulman, *Chem Phys. Lett.*, **170**, 462 (1990).

[25] R. G. Nuzzo, L. H. Dubois, D. L. J. Allara, *J. Am. Chem. Soc.*, **112**, 558 (1990).

[26] R. G. Nuzzo, F. A. Fusco, D. L. J. Allara, *J. Am. Chem. Soc.*, **109**, 2358 (1987).

[27] C. E. D. Chidsey, D. N. Loiacono, *Langmuir*, **6**, 87 (1990).

[28] L. H. Dubois, B. R. Zegarski, R. G. Nuzzo, *J. Chem. Phys.*, **98**, 678 (1993).

[29] C. E. D. Chidsey, G.-Y. Liu, P. Rowntree, G. Scoles, *J. Chem. Phys.*, **91**, 4421 (1989).

[30] L. Strong, G. M. Whitesides, *Langmuir*, **4**, 546 (1988).

[31] N. Camillone, C. E. D. Chidsey, G.-Y. Liu, G. Scoles, *J. Chem. Phys.*, **98**, 3503

(1993).

[32] P. Fenter, P. Eisenberger, K. S. Liang, *Phys. Rev. Lett.*, **70**, 2447 (1993).

[33] P. Fenter, A. Eberhardt, P. Eisenberger, *Science*, **266**, 1216 (1994).

[34] M. S. Yeganeh, S. M. Dougal, R. S. Polizzotti, P. Rabinowitz, *Phys. Rev. Lett.*, **74**, 1811 (1995).

[35] C. A. Widrig, C. A. Alves, M. D. Porter, *J. Am. Chem. Soc.*, **113**, 2805 (1991).

[36] Y.-T. Kim, A. J. Bard, *Langmuir*, **8**, 1096 (1992).

[37] X. Gao,Y. Zhang, M. J. Weaver, *J. Phys. Chem.*, **96**, 4156 (1992).

[38] R. L. McCarley, Y.-T. Kim, A. J. Bard, *J. Phys. Chem.*, **97**, 211 (1993).

[39] D. Anselmetti, A. Baratoff, H.-J. Güntherodt, E. Delamarche, B. Michel, Ch. Gerber, H. Kank, H. Wolf, H. Ringsdorf, *Europhysics Lett.*, **7**, 365 (1994).

[40] G. E. Poirier, M. J. Tarlov, *Langmuir*, **10**, 2853 (1994).

[41] G. E. Poirier, M. J. Tarlov, H. E. Rushmeier, *Langmuir*, **10**, 3383 (1994).

[42] S. J. Stranick, A. N. Parikh, Y.-T. Tao, D. L. Allara, P. S. Weiss, *J. Phys. Chem.*, **98**, 7636 (1994).

[43] S. J. Stranick, A. N. Parikh, D. L. Allara, P. S. Weiss, *J. Phys. Chem.*, **98**, 11136 (1994).

[44] C. A. Alves, E. L. Smith, M. D. Porter, *J. Am. Chem. Soc.*, **114**, 1222 (1992).

[45] J. Pan, N. Tao, S. M. Lindsay, *Langmuir*, **9**, 1556 (1993).

[46] M. Salmeron, G. Neubauer, A. Folch, M. Tomitori, D. F. Ogletree, P. Sautet, *Langmuir*, **9**, 3600 (1993).

[47] G.-Y. Liu, M. B. Salmeron, *Langmuir*, 10, 367 (1994).

[48] U. Dürig, O. Züger, B. Michel, L. Häussling, H. Ringsdorf, *Phys. Rev. B*, **48**, 1711 (1993).

[49] S. A. Joyce, R. C. Thomas, J. E. Houston, T. A. Michalske, R. M. Crooks, *Phys. Rev. Lett.*, **68**, 2790 (1992).

[50] J. Hautmann, M. L. Klein, *J. Chem. Phys.*, **93**, 7483 (1990).

[51] A. Ulman, N. Tillman, J. Eilers, *Langmuir*, **5**, 1147 (1989).

[52] H. Sellers, A. Ulman, Y. Shnidman, J. E. Eilers, *J. Am. Chem. Soc.*, **115**, 9389 (1993).

[53] N. Camillone, C. E. D. Chidsey, G.-Y. Liu, T. M. Putvinski, G. Scoles, *J. Chem. Phys.*, **94**, 8493 (1991).

[54] C. E. D. Chidsey, D. N. Loiacono, *Langmuir*, **6**, 682 (1990).

[55] L. H. Dubois, B. R. Zegarski, R. G. Nuzzo, *J. Am. Chem. Soc.*, **112**, 570 (1990).

[56] E. L. Smith, C. A. Alves, J. W. Anderegg, M. D. Porter, *Langmuir*, **8**, 2707 (1992).

[57] O. Levine, W. A. Zisman, *J. Phys.. Chem.*, **61**, 1068 (1957) and references therein.

[58] R. M. Overney, E. Meyer, J. Frommer, H.-J. Güntherodt, M. Fujihira, H. Takano, Y. Gotoh, *Langmuir*, **10**, 1281 (1994).

[59] H. Takano, M. Fujihira, *J. Vac. Sci. Technol. B*, **14**, 1272 (1996).

[60] M. Fujihira, Y. Morita, *J. Vac. Sci. Technol. B*, **12**, 1609 (1994).

[61] X.-D. Xiao, J. Hu, D. H. Charych, M. Salmeron, *Langmuir*, **12**, 235 (1996).

[62] E. B. Troughton, C. D. Bain, G. M. Whitesides, R. G. Nuzzo, D. L. Allara, M. D. Porter, *Langmuir*, **4**, 365 (1988).

[63] Q. Du, X.-D. Xiao, D. H. Charych, F. Wolf, P. Frantz, Y. R. Shen, M. Salmeron, *Phys. Rev. B*, **51**, 7456 (1995).

[64] K. L. Johnson, K. Kendall, A. D. Roberts, *Proc. Royal. Soc. London A*, **321**, 301 (1971).

[65] A. Fogden, L. R. White, *J. Colloid. Interf. Sci.*, **138**, 414 (1990).

[66] D. D. Koleske, W. R. Barger, G. U. Lee, R. Colton, *Thin Solid Films*, in press.

[67] T. Smith, *J. Colloid and Interf. Sci.*, **75**, 51 (1980).

Chapter 9

An AFM Study of the Pressure Dependent Structural and Frictional Properties of n-Octadecylthiol on Au(111)

9.1 Introduction

As introduced in chapter 8, self-assembled monolayers can be used to understand basic tribological issues. Pressures accessible by other techniques, such as SFA and NLO, are at present limited to about 100 MPa. On the other hand, in macroscopic experiments typical forces of a few Newtons are applied, with real contact areas of the order of 10^{-5} cm^2, producing contact pressures in the GPa range. In AFM experiments, the pressures applied between the tip and the surface range from a few tens MPa to a few GPa. Furthermore, in AFM the contact occurs over a single asperity. Therefore, AFM allows one to investigate a range of pressures not accessible to other techniques and without the drawback of multiasperity contact. It should be remembered once more however, that the tip geometry is difficult to control and that AFM results are not quantitative at the moment.

In the study presented in this chapter, the mechanical response of self-assembled monolayers of n-octadecylthiols (C_{18}) on Au(111) was investigated. As already described in the previous chapter, this type of layers has been widely characterized by a variety of techniques. Furthermore, their behavior under high pressures has been the subject of a few simulations.[1, 2, 3] Therefore, they represent an ideal model system for this type of studies.

Previous AFM experiments have shown that SAMs of docosylthiol (C_{22}) act as a 'cushion' for Au substrates, even beyond the plastic limit of Au, when sufficiently 'blunt' tips (radius of curvature>1,000 Å) are used.[4] Later studies showed that when using sharper tips (tip radius ≈700-1,000 Å) a reversible transition from the thiol $\left(\sqrt{3}x\sqrt{3}\right)R30^o$ to the Au(111) periodicity takes place under loads of 250 to 300 nN.[5] Because no wear of the organic layer could be observed upon reduction of the load, it was proposed that the molecules were reversibly 'displaced' from under the tip.

In an attempt to further investigate the nature and molecular mechanisms of

the above 'transition', several in depth experiments were performed on C_{18} monolayers, as described in this chapter. For these experiments sharpened tips with k^{nom}=0.5 N/m were used. In particular, the tip height during the transition and frictional force through the transition were measured.

9.2 Results

9.2.1 Topographic Mode Images

Figure 9.1 (a) is a topographic mode image of a C_{18} layer taken at low load (0.5 nN in this case). This image and the corresponding 2D-FFT spectra (figure 9.1 (b)) show an hexagonal periodicity (lattice constant 5.0±0.3 Å) similarly to that already shown in figure 8.1. Figure 9.1 (c) and (d) show that when the load is increased and reaches a critical value a new periodicity is observed in the AFM images. The lattice appears to be rotated $29^{o} \pm 1^{o}$ with respect to the low load image (C_{18}) and the lattice constant is 2.9±0.2 Å. Such a periodicity corresponds to the nearest-neighbor distance for the (1x1) structure of Au(111). These experiments therefore provide an *in situ* determination of the relationship between the thiol and Au(111) lattice. Similar experiments performed on bare Au(111) with tips of similar radius showed that the Au surface responds elastically to forces in this range, so the observed structural transition takes place below the elastic limit of gold.

As the load is decreased, the thiol periodicity is recovered (figure 9.1 (e) and (f)) and no visible permanent damage of the layer occurs.[5] In fact, large scale topographic images taken at low load after the transition did not reveal any holes or accumulation of material. However, as seen from figure 9.1 (e), molecular scale AFM images taken at low load after the transition are not as sharp as prior to it and the corresponding Fourier transform peaks (figure 9.1 (f)) are typically broadened by 30-60% and reduced in intensity by ≈20-40%.

The transition from the $\left(\sqrt{3}x\sqrt{3}\right)R30^{o}$ to the (1x1) periodicity is not abrupt. In fact, several consecutive scans are required to reveal the Au(111) lattice (figure 9.2). An analysis of the intermediate scans shows that the thiol and Au(111) lattices co-exist in different parts of the images, as seen in the image Fourier power spectra (figure 9.2 (b), (d) and (f)).

To investigate further the nature of this transition, the following experiment was performed. An area was scanned at increasing load until the transition was observed to occur at ≈23 nN , then the tip was moved to a new area and several consecutive images were acquired at a load of ≈17 nN. In this case, the thiol

Figure 9.1 (following page). Frictional force images (a, c, e) and corresponding Fourier power spectra (b, d, f) obtained in topographic mode on a C_{18} thiol layer showing the $\left(\sqrt{3}x\sqrt{3}\right)R30^{o}$ to 1x1 transition. The tip used had a radius ≈150 Å. Scale bars=5 Å.

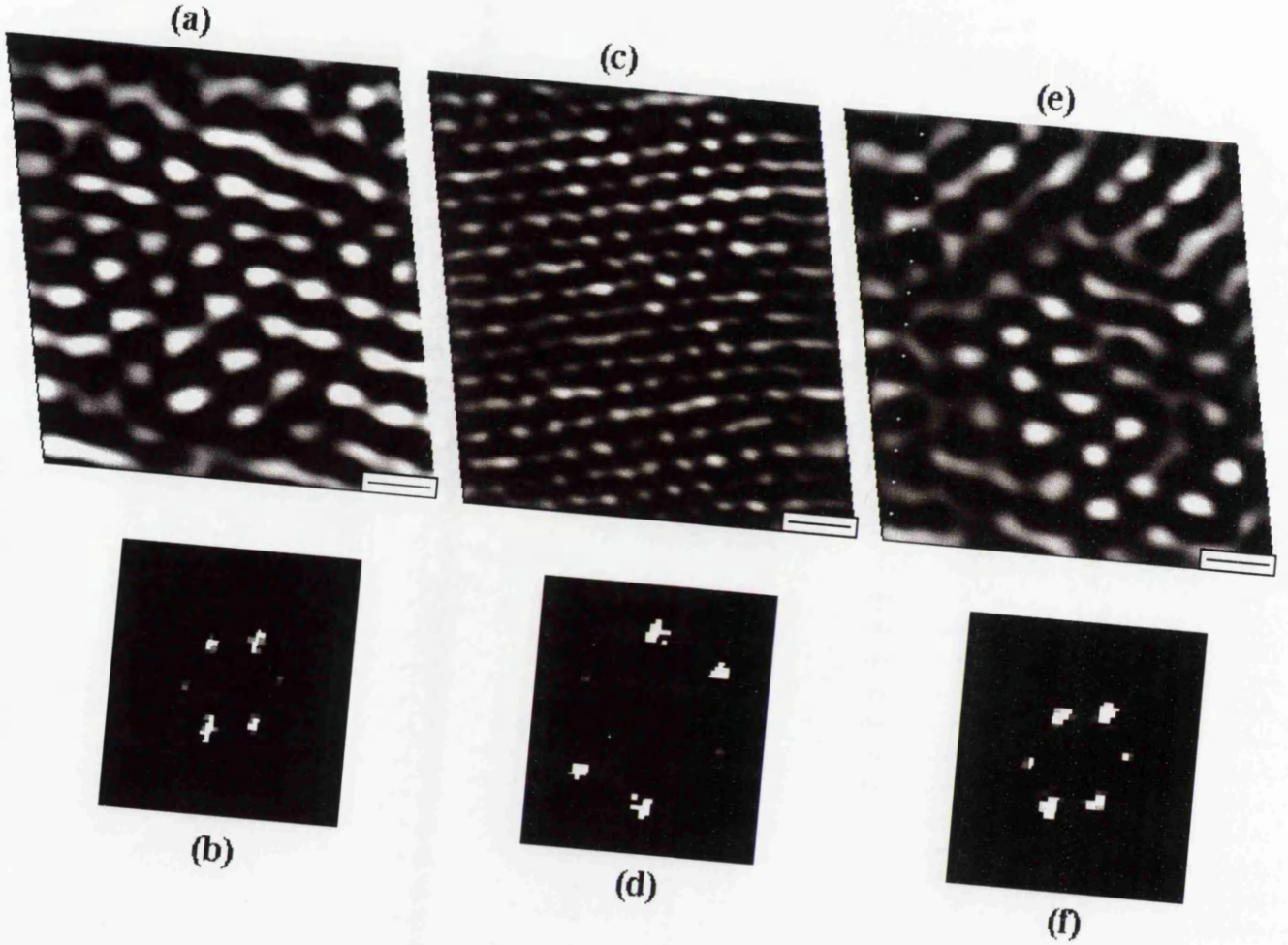
(a)
(c)
(e)
(b)
(d)
(f)

$(\sqrt{3}x\sqrt{3})R30^{o}$ periodicity is observed after multiple scans (figure 9.3 (a), (c)). The spots in the corresponding Fourier images (figure 9.3 (b), (d)) were broadened by ≈60%, consistent with the real-space images.

After increasing the load to ≈21 nN, the AFM images and corresponding Fourier images gradually became disordered (figure 9.3(e)-9.3 (h)). However, a 1x1 lattice was not observed even after multiple image scans. The Au 1x1 lattice was revealed only after increasing the load once again to ≈23 nN. The critical load F_c required to initiate the structural transition is rather well defined for a given tip.

9.2.2 Measurement of the Tip Height during the $(\sqrt{3}x\sqrt{3})R30^{o}$ to 1x1 Transition

In order to understand better the nature of the transition, the vertical displacement of the tip during the transition was monitored. Under normal operating conditions this is difficult to do since the thermal drift in z of the AFM used for these experiments is ≈0.1 Å/sec. Furthermore, piezo creep effects cause changes in z after a change in applied load. To minimize these effects, the microscope was set at the critical load of ≈23 nN and left at the desired position on the sample for several hours to reach thermal equilibrium. These precautions reduced the drift rate by almost an order of magnitude. A small shift to a new area was then made before collecting data.

The y scanning range was set to zero so that the same horizontal x line was repeatedly scanned by the AFM tip while the feedback loop maintained the load constant. Topographic data was recorded for 24 consecutive images for a total time of 196.8 secs. The Z data corresponding to each x scan line of the images were averaged together and plotted as a function of time (figure 9.4). As can be seen from the plot, the value of Z is constant for the first ≈20 secs and then starts to decrease monotonically until a first plateau is reached after ≈80 secs. At this point the decrease in Z is about 18 Å. The tip remains constant at that height for ≈45 secs then decreases again for an overall change in Z of 24 Å, after which no further changes were observed.

The thickness of the SAM, assuming an *all-trans* conformation of the alkyl chains and a tilt of 30° from the surface normal, is about 26 Å. Therefore, the tip-surface separation decreases by approximately the monolayer thickness during the transition, which is consistent with a displacement of the molecules in the tip-surface gap.

Figure 9.2 (following page). The evolution of frictional force images and corresponding Fourier power spectra obtained while scanning at the critical load, 30 nN in this case. The tip used in this experiment had a radius of ≈230 Å. The first, fourth and seventh scan of the series are shown. Scale bars=5 Å. The $\left(\sqrt{3}x\sqrt{3}\right)R30^{o}$ to 1x1 transition is not abrupt. In fact, several scans, seven in this particular experiment, are needed to reveal the Au lattice. At intermediate scans, both the thiol and Au lattices are present in different regions of the images. This is particularly clear in the Fourier plots, where the larger hexagon corresponds to the Au periodicity and the smaller one to the C_{18} overlayer.

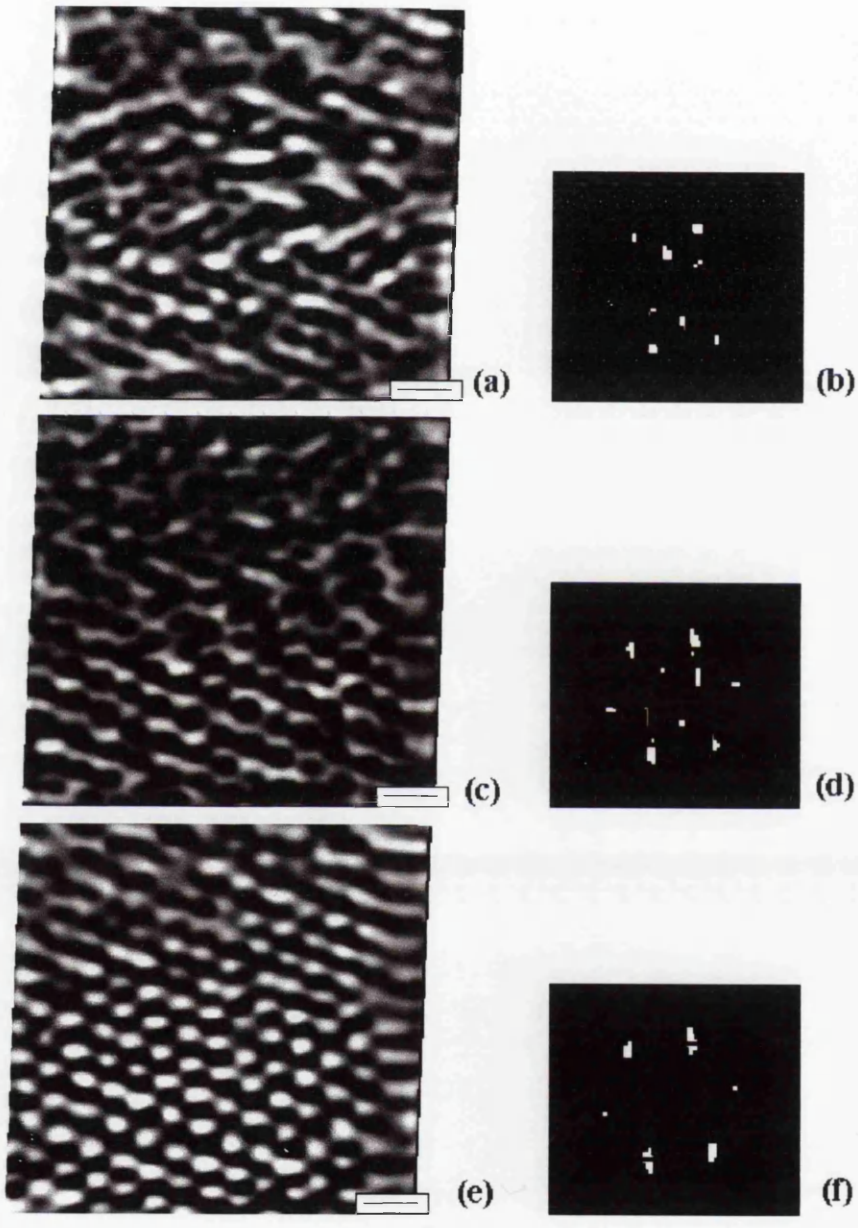
(a)
(b)
(c)
(d)
(e)
(f)

Figure 9.3 (following page). Part of a series of frictional force images and corresponding Fourier spectra obtained while approaching the critical load, 23 nN in this experiment. Ten scans were made at 17 nN, then the load was increased to 21 nN. Scale bars=20 Å. At 6 nN below F_c, the images reveal the thiol periodicity. The FWHM of the Fourier peaks were broadened by 30-60% between the second and ninth scans, indicating changes in the degree of ordering of the chains. At 2 nN below F_c, the AFM images and corresponding Fourier peaks became gradually disordered.

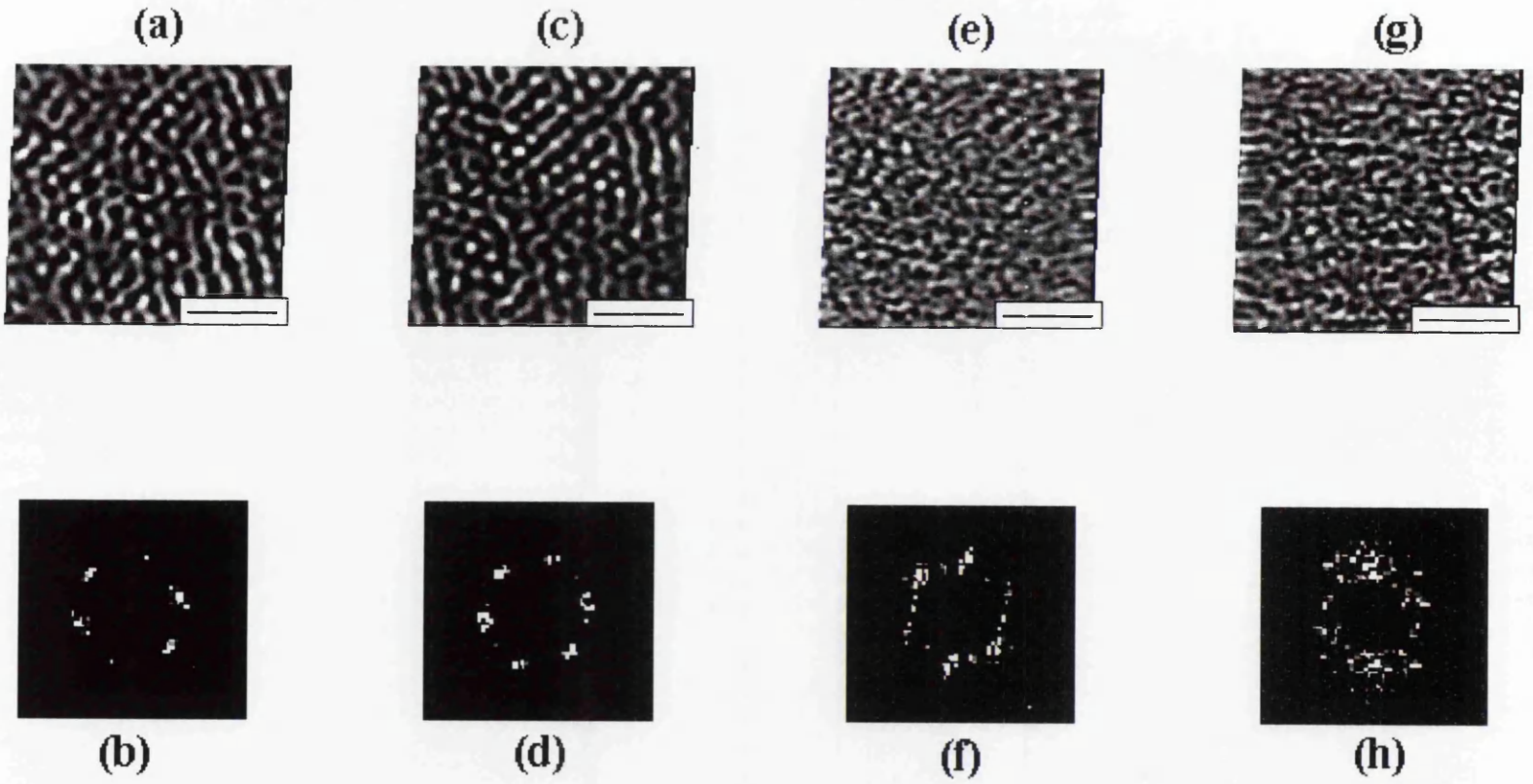
(a)
(c)
(e)
(g)
(b)
(d)
(f)
(h)

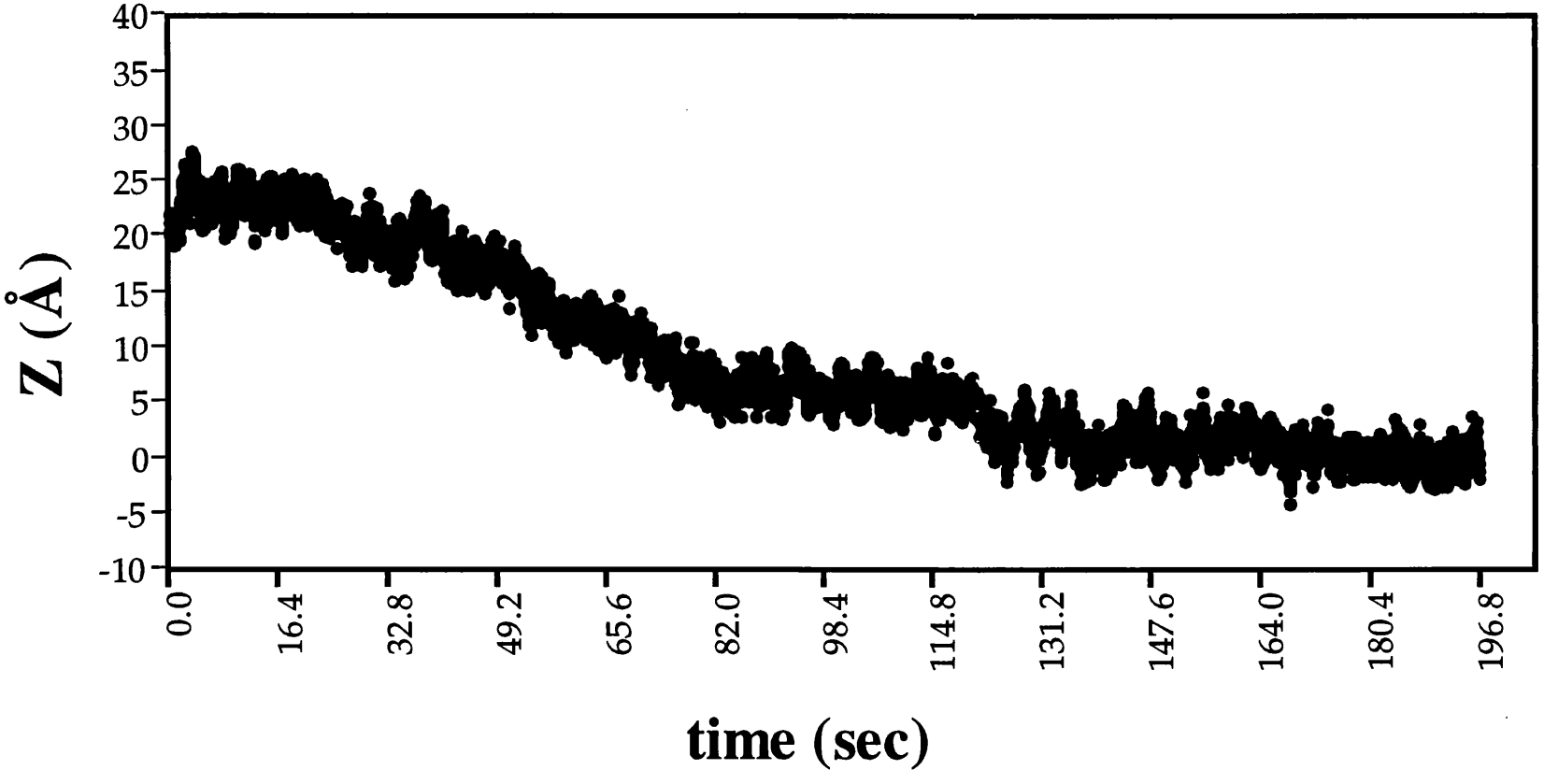

Figure 9.4. Feedback signal Z measured as a function of time at the critical load, 23 nN in this experiment. The data corresponds to 24 consecutive images where the tip was scanned in the x direction only, for a total time of 196.8 secs. Each point in the graph represents the averaged Z value from a single line. The graph shows that the decrease in z between the initial and final positions is about 24 Å, i.e. one C_{18} layer thickness.

9.2.3 Friction Measurements

Figure 9.5 (a) shows a friction *vs.* load curve obtained with a tip of radius ≈200 Å. The estimated lever normal force constant is 0.62 N/m. In this case the critical transition load was 23 nN. The frictional force increases for loads up to the critical value until the onset of the transition, where a significant change is observed (marked by T in figure 9.5 (a)). Beyond this point, the frictional force either fluctuated with increasing load, as in figure 9.5 (a), or decreased first and then stabilized (not shown). Similar behavior was observed as the load was decreased. A small amount of hysteresis was noted between the approach and retract branches.

Figure 9.5 (b) shows the frictional force plotted as a function of load for a C_{18} thiol layer as measured by a tip with a radius of ≈500 Å. The estimated normal force constant for this lever is 0.34 N/m. No transition could be observed with this tip for the range of loads investigated. As the tip radius is ≈2.5 times larger than the case of 9.5 (a), approximately six times more force, or ≈160 nN, would be required to reach the pressure corresponding to the transition in 9.5 (a). The required piezo extension of ≈400 nm exceeded the range available with this AFM. The shape of the curve in 9.5 (b) is generally similar to the pre-transition region of 9.5 (a). Some hysteresis can also be seen. The pull-off force in 9.5 (b) is larger than in 9.5 (a), and the change in the friction slope just before pull-off in 9.5 (a) is not seen in 9.5 (b).

The frictional forces shown in figure 9.5 (a) are about three times larger than those shown in 9.5 (b) for equivalent loads, even though the contact area at a given load for the sharp tip of 9.5 (a) should be a little less than half that of the blunter tip used for 9.5 (b). This means that the friction per unit contact area at a given load is significantly greater for sharp tip than for blunt tips. Although the numerical values are based on estimated force constants and approximate tip radii, the author does not think that the numerical uncertainties can account for a six-fold difference in lateral forces. Instead the shear force per unit area must increase with pressure. Pressure dependent shear forces have been reported for Langmuir-Blodgett films.[6] In the case of figure 9.5 (b), the retract branch is found to be a good fit to the 2/3 power of effective load predicted by the Hertz model. From this the tip-sample interfacial shear strength can be estimated to be about 400 MPa.

Figure 9.6 shows the frictional force measured in consecutive images for loads close to the critical load. Each point in the graph represents the average frictional force over an image. The friction increases during the first 8 images at 17 nN (circles). During this time the $\left(\sqrt{3}x\sqrt{3}\right)R30^{o}$ periodicity of the thiol layer is seen, but with increasingly broadened Fourier peaks. The next 10 images at 21 nN

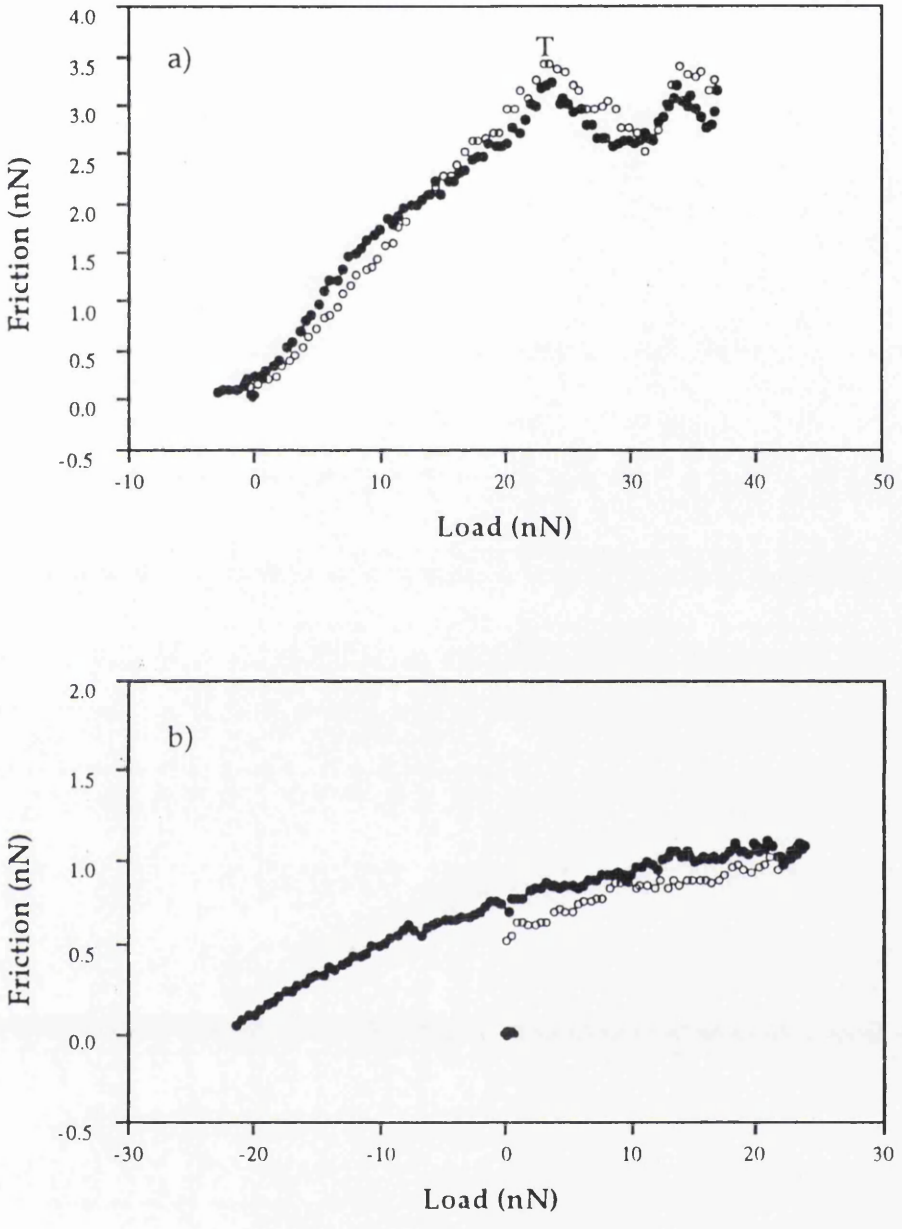

Figure 9.5. (a) Frictional forces measured through the transition from the thiol to the Au 1x1 lattice. The critical load F_c was 23 nN in this experiment (tip radius ≈200 Å). (b) Frictional forces measured with a blunter tip (tip radius ≈500 Å) well below the critical load. Curve (a) shows that the transition is characterized by changes in the frictional force. No similar behavior is observed when blunter tips are used and the transition does not occur. Approach and retract branches are shown as empty and filled symbols, respectively.

(squares) were disordered. The transition occurs during the following 8 images at 23 nN (diamonds) and the frictional force decreases as the 1x1 periodicity becomes visible. The friction is approximately constant during the final 4 images at 24.5 nN after the transition and the 1x1 periodicity is still visible.

9.3 Discussion

9.3.1 The $\left(\sqrt{3}\times\sqrt{3}\right)R30^\circ$ to 1x1 Transition

The critical load F_c that induces the $\left(\sqrt{3}x\sqrt{3}\right)R30^o$ to 1x1 structural transition clearly depends on the AFM tip radius. F_c was ≈14 nN for the ≈15 nm radius tip used in figure 9.1, and ≈23 nN for the ≈20 nm tip in 9.5 (a). An estimate of the pressures involved in the experiments reported in this chapter can be obtained from one of the contact mechanics models described in chapter 3. If friction is proportional to the contact area, the JKR model makes the specific prediction that the friction at pull-off should be 40% of the friction at zero external load.[7] This is certainly not the case in the data of 9.5 (b) and may not be in 9.5 (a). From the pull-off force of 9.5 (a) the interfacial energy for the tip-surface contact is ≈34 mJ/m^2, which is consistent with a van der Waals interaction. This yields a value for the parameter μ defined in section 3.2.2 of 0.095, therefore in the DMT regime. In 9.5 (b) the pull-off force is much larger and there seems to be a substantial capillary contribution in addition to the van der Waals term. For these reasons, a 'shifted Hertz' model will be used to estimate contact areas and pressures. The images in figure 9.2 (a) were acquired at an external load of ≈0.5 nN with a tip of ≈15 nm radius and a pull-off force of ≈2.5 nN. The shifted Hertz model would predict a contact radius of ≈0.83 nm corresponding to ≈10 molecules present in the contact and a mean contact pressure of 1.4 GPa. This estimate does not consider the modifications to the contact problem introduced by an elastic layer, the thiol molecules, on an elastic substrate, the gold film[8] - not only are the elastic properties of this layer difficult to characterize, but the stress-strain relation for the confined layer is probably not linear under the conditions of these experiments. A pressure of about 2.3 GPa is obtained at the transition load, with ≈30 (figure 9.1) to ≈50 (figure 9.5 (a)) molecules involved in the contact. In general, for the tips used in this study the critical load was found to be in the 10-40 nN range, or ≈0.5 nN/molecule. In earlier experiments when blunter tips were used (tip radius 700-1000 Å) F_c was ≈250-300 nN.[5] This is consistent with a critical load that scales with tip radius squared. In figure 9.5 (b), the maximum effective load of ≈45 nN and tip radius

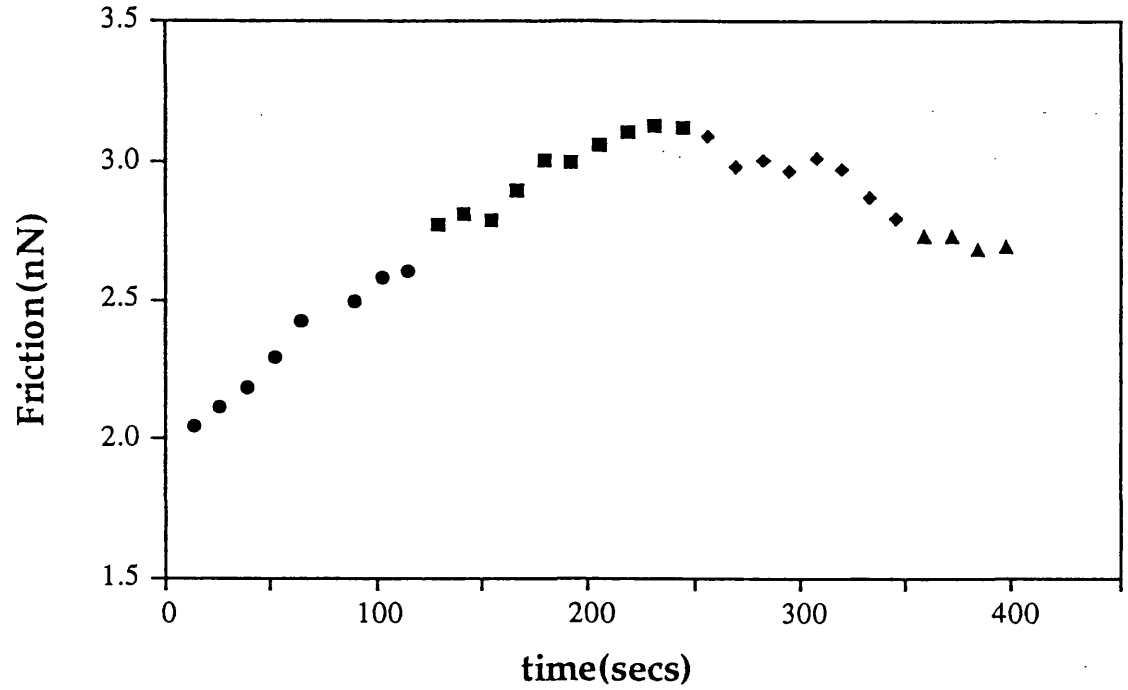

Figure 9.6. Frictional force measured for a number of sequential images at loads close to F_c (23 nN in this case). Each point in the graph is the average frictional force measured in a complete image. Load: 17 nN, circles; 21 nN, squares; 23 nN, diamonds; 24.5 nN, triangles. Except that for the points acquired at 24.5 nN, the frictional force is not constant for fixed values of the load. It increases for loads lower than F_c and decreases at F_c. This behavior is consistent with numerous defects being created in the chains, which provide modes through which energy can be dissipated (loads lower than F_c) and a decrease in the number of dissipative modes after the transition, when the tip is in contact with the Au substrate.

≈50 nm correspond to a mean pressure of ≈1.5 GPa, and the predicted critical load, which was not reached experimentally, would be ≈160 nN.

The energy associated with a single *gauche* defect (2.9 kJ/mol) is comparable to the thermal energy at room temperature (2.5 kJ/mol), so that little energy has to be spent to overcome this barrier.[9] In these conditions, the AFM images show the long-range order of the alkyl chains. As the load and the pressure increase and approach the critical value, more numerous defects are probably formed in the alkyl chains and the AFM images become gradually disordered. The binding energy of the sulfur headgroup to gold is ≈184 kJ/mol[10] and the packing energy of the C_{18} layer is ≈117 kJ/mol.[11] From the calculations of Siepmann and McDonald[1] the "spring constant" of a single thiol molecule can be estimated to be 3 N/m (E≈36 GPa). At the transition load of ≈0.5 nN per molecule, the elastic energy is ≈25 kJ/mol. It seems plausible that the alkyl chains are being "melted" and disordered under the pressure applied by the AFM tip. Displacing the molecules under the tip will lead to a compression or increase in molecular density and strain energy in the region around the tip, which will be greater for a blunt tip than for sharp tips. If the molecules were desorbed it seems likely that the transition would be irreversible. A simplified model[12] predicts a radius dependent transition force, and that tips with radii >100 nm will reach the plastic limit of gold before displacing the molecules.[4]

Finally, when the pressure is released, the layer "heals itself" and the initial configuration is recovered almost entirely. The images taken at low load after displacement are normally less well ordered. This is particularly apparent in the image Fourier transforms in which the spots have significantly broadened, indicating reduced domain size or imperfect packing in the molecular layer.

These observations are in general agreement with molecular dynamic simulations that predict disordering of a C_{16} thiol under the pressure from a sharp tip or asperity[2] and with Monte Carlo calculations which predict a concentration of gauche defects at the methyl end of the hydrocarbon chains as increasingly high pressures are applied.[1] No evidence could be seen however for a change from hexagonal to oblique molecular packing under pressure, as was found in a molecular dynamic simulation upon compression by a flat surface.[3]

9.3.2 Friction Measurements

For pressures near the transition threshold, the thiol layer is not reducing friction, but rather increasing the work done in moving the tip across the surface. The tip-surface pressure is high enough to create defects in the thiol molecules. After the tip moves on, the molecules relax and energy is dissipated. The frictional force in figure 9.5 (a) near the transition is ≈3 nN for ≈50 molecules, so the work done in

moving the tip would correspond to ≈18 kJ/mol if all the energy were dissipated in the thiol layer. The friction and energy dissipation increase in successive scans at the same load near the transition as the degree of disorder increases, as shown in figure 9.6. This effect is similar to that observed for friction versus chain length for self-assembled layers of alkylthiols on Au(111), as described in detail in chapter 8. In fact, there the friction was higher for shorter chain, more disordered molecular layers than for the better ordered, longer chain overlayers.

It is important to remember that in most AFM friction experiments where load is varied, and in all the experiments presented here, the load is changed by decreasing the tip-sample distance to bend the cantilever. For instrumental reasons, the levers are mounted at an angle of 15 to 20 degrees relative to the horizontal. A 10 nN change in force for a 0.62 N/m lever requires a 16 nm change in z, and the lever tilt means that the tip will also move across the sample by ≈4 nm, i.e. by a distance comparable to the tip-sample contact diameter. This implies that unlike macroscopic friction experiments, the AFM measurements are not conducted in the same "track". This fact should be considered when interpreting friction data where surface modification is taking place, and may account for the fluctuations in friction observed above the transition load.

At the transition load, significant changes occur as can be seen in figures 9.5(a) and 9.6. While the details of the frictional behavior above F_C vary from case to case, the frictional force always drops at the transition. Once enough molecules are displaced for the friction stick-slip to be in registry with the Au lattice, the friction decreases, even though the load and tip-surface contact area have increased.

9.4 Summary and Conclusions

AFM has been used to study the response of C_{18} alkylthiol monolayers to pressures from few hundred MPa to a few GPa. AFM images show the long-range order of the alkyl chains, revealing the $\left(\sqrt{3}x\sqrt{3}\right)R30^o$ periodicity. The molecular packing lattice is resolved with relatively sharp tips at mean contact pressures up to ≈1.5 GPa. As pressure increases the AFM images of the thiol lattice become increasingly disordered. At a well defined pressure of ≈2.3 GPa the Au(111) 1x1 lattice periodicity is observed while the tip-sample spacing decreases by approximately the thickness of the thiol layer. It is proposed that the thiol molecules are reversibly 'squeezed' out from under the tip while remaining in contact with the gold surface. When the pressure is reduced the $\left(\sqrt{3}x\sqrt{3}\right)R30^o$ thiol lattice

is observed again. Image Fourier transform have broader spots, indicating that the domain size in the molecular overlayer may be reduced, but large area low pressure AFM images show no signs of surface debris or of holes in the thiol layer. Friction first increases near the transition then drops above the critical pressure.

References

[1] J. I. Siepmann, I. R. McDonald, *Phys. Rev. Lett.*, ***70*** , 453 (1993).

[2] K. J. Tupper, R. J. Colton, D. W. Brenner,*Langmuir*, **10**, 2041 (1994).

[3] K. J. Tupper, D. W. Brenner, *Langmuir*, **10**, 2335 (1994).

[4] M. Salmeron, G. Neubauer, A. Folch, M. Tomitori, D. F. Ogletree, P. Sautet, *Langmuir*, **9**, 3600 (1993).

[5] G.-Y. Liu, M. B. Salmeron, *Langmuir*, **10**, 367 (1994).

[6] B. J. Briscoe, D. C. Evans, *Proc. Roy. Soc. London A*, **380**, 389 (1982).

[7] K. L. Johnson, K. Kendall, A. D. Roberts, *Proc. Roy. Soc. London A*, **321**, 301 (1971).

[8] K. L. Johnson, *Contact Mechanics*, (Cambridge University Press: Cambridge, 1985), art. 5.8.

[9] A. Ulman, *Introduction to Ultrathin Organic Films. From Langmuir-Blodgett to Self-Assembly*; (Academic Press: San Diego; 1991).

[10] L. H. Dubois, R. G. Nuzzo, *Annu. Rev. Phys. Chem.*, **43**, 437 (1992).

[11] J. F. Nagle, *Faraday Discuss. Chem. Soc.*, **81**, 151 (1986).

[12] M. Salmeron, G.-Y. Liu, D. F. Ogletree, in *Forces in Scanning Probe Methods* , D. Anselmetti, E. Meyer, H.-J. Güntherodt edts., Nato ASI Series E: Applied Sciences Vol. 286 (Kluwer Academic Publishers: Dordrecht, 1995).

Chapter 10

Preparation and Characterization of Self-Assembled Alkylsilanes on Mica

10.1 Introduction

One of the most widely used methods for modifying chemically the surface of an inorganic surface for the past twenty five years has been through the reaction with silane agents. The general formula of an organosilane is $R_nSiX_{(4-n)}$, where R is an organic radical that can bear different functionalities and X a hydrolyzable group, such as alkoxy or chloride. The most commonly used alkoxy groups are methoxy (OCH_3) and ethoxy (OC_2H_5). Silanes can have one, two or three hydrolyzable groups and therefore be of the form $RSiX_3$, R_2SiX_2 or R_3SiX, with the most stable films been formed from the first of these three forms. Silane compounds have been shown to successfully react with many hydroxilated surfaces, such as glass, SiO_x, alumina and titania.[1, 2, 3] However, they can also be assembled on mica surfaces that present very few hydroxyl groups at their surface.[4, 5, 6, 7] The most commonly accepted reaction mechanism at hydroxilated surfaces has been for several years the following: in the absence of water, the X groups condense with hydroxyls on the support surface; in the presence of water, the X groups hydrolyze to silanol groups (–SiOH) which react with hydroxyls on the surface. Furthermore, in the presence of water and after hydrolysis of the X groups, silanes with more than one hydrolyzable group form oligomers due to the formation of siloxane bonds (Si–O–Si) between neighboring molecules. Upon heating of the samples, covalent bonds are formed between the molecules and the substrate. Therefore, the formation of self-assembled layers involves the formation of polysiloxane. The various steps of this reaction scheme are shown in figure 10.1. However, while it has been shown by x-ray photoelectron spectroscopy studies (XPS) that indeed all of the X groups react,[8] no evidence for the formation of siloxane bonds with the surface has been provided. On the contrary, a recent low-frequency IR study has shown that in the case of alkyltrichlorosilanes self-assembled on silica surfaces, few Si–O–Si bonds are formed.[9] These studies showed that, in the absence of water, there is no reaction of octadecyltrichlorosilane (OTS) molecules with the hydroxyls groups of silica surfaces. The introduction of water produced a mixture of partially

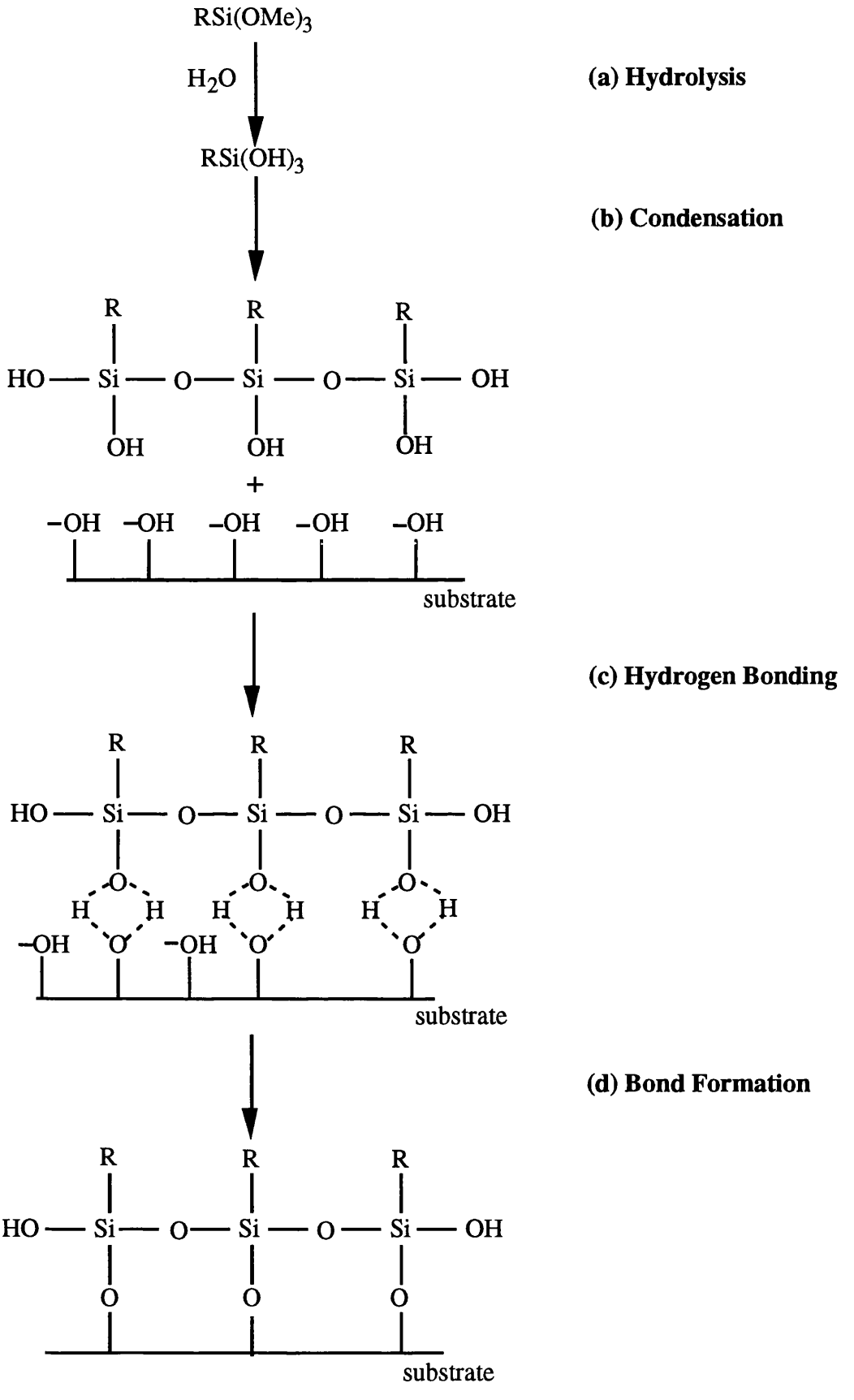

Figure 10.1. Schematic of deposition of silanes on hydroxilated surface (from reference 10).

hydrolyzed and partially polymerized species with hydrogen bonding formation between these species and hydroxyls groups on the surface, without occurrence of covalent binding.

In the case of mica, few hydroxyls groups, if any, are present at its surface. For this reason, methods have been developed to modify its chemical nature. Two of these methods involve pretreating mica by exposure to water vapor or sodium ethoxide to help introduce silanol groups.[6, 7] Another method involves pre-hydrolysis of the silane molecules followed by self-assembly and cross-linking onto the mica surface.[11] In all cases, the formation of covalent bonds between the silane molecules and the mica surface has not been established and in view of the studies cited above for alkyltrichlorosilanes on silica, covalent bonding seems unlikely.

Other methods of characterization used for self-assembled silanes in addition to IR are ellipsometry, contact angle, x-ray photoelectron spectroscopy, near edge x-ray absorption fine structure (NEXAFS) spectroscopy, x-ray reflection and grazing incidence diffraction, He-diffraction and, more recently, AFM. Most diffraction and spectroscopy were performed on long chain alkyltrichlorosilane layers on SiO_x substrates. Ellipsometry and x-ray reflectivity studies have shown that monolayers of methyl terminated octadecyltrichlorosilane (OTS) can be formed at SiO_x surfaces and the thickness is measured to be ≈25 Å.[8, 10 12, 13] FTIR and NEXAFS spectroscopy studies have also determined that the chains are well oriented, densely packed and mainly in an *all-trans* conformation. The chains are in an almost upright position with a mean molecular tilt of 10-15°, consistent with the measured value of film thickness.[14, 15, 16, 17] In contrast to their thiol counterparts, He-diffraction did not reveal any crystalline-like order at the methyl termination of n-octadecyltriethoxysilane (OTE) layers on mica down to 45K[10] and x-ray grazing incidence diffraction studies of octadecyltrichlorosilanes on SiO_x have indicated the existence of short-range liquid-like order.[18] An increase in structural disorder with decreasing chain length has also been observed, which has been attributed to an increased conformational disorder (*gauche* defects, kinks, etc.) in the hydrocarbon chains.[16] Previous AFM studies of OTE layers on mica did not detect any long-range order of the molecules either.[10, 5] Wettability studies on methyl terminated alkyltrichlorosilanes (CH_3–$(CH_2)_{n-1}$–$SiCl_3$) have shown that the measured water contact angle is largely independent of the chain length for n>5.[8] Although the reaction mechanism and kinetics are not fully explained yet, the general consensus is that, due to the tendency of silanes to polymerize, monolayers of alkylsilanes are less ordered (no long-range order, higher number of defects and/or pinholes) than self-assembled monolayers of thiols.

Applications of organosilanes range from uses as adhesion promoters of polymers to oxidized substrates,[19, 20] bonded phases in liquid and gas

chromatography,[21] coupling agents for protein immobilization[22] and boundary lubricants.[23, 24, 25, 26, 27, 28, 29] As part of this thesis work, silane layers were used for a variety of applications, as substrates for LB polymer deposition (see chapter 11), as coupling agents (see chapter 14) and their frictional and mechanical properties with respect to their chain length were investigated (this chapter). Furthermore, the comparison of layers formed by silane and thiols molecules of the same chain length, allows one to investigate how molecular order, different headgroup-substrate and interchain interactions affect frictional and mechanical properties of organic layers.

10.2 Materials and Methods

10.2.1 Materials

n-Octadecyltriethoxysilane (CH_3–$(CH_2)_{17}$–$Si(OC_2H_5)_3$, C_{18} or OTE), octanetrimethoxysilane (CH_3–$(CH_2)_7$–$Si(OCH_3)_3$, C_8 or OTMS), and hexanetrimethoxysilane (CH_3–$(CH_2)_5$–$Si(OCH_3)_3$, C_6 or HTMS) compounds were purchased from United Chemical Technologies, Inc. (Bristol, PA, USA). Dodecyltriethoxysilane (CH_3–$(CH_2)_{11}$–$Si(OC_2H_5)_3$, C_{12} or DTS) was purchased from TCI America, Inc. (Portland, OR, USA). The C_{18} silane was filtered through an 0.2 μm PTFE membrane prior to use. All other silanes were used as received. All alkylsilane materials were stored in a desiccator prior to use. House-distilled water was passed through a four-cartridge Millipore μQF purification train producing a resistivity of 18.2 MΩcm. Tetrahydrofuran (THF) and cyclohexane were spectroscopic quality. Glassware for preparation of prehydrolysis solution and for self-assembly was cleaned with chromic acid cleaning solution (Fisher Scientific). Mica chips were purchased from Asheville-Schoomaker Co. (Newport News, VA, USA) and cleaved just prior to exposure to silane solution.

10.2.2 Film Preparation Method

All silane films were prepared according to the following two-step method: 1) the methoxy or ethoxy groups were hydrolyzed to silanol groups; 2) self-assembly from cyclohexane solution. The procedure used is essentially the one used by Kessel and Granick,[10] however a few changes were made. Prehydrolysis solutions were prepared by dissolving 0.2 g of the appropriate silane in 24 mL of THF containing 0.2 g of 1N HCl. The solution was stirred at room temperature for 2-3 days. Before

further dilution of the solution for deposition onto mica, the prehydrolysis solution was filtered through 0.2 μm PTFE membrane. Following this treatment, the prehydrolysis solution (1.5-2.0 mL) was diluted with 25 mL of cyclohexane. The solution was added to cleaned Petri dishes containing freshly cleaved mica samples. The immersion time was a) 5 mins for C_{18}, b) 10 mins for C_{12} and C_8, c) 30 mins for C_6. Following deposition reaction, samples were briefly rinsed with fresh cyclohexane and dried under a stream of argon or nitrogen.

It has been common practice to heat the formed layers at temperatures 110-120 ^{o}C, since the heating is believed to drive the condensation of the adsorbed silanols and siloxane groups with the substrates. However, this step was left out here since it was shown previously[5] that the heated monolayers are undistinguishable from unheated ones. OTE samples were sonicated for 10-30 mins and all samples were stored in cyclohexane until evaluation.

10.3 Morphology of Alkylsilane Layers

Figure 10.2 (a) shows a topographic AFM image of a C_{18} sample that was sonicated for 30 mins. The layer appears smooth and the corrugation is 1-2 Å. In only a few cases incomplete layers are revealed by the images, probably as a result of impurities adsorbed on the mica surface. From these images a layer thickness of about 25 Å is measured. This value corresponds closely to the monolayer thickness measured for OTS and OTE layers as measured by other techniques.[8, 10, 12, 13] High resolution AFM images can be obtained on any flat region, see figure 10.2 (b) and (d). No long-range order is observed in this case, in contrast to monolayers formed from C_{18} thiol molecules. However, a few isolated areas show some residual short-range order, as also visible from the 2D-FFT spectra shown in figure 10.2 (c) and (e). Images obtained in holes of incomplete layers reveal the hexagonal lattice of mica, confirming that monolayers are deposited on the surface.

Figure 10.3 shows topographic (a) and corresponding frictional force image (b) of an OTE layer that was sonicated for only 10 mins. As can be seen, this film does not appear flat, but rather shows small clusters of material over an essentially complete monolayer. These small clusters are likely OTE material that is only physically adsorbed onto an OTE monolayer. In fact, simultaneous lateral force images (figure 10.3 (b)) did not reveal any frictional contrast between them. It was found that sonication times greater than 20 mins are needed to obtain smooth layers as shown in figure 10.2. The contact angle measured for both type of films,

Figure 10.2 (following page). Topographic (a) AFM image of a smooth OTE layer on mica, sonicated for 30 mins after deposition. Scale bar=2000 Å. Molecular-level topographic (b) and corresponding frictional force image (d) taken in the area shown in (a). Scale bar=10 Å. The corresponding 2D-FFT spectra are shown in (c) and (e), respectively. No long-range order is observed.

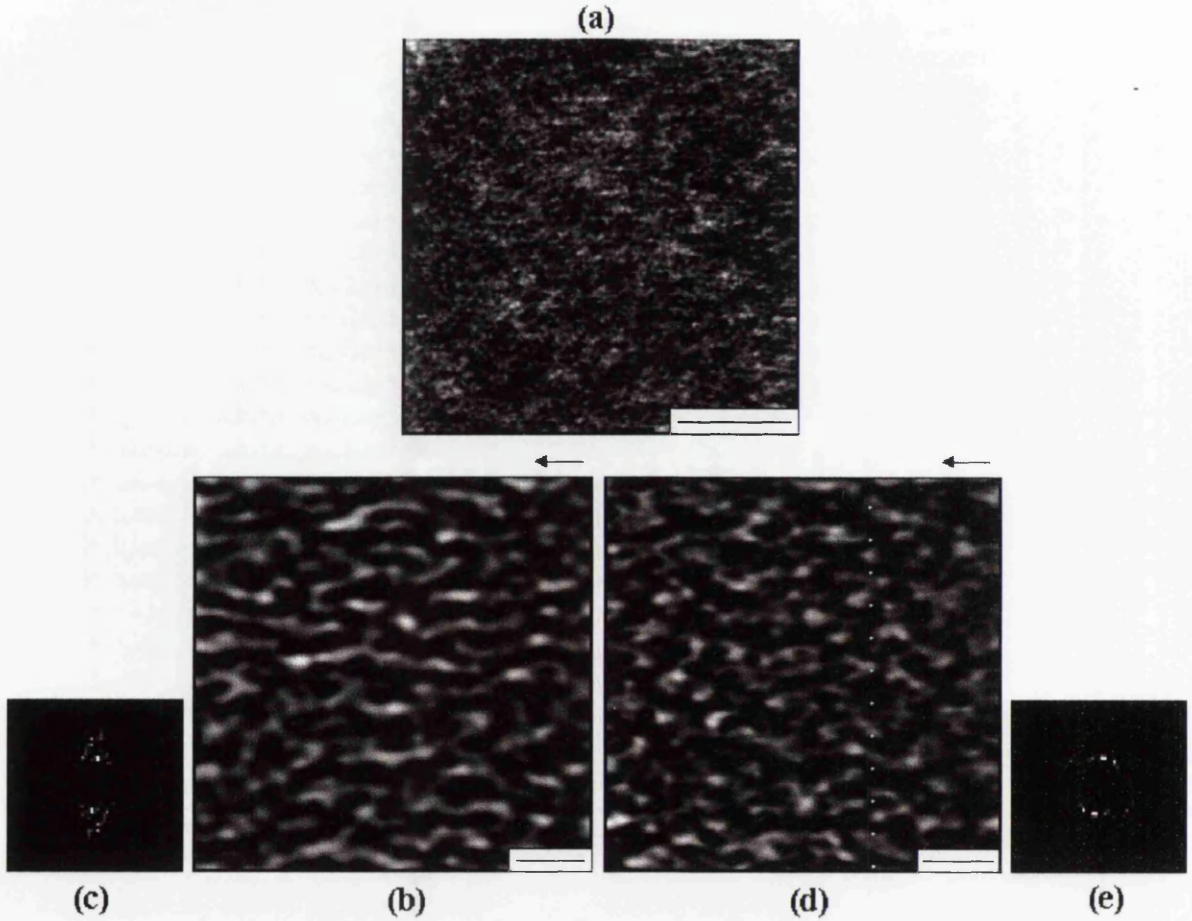
(a)
(c)
(b)
(d)
(e)

Figure 10.3 (following page). Topographic (a) and corresponding frictional force image (b) of an OTE layer on mica sonicated for 10 mins. Scale bars=1000 Å. Large clusters of material ≈15 Å high are found on the surface, as indicated by the topographic line profile (c).

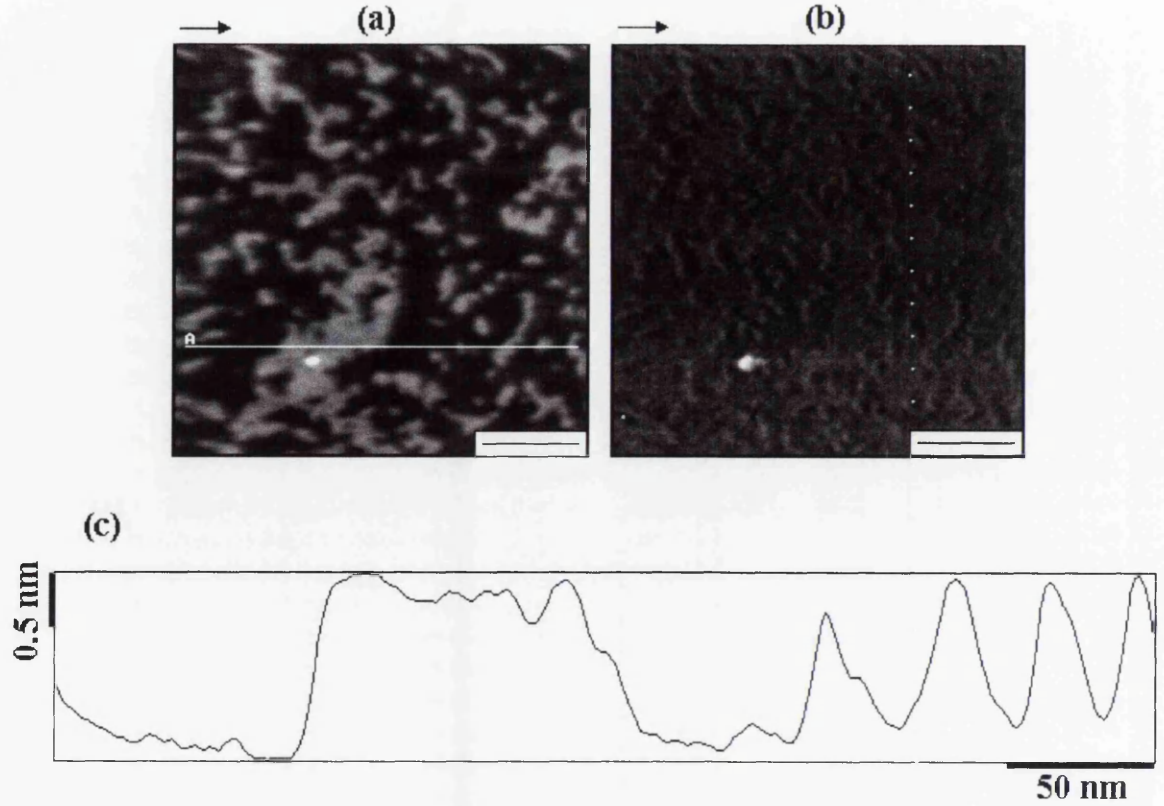
(a)
(b)
A
(c)
0.5 nm
50 nm

i.e. 'flat' and 'rough', is 111-113°, despite the drastically different molecular scale morphology. Contact angle measurements are routinely used to test the quality and 'good packing' of self-assembled monolayers and LB films. However, as also shown previously,[5] molecular level properties of such films cannot and must not be inferred simply from wettability measurements.

DTS (C_{12}) films produced similar results, while it became increasingly more difficult to obtain full monolayers for the shorter chains molecules, so that longer incubation times had to be used for C_8 and C_6 layers. However, the incubation cannot be prolonged indefinitely, since that increases the number of oligomers that will be adsorbed at the surface, resulting in 'rough' films characterized by an increasing density of large 3D clusters. The times used for this work were chosen so that smooth, although partially incomplete for the two shortest chains, layers were formed. Furthermore, no sonication was performed for C_{12}, C_8 and C_6 samples, since that resulted in the disruption of the monolayers. Contact angle for C_{12}, C_8 and C_6 layers were 110.0±2.0 °, 62.3±2.3 ° and 54.0±4.2 ° respectively. The observed decrease in contact angle has to be attributed to the increased difficulty in forming complete monolayers with shorter chain molecules. The exposure of mica, a hydrophilic surface, has the effect of decreasing the total contact angle. As it will be shown in section 10.4, the pull-off forces, which are a measure of the local surface energy, for C_8 layers are identical, within the statistical uncertainty, to the values measured on C_{18} and C_{12} layers. For the C_6 layers contribution to the measured contact angle from exposed methylene groups cannot in principle be excluded. However, it must pointed out again that, in view of the observed film morphology, direct conclusions on the molecular level morphology cannot be drawn solely from wettability measurements.

10.4 Thermal Stability of OTE Monolayers

As mentioned in section 10.2.2, the self-assembly of silane molecules onto a substrate is usually followed by curing at 110-120 °C, which is believed to covalently bind the molecules to the substrate. To date, to the author's knowledge, the occurrence of such condensation reaction has not been established, nor are, in the majority of cases, the effects of the heating treatment on monolayers morphology.

Figure 10.4 shows the effect of thermal annealing on OTE monolayers on mica. The sample was heated to temperatures up to 130 °C for 30 mins. As can be seen,

no change in the large and molecular scale morphology is observed up to 110 °C. After the layer was heated to 130 °C (figure 10.4 (i) and (j)), however, dramatic changes occurred. In fact, the film is observed to become rougher and several holes are created. At this point considerable disorder has been created in the layer due to 'melting' of the molecules. Similar results were obtained by heating the OTE films directly to 130 °C, indicating that the monolayer is effectively thermally stable only when heated to temperatures below 110-120 °C.

Figure 10.5 shows the effect of the heating treatment on 'rough' OTE films. As can be seen, the small islands found on top of the monolayer at room temperature (see figure 10.3) condense in 3D clusters, as 100-200 Å high, already after heating the film to 50 °C. The contact angle measured before and after heating gave 112°, again showing that wetting properties are no indication of monolayer morphology.

10.5 Frictional Properties of Self-Assembled Alkylsilane Monolayers and a Direct Comparison to Thiol SAMs

Figure 10.6 shows friction *vs.* load curves obtained on alkylsilane monolayers self-assembled on mica, for n=6, 8, 12 and 18. A curve taken on freshly cleaved mica is also shown as a reference. These results are similar to those obtained on the thiol SAMs on gold shown in figure 8.4. However, some important differences also exist. As for the alkylthiol monolayers, the lowest frictional forces are measured on the C_{18} and C_{12} layers. Higher frictional forces are measured on the C_8 and C_6 layers, with the C_6 layer yielding frictional forces that are one order of magnitude larger than those for the C_{18} and C_{12} layers. Strikingly they are also larger than the frictional forces measured on mica, except for very low loads corresponding to the tip being pulled from the surface (negative loads).

The pull-off forces as measured from force *vs.* distance curves are presented in table 10.I. These values are averages of several measurements on different areas of the samples. Values for C_{18}, C_{12} and C_8 layers are identical within the statistical uncertainty and, as in the case of the thiols, the pull-off forces measured on C_6 layers are ≈20% higher than those measured on the longer chains. The values measured on the organic layers are roughly half the values measured on mica, which is an hydrophilic surface.

A comparison of the friction *vs.* load curves obtained on alkylthiol and alkylsilane layers with the same chain length and as measured by the same tip is shown in figure 10.7. As the chain length decreases, the difference of frictional

Figure 10.4 (following page). Micron (a, c, e, g, i) and corresponding molecular-level (b, d, f, h, j) AFM images for a series of heat-treated smooth OTE film (sonicated for 30 mins) on mica. (a, b) No heating, (c, d) 70 ^{o}C, (e, f) 90 ^{o}C, (g, h) 110 ^{o}C, (i, j) 130 ^{o}C. Scale bars=5000 Å (a, c, e, g, i). Scale bars= 20 Å (b, d, f, h, j). No changes are observed at both the micron and molecular scale for temperatures up to 110 ^{o}C. Distortions of the layer attributed to 'melting' are seen after heating the film to 130 ^{o}C.

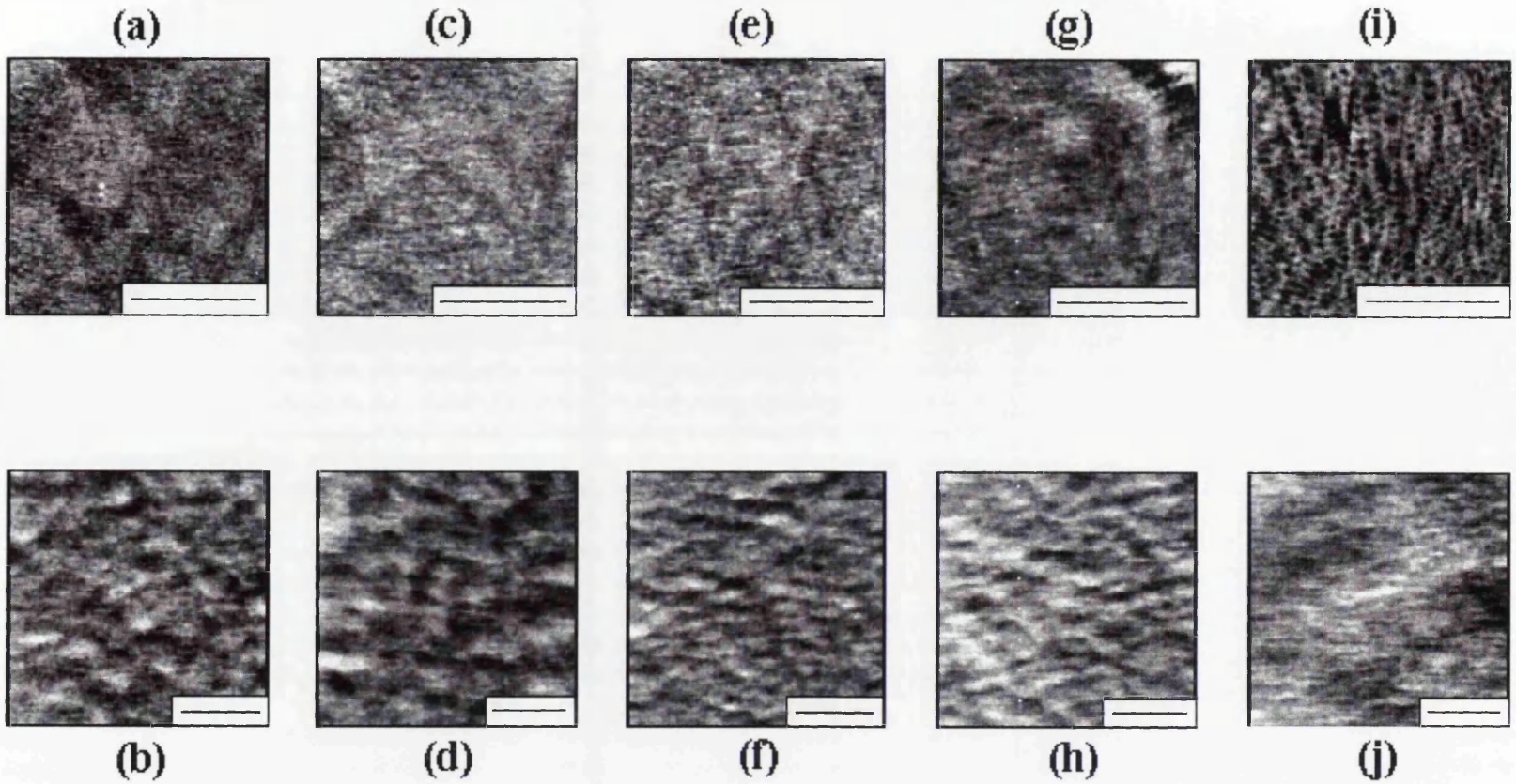
(a)
(c)
(e)
(g)
(i)
(b)
(d)
(f)
(h)
(j)

Figure 10.5 (following page). Effect of heating on OTE films sonicated for only 10 mins after deposition. The clusters of material observed before heating (a, b) condense into clusters as 150 Å high after annealing the film to 50 ^{o}C for 30 mins (c, d). Scale bars=1000 Å (a), 2000 Å (c).

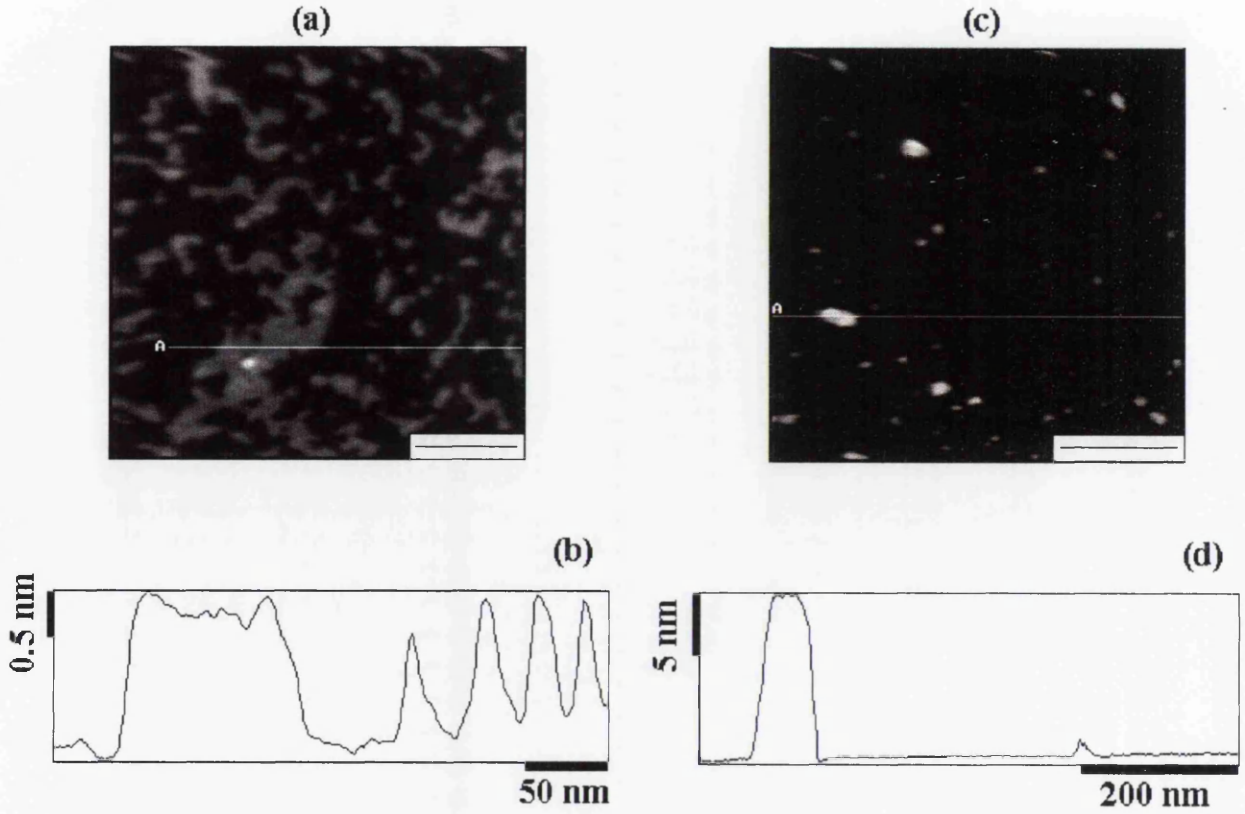
(a)
(c)
(b)
(d)
0.5 nm
50 nm
5 nm
200 nm

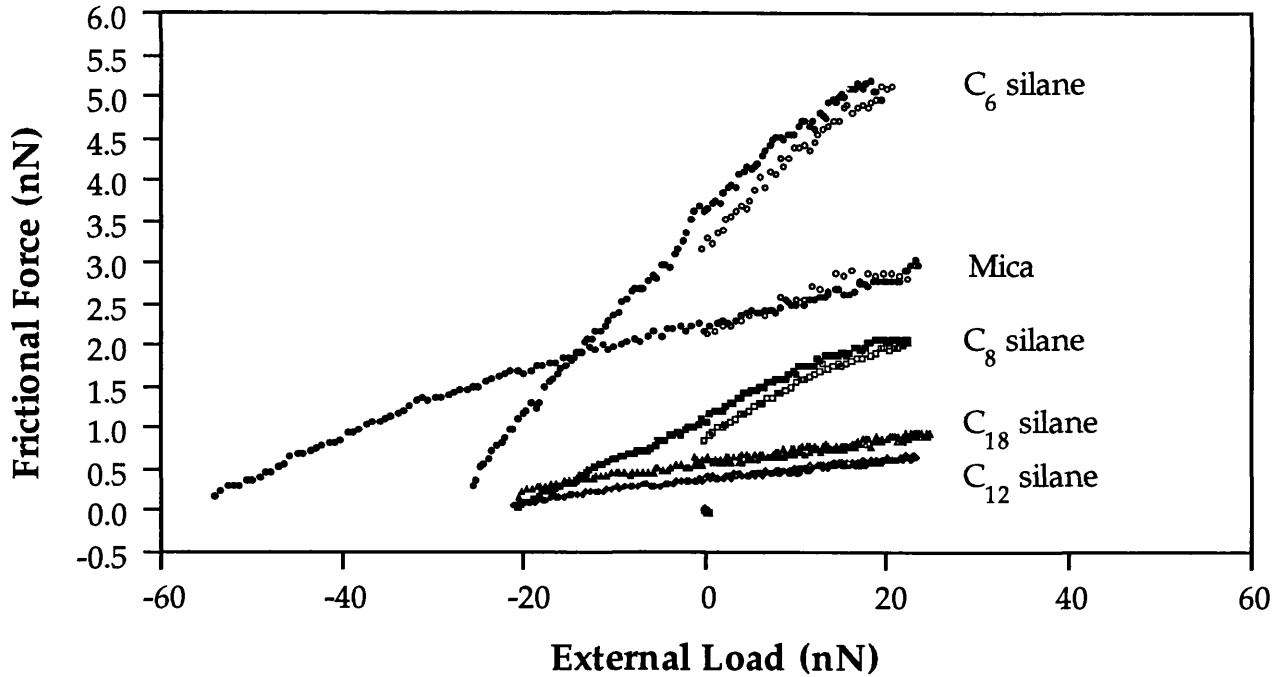

Figure 10.6. Representative friction *vs.* load curves for C_{18}, C_{12}, C_8 and C_6 alkylsilane monolayers on mica. A curve for mica is also shown as a reference. The load was limited to values that did not cause any damage on the layers being probed. All curves were obtained with the same silicon nitride cantilever with estimated normal force constant of 0.34 N/m (k^{nom}=0.58 N/m). Approach and retract branches are shown as empty and filled symbols, respectively.

Surface	Pull-off force F_{po} (nN)	ΔF_{po} (nN)
Alkylsilanes		
C_{18}	20.7	1.6
C_{12}	20.7	1.4
C_8	23.1	1.3
C_6	24.3	1.6
Mica	54.2	1.8

Table 10.I. Pull-off forces, F_{po}, as measured from force *vs.* distance curves. ΔF_{po} represents the statistical standard deviation.

forces on silanes and thiol layers increases. For the longest chains examined, the C_{18} layers (figure 10.7 (a)), the friction vs. curves are indistinguishable from one another. Larger forces are measured on the C_{12} silane with respect to the C_{12} thiol (figure 10.7 (b)), although the two curves are indistinguishable in the lowest load region. Frictional forces on the C_8 silane layers are about three times higher than the values for corresponding thiols at all loads (figure 10.7 (c)). The C_6 silane layers continue this trend, yielding frictional forces at a ratio of ~3.5:1 to the thiol values (figure 10.7 (d)).

Similarly to the observations on thiol SAMs, these results indicate that the frictional properties of surfaces do not depend only on the chemical nature of the exposed groups. The chain dependence of the frictional properties of silane monolayers can be rationalized in a way similar to their thiol counterparts. The monolayer stabilization provided by van der Waals interactions for long chain molecules explains the similarity of frictional behavior for all films, thiols and silanes, with lengths $n \geq 12$. In short chains films the poor packing of the chains favors the creation of numerous defects and energy dissipating modes, such as bending, rotation around kinks, *etc.* that are sterically quenched in the densely packed films, hence increasing friction. The higher friction of short chain silanes relative to the corresponding thiols is thus an indication and a consequence of the additional disorder in the silane layers.

Another conclusion can be drawn from the comparison of thiols and silanes with lengths corresponding to $n>10$. There are two important differences between these two types of films. One is long-range order, which is present in the thiols and absent in the silanes. The other is the cross-linking of the head groups. In thiols, cross-linking is limited to dimer formation, as seen in the disulphide bonds forming between pairs of S atoms in x-ray diffraction experiments.[30] This seems to have the effect of producing a superstructure with c(2 x 4) periodicity relative to the basic $\left(\sqrt{3}x\sqrt{3}\right)R30^{o}$ structure. In the case of the silanes, however, extensive covalent Si–O–Si networks form across the surface. Since the distance between Si atoms in the Si–O–Si bonds is 2.5 Å, while the chain diameter is ≈4.5 Å, there must be considerable chain distortion near the interface that is amplified along the network and must in turn cause a limitation in the size of the cross-linked cluster. This is probably at the origin of the lack of long-range order in the silanes, which is observed both on amorphous glass substrates as well as on crystalline mica. In spite of these differences, the film properties are similar above n=10. One must then conclude that the tight packing and short range order provided by the main body of the alkane chains is the determinant characteristic and that long-range order does not lead to lower friction.

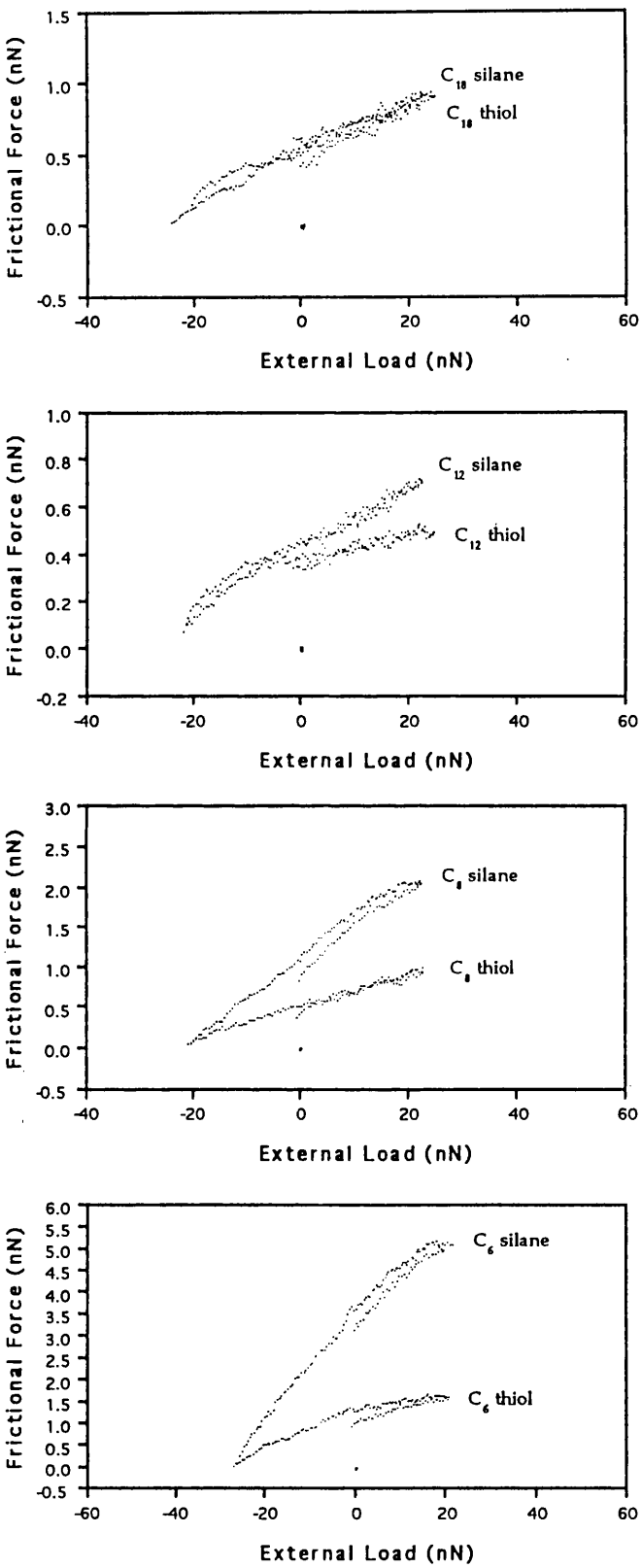

Figure 10.7. Comparison of the frictional behavior of alkylthiol and alkylsilane monolayers with the same n. (a) C_{18}, (b) C_{12}, (c) C_8, (d) C_6 layers. A certain amount of hysteresis is observed for C_8 silane and C_6 thiol and silane layers.

Surprisingly again these studies show that C_{12} silane layers yield lower frictional forces than their C_{18} counterparts, as for the thiols (chapter 8). The anomalous behavior of the C_{12} layers may be related to the purity of the chemicals employed. In the case of silanes, purity data provided by the chemical companies indicated that the dodecyltriethoxy silane chemical is purer (97%) than octadecyltriethoxy silane (95%) with the Si in the longer chain being prone to α, β isomerization and branching. As already stated previously for the thiols layers, while purity is an important factor that might affect packing and frictional properties, the observed differences are not understood at present.

10.6 Humidity Dependence of the Adhesive Properties of Bare and Silanated Mica

The interaction of water with surfaces in general and organic surfaces in particular is an extremely important topic affecting every surface exposed to ambient conditions. Of special importance is the interaction of water with surfactants layers, membranes, hydrophobic coatings, that play a role in many technologies such as paints, soaps, adhesives and polymers.

In order to investigate the effect of water on the adhesive properties of bare and silanated mica surfaces, the pull-off forces between a silicon nitride tip and freshly cleaved mica and OTE monolayers on mica were measured as a function of humidity.

Experiments were performed at LBNL with the home-built AFM and controlling the humidity in the AFM chamber by purging N_2 gas (drying process) or water vapor (wetting process) into it. Values of relative humidity (RH) from 5% to 95% were investigated. Typical ambient humidity at the AFM lab at LBNL was 45-48%. All experiments were carried out at room temperature, between 20 and 22 ^{o}C. Sharpened silicon nitride tips with nominal force constant of k= 0.1 N/m, i.e. PSM levers 2, were used. OTE layers on mica were prepared as described in section 10.2.1.

Figure 10.8 (a)-(b) shows two representative series of pull-off forces measured during a wetting-drying cycle on freshly cleaved mica (a) and OTE/mica (b), respectively. Curves were taken with different levers to avoid cross-contamination and therefore quantitative comparison of the results shown is not possible. The curve obtained on mica shows that the pull-off force greatly depends on RH. It reaches a maximum at RH close to ambient humidity and comparable values are

measured at very low and very high RH. In the case of OTE monolayers (b) no variation of the pull-off force is observed upon increase of RH, while a slight variation is observed during the drying process.

To understand these results, the hydrophilicity properties of the surfaces investigated need to be considered. Freshly cleaved mica is a very hydrophilic surface, that is it is wet by water. As already described in chapter 7, muscovite mica cleaves through the alkali containing planes, K^+ in this case. Therefore, water would be expected to form solvation spheres around K^+ ions.[31] OTE monolayers are instead hydrophobic (contact angle ≈110-113°) and only a weak van der Waals interaction (≈1 kJ/mol) could be expected with the water molecules. In addition, it has been shown by Hu *et al.*[32] that condensation of water on freshly cleaved mica proceeds in two distinct phases. Up to 22-28 % RH, the water film grows by forming two-dimensionally clusters of a few thousand angstroms in diameter (phase I). As the humidity is increased further, a second phase grows (phase II). This phase is characterized by two-dimensional islands with geometrical shapes in epitaxial relation to the mica surface. Phase II is completed when RH is about 45-50%. Above phase II, the layers of water are very mobile, characteristic of a liquid surface. Upon drying, phase II and phase I areas were seen to 'compete' for RH values between 37 and 21%, after which no contrast could be observed. Further experiments have shown that the two phases are related to the perturbation of the first water monolayer by the AFM tip.[33] The effects of such a perturbation extend over micrometers away from the contact point and are responsible for phase I patches. It is believed that this perturbation is related to a small upset in the balance of K^+ ions on the surface of mica. This unbalance diffuses away with time and perturbed phase I converts into the unperturbed phase II. The humidity has the effect of determining the amount of water on the surface, a monolayer and multilayers below and above 40-50% RH respectively,[34] but also of changing the time constant of any diffusion process of the K^+ ions on the surface.

The results obtained on mica (figure 10.8 (a)) appear to be related to the formation (and disappearance) of the different 'phases' of water as observed by Hu *et al.*, or in other words to the presence of a monolayer or multilayers of water on the surface. The increase of the pull-off force between ≈20% and 35-45%, depending on the experiment, corresponds to the formation of the first water monolayer, that is completed at ~40-50% RH (phase I and II of water). As the humidity continues to increase, liquid water layers are formed and the behavior in figure 10.8(a) can be understood in terms of capillary interaction and thermodynamics. In fact, as described in chapter 2 and 3, in these conditions water menisci of increasingly large Kelvin radius will be formed between the tip and the surface. Therefore, the contribution of the Laplace pressure to the adhesive forces decreases and tends to

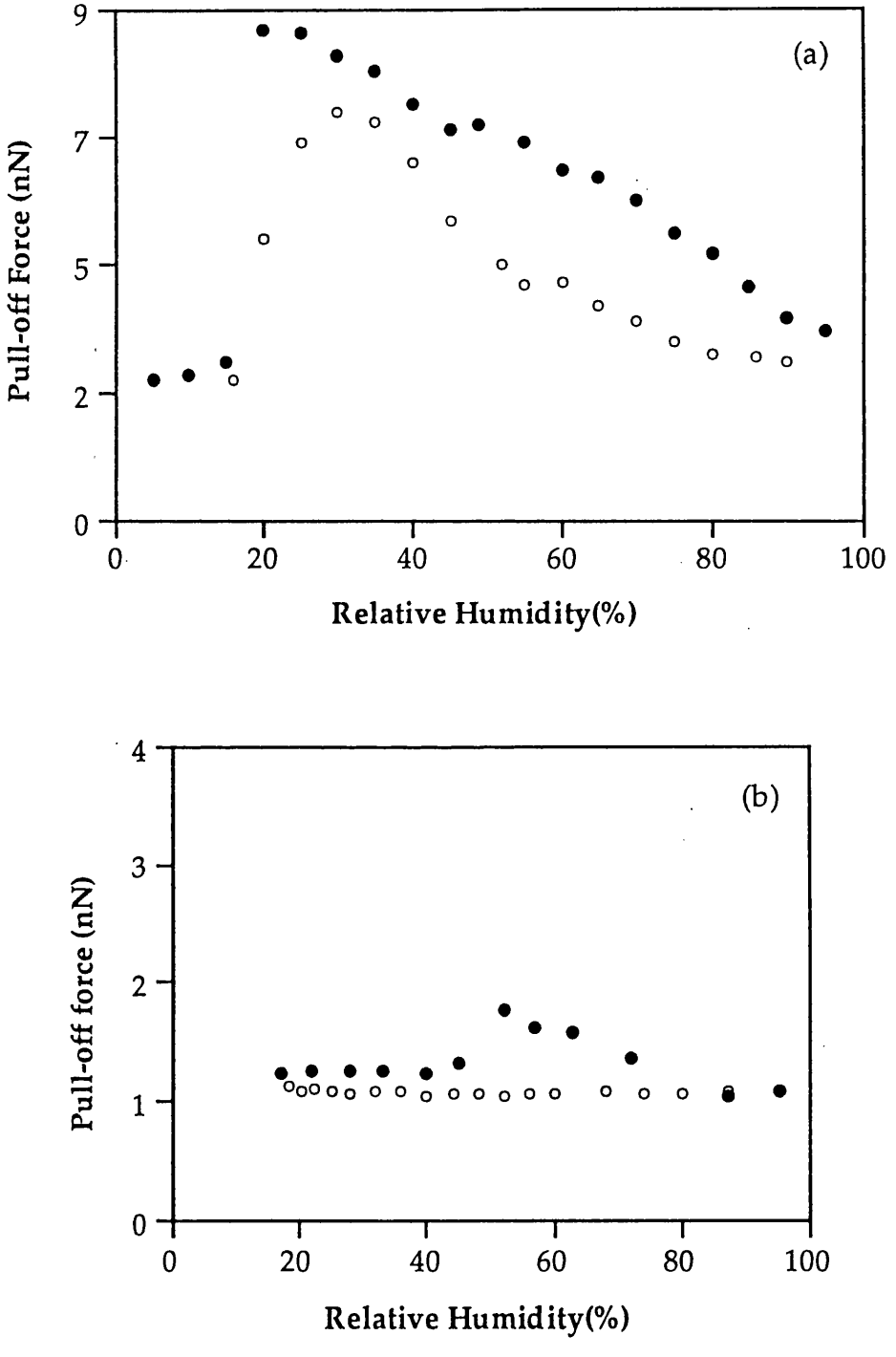

Figure 10.8. Representative pull-off force *vs.* relative humidity curves for (a) freshly cleaved mica and (b) OTE on mica. Data for increasing and decreasing humidity series are shown as open and filled circles, respectively.

zero with higher RH, consistent with the reduction in adhesive forces observed at high humidity.

Interestingly, in the course of these experiments and as RH was decreased below 20%, contrast disappeared in both topographic and lateral force images. No stick-slip pattern could be observed. The contrast recovered as the humidity increased again. At high humidity imaging was very unstable, although the lattice periodicity was still observed. This observation would seem to suggest that at normal operating conditions for most AFM experiments, i.e. ambient humidity, a 'thick' lubricant layer of water on the surface is mediating the tip-surface interaction, thus 'reducing' load. As the humidity is decreased below 20%, the tip may be now in contact with a layer of contaminants so that contrast in the images is lost.

A very different behavior is obtained on OTE/mica monolayers. In this case, little variation with RH is seen for the pull-off force, consistent with the macroscopic wettability measurements on these layers. A small change is seen, however, upon decreasing the relative humidity. This behavior may be related to the imperfect packing of these layers. In fact, unlike long chain thiol monolayers, it has been observed that OTE monolayers are not densely packed and pinholes and defects, normally invisible during contact mode imaging, may allow water to reach deeper into the chains portions.[35]

References

[1] A. Ulman, *An Introduction to Ultrathin Organic Films: from Langmuir-Blodgett to Self-Assembly*, (Academic Press: San Diego, 1991) and references therein.

[2] J. Sagiv, *J. Am. Chem. Soc.*, **102**, 92 (1980).

[3] D. G. Kurth, T. Bein, *J. Phys. Chem.*, **96**, 6707 (1992).

[4] G. A. Carson, S. Granick, *J. Appl. Polym. Sci.*, **37**, 2767 (1989).

[5] X.-D. Xiao, G.-Y. Liu, D. H. Charych, M. Salmeron, *Langmuir*, **11**, 1600 (1995).

[6] T. Nakagawa, K. Ogawa, T. Kurumizawa, *Langmuir*, **10**, 525 (1994).

[7] D. K. Schwartz, S. Steinberg, J. Israelachvili, J. A. N. Zasadzinski, *Phys. Rev. Lett.*, **69**, 3354 (1992).

[8] S. R. Wasserman, Y.-T. Tao, G. M. Whitesides, *Langmuir*, **5**, 1074 (1989).

[9] C. P. Tripp, M. L. Hair, *Langmuir*, **11**, 1215 (1995).

[10] B. Arkles in *Silane Coupling Agents Catalogue*, Hüls America, Piscataway, NJ, USA (1995).

[11] J. Peanasky, H. M. Schneider, S. Granick, C. R. Kessel, *Langmuir*, **11**, 953 (1995).

[12] J. Rühe, V. J. Novotny, K. K. Kanazawa, T. Clarke, G. B. Street, *Langmuir*, **9**, 2383 (1993).

[13] I. M. Tidswell, B. M. Ocko, P. S. Pershan, S. R. Wasserman, G. M. Whitesides, *Phys. Rev. B*, **41**, 1111 (1990).

[14] N. Tillmann, A. Ulmann, J. S. Schildkraut, T. L. Penner, *J. Am. Chem. Soc.*, **111**, 6136 (1988).

[15] M. Pomerantz, A. Segmüller, L. Netzer, J. Sagiv, *Thin Solid Films*, **132**, 153 (1985).

[16] H. Hoffmann, U. Mayer, A. Krischanitz, *Langmuir*, **11**, 1304 (1995).

[17] K. Bierbaum, M. Kinzler, Ch. Wöll, M. Grunze, G. Hähner, S. Heid, F. Effenberger, *Langmuir*, **11**, 512 (1995).

[18] I. M. Tidswell, T. A. Rabedeau, P. S. Pershan, S. D. Kosowsky, J. P. Folkers, G. M. Whitesides, *J. Chem. Phys.*, **95**, 2854 (1991).

[19] K. L. Mittal, *Adhesion Aspects of Polymer Coatings*, (Plenum Press: New York, 1983).

[20] E. Plueddemann, *Silane Coupling Agents*, (Plenum Press: New York, 1982).

[21] M. J. E. Golay, *Gas Chromatography*, D. H. Desty edt., (Butterworth: London, 1958).

[22] H. H. Weetall, *Immobilised Enzymes, Antigens, Antibodies, and Peptides. Preparation and Characterization* (Marcel Dekker Inc.: New York, 1975).

[23] F. P. Bowden, D. Tabor, *The Friction and Lubrication of Solids*; (Oxford University Press: London, 1968).

[24] M. Suzuki, Y. Saotome, M. Yanagisawa, *Thin Solid Films*, **160**, 453 (1988).

[25] T. Miyamoto, I. Sato, Y. Ando, in *Tribology and Mechanics of Magnetic Storage Systems*, B. Bhushan, N. S. Eiss edts., 1988.

[26] E. Ando, Y. Goto, K. Morimoto, K. Ariga, Y. Okahata, *Thin Solid Films*, **180**, 287 (1989).

[27] B. Bhushan, B. K. Gupta, *Handbook of Tribology: Materials, Coatings, and Surface Treatments* (McGraw-Hill: New York, 1991).

[28] H. Zarrad, P. Clechet, M. Belin, C. Martelet, N. Jaffrezic-Renault, *J. Micromech. Microeng.*, **3**, 222 (1993).

[29] B. Bhushan, V. N. Koinkar, *J. Appl. Phys.*, **75**, 5741 (1994).

[30] P. Fenter, A. Eberhardt, P. Eisenberger, *Science*, **266**, 1216 (1994).

[31] J. Glosli, M. Philpott in *Proc. Symp. on Microscopic Models of Electrolyte Interfaces*, vol. 93-95, (Electrochemical Society: Pennington, NJ, 1993).

[32] J. Hu, X.-D. Xiao, D. F. Ogletree, M. Salmeron, *Science*, **268**, 267 (1995).

[33] M. Salmeron, Personal Communication.

[34] These results are also in agreement with ellipsometry measurements performed by Beaglehole and Christenson. D. Beaglehole, H. K. Christenson, *J. Phys. Chem.*, **96**, 3395 (1992).

[35] J. Hu, Personal Communication.

Chapter 11

Preparation and Molecular Scale Characterization of Polydiacetylene Thin Films

11.1 Introduction

The low mechanical and thermal stability of most Langmuir-Blodgett films limits their use in technological applications. One approach taken to stabilize such layers is to use polymerizable amphiphiles.[1,2] In many cases, disordered products are obtained due to structural changes during the polymerization reaction. This problem can be overcome by the use of molecules containing groups which undergo topochemical reaction. Among them are diacetylene molecules of the general form:

$$R-C\equiv C-C\equiv C-R'$$

where R and R' schematically represent the side groups.[3,4] The polymerization of these molecules is started by UV or x-ray irradiation or γ quanta. While in the past twenty years increasingly high attention has been devoted to polydiacetylene thin films, early investigations of this class of polymers concentrated on single crystals.[3] In fact, this unique class of polymers polymerizes in the solid-state, as discovered by Wegner in 1969.[5] The mechanism of the polymerization is rationalized as a 1, 4 addition to the conjugated triple bonds, as shown in figure 10.1.[6] The result is a fully conjugated polymer backbone of alternating double and triple bonds (ene-yne). The polymerization of polydiacetylenes is a topochemical reaction, requiring that the monomer molecules be packed in a particular way. All reactivity comes about by very specific rotations of the monomers on their lattice sites so that the transition from the monomer molecules to the polymer chains occurs without destruction of the monomer crystal lattice. Based on the experience from the successful polymerization of many polydiacetylene derivatives and x-ray crystallographical evidence Baughman derived the conditions necessary for topochemical polymerization of diacetylene monomers:[7]

(1) the van der Waals distance between neighboring monomers has to be close to the chemical bond distance, i.e. $d_1 \sim d_2$;

(2) the distance s_1 between adjacent triple bond systems should be

smaller than 0.4 nm with a lower limit of 0.34 nm;

(3) the angle, α, between the diacetylene rod and the translational vector should be close to 45^{o}, so that carbon 4 of one molecule is very close to carbon 1' of the next molecule.

The polydiacetylene backbone is a π-bonded system which extends over many polymer units and the conjugation length increases upon polymerization. This increase in the π-electron delocalization length lowers the excitation energy, with the backbone highest occupied molecular π-orbitals moving upward and the lowest unoccupied molecular π-orbitals moving downward.[8, 9] Therefore, in contrast to conventional polymers, that have σ–bonded backbones, it is the electronic structure of the backbone, rather than that of the substituents, that controls the electronic properties of polydiacetylenes. This in turn makes polydiacetylene properties differ dramatically from those of other polymeric materials. Apart from their applications in the fields of biophysics and biochemistry, polydiacetylenes are interesting materials for possible applications in electronic devices. They show very high carrier mobilities ($\mu_e \geq 10^3$ cm^2 v^{-1} sec^{-1}) in the chain direction, when the carriers are injected from the electrode.[10] The third order non-linear susceptibility coefficient, $\chi^{(3)}$, is very high and comparable to that of GaAs below the absorption edge.[11] Polymeric diacetylenes can therefore be used as efficient elements for third harmonic generation and their use has been proposed in the fabrication of non-linear guided wave devices.[12, 13] In addition to their remarkable electrical and optical properties, polydiacetylenes have been shown to have excellent mechanical properties as well. Some polydiacetylene single crystals were found to have values of the Young's modulus in the chain direction of the order of 50-60 GPa.[14, 15]

Most of what is known about the electronic excitations of PDAs has been learned from optical and resonance Raman spectroscopy.[2, 3, 16] In addition to single crystals, solutions as well as thin films have been studied. The structure of single crystals and multilayered LB films with different side chains has been established by x-ray diffraction.[17, 18, 19, 20, 21, 22] Upon exposure to UV or γ-radiation diacetylenes are converted from a soluble monomer crystal, which is transparent, to a deeply colored blue polymer crystal, which is insoluble in all common solvents. The color arises from the lowest π-electron transition (π-π^*) of the conjugated polymer backbone. The maximum of this transition is found for many PDAs to be near 600 nm (2 eV) (blue-phase). Upon heating many PDAs convert to a new phase characterized by a peak in the optical absorption spectra at about 540 nm (2.3 eV) and the polymer appears pink-red (red-phase). Because of the color change, these transitions are referred to as thermochromic. Such transitions are observed also in PDA mono- and multilayer LB films. A blue-to-red color transition can also be observed as a result of tensile elongation

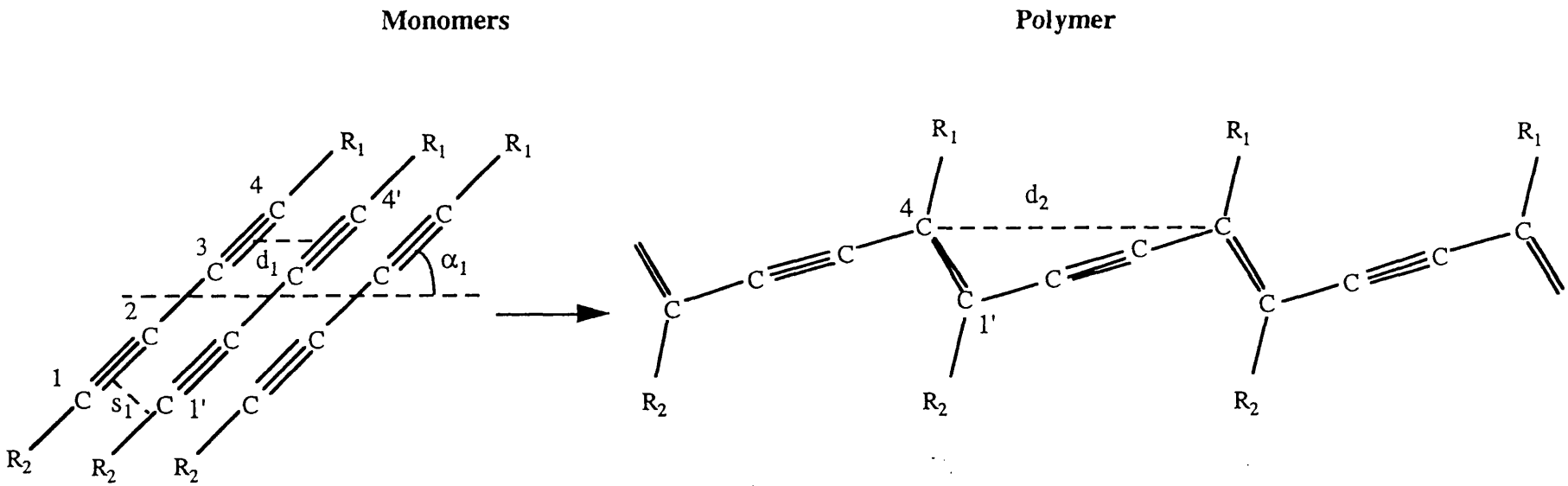

Figure 11.1. Schematic of the polymerization reaction of polydiacetylenes. The polymer backbone consists of alternating double and triple bonds (ene-yne). R_1 and R_2 represent the side chains.

(mechanochromism),[23] upon prolonged exposure to UV light,[24] pH changes of the subphase[25] or solvent treatment (solvatochromism).[26] Recently it was shown at the Center for Advanced Materials at LBNL, that carbohydrate functionalized polydiacetylene thin films undergo the blue-to-red transition upon specific binding of a biological target (affinochromism).[27] In this case sialic acid functionalized 10, 12 pentacosadiynoic acid (CH_3–$(CH_2)_{11}$–C≡C–C≡C–$(CH_2)_8$–COOH) (PCDA) films (figure 11.2) were deposited onto a hydrophobic substrate by the horizontal Langmuir-Schaefer method to resemble the spatial organization and functionalization of natural cell membranes. When these films are incubated with influenza virus, the sialic acid residues specifically bind to the protein hemagglutinin present on the virus membrane[28, 29] and the blue-to-red color transition is observed. Therefore, by incorporating a biologically active ligand into the polydiacetylene matrix it is possible to use the polymer backbone as an optical probe of ligand-receptor interactions and use the polydiacetylene thin film as a simple, direct colorimetric sensor. An in depth discussion of this newly discovered chromatic transition will be presented in chapter 13. In addition, the blue-to-red transition was observed to occur upon calcite mineralization on top of 100% PCDA films.[30] These results will be discussed in detail in chapter 13.

The increase in the electron excitation energy in the red phase is an indication of a smaller conjugation length. While it is generally accepted that changes in the structure of the polymer backbone strongly influence the extent of the π-electron delocalization, the mechanism and origin of the color changes has not been fully elucidated. Theoretical calculations have indicated that small variations in bond angles can result in large optical shifts of the absorption band.[31, 32] Although the majority of the physical properties of the polydiacetylenes are determined by the nature of the polymer backbone, the side chains play an important role in determining the structure and stability of the polymers, so that the mechanism of the color transition may be different for different PDAs. Also, fixed the molecule, the mechanism responsible for the different cases of color transition does not necessarily have to be the same.

In order to fully exploit the use of polydiacetylenes in direct colorimetric detection, it is necessary to understand the nature of the color transition with respect to affinity binding. Since the mechanism of the chromatic transition is not completely understood even for the more well-known thermochromic effect, a molecular level characterization of this effect was carried out first. These results are discussed in chapter 12. In relation to these studies, a systematic AFM characterization of PCDA films prepared in different conditions was necessary and resulted to be particularly important. In this chapter preparation, molecular scale and optical properties of thin films of 10, 12 pentacosadiynoic acid molecules

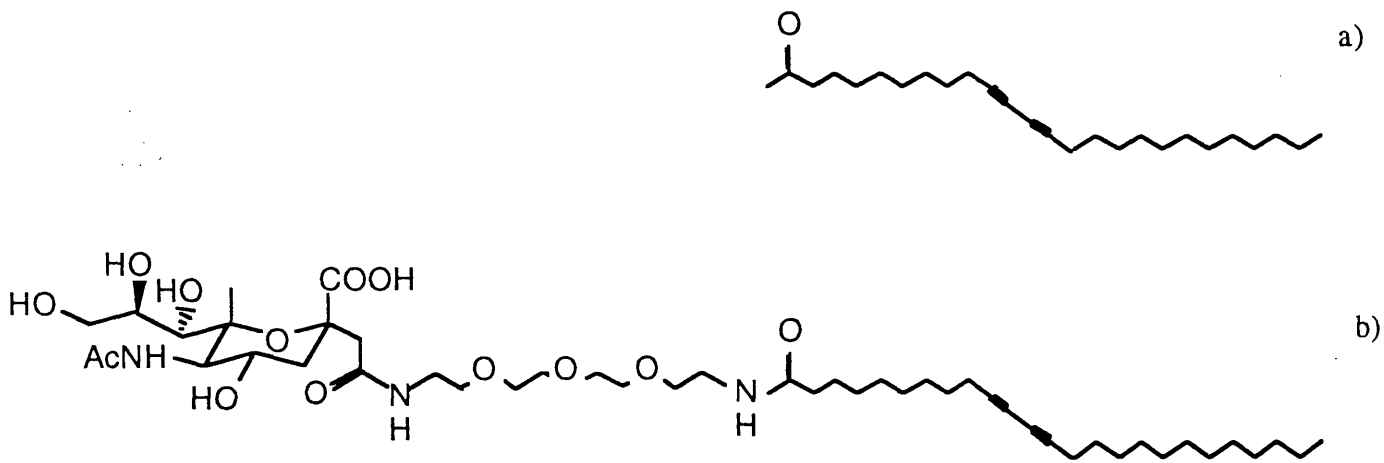

Figure 11.2. Compounds used in these studies. (a) 10, 12 pentacosadiynoic acid (PCDA); (b) sialic acid functionalized PCDA (SAc/PCDA). The polymer backbone is the chromatic detection element, while sialic acid is the receptor-binding ligand for the influenza virus.

prepared by the Langmuir-Schaefer and Langmuir-Blodgett techniques are described in detail. Monomer, blue and red polymer films of sialic acid functionalized PCDA (SAc/PCDA) molecules and blue polymer films of the pure PCDA and its Cd salt were analyzed.

11.2 Materials and Methods

11.2.1 Materials

10,12 pentacosadiynoic acid was purchased from Farchan Laboratories and used as received. The synthesis of the sialic acid lipid was performed by Dr. J. O. Nagy at the Center for Advanced Materials at LBNL and is reported in the literature.[33] n-Octadecyltriethoxysilane (OTE) was purchased from United Chemical Technologies (Bristol, PA, USA) and vacuum-distilled upon receipt. All solvents used were spectral quality. House-distilled water was passed through a four-cartridge Millipore μQF purification train producing water with resistivity of 18.2 MΩ cm. Pure MilliQ water (pH ~ 5.5) was used as the subphase for the preparation of PCDA and SAc/PCDA films. For the preparation of Cd-PCDA films, $CdCl_2$ was added to the subphase in concentration of 0.5 mM. All solutions for spreading were filtered through a 0.2 μm nylon or PTFE membrane to remove traces of polymer.

11.2.2 PCDA Film Preparation

For the Langmuir-Schaefer deposition, glass and mica surfaces were made hydrophobic by depositing a monolayer of OTE as described in chapter 10. All substrates were kept under pure cyclohexane prior to LS transfer of the polydiacetylene.

The sialic acid functionalized and pure PCDA films were prepared by spreading a chloroform solution containing 5 % sialic acid/95 % PCDA and 100 % PCDA monomer lipids respectively onto the clean water surface of a standard Langmuir trough (KSV, Finland). After spreading, the films were compressed and allowed to equilibrate for 30 minutes. For the preparation of the polymer samples, the layers were irradiated with 254 nm light from a handheld UV lamp (UVP Mineralight, 30 $\mu W/cm^2$), while cold water was circulated in the bath to keep the temperature constant at 20 ^oC. The layers were then transferred onto the hydrophobic substrates by touching the substrate parallel to the water surface

(see chapter 5). The substrates were subsequently removed from the water and blown dry with a stream of argon or nitrogen. In the case of the Cd-PCDA films, the monomer molecules were transferred by the LB method onto a freshly cleaved mica surface starting with the substrate under water and in a single upstroke motion. Once deposited, the monomer layer was polymerized for 1 minute.

11.2.3 Visible Absorption Spectroscopy

Spectra were taken with a Hewlett Packard 8452A diode array spectrophotometer using a single beam configuration, deuterium lamp and uv filter at the source output. Films on glass were placed inside a 2 mm path length cuvette. Spectra were recorded in air.

11.2.4 Atomic Force Microscopy

Images larger than 1 μm^2 were acquired at LBNL with the commercially available instrument described in chapter 4. In this case Si cantilevers were used. Images smaller than 1 μm^2 were taken with the home-built AFM, described too in chapter 4. In this case silicon nitride cantilevers with a nominal force constant of 0.1 N/m were used.

11.3 Spreading Behavior of the Monomer

The spreading behavior of the SAc/PCDA mixture and 100% PCDA amphiphiles was studied by recording the pressure-area isotherms (figure 11.3).

As can be seen, the curve recorded for the SAc/PCDA mixture (solid line) with water as the subphase shows a pressure increase at an area between 28 and 25 $Å^2$ per molecule. When the pressure reaches a value of about 12 mN/m, a collapse is observed and then the value remains nearly constant and equal to 9 mN/m down to an area of ~10 $Å^2$/molecule. After that, the pressure steeply increases while the molecular area remains nearly constant and equal to ~8 $Å^2$/molecule. The pressure-area isotherm measured for a 100 % PCDA monomer is indistinguishable from that of 5% SAc/95% PCDA, indicating that the introduction of a small percentage of sialic acid, 5 %, does not significantly alter the spreading behavior of the pure acid.[34] When $CdCl_2$ is introduced in the subphase, the collapse pressure increases to about 30 mN/m (dotted line).

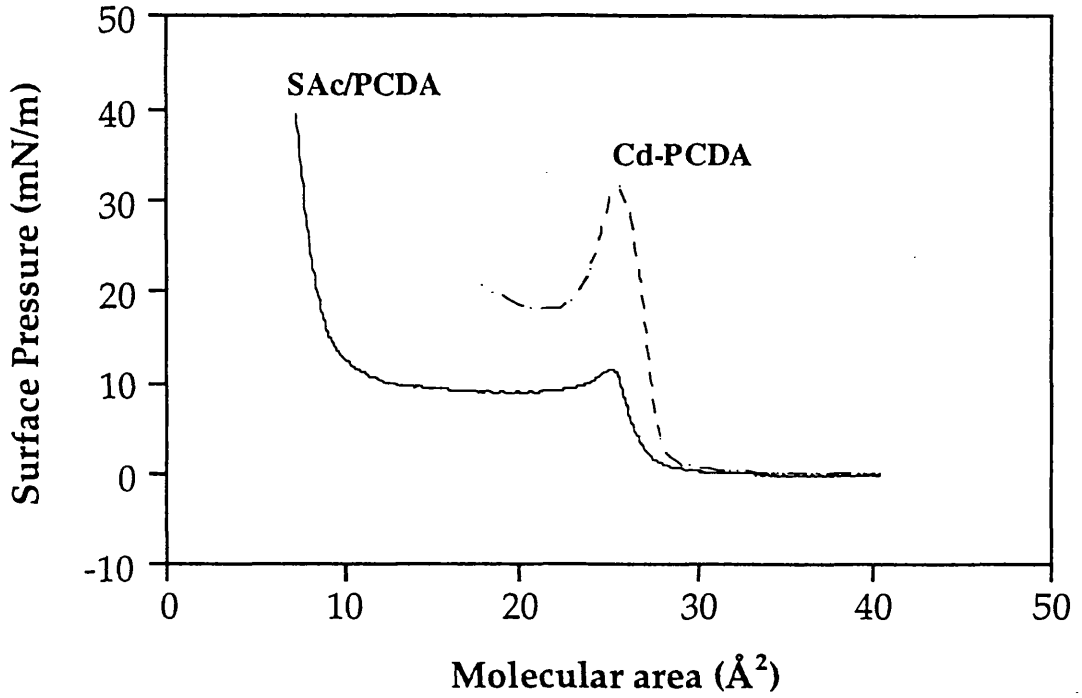

Figure 11.3. Surface pressure-molecular area isotherms for (solid line) SAc/PCDA (de-ionized water, pH=5.5) and (broken line) PCDA ($CdCl_2$, pH=6) monomer lipids.

11.4 Visible Absorption Spectroscopy

Figure 11.4 shows the optical absorption spectra for the blue and red-phase SAc/PCDA films. The blue phase film (solid line) is characterized by a main absorption peak at 640 nm and a smaller vibronic peak at 590 nm. The spectrum was obtained for a 1 minute irradiation time. As can be seen, the blue-phase film shows the presence also of the red phase, as evidenced by the small but not negligible absorption at 540 nm.

The spectrum for the red-phase film (dotted line) was obtained after exposing the monomer molecules to UV light for 20 minutes. As can be seen this phase is characterized by an increase in the intensity of the peak at 540 nm and a marked decrease in the intensity of the peak at 640 nm. A smaller vibronic peak at 500 nm is also visible.

The optical absorption spectra obtained for a pure PCDA film (not shown) do not show any significant difference with respect to the SAc/PCDA layers, indicating that the polymerization proceeds at a similar rate for the two types of film.

11.5 Morphology of Blue-Phase p-SAc/PCDA Films

Figure 11.5 shows AFM images for blue phase films (p-SAc/PCDA) lifted from molecules compressed to 20 mN/m. Domains, a few microns in size, separated by darker regions are visible in figure 11.5 (a). Within each domain an almost complete layer (layer **1**) and a 'stripe-like' morphology on top of it are visible. The stripes are most often parallel to one another within each domain, but their orientation is different in each domain and does not appear to be correlated to the direction in which the barrier is being moved. Layer **1** exhibits holes and cracks (figure 11.5 (b)) often parallel to the direction of the stripes. Interestingly the stripes are never seen to extend inside the holes of layer **1**, but rather to wrap around them.

Since OTE monolayers are featureless at this magnification (see chapter 10) it follows that the domains in figure 11.5 (a) are p-SAc/PCDA regions. Molecular scale images taken inside the holes and cracks of layer **1**, as well as in the areas between neighboring domains, reveal the disordered nature of OTE monolayers on mica. To further verify this conclusion, the AFM tip was pushed through the layer down to the mica surface. The film was irreversibly worn out and the depth of the hole was measured to be about 25 Å. This corresponds to the thickness of a single

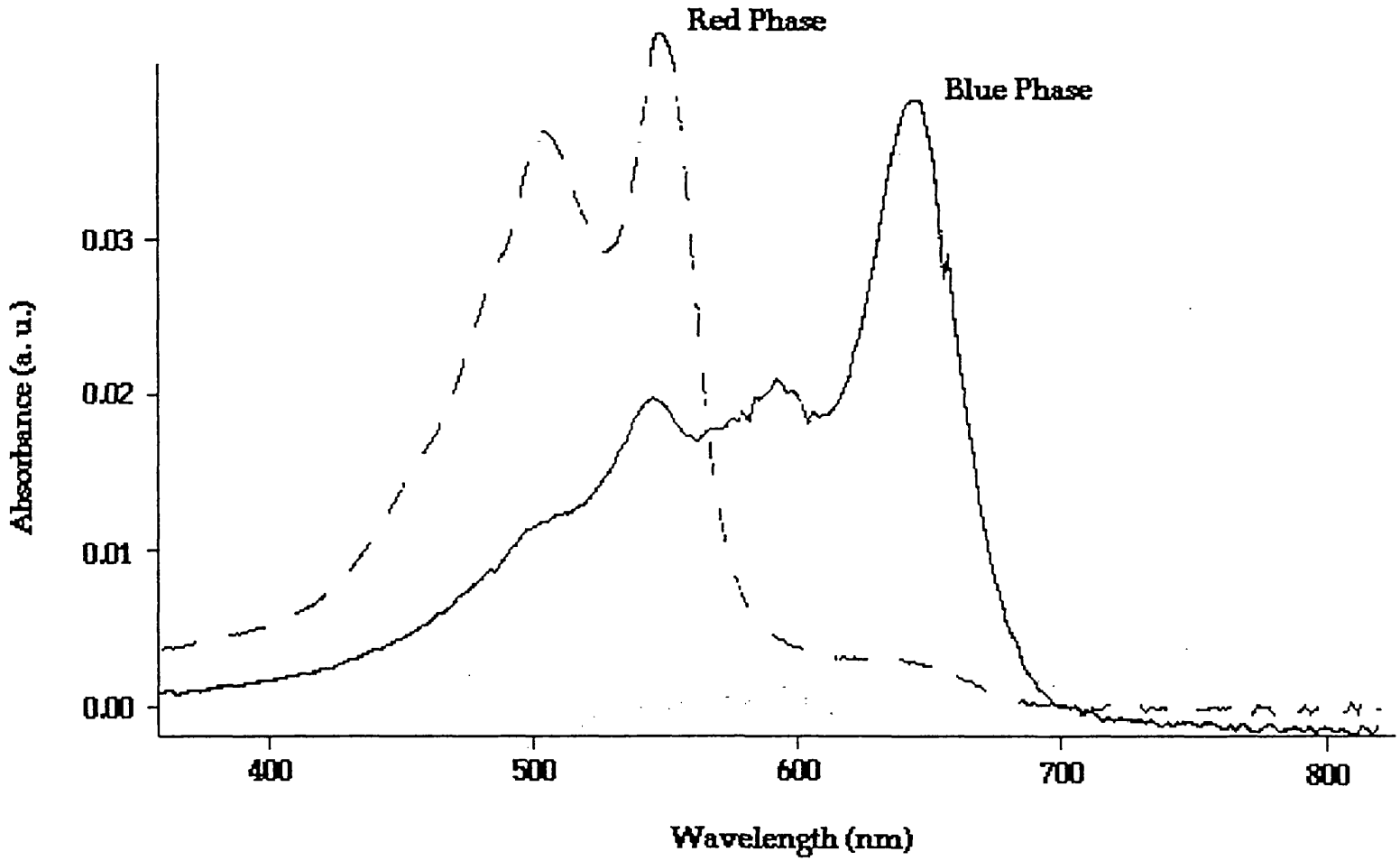

Figure 11.4. Optical absorption spectra for blue-phase (solid line) and red-phase (broken line) p-SAc/PCDA films. Monomer molecules were irradiated for 1 and 20 minutes, respectively

Figure 11.5 (following page). AFM images of blue-phase p-SAc/PCDA films on mica. (a) Micron sized domains are separated by uncovered OTE areas. Scale bar=5 μm. (b) A stripe-like morphology is observed on an almost complete layer (layer **1**). Scale bar=2000 Å. (c) Detail of layer **1**, as shown in (b). Fine striations, parallel to one another and to the stripes, are visible. Scale bar=500 Å. (d) A light shade illumination is used to enhance the contrast of the filaments found on the stripes of (b). Scale bar=1000 Å.

(a)

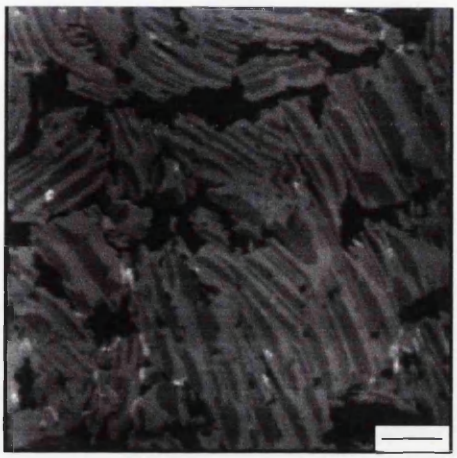

(b)

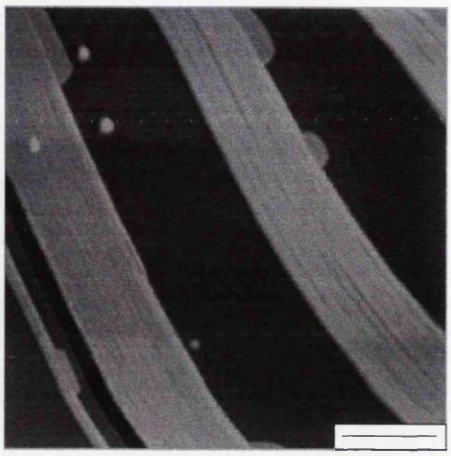

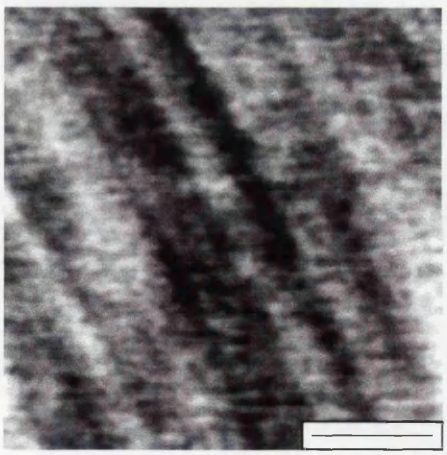

(c)

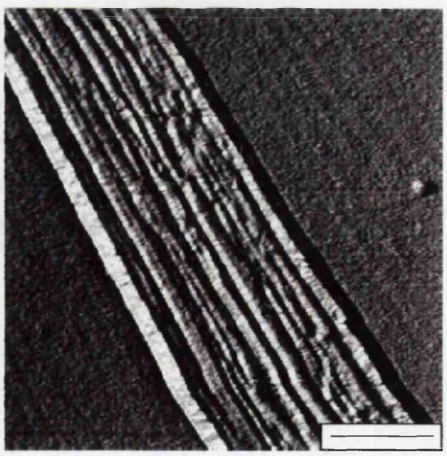

(d)

OTE layer. From this follows that the p-SAc/PCDA domains of figure 10.5 (a) are separated by uncovered OTE areas and that in each domain two layers of the polymer are present on the surface. Since the molecules are overcompressed at the air-water interface, it is not surprising that the preparation method results in the deposition of multilayers.

Higher magnification scans of layer **1** reveal very fine striations (figure 11.5 (c)) parallel to one another as well as to the stripes. The roughness across them is measured to be only 2-3 Å. These areas of the film are relatively robust and repeated scanning at low load does not cause any damage. On top of the stripes filament-like material is very often present (figure 11.5 (d)). In most cases the filaments run parallel to the direction of the stripe and often appear to be pinned at one point at one edge of the stripe. Unlike layer **1**, the stripes are easily damaged when the same area is repeatedly scanned and the filaments are seen to separate. However, as shown in figure 11.6, extra material cannot be found around the holes and therefore the tip must laterally compress the stripes and the filaments rather than wearing them out.

The height of layer **1** is measured to be 79 ± 8 Å. The height of the stripes is 78 ± 8 Å (type **3** stripes). The filaments on top of the stripes contribute for an extra 10-20 Å. In a few cases stripes 58 ± 6 Å high were found (type **2** stripes). Assuming an *all-trans* conformation for the alkyl chains on both sides of the diacetylene group, the length of a PCDA molecule is about 32 Å. The spacer and sialic acid together are about 20 Å long. Since the sialic acid is only 5% of the lipid matrix, two sialic acid molecules are spaced about 20 Å on average. In these conditions it is unlikely that they are fully extended and they would be expected to either lie flat or bend back into the PCDA matrix. In either cases they would not contribute significantly to the thickness of the layers. Indeed, this conclusion was confirmed by comparison with films of pure p-PCDA prepared in similar conditions (see section 11.8). The measured thicknesses of layer **1** and type **3** stripes correspond to a trilayer tilted about 35° from the surface normal. This finding is supported by the pressure-area isotherm shown in figure 11.3 (a). In fact, at 20 mN/m the molecular area is about 1/3 of the value before the collapse. The thickness of type **2** stripes corresponds to a PCDA bilayer tilted by approximately 25°. It should be pointed out here that these values of the tilt angle represent average values for the two alkyl chains on each side of the polymer backbone and that the two aliphatic chains could tilt of different angles.

Molecular resolution images are routinely obtained on layer **1** at low values of the load. Figure 11.7 (b) and 11.7 (c) show two lattice resolution frictional force images obtained on the area shown in figure 11.7 (a). The corresponding FFT power spectra are also shown (figure 11.7 (d) and 11.7 (e)). As can be seen, a higher

Figure 11.6 (following page). AFM images of blue-phase p-SAc/PCDA films type **3** stripes. After repeated scanning at 1 nN of the area enclosed by the rectangle shown in (a), the filaments and stripes appear damaged in the direction parallel to the stripe. The AFM tip does not wear out the layer, but rather laterally compresses it. The small bright clusters visible in (a) and (b) are likely impurities present in the SAc/PCDA solution. Scale bars=1000 Å (a), 2000 Å (b).

(a)

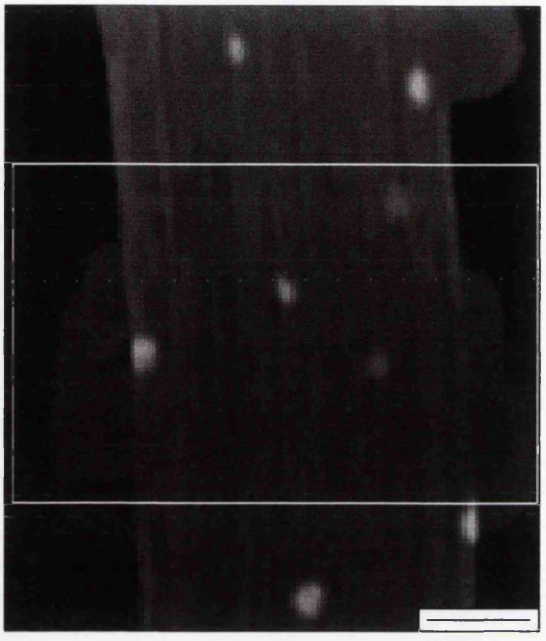

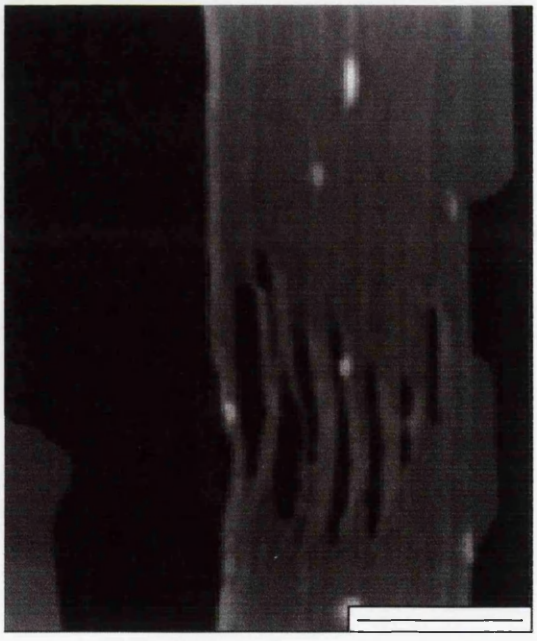

(b)

degree of order exists along the direction of the striations of figure 11.7 (a). The lattice constant in this direction, *a*, as measured from both real-space images and corresponding 2D-FFT spectra, is 4.8 Å ± 0.5 Å. This value agrees well with the intra-backbone distance measured for various polydiacetylenes by electron diffraction.[20-22] Therefore, it is most likely that the direction of the striations of layer **1** and the stripes represents the direction of the polymer backbone. A certain degree of disorder exists along the inter-backbone direction. This is most likely due to the sliding of neighboring strands with respect to one another. From the 2D-FFT spectra it is seen that two unit cells are predominant, with inter-backbone distances, *b*, of 5.6 Å and 6.3 Å respectively and molecular area, *A*, equal to about 26 $Å^2$ in both cases. Taking into account the value of the angle measured between *a* and *b* in each case, 59^o and 74^o respectively, it is found that such values of *b* are consistent with two neighboring polymer backbones sliding of about $1/3\,a$ up or down the backbone direction with respect to one another (see inset of figure 11.7). Furthermore, the variation in contrast, as seen especially in figure 11.7 (c), may be due to the hydrocarbon planes not always being parallel to one another. Figure 11.8 shows an example of simultaneous topographic and frictional force images taken on layer **1**. Although the 'contrast' is sharper in the frictional force images ((b) and (f)), the same features are observed in the topographic pages ((a) and (e)).

Lattice resolution images on the stripes are difficult to obtain and often a hole is left in the layer. This is possibly due to the mechanical interaction of the tip with the layer. In the case of the filaments, lattice resolution images show a certain degree of order, as shown in figure 11.9. Both figure 11.9 (c) and 11.9 (d) show that one molecular axis is parallel to the direction of the stripes and filaments. In figure 11.9 (d), isolated areas of molecular order are visible with lack of long-range order however, as indicated by the fact that the peaks in the 2D-FFT appear diffused.

Blue-phase films formed after compressing the molecules to surface pressures higher than 20 mN/m show a similar morphology to that shown in figure 11.5. However, the domains density appears higher and extended areas of folded material are present. At the molecular level, the AFM images are indistinguishable from those shown in figures 11.6 and 11.7. These results are supported by the pressure-area isotherm (figure 11.3). In fact, the molecular area does not exhibit any significant change upon compressing the molecules to pressures higher than 20 mN/m.

The transfer of polymer molecules after compression to a surface pressure of 10 mN/m, i.e. before the collapse in the pressure-area isotherm (figure 11.3), does not result in uniform coverage and only scattered islands of material or loosely packed fibers are seen on the surface. Under no preparation conditions could monolayers of p-SAc/PCDA molecules be transferred on the surface. This result is

Figure 11.7 (following page). AFM images of blue-phase layer **1**. (a) Striations of layer **1**. Scale bar=200 Å. (b) and (c) Frictional force images acquired in the area shown in (a). Scale bars=10 Å. (d) and (e) 2D-FFT power spectra of (b) and (c), respectively. A higher degree of order is found along the direction of the striations, i.e. along the direction of the polymer backbone (lattice constant, a=4.8 Å ± 0.5 Å). Partial disorder is found in the inter-backbone direction. The two predominant unit cells are shown in the inset (b_1 = 6.3 Å, b_2 = 5.6 Å). Lattice resolution images were corrected for piezo calibrations distortions against images of mica taken on the same sample.

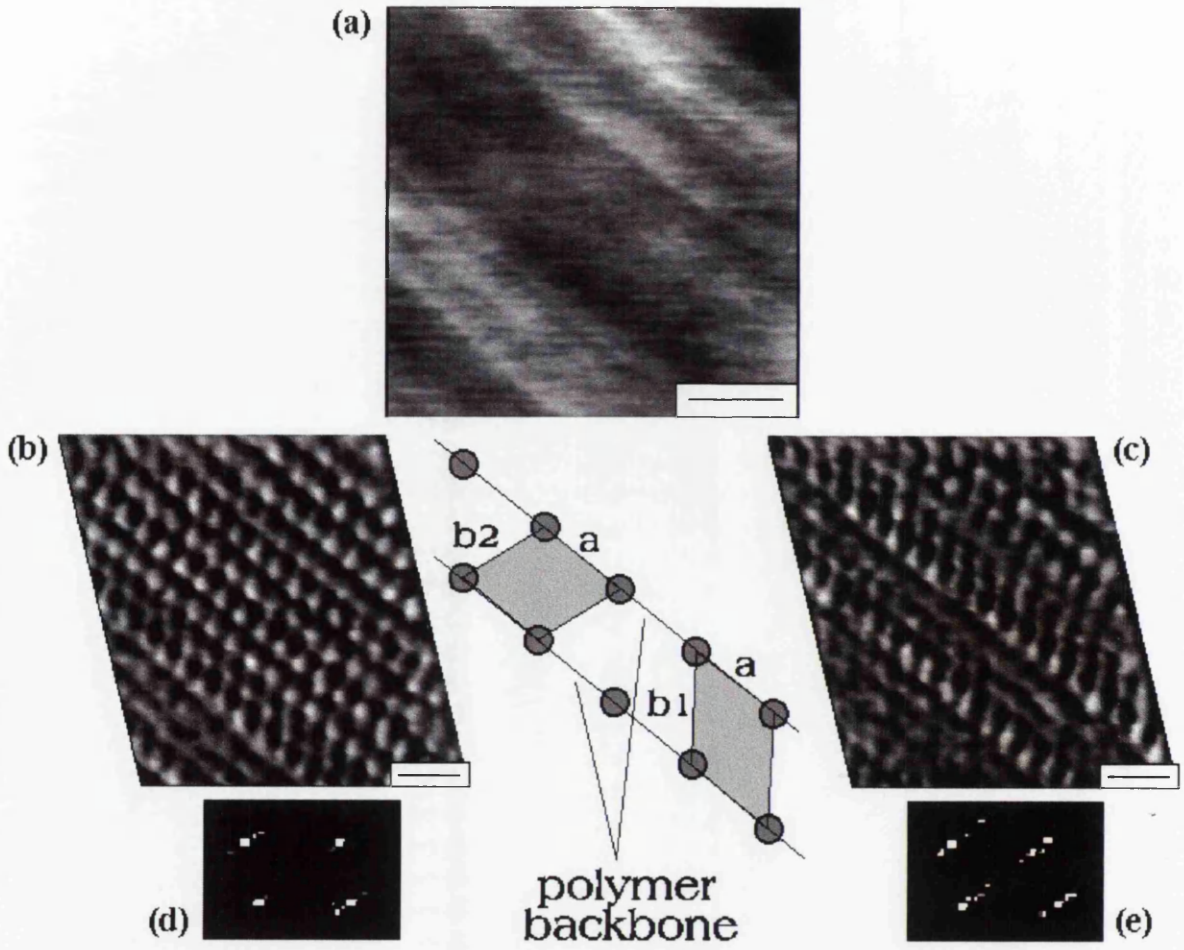
(a)
(b)
(c)
b2
a
a
b1
polymer
backbone
(d)
(e)

Figure 11.8 (following page). Simultaneous topographic (a) and frictional force (b) images taken at 0.5 nN on layer **1**. Scale bars=10 Å. The corresponding 2D-FFT power spectra are shown in (c) and (d), respectively.

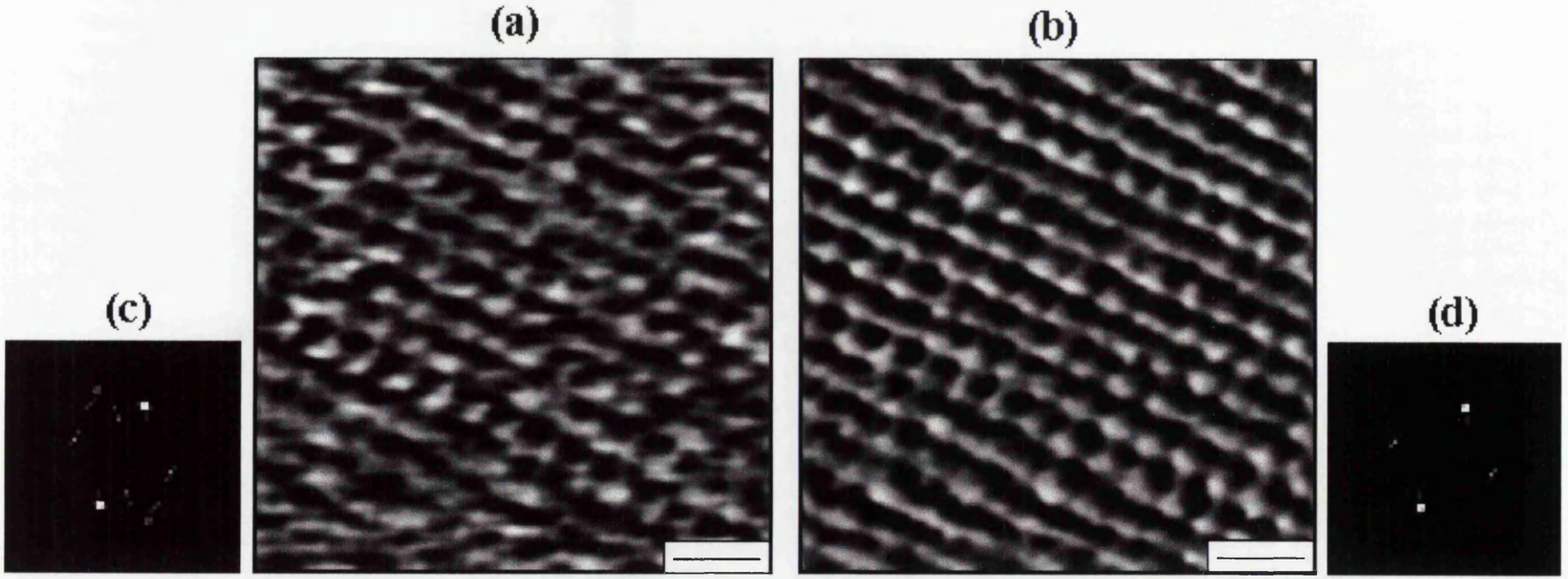
(a)
(b)
(c)
(d)

Figure 11.9 (following page). (a) and (b) Filaments present on top of type 3 stripes of blue-phase p-SAc/PCDA films. Scale bars=1000 Å. (c) and (d) Frictional force images on the filaments of (a) and (b), respectively. Scale bars=10 Å. (e) and (f) 2D-FFT spectra corresponding to (c) and (d), respectively. Only short-range order is observed.

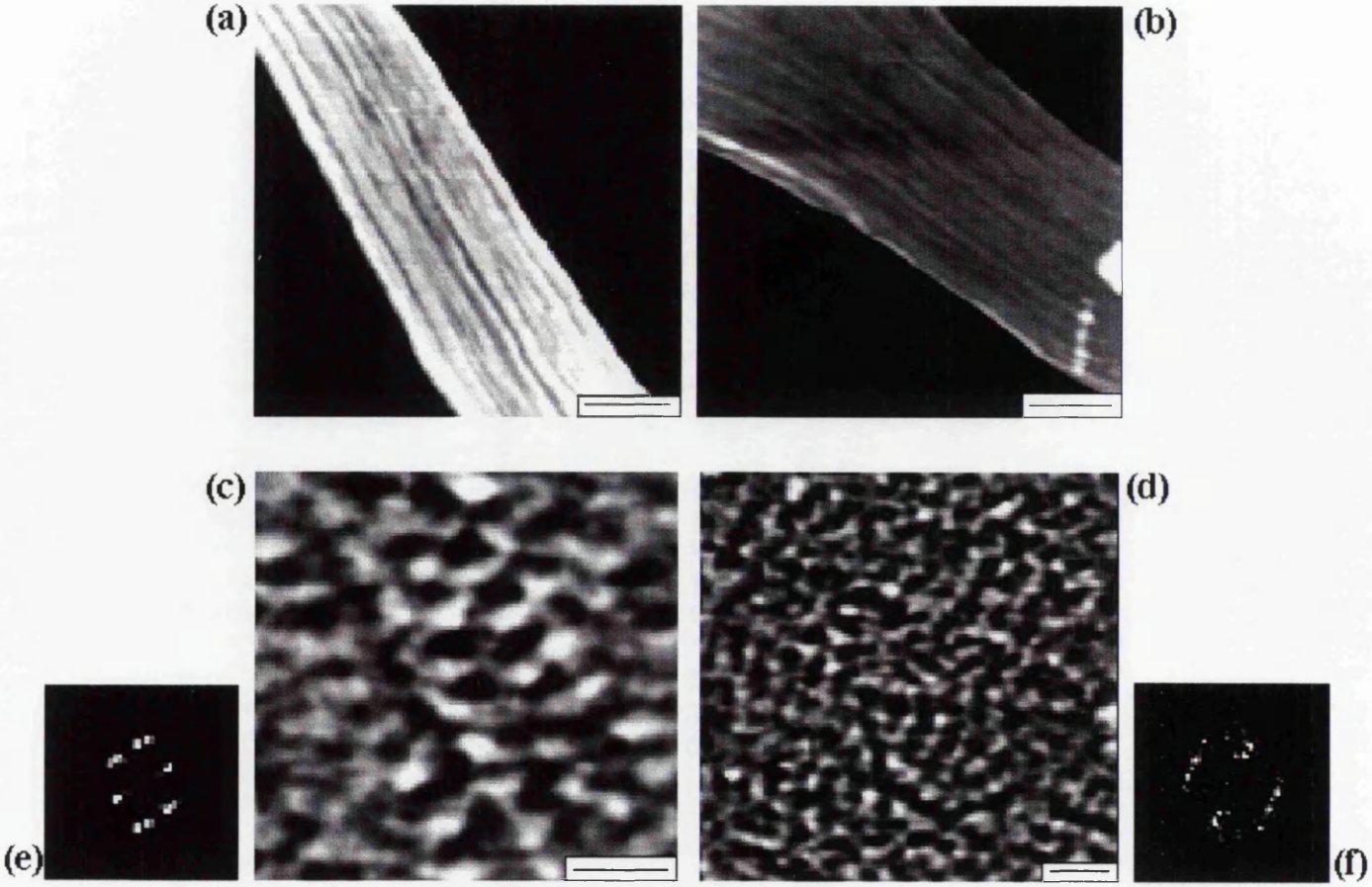
(a)
(b)
(c)
(d)
(e)
(f)

consistent with the molecules being in a liquid phase prior to the collapse. In other words, headgroup interactions prevent the molecules from being closed-packed. This behavior is similar to that previously observed for the pure acid.[22]

11.6 Morphology of Red-Phase p-SAc/PCDA Films

Figure 11.10 (a) shows a 39 x 39 μm^2 topographic image of a red-phase film lifted after compressing the monomer molecules to 20 mN/m and exposing them to UV light for 20 mins. As can be seen, the film shows micron-sized domains separated by dark areas, in an analogous way to that observed for blue-phase films (figure 11.5). However, the density of the domains appears to be lower than for blue-phase films prepared under the same pressure conditions. Figure 11.10 (b) shows a particular of a single domain. As already shown for the blue-phase films, within each domain a stripe-like morphology on top of a nearly complete layer (layer **1**) is found. In this case, however, the stripes appear more closely spaced and often are observed to form an almost complete layer. As for blue-phase films, the height of layer **1** is measured to be 79 ± 8 Å, corresponding to a trilayer tilted about 35^o from the surface normal. The height of the stripes is 58 ± 6 Å with respect to layer **1** (type **2** stripes). In several cases pronounced folding of type **2** stripes is also observed, however no filament-like structure is visible. In contrast to the observation for the blue-phase films, no type **3** stripes are observed. The height of type **2** stripes corresponds to a bilayer tilted about 25^o from the surface normal. However, it is also consistent with a bilayer in which the hydrophilic and hydrophobic side chains are untilted and tilted about 35^o from the surface normal, respectively.

Both layer **1** and type **2** stripes appear to be mechanical robust, so that repeated scanning at low load does not produce any damage. Lattice resolution images are easily obtained both on layer **1** and type **2** stripe, as shown in figure 11.10 (c) and 11.10 (d). The difference between the two layers is readily observed. The lattice observed for layer **1** (figure 11.10 (c) and 11.10 (e)) is indistinguishable from that found for the blue-phase films (see figure 11.7). Lattice resolution images obtained on type **2** stripes show a well ordered lattice (figure 11.10 (d) and 11.10 (f)). The intra-backbone distance, as defined by the direction of the stripes, is consistently found to be 4.9 ± 0.5 Å. The lattice constant for either of the two other directions is measured to be 4.6 ± 0.5 Å. Lattice resolution images are not easily obtained on folded type **2** stripes, as for the filaments on top of the blue-phase film stripes (see figure 11.9).

Figure 11.10 (following page). AFM images of red-phase p-SAc/PCDA films. (a) p-SAc/PCDA domains are separated by uncovered OTE areas. Scale bar=10 μm. (b) Detail of a single domain, showing a stripe-like morphology on top of a nearly complete layer (layer **1**). Scale bar=2000 Å. (c) Frictional force image acquired in the area of layer **1** enclosed by the white circle in (b). Scale bar= 10 Å. The molecular structure is indistinguishable from that of layer **1** of blue-phase films. (d) Frictional force image taken on the area of the stripe enclosed by the black circle in (b). Scale bar=10 Å. A well-ordered lattice is resolved (a =4.9 ± 0.5 Å, b = 4.6 ± 0.5 Å). (e) and (f) 2D-FFT spectra of (c) and (d), respectively.

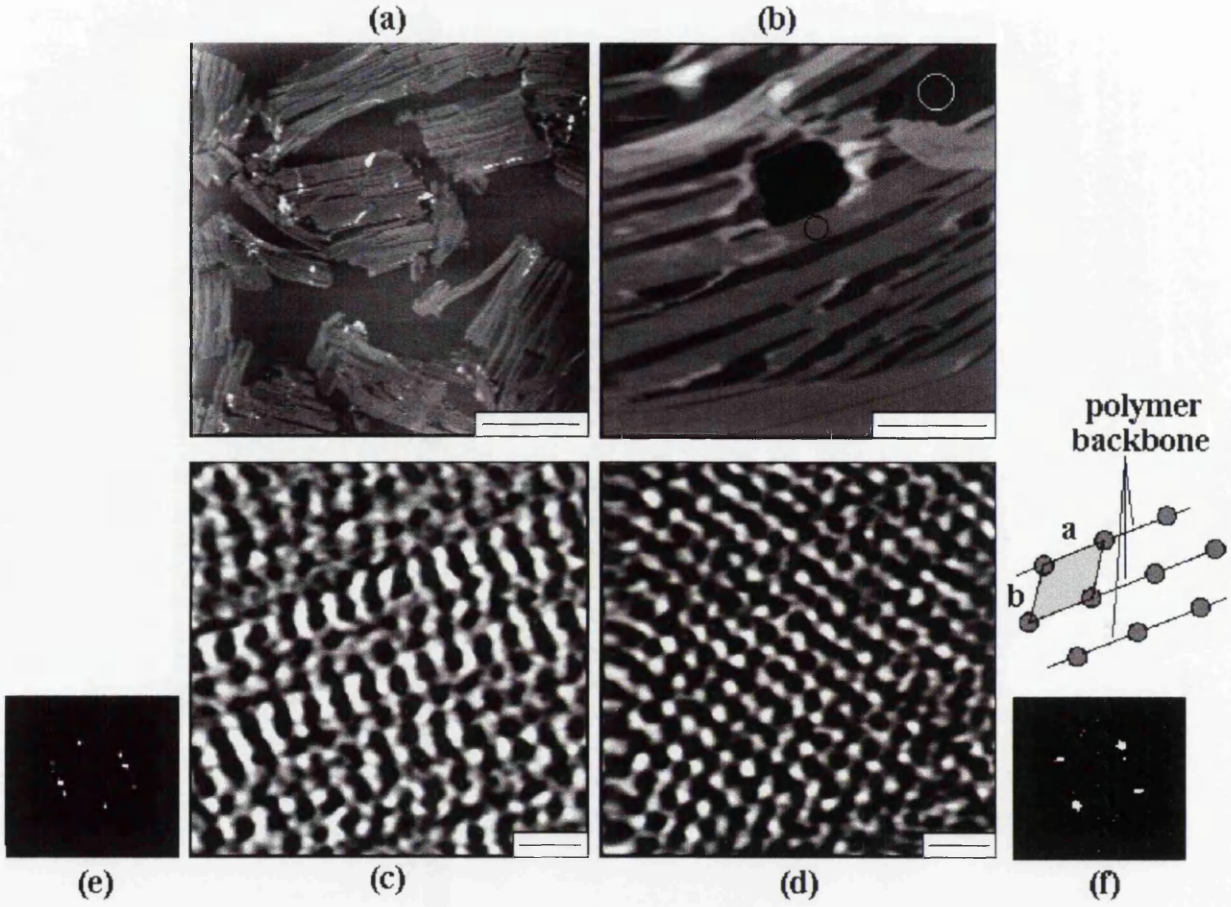
(a)
(b)
polymer
backbone
a
b
(e)
(c)
(d)
(f)

11.7 Morphology of Monomer m-SAc/PCDA Films

Figure 11.11 (a) shows a $5 \times 5\ \mu m^2$ of a monomer film (m-SAc/PCDA) transferred after compressing the molecules to a surface pressure of 20 mN/m. As can be seen, layers of material separated by dark regions are present on the surface and their structure appears essentially isotropic. Interestingly fairly straight edges are often visible, as can be seen both in figure 11.11 (a) and 11.11 (b). The dark regions are identified as being OTE areas, as described in section 11.5. Two and sometimes three layers of m-SAc/PCDA are visible in the AFM images. All layers are easily damaged when repeatedly scanned at low load, especially at the edges. However, no accumulation of material is visible in the vicinity of the holes, indicating again that the molecules are not permanently removed but rather laterally compressed. The thicknesses of the bottom and top m-SAc/PCDA layers are measured to be 82 ± 8 Å and 70 ± 7 Å respectively. In this case, while the bottom layer still corresponds to a trilayer tilted about 31° from the surface normal, the thickness measured for the top layer indicates that it is very tilted. The absence of the polymer backbone in this case could especially favor different tilt angles for the two alkyl chains on each side of the diacetylene unit. Furthermore, due to the lack of mechanical stability, it is more likely that the molecular arrangement in the layers be disturbed during the transfer onto the substrate.

Lattice resolution images can be obtained on both the bottom and the top layers. However, the resolution rapidly degrades as the tip damages the layer. Figure 11.11 (c) and 11.11 (d) show a frictional force image and corresponding 2D-FFT spectrum obtained on the bottom layer. As can be seen, while a certain degree of order exists, lack of long-range order is also observed.

11.8 Morphology of Blue-Phase Pure p-PCDA Films

Deposition of 100% p-PCDA molecules results in films that are indistinguishable from the p-SAc/PCDA ones both at the micrometer and molecular scales. Similarly to the p-SAc/PCDA films, two layers of the polymer are found and domains are separated by uncovered OTE areas. The height of layer **1** and the stripes is measured to be 78 ± 8 Å and 77 ± 8 Å respectively.

Layer **1** exhibits striations parallel to the stripes, similarly to those shown in figure 11.5 and the molecular level structure is indistinguishable from that of blue-phase p-SAc/PCDA films.

Figure 11.11 (following page). AFM images of a monomer m-SAc/PCDA film. (a) The deposition method results in two incomplete layers, that are easily damaged during scanning. Scale bar=1 μm. (b) Fairly straight edges are often observed. Scale bar=2000 Å. (c) Frictional force image taken on the bottom m-SAc/PCDA layer shown in (b). Scale bar=10 Å. Corresponding 2D-FFT spectra shown in (d). No long-range order is observed.

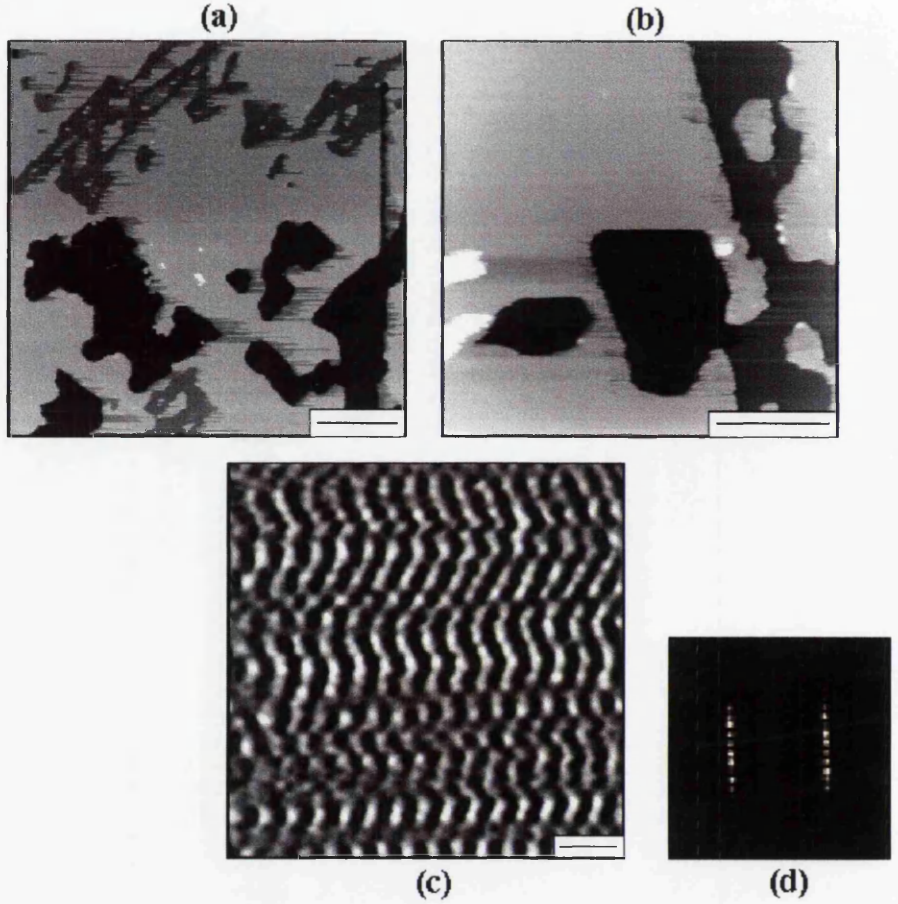
(a)
(b)
(c)
(d)

11.9 Morphology of Blue-Phase Cd-PCDA Layers

Figure 11.12 (a) shows a 0.8 x 0.8 μm^2 AFM image of a film compressed to 25 mN/m. The film was transferred as monomer onto freshly cleaved mica and then polymerized by exposing it to UV light for 1 minute. An almost complete layer is visible in the images. The presence of holes makes it possible to measure the height of the layer, that results to be 27.5 ± 3.0 Å. Lattice resolution images obtained inside the holes of figure 11.12 (a) show the hexagonal lattice characteristic of a mica surface. Therefore, it can be concluded that the deposition method results in the formation of one monolayer. The thickness of the layer is consistent with a monomolecular layer tilted about 31^o from the surface normal. Previous x-ray reflectivity studies similarly found a tilt angle of ~30^o for blue Cd salt multilayers of the same molecule used here.[21] The formation of monolayers in this case is the result of the introduction of Cd^+ ions in the subphase. Each of these ions strongly ion pairs to two COO^- of the SAc/PCDA headgroup and increases inter-molecular interactions, thus stabilizing the film.

Similarly to the observation for the blue p-PCDA and p-SAc/PCDA films, fine striations are visible. However, in contrast to the other two types of films they are not seen to extend over large distances, but rather look like short segments. A lattice resolution image obtained in the middle of figure 11.12 (a) and corresponding 2D-FFT spectrum are shown in figure 11.12 (b) and 11.12 (c) respectively. As can be seen a higher degree of order exists along the direction of the striations as previously observed. The lattice constant in this direction is found to be 4.9 ± 0.5 Å in agreement with that observed for the other layers under study. Furthermore, also for these layers a certain degree of disorder is shown to exist along the inter-backbone direction.

11.10 Frictional Properties of Films

Additional information about organic films can be obtained from the frictional force images acquired simultaneously to the topographic ones. Atomic force microscopy can help in the chemical identification of layers thanks to the distinct frictional properties of different chemical functionalities.[35, 36, 37] Absolute measurements are still out of reach in most cases due to the uncertainty on the tip geometry and levers calibration. However, relative measurements performed on different samples with the same tip, or on the same sample where different

Figure 11.12 (following page). AFM images of blue-phase Cd-PCDA layers. (a) A monolayer tilted about 31^{o} from the surface normal is deposited on mica by the LB deposition method. Short striations are visible. Scale bar=2000 Å. (b) Frictional force image taken at the center of the area shown in (a). Scale bar=10 Å. More order is found in the direction of the striations (lattice constant=4.9 $\pm$ 0.5 Å). Partial disorder in the inter-backbone direction may stem from irregular packing of the aliphatic chains. The 2D-FFT spectrum of (b) is shown in (c).

(a)

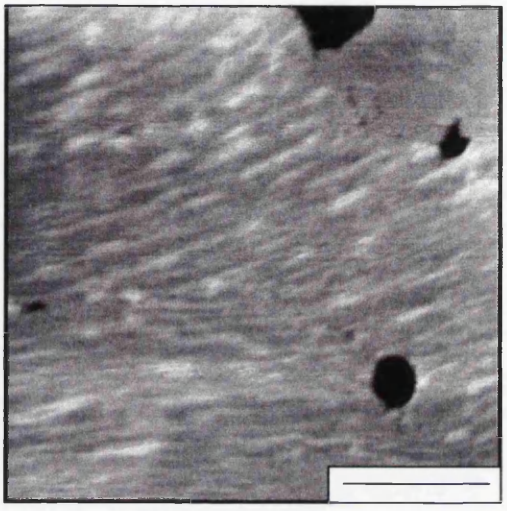

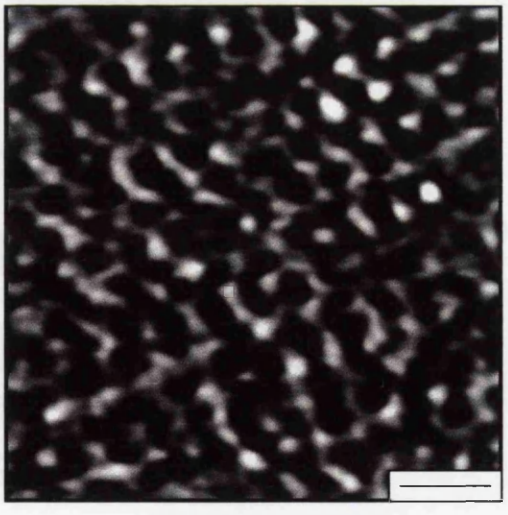

(b)

(c)

functionalities co-exist, can provide much information, as also discussed in chapters 8 and 10.[35-37, 38]

For the work described in this chapter, the simplest case is that of Cd-PCDA films. The films are transferred by the LB deposition method onto an hydrophilic surface, so that the hydrophobic tails are expected to be exposed to air. Indeed, the topographic images show that a monomolecular layer is on the surface and frictional force images show that the material in the holes (mica, hydrophilic) exhibits a higher frictional force than the p-Cd-PCDA layer, as shown in figure 11.13 (a) and (b). This result is consistent with a hydrophobic p-Cd-PCDA layer, that is the CH_3 termination is exposed to air, as expected.

In the case of the horizontal deposition method, the hydrophilic headgroups would be expected to be exposed to air, if a monolayer were transferred. In that case a friction contrast could be expected between the hydrophobic termination of an OTE monolayer and the hydrophilic termination of the acidic surface. However, topographic images show that multilayers are transferred onto the surface, in agreement with the overcompression of the molecules on the water surface. A schematic of the molecular arrangements that could be expected is shown in figure 11.14. Frictional force images of blue-phase p-SAc/PCDA and pure p-PCDA films show no friction contrast between the OTE and layer **1** areas (figure 11.13 (c) and (d)). The determination of the frictional properties of type **3** stripes is difficult because most often the stripes are covered by filament-like material, as described in section 11.5. Images like the one shown in figure 11.13 (c) and (d) show no frictional contrast for type **3** stripes compared to OTE and layer **1** areas. Changes in the humidity inside the AFM chamber left the frictional contrast unchanged. The frictional properties of the filaments are also difficult to determine, since these are usually closely spaced and their lateral dimension is comparable to the typical radius found for the tips used in these studies (200-400 Å). Because an increase in the lateral force signal is usually observed when the AFM tip scans across a step, a reliable friction measurement cannot be made in this case.

These results would not seem to be consistent with the expected molecular arrangement within the trilayers, as shown in figure 11.14. Previous angle-resolved XPS measurements performed on layers prepared in similar conditions were consistent with the layers having their hydrophilic head group exposed to air.[39] Separate evidence in favor of the conclusion that at least part of these films is acidic, comes from calcite mineralization experiments that will be described in detail in chapter 13. In this case, the blue-to-red color transition is observed upon the oriented growth of calcite crystals on blue 100% p-PCDA LS films. The chromatic transition cannot be observed, however, when the mineralization reaction is performed on hydrophobic LB 100% p-PCDA films (that is films prepared, in the

Figure 11.13 (following page). Simultaneous topographic and lateral force images for blue-phase p-Cd-PCDA (a, b), blue-phase p-SAc/PCDA (c, d) and red-phase p-SAc/PCDA (e, f) layers. Brighter areas in the lateral force images indicate a higher value of the lateral force. Scale bars=2000 Å. The contrast observed in (b) is consistent with the Cd-PCDA molecules exposing their tails to air. Surprisingly, no friction contrast is observed in (d) and a higher frictional force is measured on type **2** stripes of red-phase films as compared to layer **1** and OTE areas (f).

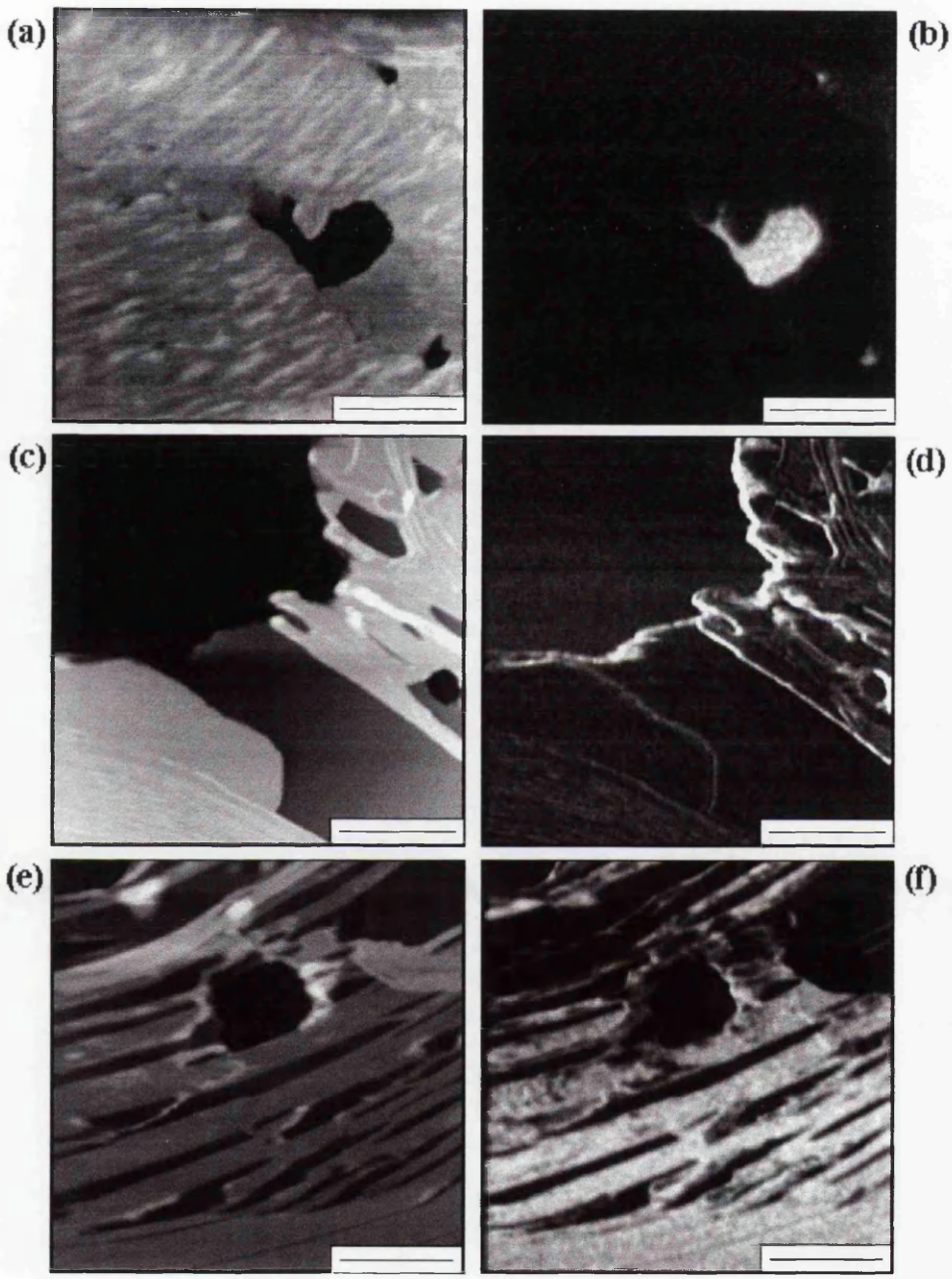
(a)
(b)
(c)
(d)
(e)
(f)

Figure 11.13

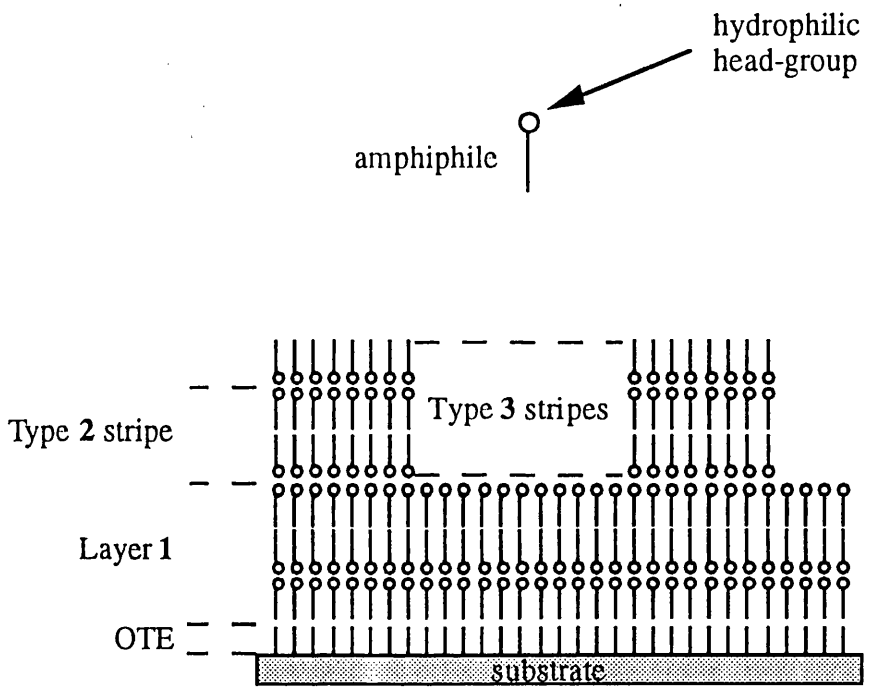

Figure 11.14. Schematic of the molecular arrangement expected for PCDA films deposited on a hydrophobized substrate.

same pressure conditions described here, by the LB technique). The above friction results may be explained if the hydrophilic properties of the OTE monolayer and the PCDA film change. Contact angle measurements of OTE monolayers after rinse in de-ionized water, i.e. in conditions similar to the LS or LB preparation of PCDA layers, gives a value of ~70° as opposed to ~112° obtained for untreated film. This is attributed to the intercalation of water inside the pinholes and defects of OTE monolayers, as discussed in chapter 10. On the other hand, COOH terminated thiol monolayers on gold were shown to become contaminated after exposure to air and the contact angle was seen to increase from 0° to ~75°. Although, correspondence between contact angle measurements and frictional properties as measured by AFM is not straightforward, these wettability results could explain the frictional properties observed for blue-phase p-SAc/PCDA and p-PCDA layers.

Frictional force images of red-phase p-SAc/PCDA films show that no friction contrast exists between layer **1** and OTE areas, while a higher frictional force is measured on type **2** stripes compared to layer **1**. No friction contrast exists between folded type **2** stripes and layer **1** or OTE areas (figure 11.13 (e) and (f)). In one occasion when mica, OTE and p-SAc/PCDA areas could be imaged at the same time, the following friction contrast was observed: type **2** stripes > mica > layer **1** = OTE.

These results, together with those discussed in sections 11.5 and 11.6, indicate that the structure and frictional properties of layer **1** in both blue and red-phase layers, are similar. A clear difference exists instead between type **3** stripes of blue-phase films and type **2** stripes of red-phase layers. Whether their frictional properties are the result of two different chemical terminations, or can be attributed to their different structural properties and/or be the result of the polymerization process itself, cannot be established from this data.

11.11 Polymerization and Transfer Mechanisms

The first question that arises in all LB experiments is how much of the film structure visible on the substrates already exists at the air-water interface. The horizontal transfer technique in principle offers the possibility of reproducing the molecular arrangement present at the air-water interface onto the substrate, as schematically indicated in figure 11.14. Such a possibility is higher in the case of polymerizable amphiphiles, due to their high viscosity and in particular for polydiacetylenes, because of their polymerization in the solid state.

In the cases discussed in this chapter, polymeric p-SAc/PCDA layers were formed at the air-water interface. The low percentage (5 %) of sialic acid introduced into the matrix was not shown to affect greatly neither the polymerization kinetics nor the final structure of the films. Percentages higher than 10 % were found to hinder polymer formation,[40] likely because the topochemical reaction requirements cannot be fulfilled due to steric effects.

As far as the nature and origin of the domains, their formation and morphology appears to be related to the polymerization process since no striations and stripe-like structures are visible on the monomer films. Furthermore, the stripes are probably already present at the air-water interface, since they are only found on top of layer **1** and they do not fill the holes and breaks of layer **1** onto the OTE, but rather wrap around them (see, for example, figure 11.10 (b)). It is possible, however, that the mutual orientation of single domains with respect to one another changes during transfer. The filaments often visible on the stripes of blue-phase films appear as bundles of material that fold over during the transfer of the film due either to the presence of impurities and defects or mechanical instability during transfer. In many cases the stripes appear to have folded in a way similar to the turning of the pages of a book and it is possible that each filament is in fact a trilayer collapsed on itself. This might explain the lack of interaction between adjacent filaments. As to why the stripes of blue-phase films are mechanically less stable than layer **1**, a possibility is that their degree of polymerization is lower due to the fact that they are deeper into the water and hence further away from the UV source. In addition, the large tilt observed for the top layer in monomer films may prevent the molecules from adopting the spatial arrangement necessary for the polymerization to occur. In the case of red-phase p-SAc/PCDA films, the longer polymerization time coupled to the higher mobility, both in the lateral as well as in the vertical direction, of the molecules in the stripes with respect to those of layer **1**, may favor the formation of well ordered, fully polymerized and mechanically stable structures. That in turn may impose strain on the polymer backbone, causing a decrease in the extent of overlap of the π-π bonds and with that the changes in the optical spectra. Spectroscopic studies have long suggested that the electronic properties of the polymer backbone are strongly coupled to the side chain conformation.[41, 42] As it will be shown in chapter 12, the side chains of p-SAc/PCDA films re-organize into a completely ordered structure upon the blue-to-red thermochromic transition. That in turn very strongly suggests that the strain imposed by the side chains on the polymer backbone, as evidenced by the changes in the optical spectra, is the cause of thermochromism for this type of films. A previous report,[43] based on FTIR and Raman spectroscopy results, showed that the formation of the red phase after prolonged exposure to UV light has to be attributed to thermal effects. However, as

it is shown in this thesis for the first time, the fact alone that the same spectroscopic data is obtained in both cases does not ensure that micron and molecular scale morphology are the same. Indeed, the micron scale morphology of heated samples (chapter 12) is very different from the one of samples obtained by prolonged exposure to UV light at the air-water interface (section 11.6). As will be described in detail in the next chapter, in the case of thermochromism, the blue-phase domains separate into fine polymer fibers, that are highly ordered and remain such at temperatures well beyond the thermochromic transition.

Finally, the reason why type **3** stripes are found in the blue-phase films, while type **2** stripes are mostly common in the red-phase films is not clear, but the results presented here suggest that it might be related to the polymerization process itself.

Another important question that arises in these studies, concerns the collapse mechanism for the monolayer at the air-water interface. While this has been a point of great interest for the past twenty years, the answer is very difficult to find since usually there is not enough direct experimental evidence to support proposed mechanisms. The mechanism most commonly accepted was proposed by Reis.[44, 45] It depicts the collapse process as a sequence of weakening and folding/bending of the monolayer (figure 11.15) with formation of stable ridges and platelets. The existence of such ridges and platelets has been confirmed by electron microscopy,[44, 45] however, to the author's knowledge, there is no experimental evidence on the orientation of the molecules within the collapsed monolayer. The orientation of the molecules in the collapsed monolayer at the air-water interface cannot be determined from the results presented in this thesis. However, if major disruption and/or overturn of molecules occurred during the films transfer, it seems unlikely that a very regular morphology, such as the one observed for the films described here, would be observed over several tens of microns.

11.12 Summary and Conclusions

Atomic force microscopy was used for the first time for a detailed and systematic characterization of thin films of 10,12 pentacosadiynoic acid. Monomer, blue and red phase films of sialic acid functionalized PCDA molecules, blue p-PCDA and p-Cd-PCDA films were studied. In contrast to diffraction methods, both monolayers and multilayers films could be successfully characterized at a very high lateral resolution and in a non-destructive manner.

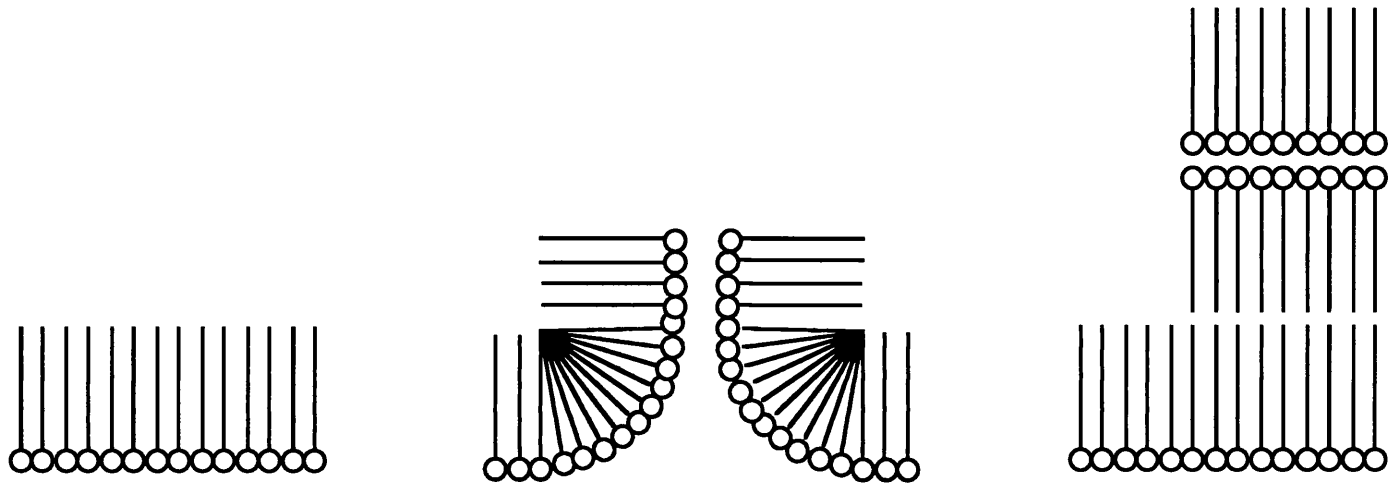

Figure 11.15. The stages of collapse of an overcompressed monolayer. (a) Uncollapsed monolayer at the air-water interface. (b) Upon overcompression, the molecules are pushed up from the water surface in a ridge two molecules thick. (c) The ridge finally breaks off and lies on the remaining monolayer film as a collapsed fragment. (Adapted from references 44 and 45).

Monolayers of the pure acids are unstable at the air-water interface and overcompression of the molecules leads to the formation of multilayers. Distinct differences are found between blue and red phase p-SAc/PCDA films, both at the micron and molecular scale. In both cases films consist of micron-sized domains separated by uncovered OTE areas. Within each domain a stripe-like morphology is found on top of a nearly complete layer. The bottom layer reveals similar characteristics in both blue and red films and it is equivalent to a PCDA trilayer tilted about 35^{o} from the surface normal. The direction of the polymer backbone can be identified and a high degree of order is found along this crystal axis in both chromatic phases. Different types of stripes are found for the two forms of the polymer. The stripes of the blue films are mechanically unstable and their thickness corresponds to a tilted trilayer, while those of the red films are more robust, well ordered and equivalent to a tilted bilayer. Frictional force images do not show any contrast between OTE, layer **1** and type **3** stripes, while a higher frictional force is measured on top of type **2** stripes. The very regular film morphology, observed to extend over several microns for each type of film, also suggests that much of the larger scale morphology is already present at the air-water interface.

Blue pure p-PCDA films are indistinguishable from p-SAc/PCDA films prepared in the same conditions, indicating that small percentages of the carbohydrate sialic acid do not affect the polymerization process.

The addition of $CdCl_2$ to the subphase at moderate pH increases the collapse pressure enabling the deposition of p-Cd-PCDA monolayers. Blue layers show a higher degree of order along the direction of the polymer backbone, while lack of long-range order is observed along the inter-backbone direction.

References

[1] A. Ulman, *An Introduction to Ultrathin Organic Films: from Langmuir-Blodgett to Self-Assembly*, (Academic Press: San Diego, 1991).

[2] H. Ringsdorf, B. Schlarb, J. Venzmer, *Angew. Chem. Int. Ed. Engl.*, **27**, 113 (1988).

[3] *Polydiacetylenes*, D. Bloor and R. R. Chance edts. NATO ASI Series E: Applied Sciences, vol. 102 (Martinoff Nijhoff Publishers: Dordrecht, 1985).

[4] *Polydiacetylenes*, H.-J. Cantow edt., Advances in Polymer Science Series, vol. 63 (Springer-Verlag: Berlin, 1984).

[5] G. Wegner, *Z. Naturforsch*, **24B**, 824 (1969).

[6] G. Wegner, *Pure & Appl. Chem.*, **49**, 443 (1977).

[7] R. H. Baughman, *J. Polym. Sci. Polym. Phys. Ed.*, **12**, 1511 (1974).

[8] R. H. Baughman, R. R. Chance, *J. Polym. Sci. Polym. Phys. Ed.*, **14**, 2037 (1976).

[9] G. J. Exarhos, W. M. Risen Jr., R. H. Baughman, *J. Am. Chem. Soc.*, **98**, 481 (1976).

[10] W. Spannring, H. Bässler, *Chem. Phys. Lett.*, **84**, 54 (1981).

[11] C. Sauteret, J. P. Hermann, R. Frey, F. Pradiere, J. Ducuing, R. H. Baughman, R. R. Chance, *Phys. Rev. Lett.*, **36**, 956 (1976).

[12] D. Sarid, *Opt. Lett.*, **6**, 552 (1981).

[13] R. J. Seymour, G. M. Carter, Y. J. Chen, B. S. Elman, C. J. Jagannath, M. F. Rubner, D. J. Sandman, M. K. Thakur, S. K. Tripathy, *Proc. SPIE*, **578**, 137 (1985).

[14] R. H. Baughman, H. Gleiter, N. Sendfeld, *J. Polym. Sci. Polym. Phys. Ed.*, **13**, 1871 (1975).

[15] C. Galiotis, R. J. Young, *Polymer*, **24**, 1023 (1983).

[16] D. N. Batchelder, D. Bloor in *Advances in Infrared and Raman Spectroscopy*, R. J. H. Clark, R. E. Hester edts., vol. 11 (Wiley Heyden, 1984).

[17] D. Kobelt, E. F. Paulus, *Acta Crystallogr. B*, **30**, 232 (1974).

[18] V. Enkelmann, G. Wegner, *Makromol. Chem.*,**178**, 635 (1977).

[19] V. Enkelmann, R. J. Leyrer, G. Wegner, *Makromol. Chem.*, **180**, 1787 (1979).

[20] D. Day, J. Lando, *Macromolecules*, **13**, 1478 (1980).

[21] G. Lieser, B. Tieke, G. Wegner, *Thin Solid Films*, **68**, 77 (1980).

[22] B. Tieke, G. Lieser, *J. Coll. Interf. Sci.*, **88**, 471 (1982).

[23] R. A. Nallicheri, M. F. Rubner, *Macromolecules*, **24**, 517 (1991).

[24] M. Wenzel, G. H. Atkinson, *J. Am. Chem. Soc.*, **111**, 6123 (1989).

[25] H. Mino, H. Tamura, K. Ogawa, *Langmuir*, **8**, 594 (1992).

[26] R. R. Chance, *Macromolecules*, **13**, 396 (1980).

[27] D. H. Charych, J. O. Nagy, W. Spevak, M. D. Bednarski, *Science*, **261**, 585 (1993).

[28] J. C. Paulson in *The Receptors*; M. Conn Ed., vol. 2. (Academic Press: New York, 1985).

[29] W. Spevak, J. O. Nagy, D. H. Charych, M. E. Schafer, J. H. Gilbert, M. D. Bednarski, *J. Am. Chem. Soc.*, **115**, 1146 (1993).

[30] A. Berman, D. J. Ahn, A. Lio, M. Salmeron, A. Reichert, D. Charych, *Science*, **269**, 515 (1995).

[31] B. J. Orchard, S. K. Tripathy, *Macromolecules*, **19**, 1844 (1986).

[32] V. Dobrosavljevic, R. M. Stratt, *Phys. Rev. B*, **35**, 2731 (1987).

[33] J. O. Nagy, P. Wang, J. H. Gilbert, M. E. Schaefer, T. G. Hill, M. R. Callstrom, M. D. Bednarski, *J. Med. Chem.*, **35**, 4501 (1992).

[34] The percentage of sialic acid in the matrix was chosen according to previous studies which had shown that optimal binding of influenza virus occurs for sialic acid concentrations of 1-10%.

[35] R. M. Overney, E. Meyer, J. Frommer, H. -J. Güntherodt, M. Fujihira, H. Takano, Y. Gotoh, *Langmuir*, **10**, 1281 (1994).

[36] C. D. Frisbie, L. F. Rozsnyai, A. Noy, M. S. Wrighton, C. M. Lieber, *Science*, **265**, 2071 (1994).

[37] A. Kumar, H. A. Biebuyck, G. M. Whitesides, *Langmuir*, **10**, 1498 (1994).

[38] X.-D. Xiao, J. Hu, D. H. Charych, M. Salmeron, *Langmuir*, **12**, 235 (1996).

[39] T. E. Wilson, W. Spevak, D. H. Charych, M. D. Bednarski, *Langmuir*, **10**, 1512 (1994).

[40] D. H. Charych, Personal Communication.

[41] R. R. Chance, *Macromolecules*, **13**, 396 (1980).

[42] M. F. Rubner, D. J. Sandman, C. Velasquez, *Macromolecules*, **20**, 1296 (1987).

[43] M. Wenzel, G. H. Atkinson, *J. Am. Chem. Soc.*, **111**, 6123 (1989).

[44] H. E. Ries Jr., *Nature*, **281**, 287 (1979).

[45] H. E. Ries Jr., H. Swift, *Langmuir*, **3**, 853 (1987).

Chapter 12

A Structural Study of Thermochromism in Polydiacetylene Thin Films

12.1 Introduction

The blue-to-red color transition of polydiacetylenes has inspired researchers for several decades.[1, 2, 3] These color changes occur in polydiacetylene single crystals, cast films, solutions, and Langmuir-Blodgett films. They arise from a variety of environmental perturbations including temperature (thermochromism),[4] mechanical stress (mechanochromism),[5] pH changes,[6] upon specific binding of a biological target (affinochromism)[7] and upon the controlled deposition of co-aligned calcite crystals.[8] As described in chapter 11, the delocalized π-bonding structure of the polymer backbone gives rise to intense absorption in the visible region of the spectrum, imparting a vivid color to the polymer.

In order to fully exploit the use of functionalized polydiacetylenes in direct colorimetric detection, it is necessary to understand the nature of the color transition with respect to affinity binding. In addition, if the mechanism of color transitions can be understood for a variety of perturbations, it should be possible to optimize the design of the sensor for a multitude of technical and fundamental applications.

Besides the newly discovered phenomena,[7, 8] the blue-to-red color transition is not completely understood, even for the more well-known thermochromic effect. Numerous investigations on color transitions have relied on data obtained from employing one or two spectroscopic techniques, typically visible absorption[9, 10] and resonance Raman spectroscopy.[11, 12, 13, 14] These techniques directly probe the diacetylenic backbone chromophore, but not the side chain conformation. ^{13}C NMR[15, 16] methods probe the side chains, however, the assignment of specific conformational changes requires the use of synthetic model compounds with known conformation.[17] Generally, these studies suggest that the electronic properties of the polymer backbone are strongly coupled to side chain conformation, however, the exact relationship between them has not been fully elucidated.[18, 19] Therefore, a more detailed and direct molecular level probe of side group structure during the color transitions is desirable. Atomic force microscopy is particularly suitable for

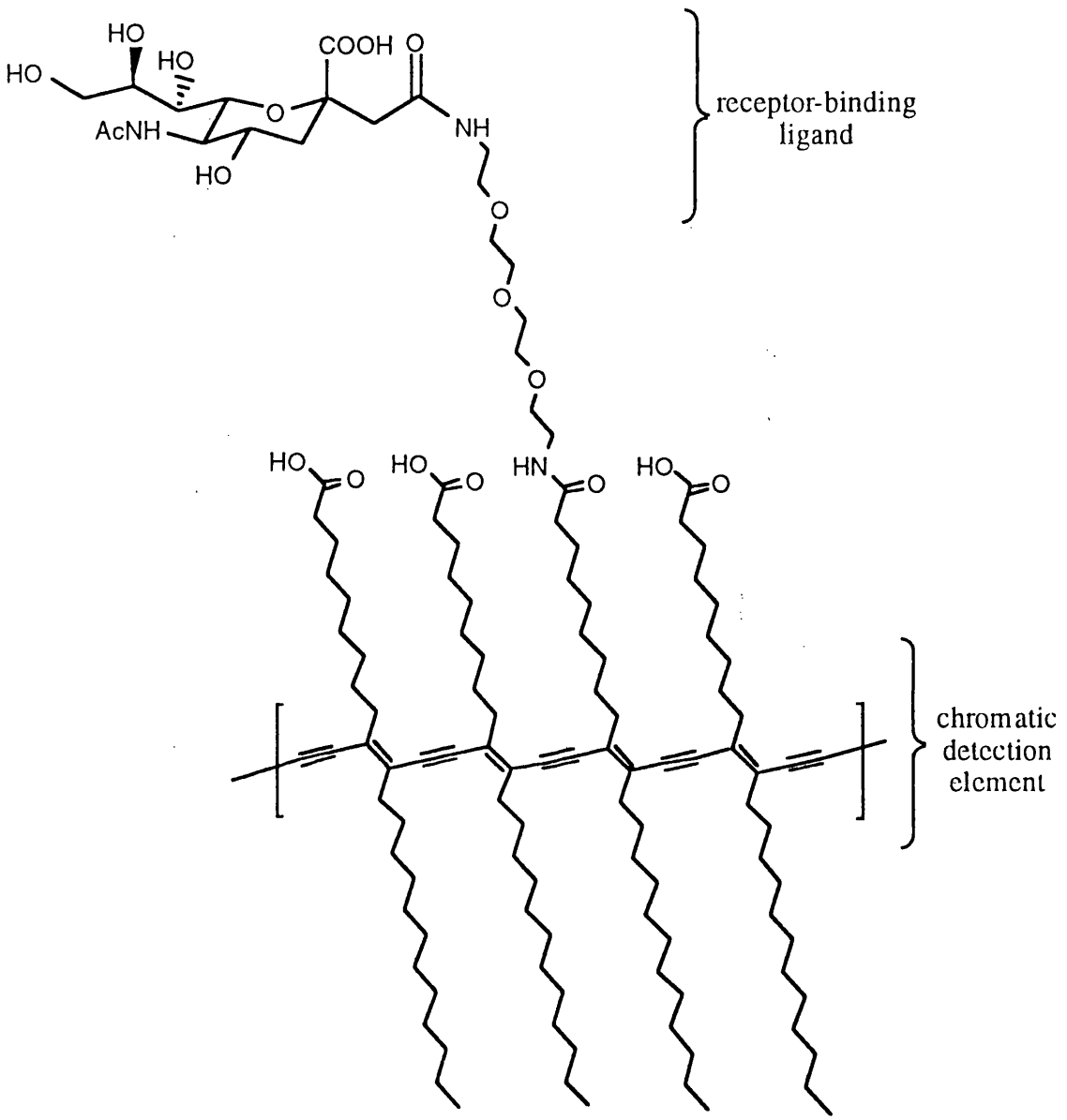

Figure 12.1. Schematic diagram of the bilayer assembly used for these studies. The conjugated polymer backbone of alternating double and triple bonds constitutes the chromatic detection element. The sialic acid is the receptor-binding ligand for the influenza virus.

directly investigating the structure and extent of long-range order in the side groups, but does not provide information about specific chemical bonds. Fourier transform infrared spectroscopy readily provides this information.[3] Therefore to perform a thorough analysis of conformational changes occurring in both the conjugated polymer backbone and in the side chains both techniques have been used. In this chapter, a systematic investigation, which combines visible absorption (for backbone conformation) with atomic force microscopy and FTIR (for side chain structure), is reported in relation to the thermochromic effect of Langmuir-Schaefer films of sialic acid functionalized 10, 12 pentacosadiynoic acid. The molecular assembly is shown in figure 12.1. The assembly displays the carbon-linked glycoside of the carbohydrate sialic acid which is known to bind to the surface lectin of the influenza virus.[20, 21, 22] The polydiacetylene backbone functions as the chromatic detection element.

12.2 Experimental Section

12.2.1 PCDA Film Preparation

Glass and mica surfaces were made hydrophobic as described in chapter 11. All substrates were kept under pure cyclohexane prior to transfer of the polydiacetylene film.

The blue-phase p-SAc/PCDA films were prepared by the LS method as described in chapter 11, after compressing the molecules to a surface pressure of ~20 mN/m.

12.2.2 Heat Treatment of Blue-Phase Samples

The blue samples were heated in a vacuum oven for 30 minutes at each temperature (50, 70, 90, 110, 130 °C). The samples were cooled to room temperature before being characterized.

12.2.3 Atomic Force Microscopy

Images larger than 1 μm^2 were acquired at LBNL with the commercially available instrument described in chapter 4. Images smaller than 1 μm^2 were taken at LBNL with the home-built AFM. Silicon nitride cantilevers with a nominal force constant of 0.1 N/m were used. All measurements were carried out under ambient laboratory conditions.

12.2.4 Fourier Transform Infrared Spectroscopy[23]

Spectra were collected with a Perkin-Elmer FTIR 2000 spectrometer equipped with an MCT-A (mercury-cadmium-telluride) detector which was cooled at liquid nitrogen temperature. The spectrometer was purged continuously with dry nitrogen gas to minimize water vapor bands. 512 scans at a resolution of 4 cm^{-1} were added in order to achieve a reasonable signal-to-noise ratio. A non-polarized beam in transmission mode at perpendicular incidence angle was employed. The background single beam spectrum was obtained with a clean glass substrate. From each polydiacetylene sample spectrum was subtracted that of an OTE film treated at the same temperature. The transmission spectra showed a typical cut-off below ~2200 cm^{-1}, since glass substrates were used as sample supports. In order to investigate IR bands below the cut-off wavenumber, which are related to head groups of the polydiacetylene film, the external reflection mode at a near normal incidence angle (10^{o} off from the surface normal) was employed. After heating, all samples were probed in a sample chamber at room temperature. The IR spectra reported here are raw data.

12.3 Results and Discussion

12.3.1 Visible Absorption Spectroscopy

Figure 12.2 shows the optical absorption spectra obtained at different temperatures (25, 50, 70, 90, 110 °C). See figure 11.4 for comparison.

The optical absorption spectrum for the blue-phase film is shown in figure 12.2 (a). The main excitonic peak of the blue form occurs at 640 nm, with smaller vibronic maximum occurring at 590 nm. At 25 °C the blue-phase film also shows the presence of the red phase, as evidenced by the small but non-negligible absorption at 540 nm.

The heat treatment of blue phase films leads to the red phase (thermochromism). Optical spectra of heat-treated films are shown in figure 12.2(b) - 12.2(e). Heating the blue-phase films to 50 °C produces only a slight increase in the red phase peak at 540 nm (figure 12.2 (b)). This film appears blue-purple to the naked eye. Upon increasing the temperature to 70, 90 and 110 °C, the blue-phase absorption maximum at 640 nm gradually disappears while the pink phase peak at 540 nm increases in intensity (figure 12.2(c) - 12.2(e)). The film appears dark pink at this point. As it can be seen, complete conversion to the red phase for the films described here occurs at temperatures between 70 and 90 °C.

Figure 12.2 (following page). Optical absorption spectra for blue-phase p-SAc/PCDA films (a) and films annealed to 50, 70, 90 and 110 ^{o}C (b-e).

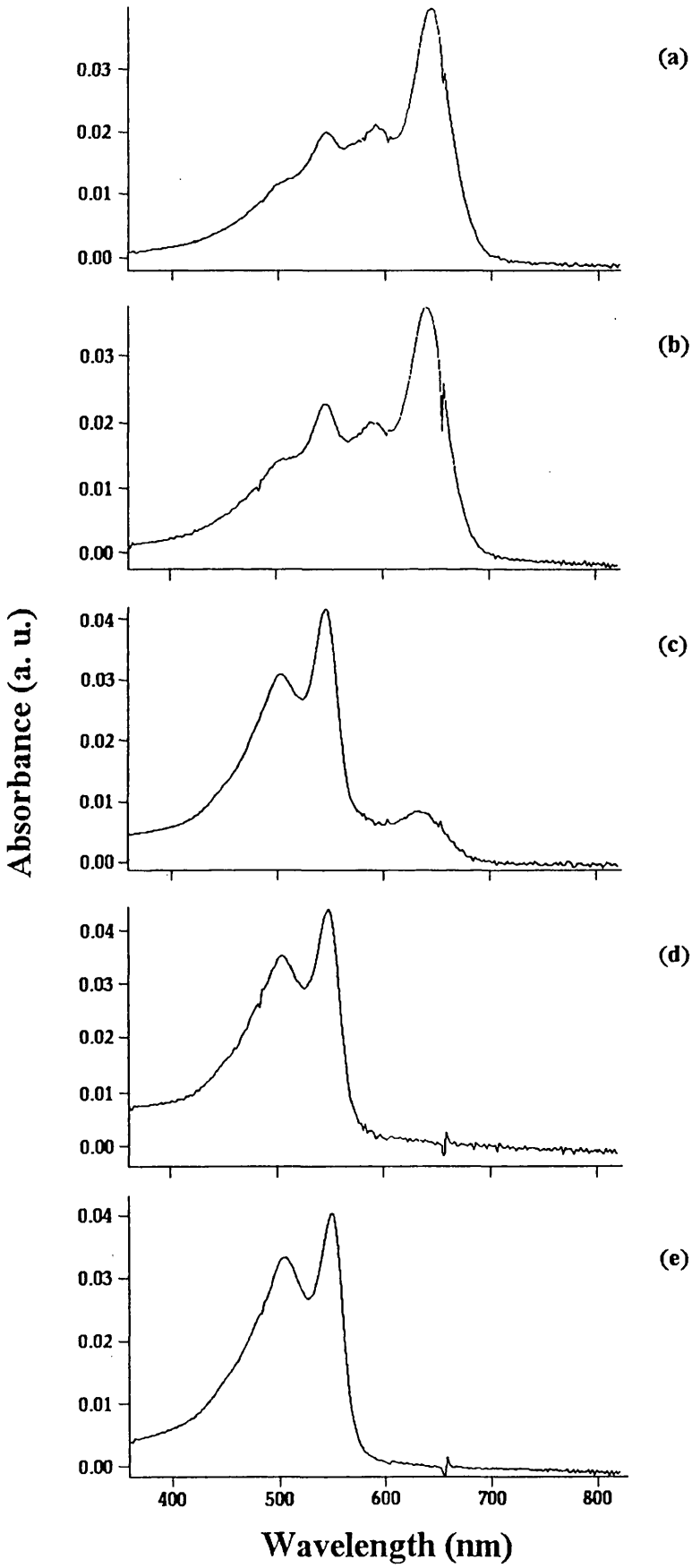
(a)
(b)
(c)
(d)
(e)
Absorbance (a. u.)
0.00
0.01
0.02
0.03
0.04
400
500
600
700
800
Wavelength (nm)

12.3.2 Structure of Heat-Treated Red-Phase Films

Figure 12.3 shows the micron-sized morphology of the p-SAc/PCDA films on glass upon heating. From (a) to (d), the film was heated to 25, 70, 90, and 110 °C, respectively. The same area of the sample was imaged at all temperatures by using commercially available photolithographically patterned glass slides (Bellco Glass Inc, Vineland, NJ). In this way the same area can be imaged at each stage and micron-scale morphological changes can be identified. The behavior of the p-SAc/PCDA films on glass upon heating is observed to be similar to that observed for films deposited on mica.

Heating the film to 50 °C changes the color from blue to blue-purple as indicated by the optical absorption spectra in figure 12.2(b). However, the morphology of the film is very similar to that of the blue film, shown in figure 12.3(a). A few more cracks start appearing in layer **1** and the stripes are still parallel to each other. The molecular scale structure is undistinguishable from that of the blue films. At 70 °C, more numerous cracks parallel to the direction of the polymer backbone are formed in layer **1** (figure 12.3 (b)). By comparison with figure 12.3(a), it can be seen that the breakage of layer **1** starts where cracks and holes already existed in the blue film. Heating the film at 90 °C produces more cracks (figure 12.3(c)). The stripes now show a high degree of bending and in many cases they are no longer parallel. The separation of layer **1** into fine, flexible fibers proceeds further after the film is heated at 110 °C (figure 12.3(d)) and 130 °C (not shown). The flexibility of the polymer fibers in many cases results in the formation of 'nets' that, in some cases, extend for several microns (see figure 12.4(j)). Importantly, repeated scanning at low load over any p-SAc/PCDA region in the red phase films does not result in any damage, in contrast to that observed for blue phase films. The step heights measured from AFM images for the red phase films indicate that the molecular tilt of the SAc/PCDA chains decreases upon the thermochromic blue-to-red color transition. The layers thickness increases of about 15% with respect to the blue phase films and the tilt angle decreases to about 19°. Previous small angle x-ray scattering measurements have determined a ~10% increase in the thickness of the layers for red polymerized p-Cd-PCDA multilayers.[24] Figure 12.4 shows details of single p-SAc/PCDA domains (left column of images) and corresponding molecular scale images (middle column of images) for films at 25, 70, 90, 110, 130 °C. The corresponding 2D-FFT spectra are also shown (right column). These images are for films deposited on mica. As can be seen, the thermochromic transition is characterized by significant changes in the molecular structure of the films. The structure for the films heated to 50 °C and 70 °C (figure 12.4(e)) is indistinguishable from the blue films one (figure 12.4(b)). However, after the films have fully converted to the red phase (figure 12.4(h),

Figure 12.3 (following page). AFM images for a series of heat-treated red-phase p-SAc/PCDA films. Films were deposited on OTE/glass. Scale bars=2 μm. (a) no heating (blue-phase); (b) 70 °C, 30 minutes; (c) 90 °C, 30 minutes; (d) 110 °C, 30 minutes. Upon annealing, layer 1 starts separating parallel to the direction of the polymer backbone into fine fibers. The process starts from the holes and cracks already present in the blue-phase films.

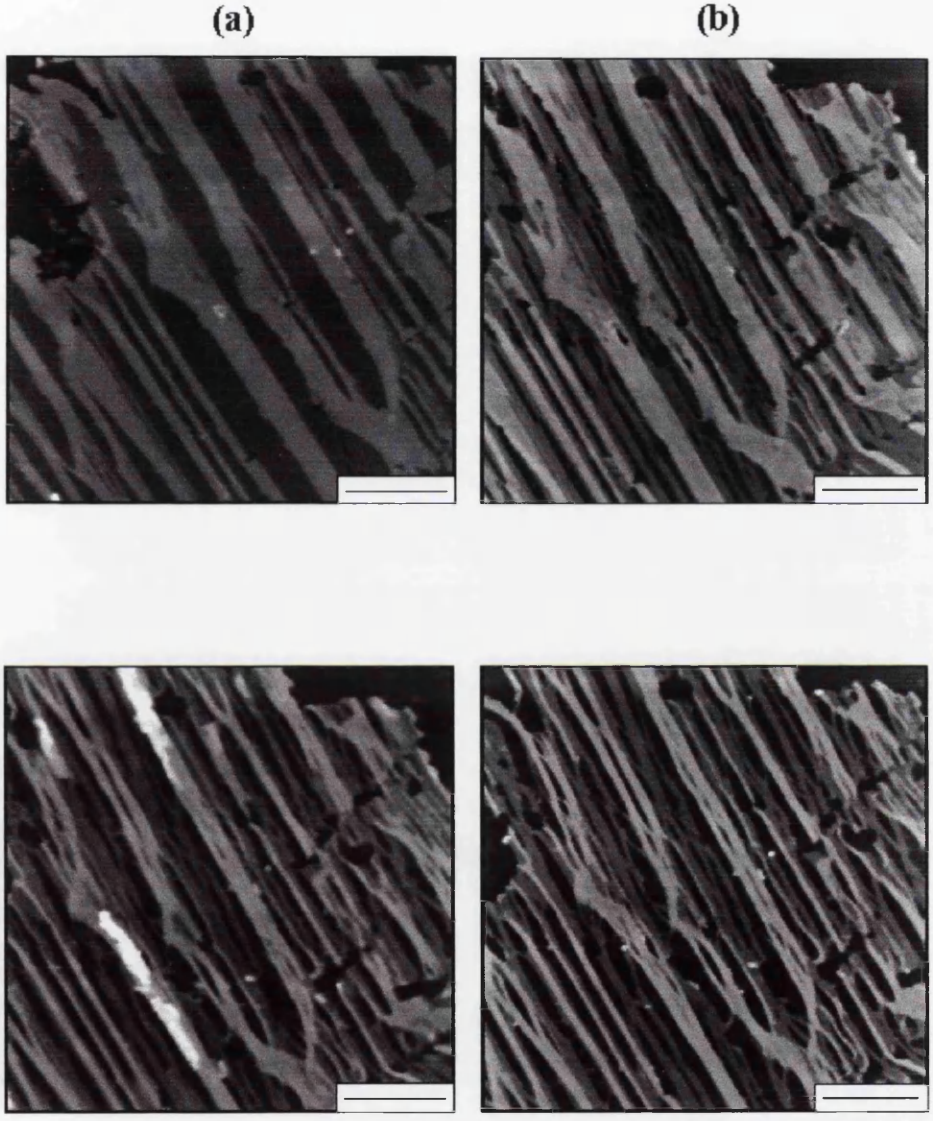
(a)
(b)
(c)
(d)

Figure 12.3

12.4(k) and 12.4(n)) the AFM images reveal a well ordered structure, with a hexagonal periodicity, as clearly shown by the corresponding 2D-FFTs spectra. The lattice constant is measured to be 5.0 Å ± 0.5 Å. By comparison with figure 12.4(g), 12.4(j) and 12.4(m) respectively, it can be also be seen that one of the crystal axes is still parallel to the direction of the polymer backbone (that is the direction of the fibers).

These AFM studies show that the thermochromic changes in the electronic structure of the conjugated polymer backbone, revealed by the changes in the optical absorption spectra, are accompanied by the re-organization of the side chains into a completely ordered structure. Strikingly, this order is maintained even after annealing the films to 130 °C, i.e. well above the thermochromic transition, temperature at which the OTE layer is no longer flat and uniform (see chapter 10).

Preliminary results obtained for the thermochromic transition of p-Cd-PCDA monolayers suggest that the retention of molecular order at elevated temperatures is not limited to the multilayered structures of the study described here, but occurs also for p-Cd-PCDA monolayers.

12.3.3 FTIR Spectroscopy

The transmission spectra presented in figure 12.5 shows that the peak intensity for the symmetric methylene stretching band (ν_s CH_2) at 2848 cm^{-1} changes little as the p-SAc/PCDA film is heated up to 110 °C. Upon heating at 130 °C, the intensity decreases about 13%. Its peak position also remains nearly constant throughout the sample treatment. By contrast, the peak intensity for the asymmetric methylene stretching band (ν_a CH_2) at ~2917 cm^{-1}, increases gradually as the p-SAc/PCDA film is heated up to 70 °C. Its net increase is about 17 ± 5 % of the initial value (table 12.I). The peak position also shifts to a lower wavenumber. Then the values remain unchanged until the temperature is raised to 110 °C. As the transition dipole moment of the methylene stretching band becomes parallel to the surface and hence to the electric field of the IR beam, its peak intensity increases, indicating that the alkyl side chains reorient toward the surface normal. The amount of intensity increase upon heating is roughly consistent with AFM results of decreased tilt. That the intensity increases only in the asymmetric methylene band, not in the symmetric one, is most probably due to a rotation about a methylene C-C bond pendant to the PCDA backbone, bringing the C-C-C plane of the alkyl side chain toward orthogonality with respect to the polymer backbone.[25, 26] It is likely that the C-C bond can be assigned to the one β to the polymer backbone (figure 12.6), since this has been implicated previously by NMR spectroscopy in the thermochromic transition of polydiacetylenes.[17] Upon heating

Figure 12.4 (following page). AFM images for a series of heat-treated red-phase p-SAc/PCDA films. Films were deposited on OTE/mica. (a-c) no heating (blue-phase); (d-f) 70 °C, 30 minutes; (g-i) 90 °C, 30 minutes; (j-l) 110 °C, 30 minutes; (m-o) 130 °C, 30 minutes. Scale bars=2000 Å (a, d, g, j, m); 10 Å (b); 5 Å (e, h, k, n). Molecular scale pictures (middle column) are frictional force images obtained on the corresponding areas shown in the far left column. The farthest right column shows the corresponding 2D-FFT spectra. Upon the thermochromic conversion of films to the red-phase, the side chains re-organize into a completely ordered structure (h, i, k, l, n, o).

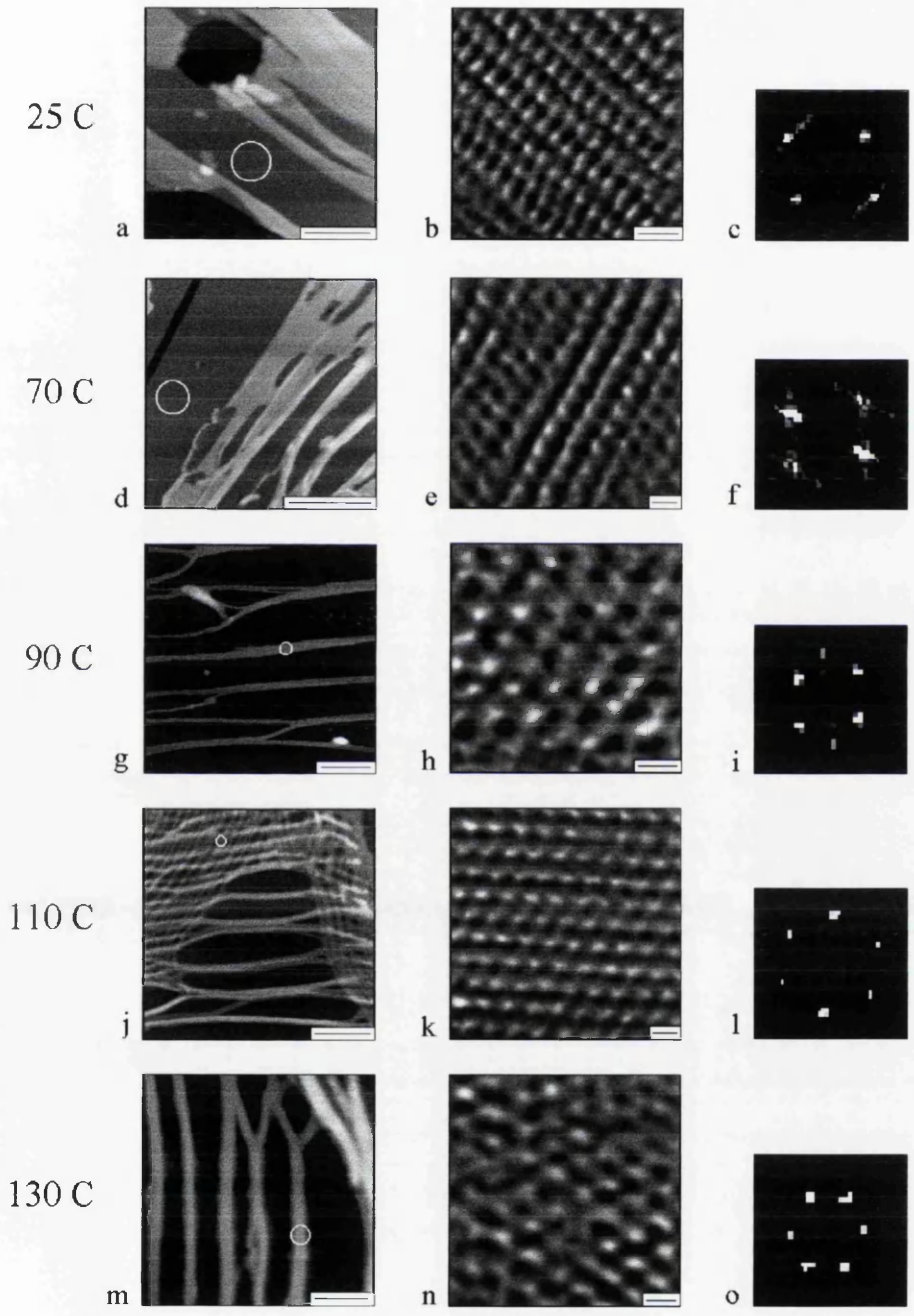
25 C
a
b
c
70 C
d
e
f
90 C
g
h
i
110 C
j
k
l
130 C
m
n
o

Figure 12.4

Figure 12.5 (following page). Transmission FTIR spectra for a series of a heat-treated red phase p-SAc/PCDA films. The CH stretch region. Films were deposited on OTE/glass. Only data relative to 25, 50 and 70 ^{o}C are shown for clarity. Remaining data is shown in table 12.I.

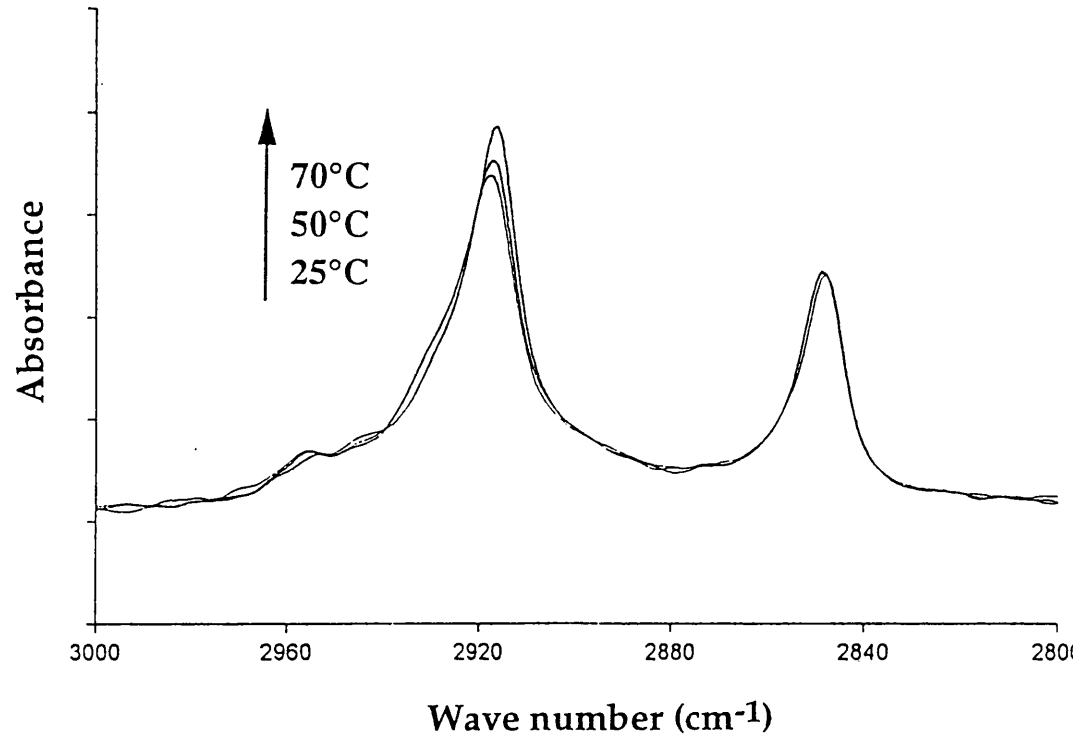
70°C
50°C
25°C
Absorbance
3000
2960
2920
2880
2840
2800
Wave number (cm-1)

	ν_a CH_2		ν_s CH_2			
Temperature (°C)	Intensity*	Position** (cm^{-1})	Intensity	Position** (cm^{-1})	Side Chain Structure	Film Color
25	0.0032	2917.4	0.0023	2848.8	Partially Ordered	Blue
50	0.0034	2917.0	0.0022	2848.6	Partially Ordered	Blue-purple
70	0.0038	2916.4	0.0023	2848.3	Partially Ordered	Pink
90	0.0037	2916.3	0.0022	2848.2	Ordered	Pink
110	0.0037	2916.4	0.0022	2848.3	Ordered	Dark pink
130	0.0034	2916.5	0.0019	2848.4	Ordered	Dark pink

* ± 0.0001

** ± 0.1

Table 12.I. Summary of spectroscopic and structural data obtained for p-SAc/PDA films converted to the red phase by heat treatment for 30 minutes. Spectra and images were obtained after cooling to room temperature.

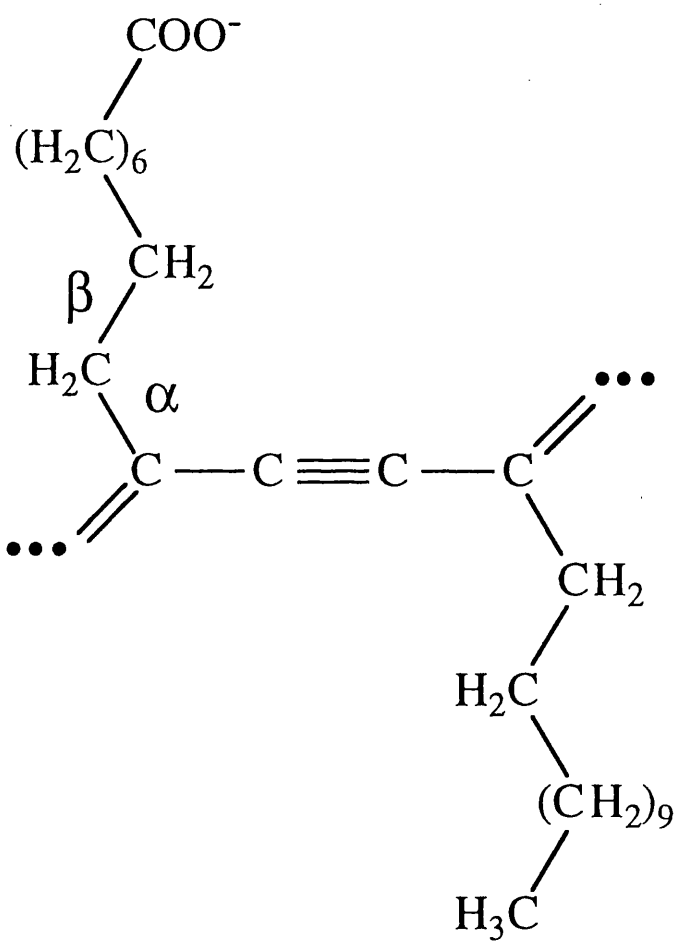

Figure 12.6. Schematic of p-10, 12 pentacosadiynoic acid.

at 130 °C, the intensity of ν_a CH_2 decreases about 8%, as similarly observed for the symmetric methylene band. The reason for the intensity decreases both in the asymmetric and symmetric bands most likely arises from structural deformations at high temperature of the OTE layer underneath the p-SAc/PCDA film due to melting, as described in chapter 10.

The head group region of the p-SAc/PCDA film is also readily observed in the near normal external reflection spectra as shown in figure 12.7. Initially, at 25 °C, the carbonyl band (ν C=O) is observable at 1696 cm^{-1}, indicating strong hydrogen bonding has been formed in the carboxylic acid head groups, as appeared in Langmuir-Blodgett films of fatty acids.[27] The peak appearing at 1562 cm^{-1} is assigned to the CNH group of the sialic acid head group. Also observable is the scissoring band of the methylene group at 1465 cm^{-1}. As the p-SAc/PCDA is heated up to 70 °C, a significant decrease in the carbonyl stretching band occurs, while other bands remain unchanged. Considering the change in the methylene stretching bands as discussed above, this decrease might be caused by head group re-orientation due to the rotation of the β bond to the PCDA backbone. At 90 °C, the carbonyl stretching band becomes broad, indicating less hydrogen bonding in the head group as dehydration occurs. When the film is heated at 110 °C and 130 °C, the peak at 1562 cm^{-1} is significantly enhanced. Since the amount of sialic acid remains constant, this large enhancement is attributed to the transition of PCDA carboxylic acid into carboxylate after prolonged dehydration. (This is reasonable since the frequencies of the CNH group and the deprotonated carboxylate both appear at ~1560 cm^{-1}).

12.3.4 Mechanism for Thermochromic Transition

From these spectroscopic and AFM observations, it is possible to construct a microscopic model which accounts for the color transition induced by heat treatment. Heating through the thermochromic transition does not induce an order-to-disorder transition of the alkyl chains (see figure 12.4). This observation refutes previous hypotheses which have suggested that the color change is accompanied by side chain entanglement and disorder.[9, 11] Since molecular order is retained also when heating p-Cd-PCDA monolayers beyond the thermochromic transition, neither the multilayered structure nor the presence of the sialic acid can be responsible for the results on p-SAc/PCDA films. Therefore, side chain entanglement cannot be invoked as a possible mechanism of the blue-to-red transition in these films.

Many researchers have suggested (as seems intuitively likely) that the blue to red color change arises from the decrease in the conjugation (or delocalization)

Figure 12.7 (following page). Near-normal external reflection FTIR spectra for a series of heat-treated red-phase p-SAc/PCDA films. The C=O stretch region. Films were deposited on OTE/glass. Data relative to 25, 50, 70, 90, 110, 130 ^{o}C are shown.

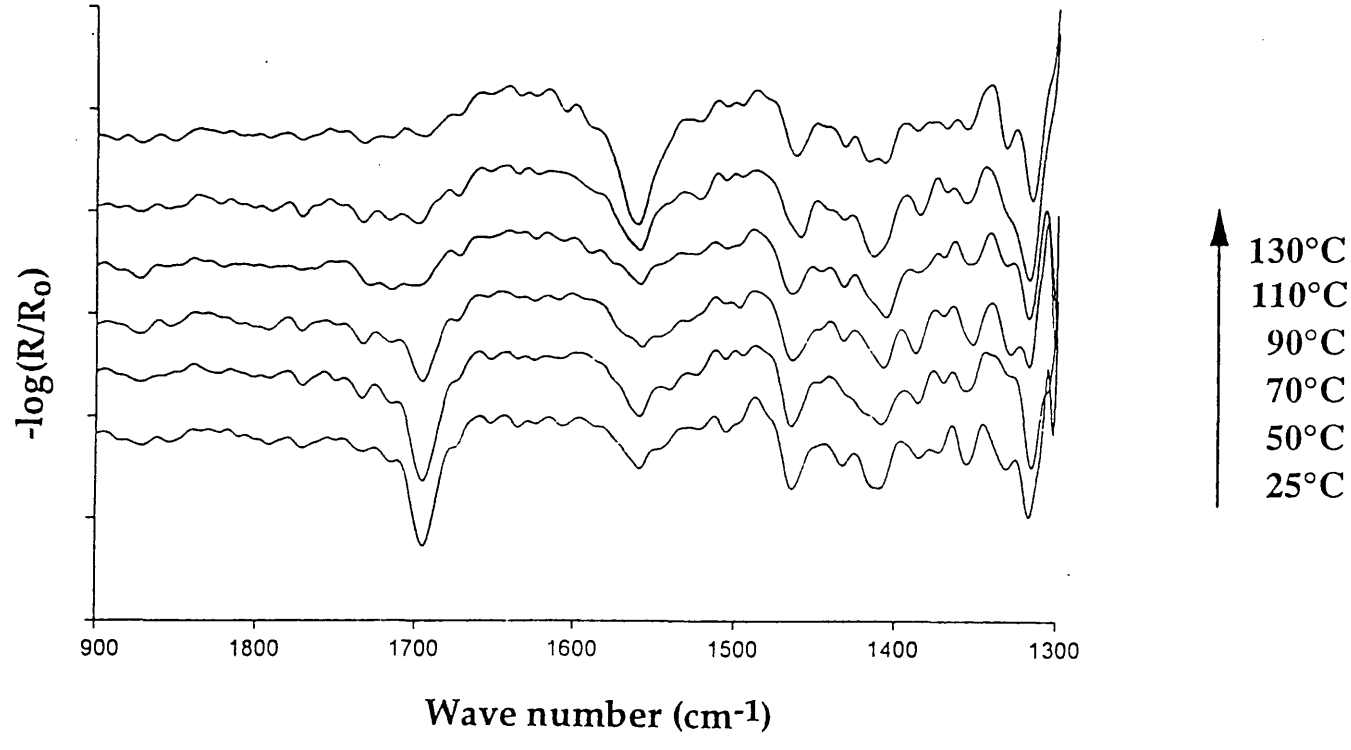
-log(R/R$_o$)
900
1800
1700
1600
1500
1400
1300
Wave number (cm^{-1})
130°C
110°C
90°C
70°C
50°C
25°C

length of the polymer backbone.[14, 28, 29] The polymer backbones, composed of conjugated double and triple bonds, are planar in the blue-phase films.[30] In these conditions the conformation of the alkyl side chains is determined by the spatial requirements imposed by the solid state polymerization that prohibits the chains from assuming their lowest energy planar configuration. AFM images reveal that the alkyl chains are well packed along the polymer backbone, while irregular packing is observed in the inter-backbone direction.

Upon heating, the side chains tend to reorganize and recuperate their planar conformation. As suggested by FTIR results, this re-arrangement is characterized by a conformational change in a single bond pendant to the conjugated backbone. The combination of the AFM and FTIR data suggest that the side chain becomes more extended, suggesting that the conformational change is most likely *trans-gauche*. Figure 12.8 illustrates schematically the re-arrangement of the side chains. The more planar conformation of the side chains imposes strain on the polymer backbone, that may result in slight rotations around its single bond. As a result, imperfect overlap of the π-π bonds occurs, accounting for the increased energy of the π-π^* transition. Theoretical calculations have indicated that very slight rotations around the C-C bond of the polymer backbone (5^o) are enough to produce a marked decrease in the π-electron conjugation length as a result of reduced π-orbital overlap.[30,31] As a result, the observed blue shift in the visible absorption spectra can be anticipated. The energy difference between the *gauche-trans* conformations is only of the order of 0.5 Kcal/mol.[17, 32] The slightly higher energy of the non-planar conformation of the polymer backbone ($\approx$2 Kcal/mol) in the red phase is offset by the lower side chain packing energy (because of the extended, more planar side-chain conformation).[33] The reduced extent of hydrogen bonding as evidenced by the FTIR data may explain the lack of thermochromic reversibility in this system. Reversibility has previously been attributed to maintenance of the hydrogen-bonded network in various other PDA derivatives, such as polydiacetylene-functionalized polyamide[15] and polydiacetylene crystals and cast films substituted with urethane containing side groups.[16, 19] In addition, the cracking and bending of the polymer fibers may also account for the decreased π-orbital overlap between neighboring filaments.

Strikingly, despite the dramatic changes in the micron-scale morphology of p-SAc/PCDA film and in the OTE layer, the order in the p-SAc/PCDA alkyl chains is preserved at temperatures well beyond the thermochromic transition, indicating the remarkable thermal stability of these films.

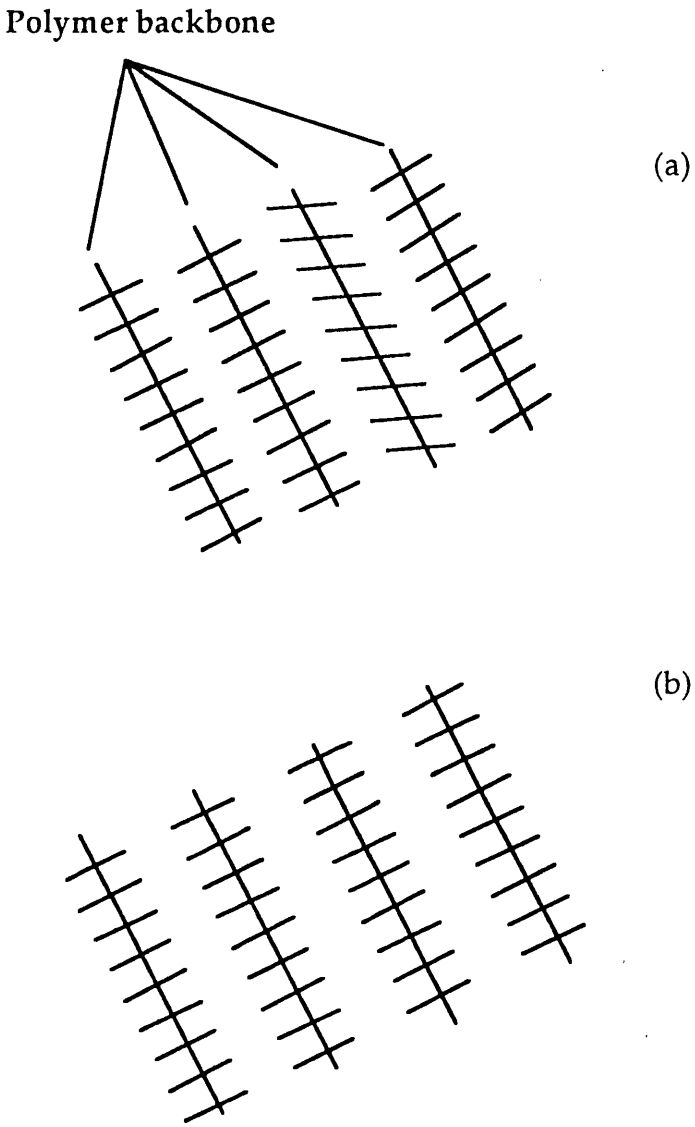

Figure 12.8. Schematic showing the potential re-arrangement of the side chains upon the thermochromic transition. The diagrams show the direction of the polymer backbone and projections of the hydrocarbon planes on the polymer backbone plane. (a) Blue-phase films. Neighboring polymer strands can slide with respect to one another and the hydrocarbon planes may not be parallel. (b) Thermochromic red-phase. The side chains re-organize into a completely ordered structure.

12.4 Conclusion

Systematic and detailed spectroscopic and molecular-level structural analysis were carried out on Langmuir-Schaefer films of functionalized polydiacetylenes films converted to the red phase by heat. It was found that the complementary techniques of AFM, FTIR and visible absorption spectroscopies provided a complete visual and spectroscopic picture of the color transition process. AFM probes the molecular ordering and morphology of the polymeric assembly, most notably the side chain groups. FTIR provides the complementary chemical identification of specific functional groups in the side chains, visible spectroscopy probes the electronic structure of the chromophore (polydiacetylene backbone).

The data suggests that the thermochromic transition of polydiacetylene films composed of sialic acid-PCDA and PCDA is accompanied by rotation of a C-C bond pendant to the polymer backbone. Both the AFM and the FTIR data indicate decreased tilt of the side chain as the film transitions from the blue to the red form. Although the micron-scale morphology of the p-SAc/PCDA film changes dramatically (and seems to be highly disordered *macroscopically* compared to the uniform striped morphology of the blue form), the molecular-scale ordering is actually *increased* at temperatures well beyond the thermochromic transition. Thus, no side chain entanglement or disordering is observed for the red phase p-SAc/PCDA film. Detailed understanding of the chemical and morphological nature of these unique lipid-polymer membranes will aid investigations of these materials in molecular devices, biosensors and non-linear optical devices.

References

[1] *Polydiacetylenes*, D. Bloor, R. R. Chance edts., NATO ASI Series E: Applied Sciences, vol. 102 (Martin Nijhoff Publishers: Dordrecht, 1985).

[2] B. Chu, R. Xu, *Acc. Chem. Res.*, **24**, 384 (1991).

[3] M. Wenzel, G. H. Atkinson, *J. Am. Chem. Soc.*, **111**, 6123 (1989).

[4] R. R. Chance, G. N. Patel, J. D. Witt, *J. Chem Phys.*, **71**, 206 (1979).

[5] R. A. Nallicheri, M. F. Rubner, *Macromolecules*, **24**, 517 (1991).

[6] H. Mino, H. Tamura, K. Ogawa, *Langmuir*, **8**, 594 (1992).

[7] D. .H. Charych, J. O. Nagy, W. Spevak, M. D. Bednarski, *Science*, **261**, 585 (1993).

[8] A. Berman, D. J. Ahn, A. Lio, M. Salmeron, D. H. Charych, *Science*, **269**, 515 (1995).

[9] N. Mino, H. Tamura, K. Ogawa, *Langmuir*, **7**, 2336 (1991).

[10] A. A. Deckert, L. Fallon, L. Kiernan, C. Cashin, A. Perrone, T. Encalarde, *Langmuir*, **10**, 1948 (1994).

[11] A. Saito, Y. Urai, K. Itoh, *Langmuir*, **12**, 3938 (1996).

[12] D. N. Batchelder, D. Bloor, in *Advances in Infrared and Raman Spectrosocopy*, vol 11, R. J. H. Clark, R. E. Hester, edts., (Wiley: Heyden, 1984), Chapter 4.

[13] B. E. J. Smith, D. N. Batchelder, *Polymer*, **32**, 1761 (1991).

[14] G. L. Exarhos, W. M. Risen Jr., R. H.Baughman, *J. Am. Chem. Soc.*, **98**, 481 (1976).

[15] H. W. Beckham, M. F. Rubner, *Macromolecules*, **26**, 5192 (1993).

[16] H. Tanaka, M. Thakur, M. A. Gomez, A. E. Tonelli, *Macromolecules*, **20**, 3094

(1987).

[17] H. Tanaka, M. A. Gomez, A. E. Tonelli, M. Thakur, *Macromolecules*, **22**, 1208 (1989).

[18] R. R. Chance, *Macromolecules*, **13**, 396 (1980).

[19] M. F. Rubner, D. J. Sandman, C. Velazquez, *Macromolecules*, **20**, 1296 (1987).

[20] J. White, M. Kelian, A. Helenius, *Quart. Rev. Biophys.*, **16**, 151 (1983).

[21] J.C. Paulson in *The Receptors*, M. Conn edt., (Academic Press: New York, 1985), volume 2.

[22] W. Spevak, J. O. Nagy, D. H. Charych, M. E. Schaefer, J. H. Gilbert, M. D. Bednarski, *J. Am. Chem. Soc.*,**115**, 1146 (1993).

[23] The FTIR measurements were performed by Dr. Dong June Ahn, LBNL.

[24] G. Lieser, B. Tieke, G. Wegner, *Thin Solid Films*, **68**, 77 (1980).

[25] A. Berman, D. J. Ahn, A. Lio, M. Salmeron, A. Reichert, D. H. Charych, *Science*, **269**, 515 (1995).

[26] D. J. Ahn, A. Berman, D. H Charych, *J. Phys. Chem.*, **100**, 12455 (1996).

[27] F. Kimura, J. Umemura, T. Takenaka, *Langmuir*, **2**, 96 (1986).

[28] R. R. Chance, R. H. Baughman, H. Muller, C. J. Eckhardt, *J. Chem. Phys.*, **67**, 3616 (1977).

[29] C. Kolmer, H. Sixl, *J. Chem. Phys.*, **88**, 1343 (1988).

[30] B. J. Orchard, S. K. Tripathy, *Macromolecules*, **19**, 1844 (1986).

[31] V. Dobrosavljevic, R. M. Stratt, *Phys. Rev. B.*, **35**, 2731 (1987).

[32] A *gauche* conformation describes the specific staggered rotational orientation in which next-nearest neighbor functional groups are situated adjacent to one another when looking along the axis of rotation. See, for example, A. Streiwieser Jr., C. H. Heathcock, *Introduction to Organic Chemistry*, (MacMillan: New York, 1985).

[33] G. C. Pimentel, A. L. McClellan, *The Hydrogen Bond*, (W. H. Freeman Publishers: San Francisco, 1960).

Chapter 13

New Mechanisms of Blue-to-Red Color Transition in Polydiacetylene Thin Films

13.1 Affinochromism

13.1.1 Introduction

As already seen in chapters 8-10, organic films provide an attractive way to modify properties such as adhesion and friction of the underlying material. Functionalization of these films with receptor-binding ligands has extended the field to biotechnology applications. For example, peptide or nucleotide libraries based on self-assembled monolayers offer the possibility of screening for new receptor-binding ligands.[1] Biosensors based on LB films[2] have been used to detect molecules of diagnostic significance, such as glucose[3] and urea.[4] In a typical biosensor, there is a biological sensing element, such as an enzyme, an antibody or a cell, in contact with a physico-chemical transducer, such as an electrode or an optical fiber. Measurement of the target analyte is achieved by selective transduction of a parameter of the biomolecule-analyte reaction into a quantifiable electrical or optical signal (figure 13.1). In the case of surface libraries, for example, transduction has been accomplished by way of enzyme-linked immunosorbent assay (ELISA)-type essay.

In an effort to design a simple and more direct method of detecting molecular recognition events, researchers at the Center for Advanced Materials at LBNL chose to exploit the known chromatic properties of polydiacetylene LB films, described in chapter 11. By developing a functionalized polydiacetylene matrix they demonstrated that it is possible to use the blue-to red color transition of the organic bilayer to detect a receptor-ligand interaction occurring at the surface of the bilayer.[5] Since both binding and detection occur within a single supramolecular assembly, this detection strategy does not require that the recognition site be coupled to a secondary device in order to transduce the binding event into a measurable signal. In addition, it is not necessary to employ secondary molecules such as antibodies and enzymes, typically used in ELISA detection methods. This simple, color-based sensor therefore enables rapid, qualitative detection of binding by visible inspection (due to the remarkable optical properties of polydiacetylene

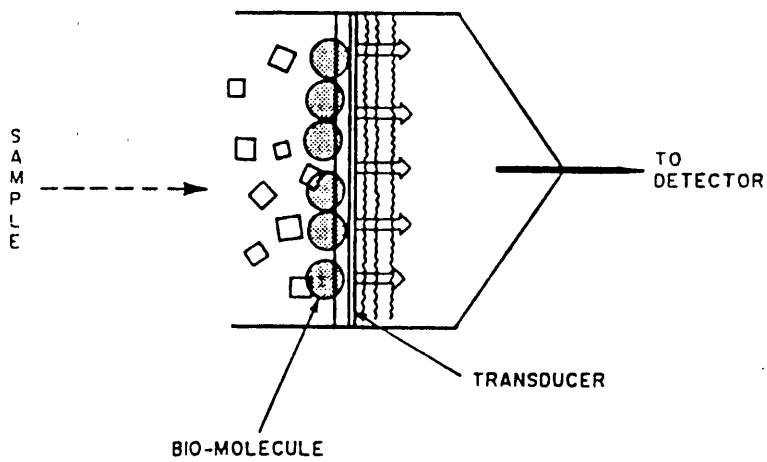

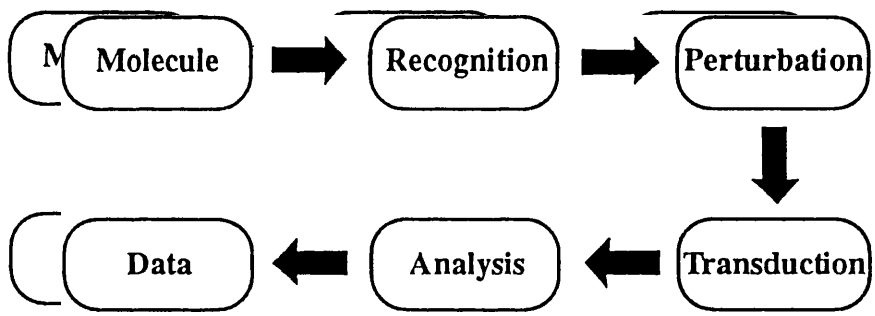

Figure 13.1. Operational principle of a biosensor. The molecule is recognized by the sensor and a detectable physical change is triggered. This change is then transformed into a measurable signal, which can be analyzed.

films), or quantitative detection by visible absorption spectroscopy.[5]

As a first example of colorimetric detection, they focussed their attention on the binding of the influenza virus to sialic acid. Influenza viruses are particles of ca. 1000 Å diameter enveloped by a lipid bilayer in which the glycoprotein, hemagglutinin (HA), is embedded. HA binds to sialic acid residues on cell surface glycoproteins and glycolipids initiating the fusion of the bound viral lipid envelope with the cell membrane (figure 13.2).[6] The molecular assembly used (see figure 12.1) represents a synthetic version of sialic acid functionalized cell surfaces. It contains a carbon-linked sialic acid[7] rather than the natural occurring oxygen-linked glycoside. It was shown that this modification does not alter the binding affinity of hemagglutinin.[8] The mixed lipid assembly contains 5% of the glycolipid monomer (b) shown in figure 11.2 dispersed in the matrix lipid monomer (a). In this way, the matrix lipid uniformly disperses the sialoside lipid to allow optimum binding of the virus. Films were deposited on OTE hydrophobized mica, as described in chapter 11. When a blue-phase film is incubated with X31 influenza A virus (PBS buffer, pH=7.4) a blue-to-red color transition is observed both visually and by UV visible spectroscopy, as a result of the specific binding of the viral hemagglutinin to the sialic acid residues on the bilayer surface. From this affinity binding the term *affinochromism* is used to denote this color transition. If a carbohydrate other than sialic acid is used (for example, lactose), or if the virus is inhibited by free sialic acid, the color transition is not observed.[5] Importantly, it was demonstrated that non-specific absorption of virus or other protein induces only a very small change in the optical spectra and therefore does not affect the sensitivity of the sensor, in contrast to other types of biosensors.

Since ligands other than sialic acid could be incorporated into the film, affinochromism offers the possibility of a general method for the direct detection of receptor-ligand interactions opening the way to a wide range of applications in the areas of diagnostics and therapeutics.

As already pointed out in the previous two chapters, to exploit fully the use of functionalized polydiacetylenes in direct colorometric detection, it is necessary to understand the nature of the color transition with respect to affinity binding. As shown clearly in chapter 12, AFM is particularly suitable to investigate the structure and extent of long-range order in the side groups. In this chapter, an AFM study performed on sialic acid functionalized 10, 12 pentacosadiynoic acid membranes converted to the red phase by affinity binding of the influenza virus, is described.

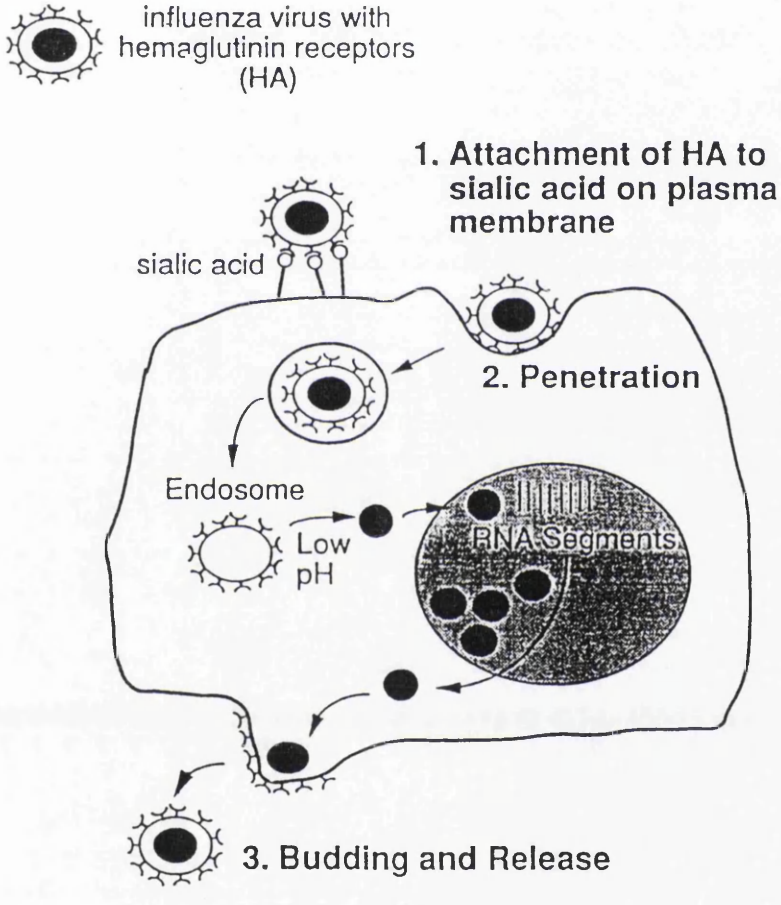

Figure 13.2. Schematic of the fusion of the influenza virus lipid membrane with the cell membrane.

13.1.2 Sample Preparation

Blue-phase sialic acid functionalized 10, 12 pentacosadiynoic acid films were prepared as described in chapter 11.

For virus-induced color changes, an aliquot of X31 influenza A virus was diluted 7-fold with PBS buffer (pH=7.4), placed on the surface of the blue-phase film and typically left overnight (although the color change is apparent after several minutes).

Samples prepared on hydrophobized glass were used for visible absorption spectroscopy characterization and samples deposited on mica were investigated by AFM.

13.1.3 Visible Absorption Spectroscopy

Visible absorption spectra of the p-SAc/PCDA film before and after viral binding are shown in figure 13.3. The spectra obtained after incubation of the synthetic membrane with the virus shows a decrease in the intensity of the peak at 640 nm and a corresponding increase in the intensity of the peak at 540 nm. The sample at this point appeared light pink. It can also be seen, however, that the conversion to the red phase is not complete, as evidenced by the residual absorption at 640 nm. This may be due to inactivated portions of the film where the sialic acid headgroup is not accessible. The narrow linewidths for both the 640 nm and the 540 nm peak indicate that a narrow distribution of conjugation lengths exists in both the blue and the red-phase films.

13.1.4 AFM Studies of Affinochromism

Figure 13.4 (b) shows a 5x5 μm^2 AFM image of a blue-phase p-SAc/PCDA layer (figure 13.4 (a)) converted to the red-phase after exposure to the influenza virus. As can be seen, the image for the red-phase film appears fairly 'dirty'. Small particles are present on both p-SAc/PCDA layers and OTE regions. By comparison with blue-phase films incubated with PBS (no change in the optical spectrum), they can be attributed to the residue left on the surface by the buffer solution. Similar residues were observed in other AFM studies of biological materials.[9] They could be avoided perhaps by using a different buffer, however such experiment was not tried during the studies presented here. Large bright clusters visible in figure 13.4(b) are

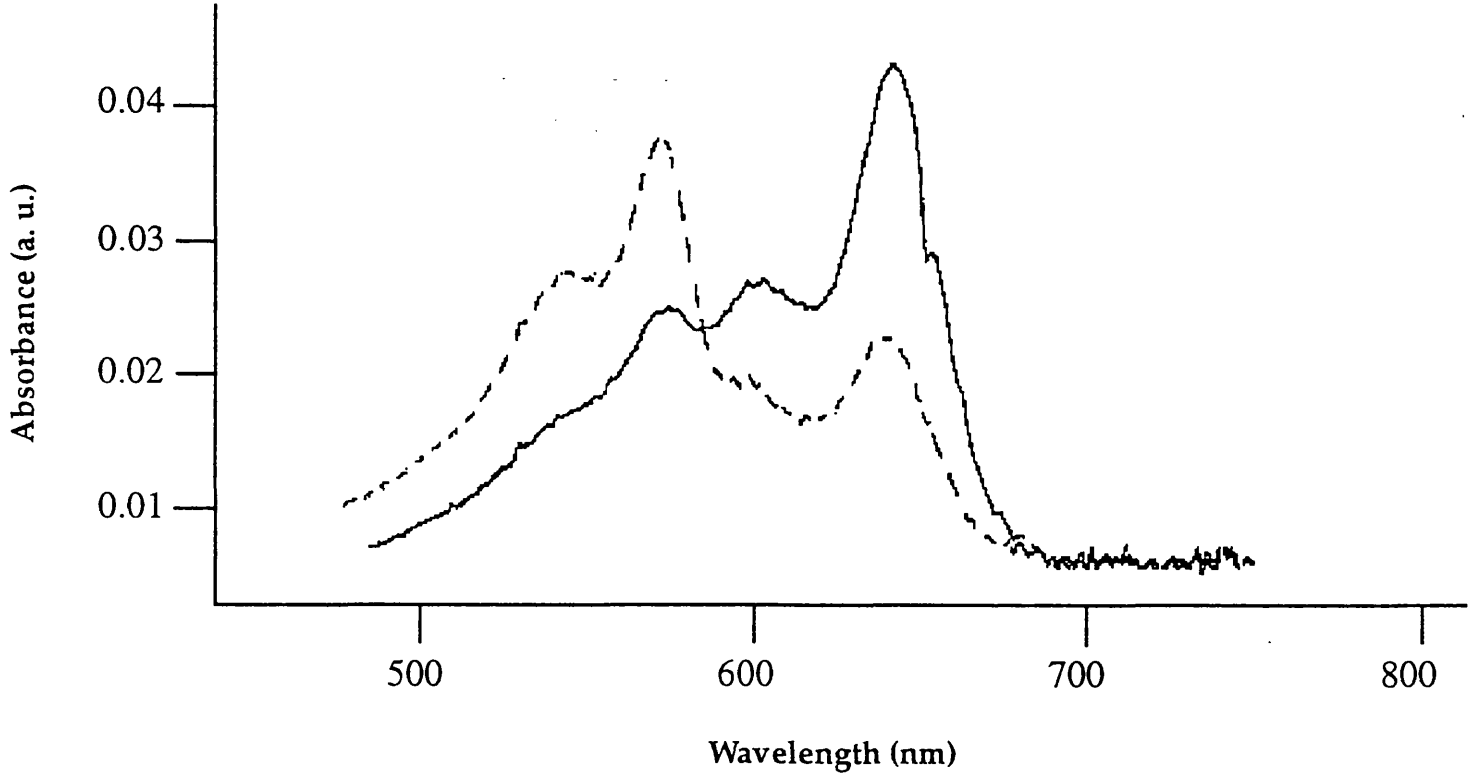

Figure 13.3. Optical absorption spectra for a blue-phase p-SAc/PCDA film prior to (solid line) and after (dashed line) viral incubation. The incubation period was 30 minutes.

Figure 13.4 (following page). (a) and (b) AFM images of p-SAc/PCDA films on glass before (a) and after (b) incubation with the influenza virus. The same area of the sample is shown. Scale bars=1 μm. Viruses are seen to aggregate on type **3** stripes. (c) and (d) Topographic and simultaneous frictional force images obtained on layer **1** after viral incubation. The broken line represents the direction of the polymer backbone. Scale bars=10 Å. The molecular level structure shown is undistinguishable from that of untreated blue-phase films. (e) and (f) 2D-FFT spectra of (c) and (d), respectively.

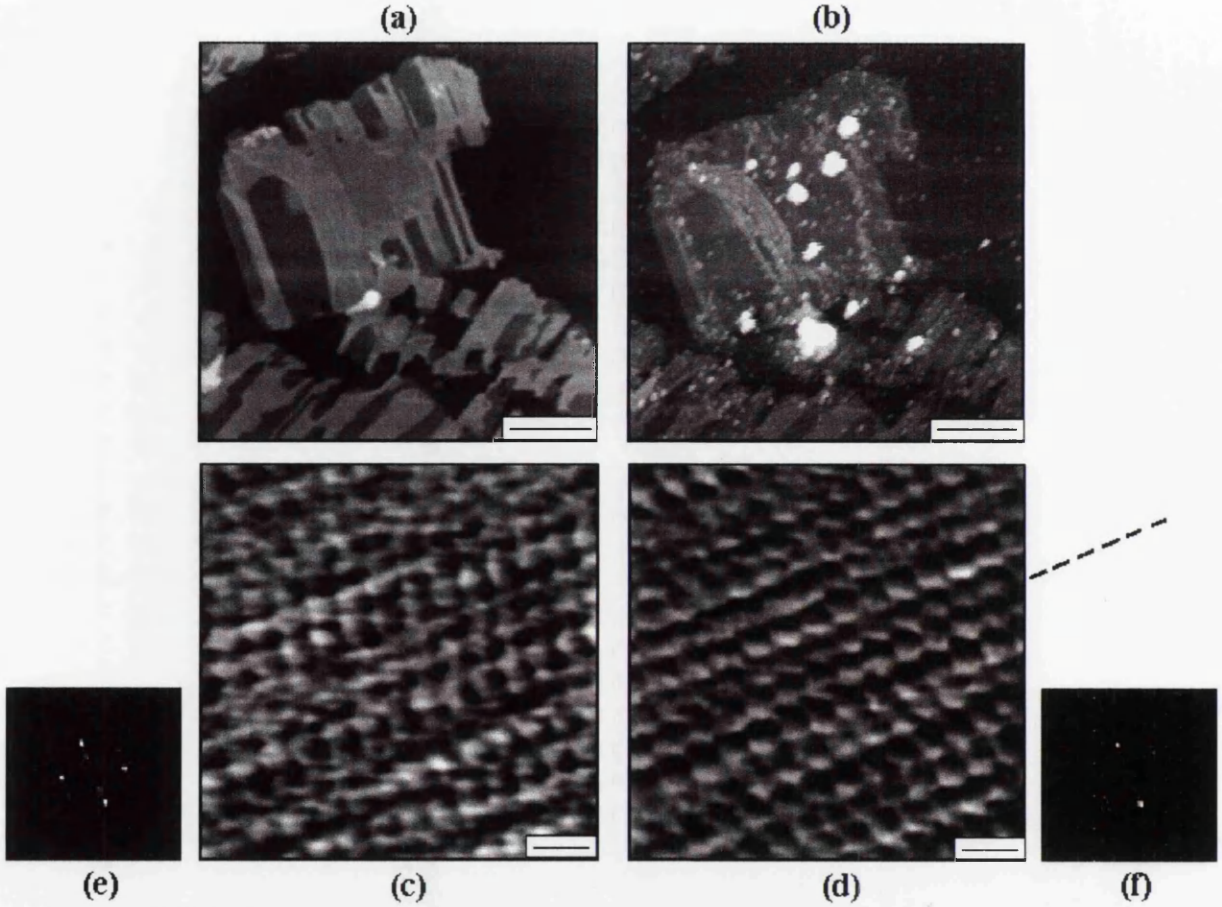
(a)
(b)
(e)
(c)
(d)
(f)

most likely aggregates of influenza viruses. A careful analysis of images, such as the one shown in figure 13.4(b), and comparison with images of the same area of untreated samples, show that the PCDA areas mostly affected by the virus treatment are the stripes on top of layer **1**. In fact, they have a rather 'fuzzy' appearance. Furthermore, the large bright clusters are observed primarily on top of the stripes. Some smaller bright round-shaped particles are also seen on the stripes. The size of these particles, ~ 1000 Å diameter, corresponds closely to the size of influenza viruses as determined by electron microscopy.[10] Figure 13.5(a) shows an AFM picture of a virus particle taken with the home-built AFM. A line cursor is shown in figure 13.5(b). The 'streaky' appearance of the virus is most likely due to the tip dragging the soft, biological material. The 'ghost' image is attributed to a double tip. The reduced height of the virus, as shown by the line cursor, is likely due to the compression of the virus by the AFM tip.

In order to understand the molecular level origin of affinochromism, molecular images were taken on regions of layer **1**, as shown in figure 13.4(c) and 13.4(d). Layer **1** appears largely unaffected. No changes could be detected at the μm level (not shown) and the molecular structure is similar to that observed for the blue-phase, untreated films (see chapter 11). No molecular resolution images could be obtained on the stripes, indicating that if re-organization of the side chains occurs no long-range order exist in these regions, unlike the effects in the heat-treated films (see chapter 12). Occasionally, viruses were found on layer **1** regions. This may due to non specific absorption and it is likely favored in areas of the film where the stripes area is small compared to the size of the virus.

13.1.5 Mechanism for Affinochromism

Following treatment of the blue-phase films with influenza virus, the partially ordered arrangement observed for layer **1** persists and layer **1** regions are mostly unaffected by the treatment. On the contrary, the stripes appear greatly distorted and numerous viruses can be found on these regions. It is proposed that the virus interacts with the side chain groups of type **3** stripes via multipoint attachment and intercalation of the viral lipid into the polydiacetylene side chain lipid. The intercalation of the viral lipid would disrupt van der Waals and hydrogen bonding interactions between the side chain terminal groups, causing the 'fuzzy' appearance observed in AFM images. As for the heated films, the strain induced on the polymer backbone in these regions would be sufficient to change the conformation of the polymer backbone and hence give the observed color transition. However, unlike the observation for the thermochromic transition, where the re-arrangement of the

Figure 13.5 (following page). (a) AFM image of an influenza virus. The distorted appearance is an effect of the scanning tip dragging the virus. The 'ghost' image is likely the result of a double-tip. Scale bar=500 Å. (b) Line profile A. The virus is approximately 1000 Å in size.

(a)

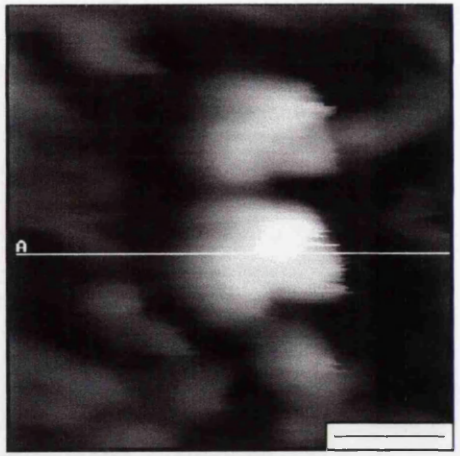
A

(b)

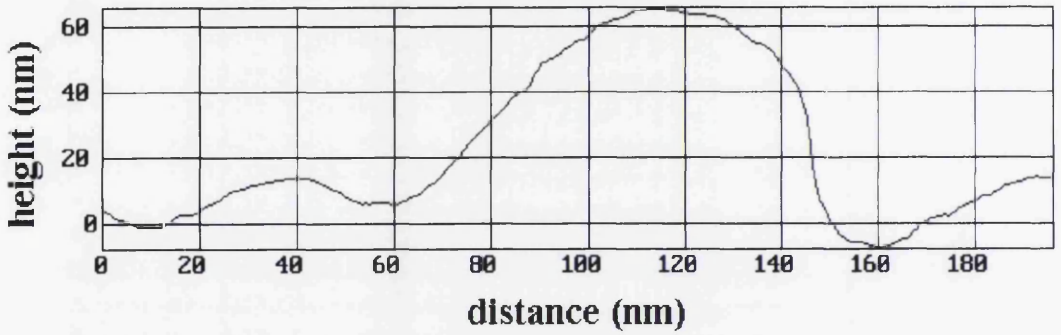
height (nm)
60
40
20
0
0
20
40
60
80
100
120
140
160
180
distance (nm)

side chains starts at the methylene groups close to the polymer backbone and involves the whole film, in the case of virus treatment the film seems to be affected from the 'outside-in', that is, in the region of the headgroups, as would be anticipated given the specific nature of the virus-sialic acid interaction. It is possible that the disordering of the chains arises from an attempt at membrane fusion by the virus particle, similar to the receptor-mediated fusion observed in natural systems. The fact that only the stripes appear affected by the treatment, indicates that these are the regions of the films where the sialic acid is more readily accessible for binding to the viral lectin. That is turn suggests that the sialic acid molecules are either directly exposed at the film-air interface or are in a semi-buried configuration in the filaments present on top of type 3 stripes.

13.2 Oriented Growth of Calcite at Polydiacetylene Films

13.2.1 Introduction

Biological organisms are capable of controlling inorganic crystal growth to a remarkable degree.[11, 12] This exquisite control is usually achieved with the use of an organic polymeric "matrix" of highly acidic macromolecules. In certain cases, the minerals that are formed by biological organisms are uniquely oriented or co-aligned relative to the organic matrix.[13] The *in vitro* synthesis of novel organic-inorganic composites with properties analogous to those produced by Nature continues to challenge the materials scientist. The use of simplified surfactant molecular assemblies[14, 15] resembling biological membranes (for example, monolayers, multilayers, or vesicles) is one approach toward achieving this goal. These structures provide modifiable interfacial functionalization and well-defined spatial organization. A number of elegant examples demonstrate the nucleation and growth of organic[16] and inorganic crystals at monolayer assemblies.[17, 18, 19] However, the crystals produced by these methods are oriented only in the direction normal to the membrane plane.[18, 19] The crystal axes in the plane of nucleation do not appear to be aligned with a structural parameter of the nucleation surface.

Previous studies have indicated that stereochemical match between the organic and inorganic interfaces is a predominant factor in determining the specific nucleation face type, in addition to lattice match and electrostatic interactions.[20, 21, 22] One difficulty is that structural information regarding the organic template has so far been obtained in the absence of mineralization at the monolayer (for example, from grazing incidence x-ray diffraction, electron diffraction, and x-ray reflectivity[23, 24]), yielding the average spacing between organic functional group and the two-dimensional unit cell dimensions. Furthermore, it has been suggested that synergistic changes in the organic template structure occur upon interaction with solid interfaces, as is the case when crystals are forming at the hydrophilic head-group region.[22] In such cases, *in situ* structural information regarding the organic template is even more elusive as dynamic changes in monolayer organization may occur.

This section will show that cooperativity at the organic-inorganic interface can result in complete alignment of calcite crystals along an identifiable structural feature of the p-PCDA matrix. Lattice match between calcite and p-PCDA dominates along the *a* axis of the calcite crystal. Symmetry reduction in the p-PCDA template coupled with proper stereochemical match ultimately control the co-alignment of the crystals and determines the nucleation face type. Structural

re-orientation of a p-PCDA matrix occurs upon calcite mineralization to optimize the stereochemical fit. The re-orientation is readily observed in p-PCDA as a blue-to-red chromatic transition in the polydiacetylene film. A more detailed analysis with Fourier transform infrared spectroscopy under mineralizing conditions indicates that rotation of the alkyl side chain about the single bond (C8-C9), β to the polydiacetylene backbone, may be responsible for the observed color transition, in a way similar to that described in chapter 12 for the thermochromic color transition.

13.2.2 Sample Preparation

The blue-phase p-PCDA films were prepared on hydrophobized glass by the Langmuir-Schaefer method, as described in chapter 11. Calcite crystallization was initiated simply by placing an aliquot of supersaturated $CaCO_3$ solution on the p-PCDA film. The supersaturated solution was prepared by purging stirred aqueous suspensions of $CaCO_3$ with CO_2 followed by filtration.

13.2.3 Experimental Methods

Polarized-light optical microscopy was used to investigate calcite crystal growth in the minutes following the placement of the $CaCO_3$ solution on the blue p-PCDA film.

Optical visible absorption spectroscopy was used to determine the chromatic phase of the polydiacetylene films before and after calcite growth. Scanning electron microscopy and powder x-ray diffraction (Siemens) measurements were carried out to identify the nucleation face and absolute orientation of the calcite crystals with respect to the direction of the polymer backbone.

In-situ FTIR spectroscopy[23] was used to determine the role of side-chain re-organization with respect to calcite nucleation. Spectra were taken at the gas-water interface by the external reflection method, with a plane-polarized beam irradiating at $\approx 10^{o}$ from the surface normal. The reflected signal was divided by the background signal from a bare water surface. The C-H and C=O stretch bands were investigated.

13.2.4 Results and Discussion

The morphology of blue p-PCDA films has been discussed in detail in chapter 11. Two significant phenomena were observed upon calcite formation at the p-PCDA films. First, in the regions where calcite crystals were formed, the crystals were all aligned in the same direction within the p-PCDA domain boundary (figure 13.6). The morphological symmetry axis of the crystals were perpendicular to and asymmetrically oriented with respect to the linear striations (figure 13.7). Second, the initially blue film changed color to red-phase polydiacetylene immediately after the onset of calcite growth (figure 13.8).

The structural features of the p-PCDA film that induce the calcite alignment were identified by AFM. The fibrous structures of the p-PCDA observed in the optical micrographs (figure 13.7) persist down to the molecular scale and correspond to the direction of the conjugated ene-yne polymer backbone. The asymmetry in the crystal alignment is therefore about the polymer backbone axis. The average periodicity along a given polymer backbone (intra-backbone), was 4.9 ± 0.5 Å (see chapter 11).

For identification of the nucleation face and the absolute orientation of the calcite crystals with respect to the p-PCDA backbone direction, x-ray diffraction and scanning electron microscopy were carried out. In the oriented calcite/p-PCDA system, reflections of the type (012) were unproportionably intense relative to randomly oriented calcite (figure 13.9). All other reflections were absent [except for the (104) reflection, which was relatively weak compared to randomly oriented calcite]. Hence, the (012) plane was oriented parallel to the p-PCDA membrane plane. The calcite (012) direction consists of alternating layers of calcium and tilted carbonate molecules. The exact angle that the crystal faces were inclined with respect to the film plane was determined by changing the SEM microscope stage tilt (figure 13.10). The micrographs also enabled identification of the cleavage rhombohedron dihedral angles that determine the direction of the calcite symmetry (*c*) axis (figure 13.11). Tilt angle measurements yielded a $17° \pm 1°$ inclination between the film normal and the $(01\bar{4})$ face, which confirms the assignment of the (012) basal plane, on the basis of the known structure of calcite.[25] The crystal's *a* axis [long direction of the $(01\bar{4})$ face] was perpendicular to the projected symmetry axis (c') and parallel to the polymer backbone direction (figure 13.11 (b)). Both the crystal and the p-PCDA polymer had a periodicity ≈5 Å along this direction. The carboxylate head groups of the p-PCDA film, therefore, fit closely to the calcite crystal structure along the polymer backbone, completing the co-ordination sphere around the calcium ions, which would otherwise be occupied

Figure 13.6 (following page). Polarized-light optical micrograph of aligned calcite crystals on p-PCDA. The micrograph shows groups of crystals aligned within different p-PCDA domains. Larger (rounded) and smaller (triangular) crystallites are visible. The larger crystals are the same morphology and orientation that grew to develop the opposite faces.

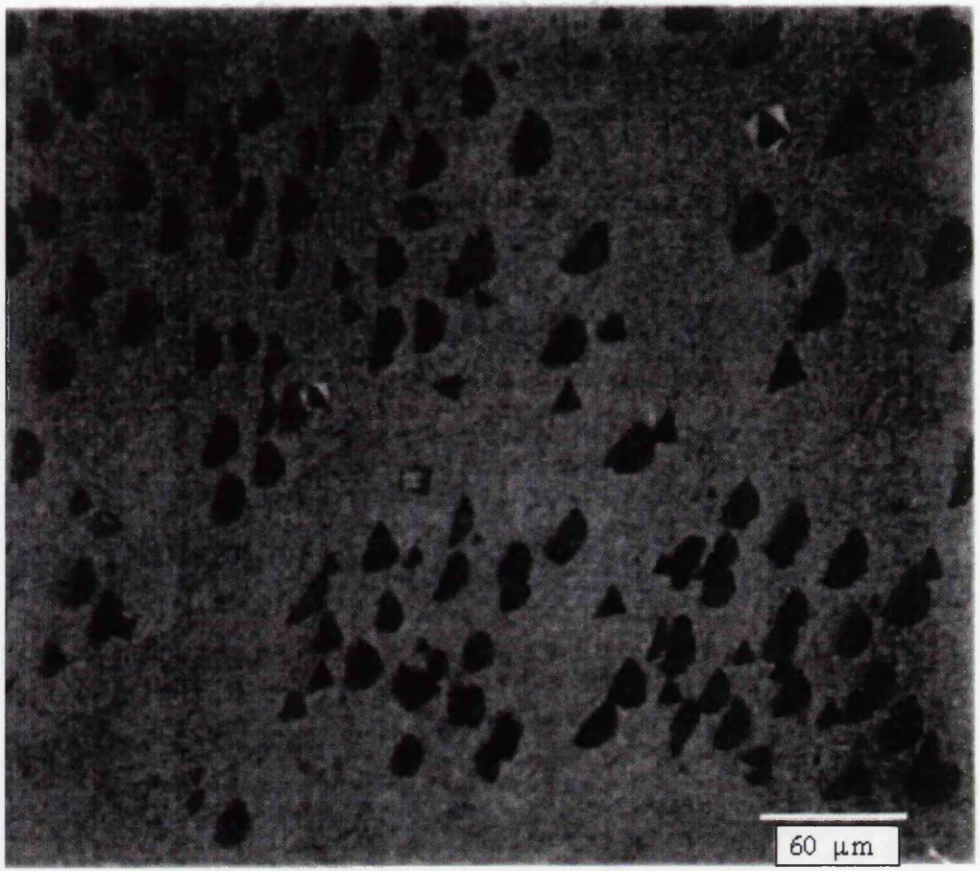
60 µm

Figure 13.7 (following page). Close-up of a single calcite crystal from 13.6 oriented along the p-PCDA backbone striations of one domain in 13.6.

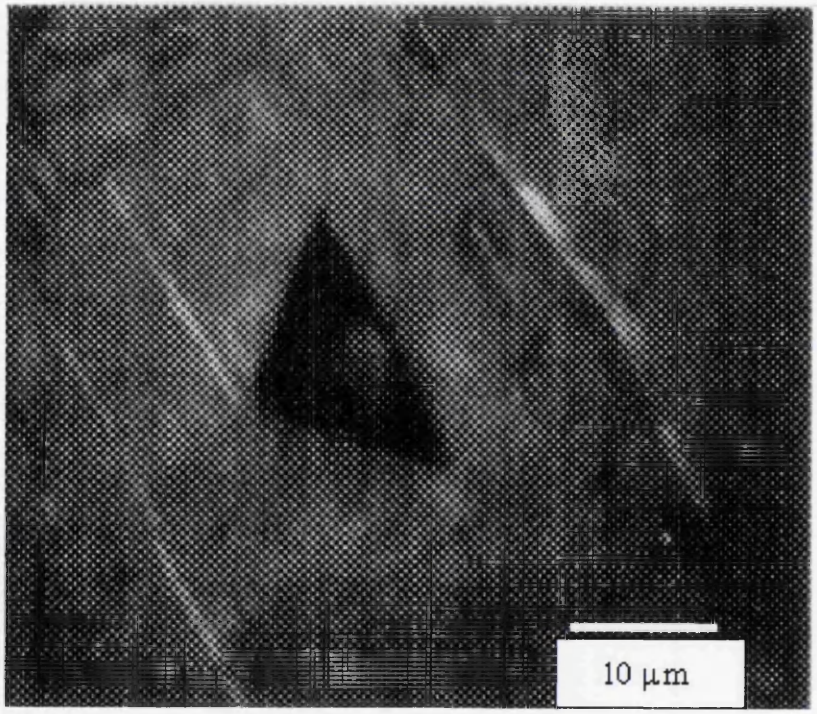
10 μm

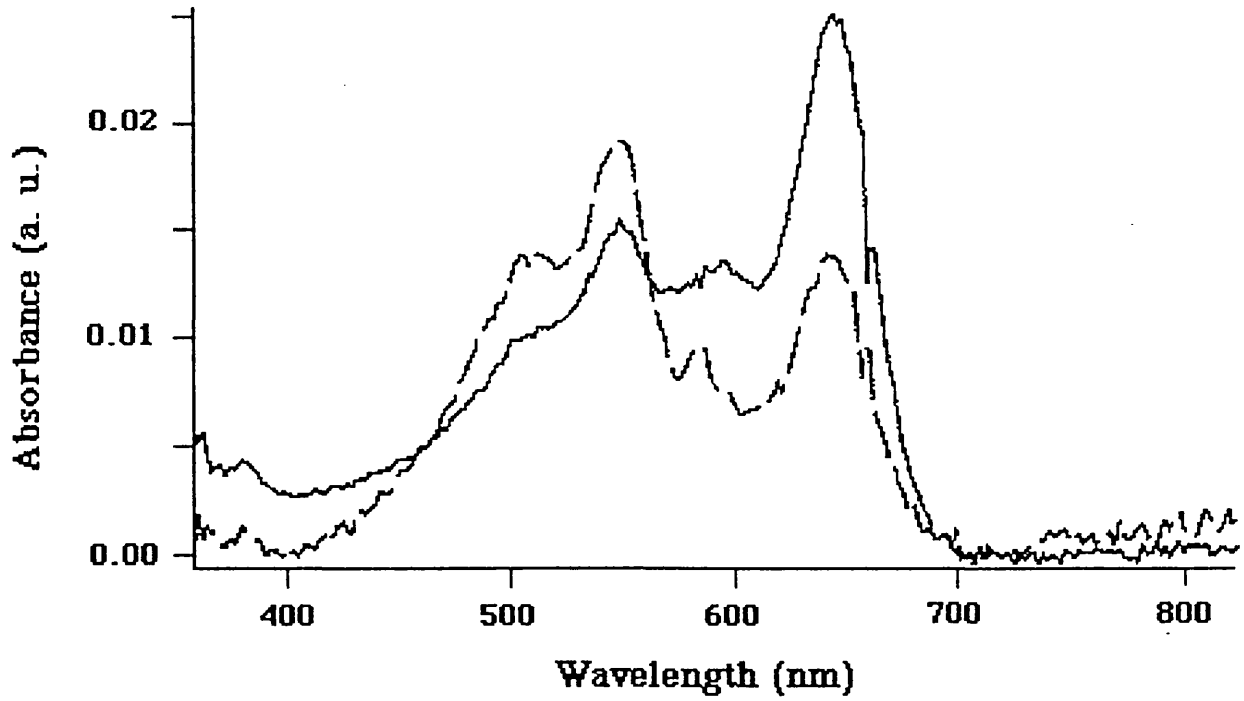

Figure 13.8. Optical absorption spectra for blue-phase p-PCDA template before calcite formation (solid line) and red-phase p-PCDA after the formation of calcite crystals (broken line). The spectra are characteristic of the blue-to-red color transition (see figures 11.4, 12.2 and 13.3 for comparison).

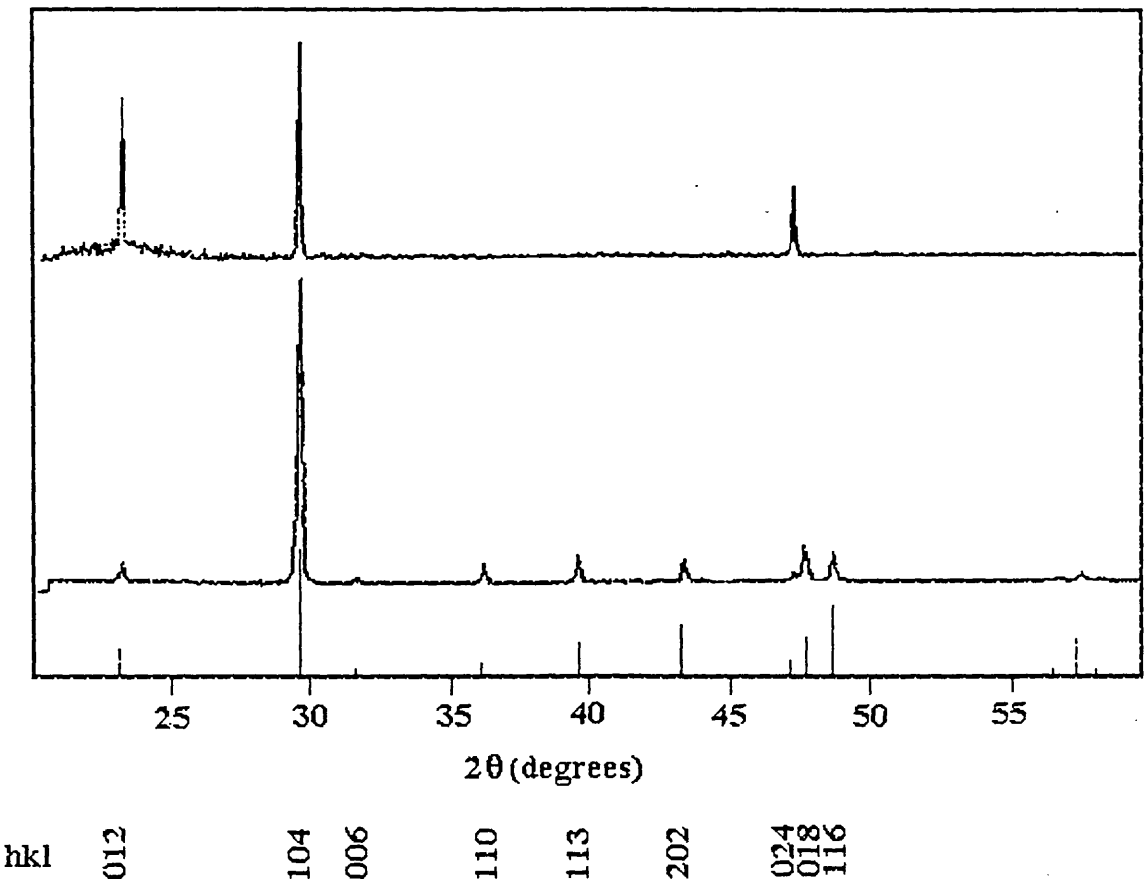

Figure 13.9. Powder x-ray diffraction data. Axes depict relative intensity *vs.* Bragg diffraction angle (2θ). The Miller indeces *hkl* of crystal planes associated with the diffraction lines are indicated below each line. (Top) Diffraction from (012) uniformly oriented calcite crystals grown on p-PCDA template. (Middle) Diffraction pattern from randomly oriented calcite powder. (Bottom) Calculated positions and relative intensities of calcite powder diffraction pattern.

Figure 13.10 (following page). Scanning electron micrograph of the (012) uniformly co-aligned calcite crystals. Larger crystals develop opposite faces yielding the rounded shapes seen in the optical micrograph of figure 13.6.

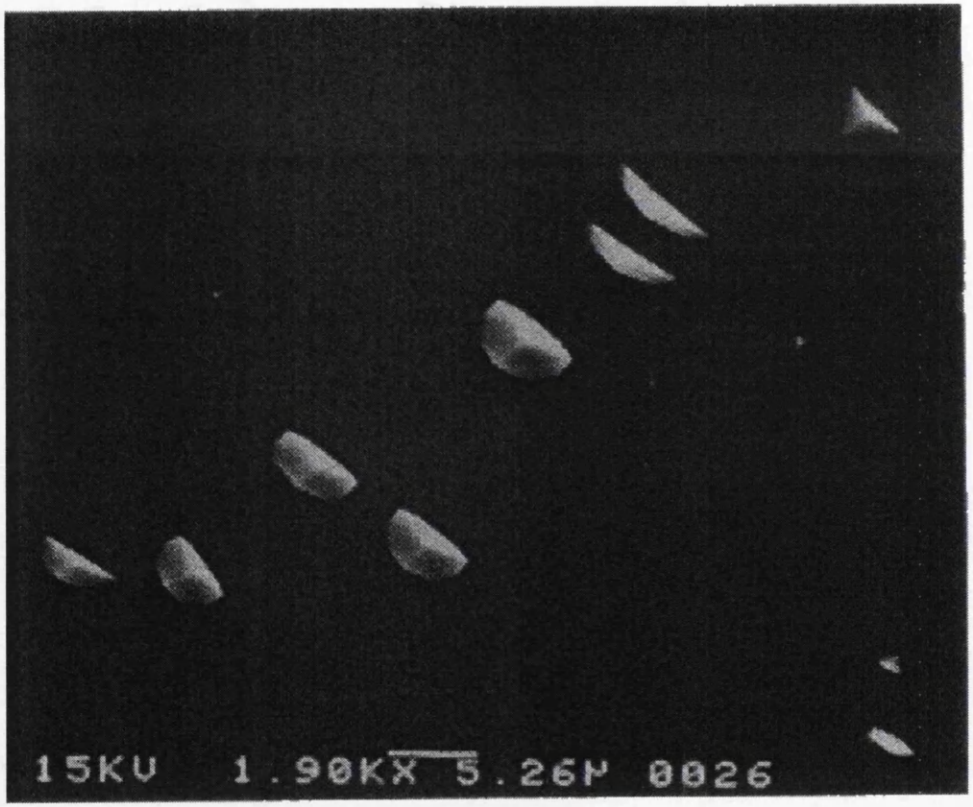
15KV 1.90KX 5.26M 0026

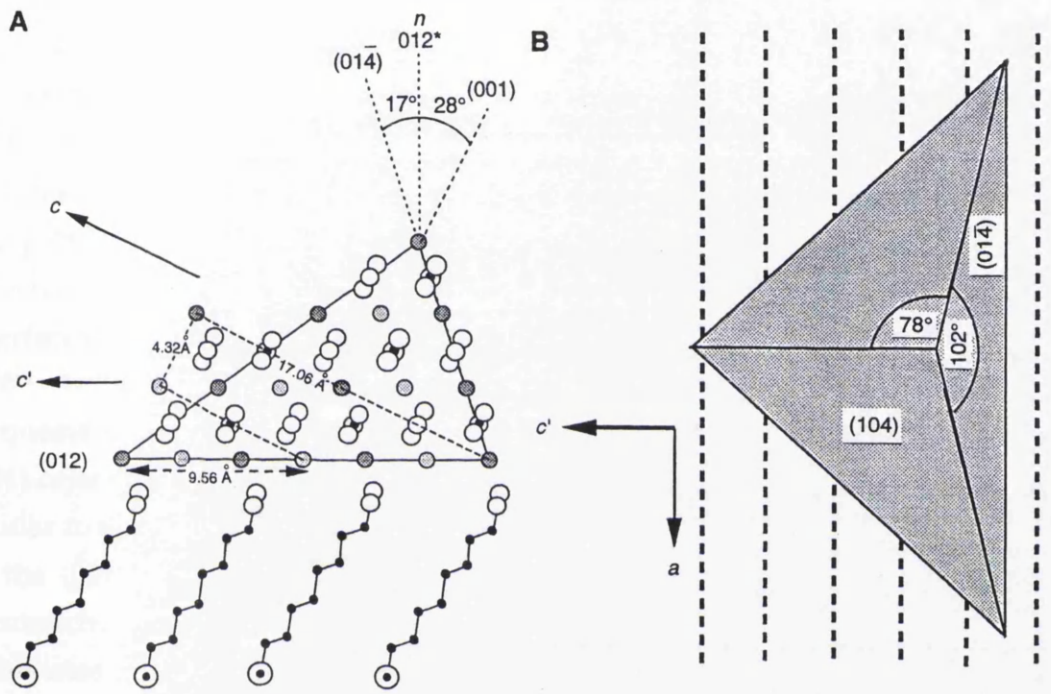

Figure 13.11. Schematic showing the potential geometric relation between the (012) face of calcite and the p-PCDA template. (A) View along the calcite *a* axis, down the polymer backbone and edge-on the (012) basal plane. The alternating calcium (gray circles: dark in front, lighter toward the back) and the tilted carbonate layers characteristic of the (012) plane are depicted. The calcite unit cell is shown as a dashed, truncated rectangle. The partial structure of the p-PCDA film is shown. The polymer backbone axis is symbolized as ⊙. The tilt angle of the polymer alkyl chain and head groups (o) emulate the carbonate stereochemistry and are implicated in the alignment of the crystal about the backbone axis. (B) Top view schematic of a single calcite crystal with respect to the polymer backbone direction, indicating the dihedral angles. The $(01\bar{4})$ face corresponds to that viewed edge-on in (A).

by carbonate.

This analysis alone is insufficient to explain the asymmetric orientation of the crystals relative to the polymer backbone. If lattice match alone were important, the calcite crystals would orient symmetrically about this axis. It is postulated that reduction of symmetry in the p-PCDA film structure induces the observed orientation of the calcite crystals. One such possibility is that the polymer alkyl side chains are parallel to each other and tilted with respect to the polymer backbone axis, resulting in a stereochemical match between the tilted carboxylates of the film and the carbonate of the crystal (figure 13.11(a)). A tilt of ~30° from the film normal was calculated by AFM, as described in chapter 11. The 30° tilt of the p-PCDA alkyl side chain closely matches the 28° tilt of the carbonate in the (012) direction (figure 13.11(a)), indicating good stereochemical match between calcite and p-PCDA. Although charge balance can be accounted for in the intra-backbone direction, an excess positive charge shared between two Ca^{2+} ions exists at the interface in the interbackbone direction. This excess charge may be neutralized by an intercalated HCO_3^-.[22] Water intercalation is another possibility, as suggested by Jacquemain in reference 23. These results are consistent with the absence of the (001)-oriented calcite on p-PCDA. Although the chemistry of the (001) face was similar to that of (012) (alternating layers of calcium and carbonate), the carbonate in the (001) direction is parallel to the plane and therefore stereo-chemically mismatched to the p-PCDA structure. The data indicates that lattice match dominates along the *a* direction. Stereochemical registry coupled to symmetry reduction in the p-PCDA template dominates the interactions in the *c'* direction and appears to ultimately be responsible for the co-alignment and unidirectionality of the crystals with respect to the polymer backbone. The color changes observed upon calcite mineralization suggest that, while the p-PCDA may be pre-organized into the 30° tilted structures, further re-organization of p-PCDA occurs, most likely to optimize the specific stereochemistry of the carboxyl group. It was shown in chapter 12 that the re-organization of the side chains is ultimately responsible for the thermochromic transition of SAc/PCDA layers. To ascertain the role of side-chain re-organization with respect to calcite nucleation, an *in-situ* analysis by Fourier transform infrared spectroscopy was performed.[26] Vibrational bands arising from both the growing crystal and the p-PCDA film were observed (figure 13.12). In concurrence with the onset of calcite deposition, a significant increase in intensity of ~26% occurred in the asymmetric CH_2 vibrational band (figure 13.12, inset). One explanation for this observation is a rotation about the single bond (C8-C9), β to the p-PCDA backbone (see figure 12.6), bringing the C-C-C plane toward orthogonality with respect to the polymer backbone, similarly to that observed for the thermochromic transition. Because the plane of the carboxylate lies

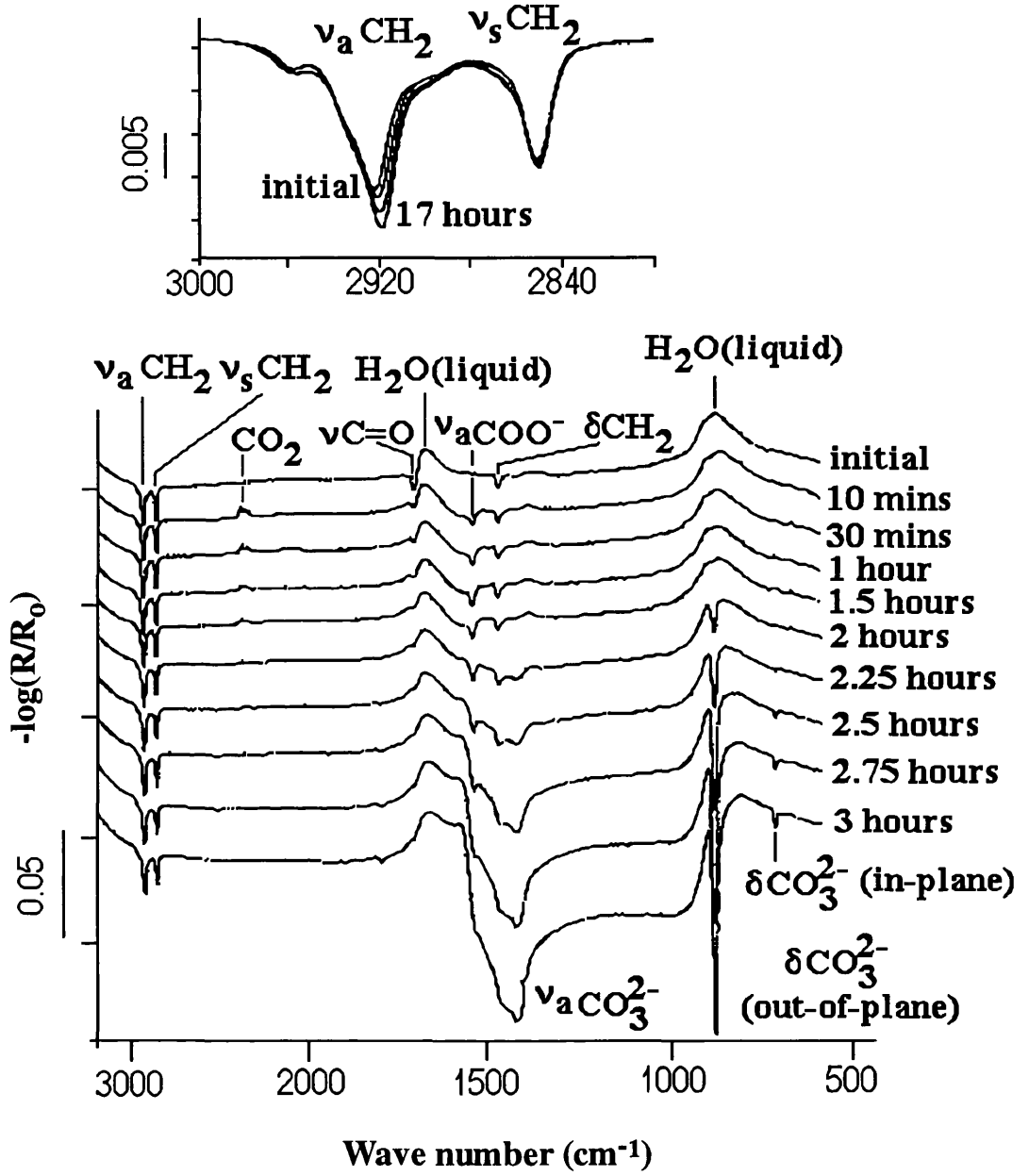

Figure 13.12. *In-situ* FTIR spectra of the p-PCDA template and the growing calcite crystal during the course of mineralization. The reflected signal R was divided by the background signal R_0 from a bare water surface. Upon calcium ion binding to the carboxylic acid head group, the frequency of the carbonyl band (ν C=O) at 1698 cm^{-1} shifted to 1538 cm^{-1} (ν_a COO$^-$), typical of the salt form of the acid. Calcite crystals formation is identified by increasing carbonate bands (ν_a at 1423 cm^{-1} and δ bands at 880 and 712 cm^{-1}). In occurrence with the onset of calcite deposition, the p-PCDA film undergoes re-organization, as observed in the methylene stretching bands (inset).

perpendicular to the C-C-C plane upon calcium binding,[27] this rotation would bring the carboxylate into the optimal position for stereochemical match (figure 13.11(a)). Calcium binding alone is insufficient to induce the color change, as evidenced by the negative response of the films to calcium chloride solutions.

The morphology of most of the calcite crystals nucleated at p-PCDA (figure 13.10) indicates faster growth along the *a* direction compared with that along *c'*, suggesting different kinetics for growth along the lattice matched direction (*a*) compared to the mismatched (and therefore inhibiting) direction (*c'*). This observation is in keeping with the stereochemical rule that relates crystal morphology to different growth rates arising from growth inhibition at specific crystallographic directions.[28]

The extended range of the co-aligned crystals (up to 1 mm) and the total control exerted over their orientation is, to the authors knowledge, unprecedented in crystal growth at the *in-vitro* organic-inorganic interface. This degree of three-dimensional control is observed in many living systems where organisms control crystallographic orientation as well as crystal size and morphology. For example, large arrays of distinct crystallites are co-aligned in certain forms of nacre[29] and in the radial segments of coccoliths.[30] Interestingly, reduction of calcite crystal symmetry in calcareous sponge spicules presumably also occurs through oriented nucleation on the (012) calcite plane.[31] Although simplified, this polymeric model system suggests that symmetry reduction of the organic matrix is a mechanism by which organisms control the co-alignment and the precise crystallographic orientation of the deposited crystals. This mechanism is in addition to previously recognized mechanisms such as charge distribution, lattice match, and stereochemical registry.

This method demonstrates that new crystalline materials can be synthesized by taking some cues from Nature. In turn, materials design and synthesis can also "feed back" into a better understanding of Nature's biomineralization.

References

[1] S. P. A. Fodor, J. L. Read, M. C. Pirrung, L. Stryer, A. T. Lu, D. Solas, *Science*, **251**, 767 (1991).

[2] J. I. Anzai, T. Osa, *Selective Electrode Rev.*, **12**, 3 (1990).

[3] Y. Okahata, T. Tsuruta, K. Ijiro, K. Ariga, *Thin Solid Films*, **180**, 65 (1989).

[4] S. Arisawa, R. Yamamoto, *Thin Solid Films*, **210**, 443 (1990).

[5] D. H. Charych, J. O. Nagy, W. Spevak, M. D. Bednarski, *Science*, **261**, 585 (1993).

[6] J. White, M. Kielian, A. Helenius, *Quart. Rev. Biophys.*, **16**, 151 (1983).

[7] J. O. Nagy, P. Wang, J. H. Gilbert, M. E. Schaefer, T. G. Hill, M. R. Callstrom, M. D. Bednarski, *J. Med. Chem.*, **35**, 4501 (1992).

[8] W. Spevak, J. O. Nagy, D. H. Charych, M. E. Schaefer, J. H. Gilbert, M. D. Bednarski, *J. Am. Chem. Soc.*, **115**, 1146 (1993).

[9] W. F. Kolbe, D. F. Ogletree, M. Salmeron, *Ultramicroscopy*, **42-44**, 1113 (1992).

[10] F. P. Booy, R. W. H. Ruigrok, E. F. J. van Bruggen, *J. Mol. Biol.*, **184**, 667 (1985).

[11] H. A. Lowenstam, S. Weiner, *On Biomineralization*, (Oxford University Press: New York, 1989).

[12] A. Berman, J. Hanson, L. Leiserowitz, T. F. Koetzle, S. weiner, L. Addadi, *Science*, **259**, 776 (1993).

[13] S. Weiner, *CRC Crit. Rev. Biochem.*, **20**, 365 (1986).

[14] A. Ulman, *An Introduction to Ultrathin Organic Films: from Langmuir-Blodgett to Self-Assembly*, (Academic Press: New York, 1991), and references therein.

[15] J. H. Fendler, *Memmbrane Mimetic Chemistry*, (Wiley: New York, 1982).

[16] E. M. Landau, M. Levanon, L. Leiserowitz, M. Lahav, J. Sagiv, *Nature*, **318**, 353 (1985).

[17] E. M. Landau, R. Popovitzbiro, M. Levanon, l. Leiserowitz, M. Lahav, J. Sagiv, *Mol. Cryst. Liq. Cryst.*, **134**, 323 (1986).

[18] B. R. Heywood, S. Mann, *Adv. Mater.*, **6**, 9 (1994), and references therein.

[19] X. K. Zhao, J. Yang, L. D. McCormick, J. H. Fendler, *J. Phys. Chem.*, **96**, 9933 (1992).

[20] L. Addadi, S. Weiner, *Proc. Natl. Acad. Sci. USA*, **82**, 4110 (1985).

[21] S. Mann, D. D. Archibald, M. Didymus, B. R. Heywood, F. C. Meldrum, V. J. Wade, *MRS Bull.*, **17**, 32 (1992).

[22] B. R. Heywood, S. Rajam, S. Mann, *J. Chem. Soc. Faraday Trans. Part 2*, **87**, 735 (1991).

[23] D. Jacquemain, S. G. Wolf, F. Leiveller, M. Deutsch, K. Kjaer, J. Alsnielsen, M. Lahav, L. Leiserowitz, *Angew. Chem. Intl. Ed. Engl.*, **31**, 130 (1992).

[24] J. Majewski, L. Margulis, I. Weissbuch, R. Popovitzbiro, T. Arad, Y. Talmon, M. Lahav, L. Leiserowitz, *Adv. Mater.*, **26**, 7 (1995).

[25] F. Lippmann, *Sedimentary Carbonate Minerals*, (Springer-Verlag: Berlin, 1973).

[26] D. J. Ahn, A. Berman, D. H. Charych, *J. Phys. Chem.*, **100**, 12455 (1996).

[27] T. L. Marshbanks, D. J. Ahn, E. I. Franses, *Langmuir*, **10**, 276 (1994).

[28] L. Addadi in *Topics in Stereochemistry*, E. L. Eleiel, S. L. Willen, N. L. Allinger edts., vol. 16, (Wiley: New York, 1986).

[29] S. Weiner, Y. Talmon, W. Traub, *Int. J. Biol. Macromol.*, **5**, 325 (1983).

[30] J. R. Young, J. M. Didymus, P. R. Bown, B. Prins, S. Mann, *Nature*, **356**, 516 (1992).

[31] J. Aizenberg, J. Hanson, T. F. Koetzle, L. Leiserowitz, S. Weiner, L. Addadi, *Eur. J. Chem. A*, **1**, 414 (1995).

Chapter 14

An Immobilization Technique for Oxidized Surfaces

14.1 Introduction

A wide and important field of application of self-assembled monolayers is in the development and fabrication of biosensors. Apart from the newly discovered colorimetric detection method (chapters 11-13), biosensors usually consist of immobilized biological material in contact with a suitable transducer device, that converts the biochemical signal into a measurable electrical signal. The biological element can be, for example, an enzyme (enzyme sensors), a cell (whole-cell biosensors) or an antibody/antigen (immunosensors). One of the critical factors determining the reliability of a biosensor is the attachment of the biological component to the sensor surface. The strength of this attachment ultimately determines the life of the sensor. 'Entrapment' in a polymer matrix or membrane is one of the most popular immobilization methods, together with chemical bonding to the surface. In either cases, one of the major concerns is the retention of the biological activity *in-vitro*. Another important aspect of biosensors is the device fabrication and miniaturization. In fact, for a wide commercial utilization of biosensors, small devices need to be fabricated. To do so microelectronic techniques, borrowed from semiconductor technology, are most often used.

During the initial stage of this doctoral project and as part of a concerted effort by the Biolectronics Group at Glasgow University, efforts were made to develop micron and submicron fabrication and analysis methods for biomaterials with biocompatible and biolectronic properties. Within this project and this thesis project in particular, research was performed to find new substrate materials and develop appropriate immobilization methods at the chosen substrates. Within this project, scanning tunneling microscopy was proposed as an analysis technique at the molecular level. However, despite early promise, STM imaging has not yielded a large amount of results on biological samples. A sample must conduct electrons if it is to be imaged by STM and most of biological samples do not conduct electrons at the required current level, i.e. about 10^{10} electrons/second in an area a fraction of a nanometer on a side. In addition, as discussed in chapter 2, the interpretation of

STM images is rather complex and topographic information is not immediately available. Imaging interpretation is even more challenging and delicate in the case of very complex molecules, such as for example proteins. Many of the early results were obtained on layered materials, such as graphite[1, 2, 3, 4, 5, 6] and in many cases they were later recognized to be the results of substrate artifacts.[7, 8, 9] Therefore, later in this project it was recognized that AFM is more appropriate for the characterization of such samples.

The material chosen as a substrate was indium tin oxide (ITO). ITO is a semiconductor material used in optoelectronics applications, such as flat panel display components and solar windows in solar cells.[10, 11, 12] The choice was determined by the possibility of developing fabrication methods using semiconductor technology and because ITO has a high enough conductivity to allow for eventual STM imaging. Materials that are knowingly non biocompatible, such as for example GaAs, had to be excluded. Commercially available ITO films were characterized by high resolution scanning electron microscopy (HRSEM) and STM.

In order to immobilize biomolecules on an ITO surface a coupling technique must be employed. To that aim, the substrate was activated by reaction with a silane agent bearing an organo functional headgroup (such as an amino group), which then serves as a 'bridge' between the substrate itself and the biomolecule. This method is necessary for a chemical bond of the biomolecule to the substrate to occur. In fact, in absence of the coupling agent only physical absorption will take place and the attachment to the substrate will not be strong enough for biosensors related applications. The silane molecule chosen for the experiments reported in this chapter was aminoethyl-3-aminopropyltrimethoxysilane (AEAPS):

$$H_2N\text{–}(CH_2)_2\text{–}NH\text{–}(CH_2)_3\text{–}Si(OCH_3)_3$$

The idea was to use the amine head group of AEAPS to cross-link the silane activated support to biomolecules, such as proteins.

Silane chemistry and semiconductor patterning technology can be combined to spatially define areas on oxidized substrates, such as ITO, with specific chemical and/or biological functionalities. Lithography techniques are commonly, but not solely, used for this purpose. During this thesis project, patterning techniques aimed at biosensor applications were developed and the patterned samples were characterized by AFM.

To test the immobilization method, as a first step small molecules, rather than proteins, were used. For biosensor related applications, it is important that the organic-biological interface be well characterized in order to achieve the highest degree of control of such interface and in turn obtain reproducible results. The intent was to use molecules that, unlike proteins, do not have multiple active sites available for intermolecular bonds, that would contribute to the stability of the

assembly. By using molecules with only one or two active sites, it should be possible to determine the buoyancy of the coupling technique itself by avoiding 3D-clustering. For this purpose, a small fluorescent molecule, fluorescein isothiocyanate (FITC), commonly used as a fluorescent label in the optical detection of proteins, was employed (figure 14.1). Its excitation spectra has a peak at 495 nm (blue) and its emission has a maximum at 520 nm (green). If the AEAPS and FITC are schematically indicated as:

$$H_2N\text{–}R \quad \text{(AEAPS)}$$
$$I\text{–}CNS \quad \text{(FITC)}$$

the reaction taking place between them can be schematically written as

$$I\text{–}CNS + H_2N\text{–}R \rightarrow I\text{–}NH\text{–}\overset{\overset{S}{\|}}{C}\text{–}NH\text{–}R$$

and a strong covalent bond is formed.

Quantitative fluorescence microscopy was used to determine the occurrence of the reaction with the aminosilane layer and optimum coverage.

14.2 Materials and Methods

14.2.1 Materials

Indium tin oxide films were purchased from Balzers. Fully oxidized films (300 Å nominal thickness) deposited on glass substrates and with (sample A) or without a SiO_2 (sample B) adhesion-promoting layer were used. A third type of ITO substrate (sample C) was kindly donated by Dr. Fröller of Siemens (Germany).

Aminoethyl-3-aminopropyltrimethoxysilane was purchased from Johnson Matthey Alfa Products (UK) and used as received. Florescein isothiocyanate was purchased from Sigma Chemical Company and used as received.

14.2.2 Preparation of AEAPS Films on ITO

ITO wafers were cut to ~1 cm^2 with a diamond pen and cleaned by washing with ultrasonic agitation in i) Opticlear™, ii) acetone, iii) methanol and iv) reversed osmosis (RO) water for 5 minutes each.

AEAPS was deposited on ITO substrates according to a procedure widely described in the literature for the silanation of oxidized surfaces.[13] The ITO substrates were immersed in a 1% (v/v) solution of AEAPS in 95% ethanol/5% RO

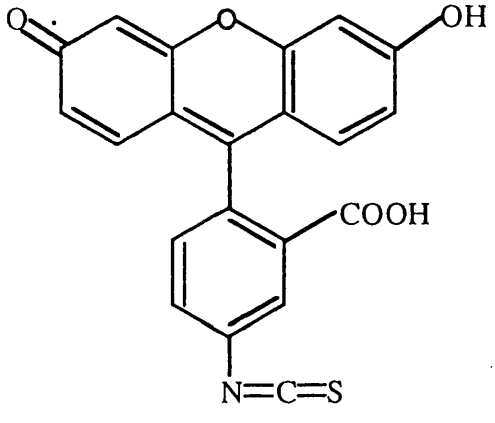

Figure 14.1. Molecular structure of fluorescein isothiocyanate.

water (pH adjusted to 5.0 with acetic acid) for 30 secs, then rinsed twice in 95% ethanol to remove excess molecules and finally blown dry in a stream of N_2. Samples were then cured at 120 ^oC for 30 minutes.

14.2.3 Patterning of Silanated ITO Substrates

Two types of patterns were written on ITO surfaces. In the first case, a method was developed to pattern AEAPS molecules on ITO surfaces (pattern A). In the second case, a method previously developed by the Bioelectronics Group, was used to spatially define a pattern of AEAPS and the protein bovine serum albumin (BSA) on ITO surfaces (pattern B).

For pattern A, ITO samples were first coated with a semiconductor photoresist (Shipley AZ 1400-31) by spinning at 4000 rpm for 30 secs, yielding a thickness of 1.8 μm. Samples were then baked at 90 ^oC for 30 minutes. The resist was patterned by exposure to UV light through a chrome mask (6 μm grating) and then developed in Shipley developer. A film of CaF_2 (100 nm) was then evaporated. Afterwards, samples were soaked in acetone to remove excess photoresist, rinsed with RO water and blown dry in a stream of N_2. Samples were then silanated with AEAPS as described in section 14.2.2. Finally, CaF_2 was removed by ultrasonication in hot RO water (80 ^oC) for 10 minutes. Steps involved in the formation of pattern A are shown in figure 14.2.

For pattern B (figure 14.3), ITO substrates were first silanated with AEAPS as described in section 14.2.2. Substrates so obtained were spin coated with a semiconductor photoresist (Shipley AZ 1400-31) and then baked at 90 ^oC for 30 minutes. A pattern was formed by exposing the resist to UV light through a chrome mask (6 μm grating) and developed in Shipley developer. The exposed aminosilane was then reacted with BSA using the following cross-linking method.[14] Samples were first soaked for 15 minutes in a solution of 1% glutaraldehyde/PBS at room temperature. The glutaraldehyde was then poured off and a solution of 300 μg/ml BSA in 40 mM sodium cyano borohydride ($NaCNBH_3$)/PBS added, left to soak for 30 minutes and then thoroughly rinsed with PBS. The glutaraldehyde cross-links the BSA to the AEAPS by activating its amino groups. A wash in acetone removes the photoresist and leaves an AEAPS/BSA pattern on the surface.

At this point, a second protein could be immobilized on the exposed AEAPS regions, as described in reference 15.

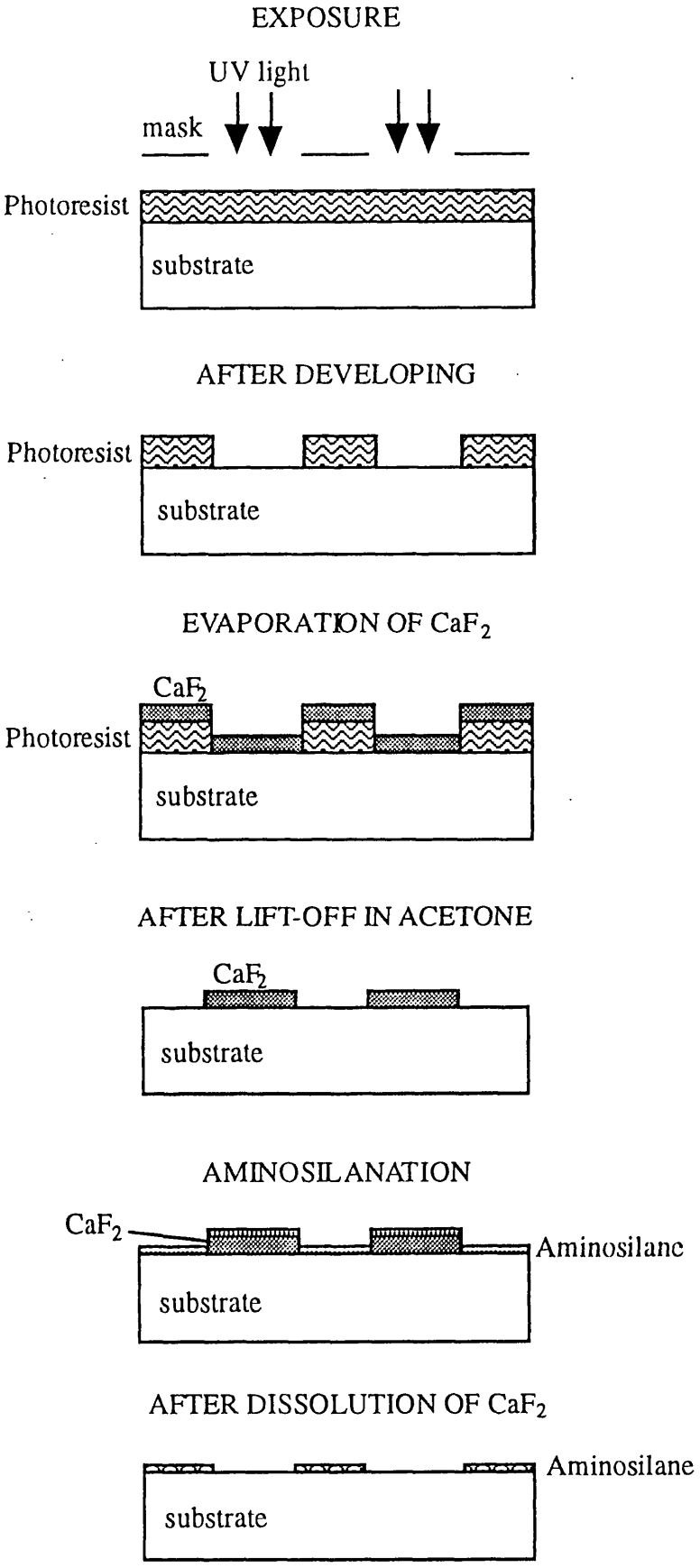

Figure 14.2. Patterning method of AEAPS on ITO using photolithography and silane chemistry (pattern A).

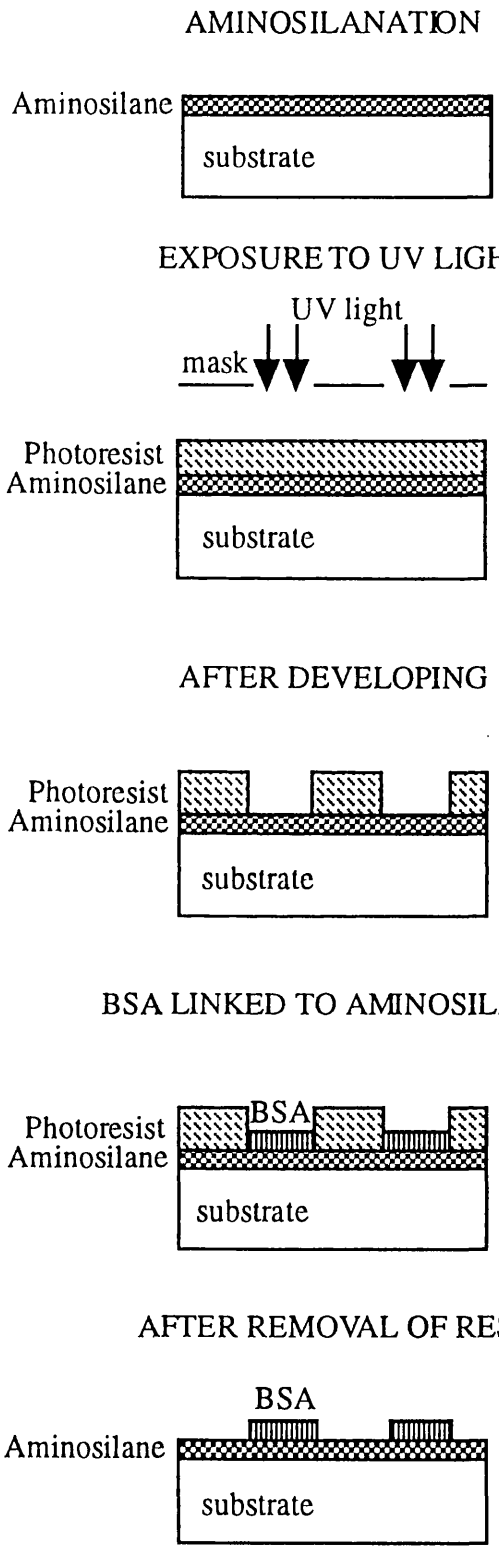

Figure 14.3. Patterning method for bovin serum albumin (BSA) and AEAPS on an ITO surface (pattern B).

14.2.4 Deposition of FITC Molecules

Fluorescein isothiocyanate was first dissolved in N,N-dimethylformamide (DMF) (pH=6) and then diluted to working concentration with phosphate buffer saline (pH=7.4) or 0.25 M Carbonate/Bicarbonate Buffer (pH=9.1). Freshly prepared FITC solutions were used.

Samples for fluorescence microscopy detection were prepared by reacting FITC molecules onto plain AEAPS films on ITO.

Samples were incubated overnight at 4 ^{o}C and in the dark in FITC solution. They were then rinsed thoroughly in PBS or Carbonate/Bicarbonate buffer and left in solution, still in the dark until examination.

14.2.5 SEM Analysis of ITO Films

A high-resolution scanning electron microscope (Hitachi 900, Hitachi, Japan) with a nominal lateral resolution of 7 Å was used. All images were taken using the secondary electron detection method. SEM of ITO films is not straightforward due to the non conductive nature of the surface. In SEM imaging, following an electron bombardment, the sample emits electrons by secondary emission and backscattering. If the electron yield δ, defined as number of electrons emitted per incident primary electron,[16] is not unity the specimen will charge up. The result is a distortion and loss of resolution of the image. Two solutions are available to this problem: coating the sample with a conducting film or decreasing the electron gun voltage to a value at which δ is unity. In the case discussed here, a conductive coating might have obscured the sample structure, hence electrical contact between the specimen surface and the holder was alternatively made by a conductive paint. All samples were glued on the microscope's sample holder by silver dag and a very small drop of it on the top surface of the sample ensured electrical contact between bottom and top layer. Furthermore, during imaging a relatively low electron voltage was used. However, the electron voltage could not be lowered too much, since the image contrast also decreases.

14.2.6 STM Characterization of ITO Films

The scanning tunneling microscope used was described in chapter 4. All images were taken in the constant current mode (topographic mode) and they all refer to forward scan, i.e. with the tip moving from left to right along one scan line. The number of image points is 256 per line and the number of lines is 256 too. Films were imaged using a tunnel current of 0.1 nA and at 100-500 mV bias voltage (positive respect to the sample).

14.2.7 AFM Characterization of Patterned ITO Samples

AFM images were acquired at the Institute of Biophysics of the National Research Council (Pisa, Italy). The setup of the microscope was described in chapter 4. Images were taken using uncoated silicon nitride rectangular cantilevers of nominal force constant k=0.032 N/m. AEAPS patterns A on ITO and BSA/AEAPS patterns B on ITO were characterized. All images consist of 128 x 128 points.

14.2.8 Fluorescence Microscopy

Examination of FITC samples was performed using a Vickers optical microscope equipped with epi-fluorescence attachment. The microscope uses a high pressure 200 W mercury lamp for fluorescence analysis and allows for simultaneous normal dia-illumination microscopy. This is very useful when examining fluorescence light that rapidly fades upon excitation, since the sample can be focussed on by using white light therefore avoiding prolonged exposure to exciting light. The microscope uses a dichroic mirror (Vickers), reflecting wavelengths shorter than 514 nm and transmitting wavelengths greater than 540 nm, for detection of the fluorescence signal from FITC molecules.

The fluorescence signal is sent to a Falcon LTC1162 ISIT very low level TV camera (Custom Camera Designs Ltd., UK). The camera operates in conjunction with a Control Unit, which provides the voltage to the camera and contains all the user's controls. Images are displayed on a high-resolution black and white monitor. The signal from the Control Unit is finally sent to a PC through a frame digitizer and the fluorescence signal is measured through a program written in C language. The output on the screen of the computer is a histogram which has grey levels of brightness (256 levels) in abscissa and areas in pixels on a logarithmic scale in ordinate. The integral of the histogram, i.e. the Integrated Brightness, is the signal used for quantification of fluorescence. This apparatus allows for quantification of fluorescence and detection of very small fluorescence signals.

Samples with different concentrations of FITC molecules were prepared and a sample of plain AEAPS on ITO was used as a reference. Reported data is the statistical average of 5 measurements taken at the bottom right, bottom left, top left, top right and center of the sample. The corners are avoided to reduce the problems of light diffracted from the edges. Furthermore, between two measurements the blue light is turned off to reduce fading of fluorescence to a minimum.

Measurements were taken 1) after incubation, 2) after 1 wash in acetone, 3) after 2 washes in acetone. Furthermore, 'bleaching' measurements were performed

after 1) and 3) on two different areas of the sample. It is characteristic of fluorescent specimens to 'fade' during irradiation. FITC preparations are usually observed to fade very rapidly. 'Bleaching' measurements were taken at intervals of one minute leaving the blue exciting light on.

14.3 Results and Discussion

14.3.1 Fluorescence Microscopy Characterization of FTIC Films

FTIC concentrations of 200, 50, 10, 5, 1, 0.5 and 0.1 μg/ml were used. Results obtained on these samples are shown in figures 14.4-14.10. They show for each sample the Integrated Brightness (IB) averaged over the five measurements performed and having subtracted the Mean Integrated Brightness obtained for the reference sample. The Relative Mean Integrated Brightness (RMIB) for each sample and each measurement is reported in table 14.I, together with the standard deviation. In addition, 'bleaching' curves for measurements after the incubation and after the second wash in acetone are shown for each specimen. In this case the Integrated Brightness is plotted versus time of observation. Graphs of the Relative Mean Integrated Brightness versus concentration are shown in figure 14.11.

As can be seen, results for samples incubated in 200 and 50 μg/ml FITC solutions (figure 14.4 and 14.5) show a considerable decrease of fluorescent signal after the first wash in acetone and to some extent after the second one. Samples incubated in 10 and 5 μg/ml FITC solutions showed a smaller decrease after the first wash and almost no variation after the second rinse. The sample incubated in 1 μg/ml FITC solution gave origin to almost the same fluorescent signal at all three stages. Finally, samples incubated in 500 and 100 ng/ml FITC solutions exhibited a very irregular behavior. These results can be interpreted as follow: for samples incubated in highly concentrated solutions, a large number of excess molecules is present on the surface after the rinse in buffer. These excess molecules are removed by the washes in acetone. Decreasing the concentration tends to a situation where no excess, or a small amount of excess, molecules are present on the surface. The result for the last two samples is most likely due to an uneven distribution and partial coverage of the surface. Since it is very difficult to perform the measurements always on the same area, discontinuity in the molecular layer may produce the results reported.

The 'bleaching' curves for samples incubated in 200 and 50 μg/ml solutions show a rapid decrease of the fluorescent signal after incubation and linear decrease

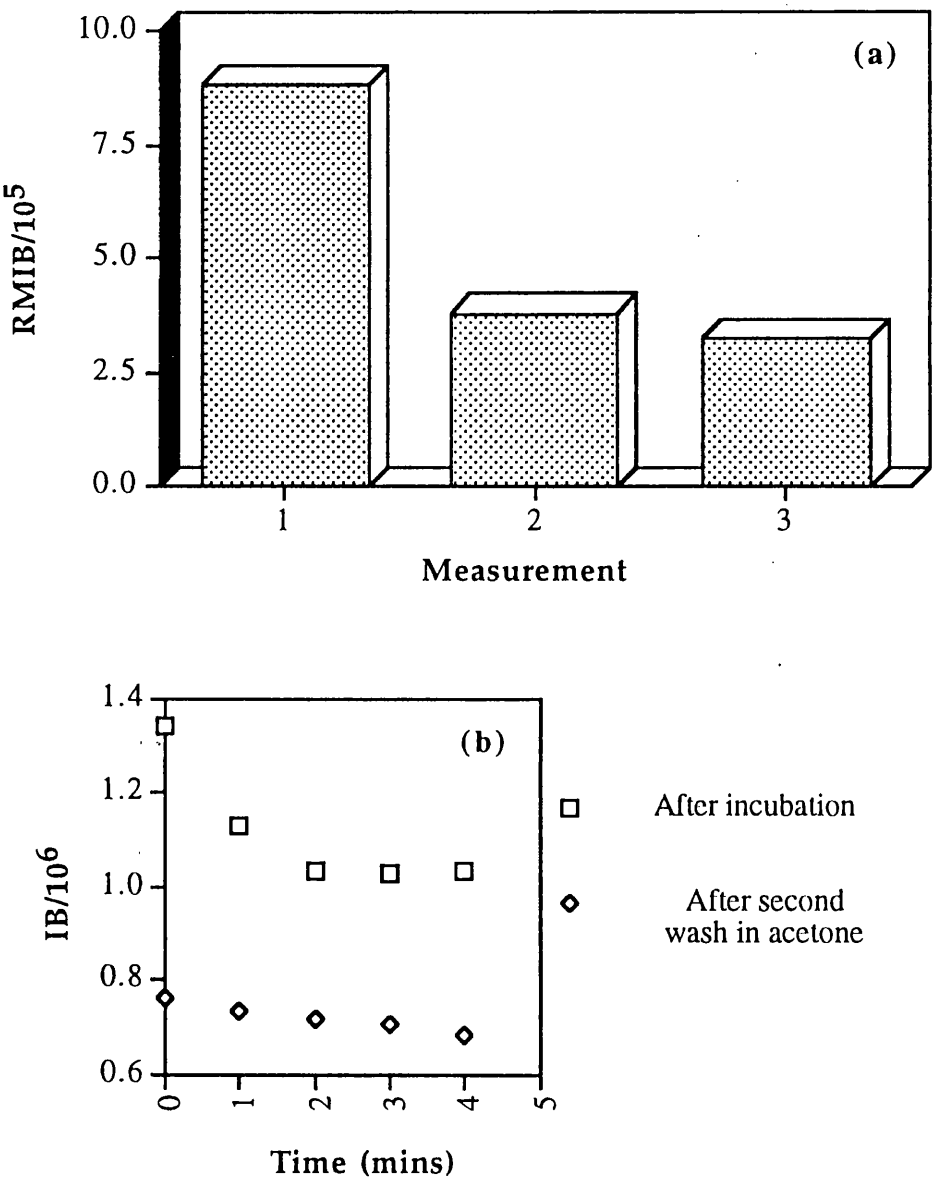

Figure 14.4. Fluorescence microscopy results for the 200 µg/ml FITC sample. (a) Relative Mean Integrated Brightness (RMIB) after incubation (**1**), one wash in acetone (**2**) and two washes in acetone (**3**). (b) 'Bleaching' curves, i.e. Integrated Brightness (IB) versus exposure time.

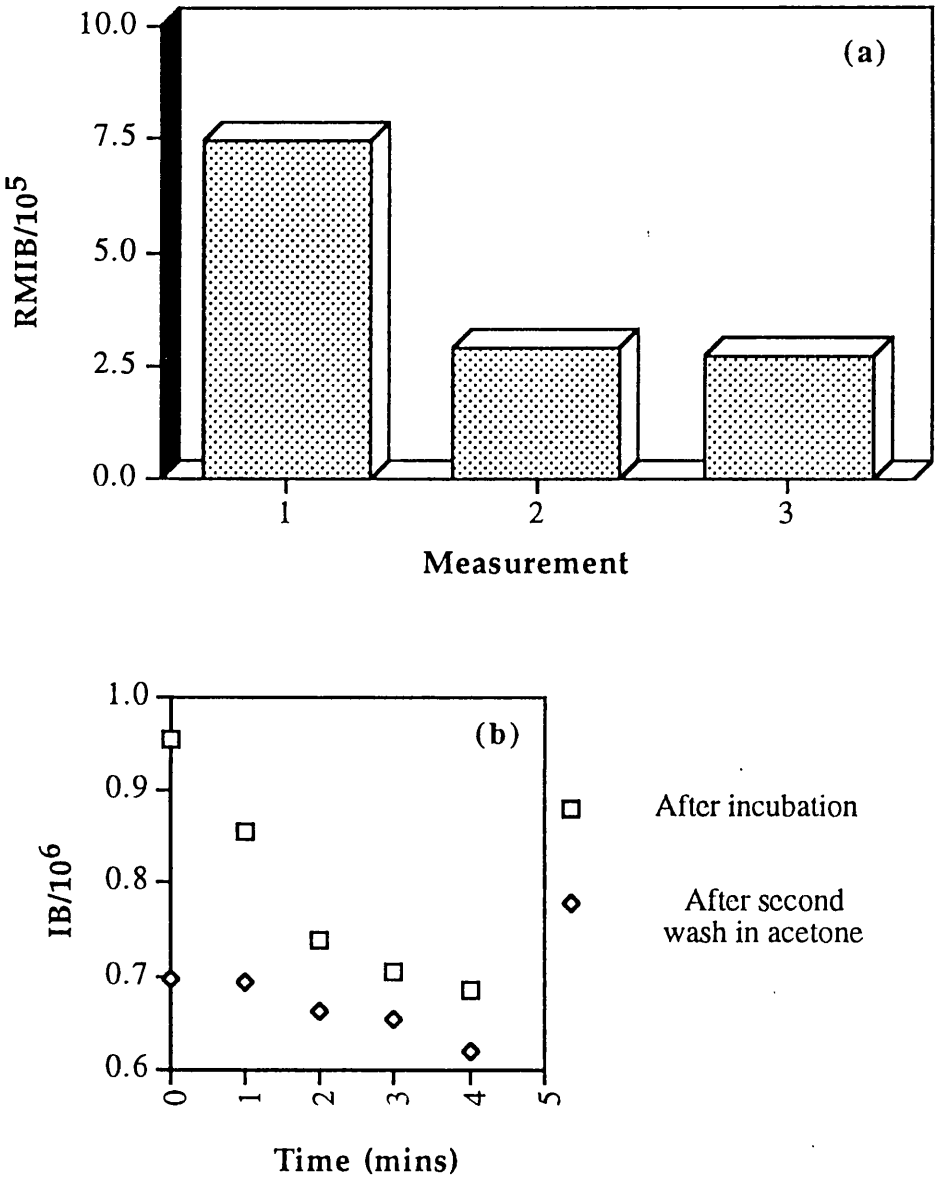

Figure 14.5. Fluorescence microscopy results for the 50 µg/ml FITC sample. (a) Relative Mean Integrated Brightness (RMIB) after incubation (1), one wash in acetone (2) and two washes in acetone (3). (b) 'Bleaching' curves, i.e. Integrated Brightness (IB) versus exposure time.

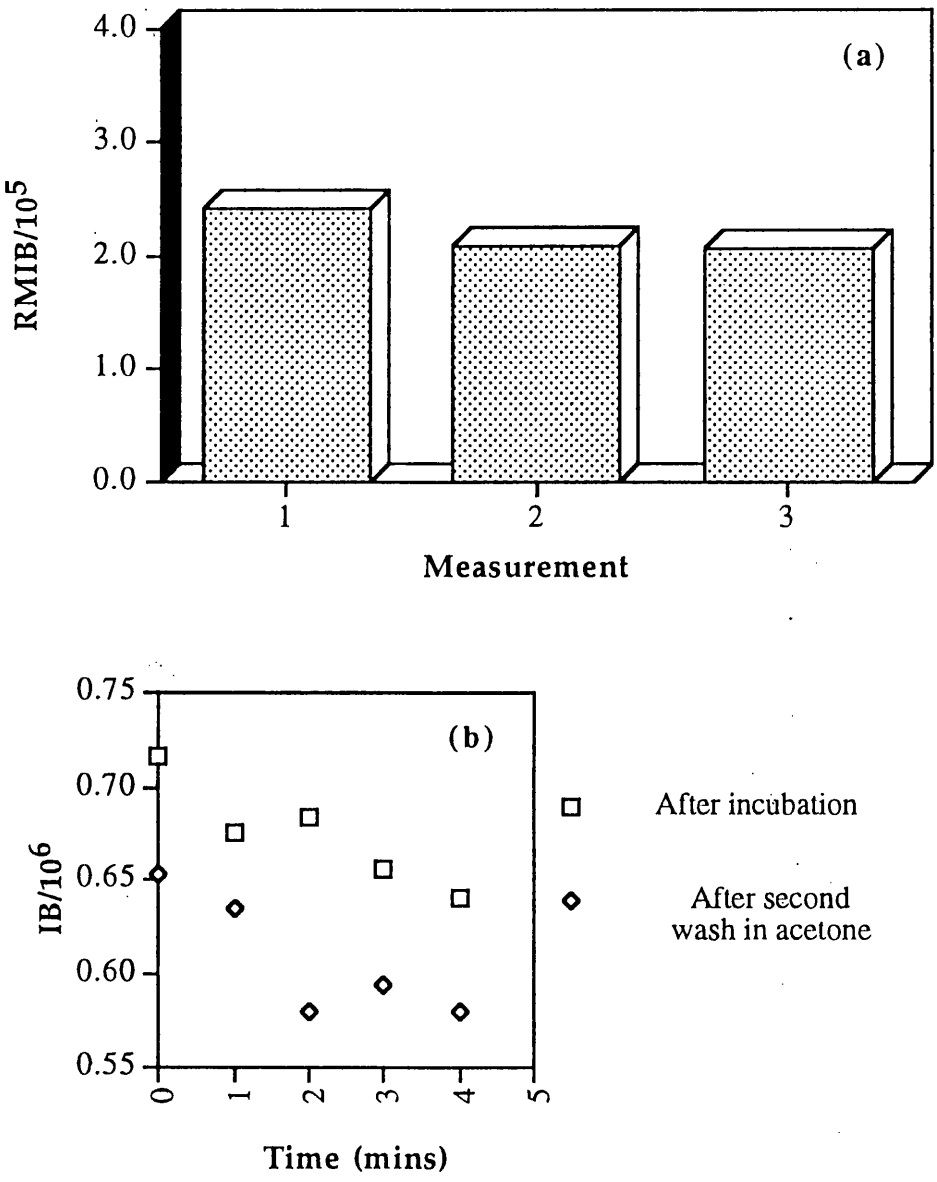

Figure 14.6. Fluorescence microscopy results for the 10 μg/ml FITC sample. (a) Relative Mean Integrated Brightness (RMIB) after incubation (1), one wash in acetone (2) and two washes in acetone (3). (b) 'Bleaching' curves, i.e. Integrated Brightness (IB) versus exposure time.

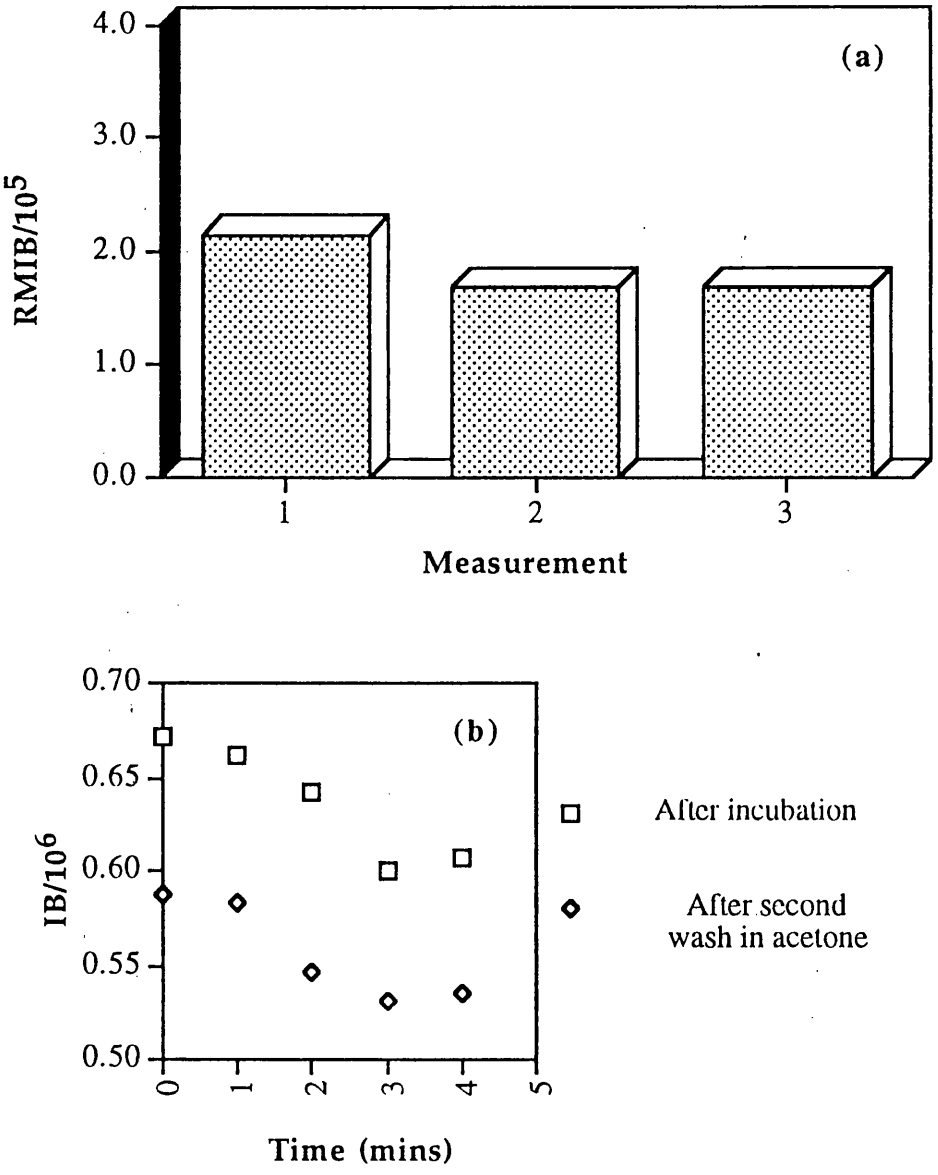

Figure 14.7. Fluorescence microscopy results for the 5 µg/ml FITC sample. (a) Relative Mean Integrated Brightness (RMIB) after incubation (1), one wash in acetone (2) and two washes in acetone (3). (b) 'Bleaching' curves, i.e. Integrated Brightness (IB) versus exposure time.

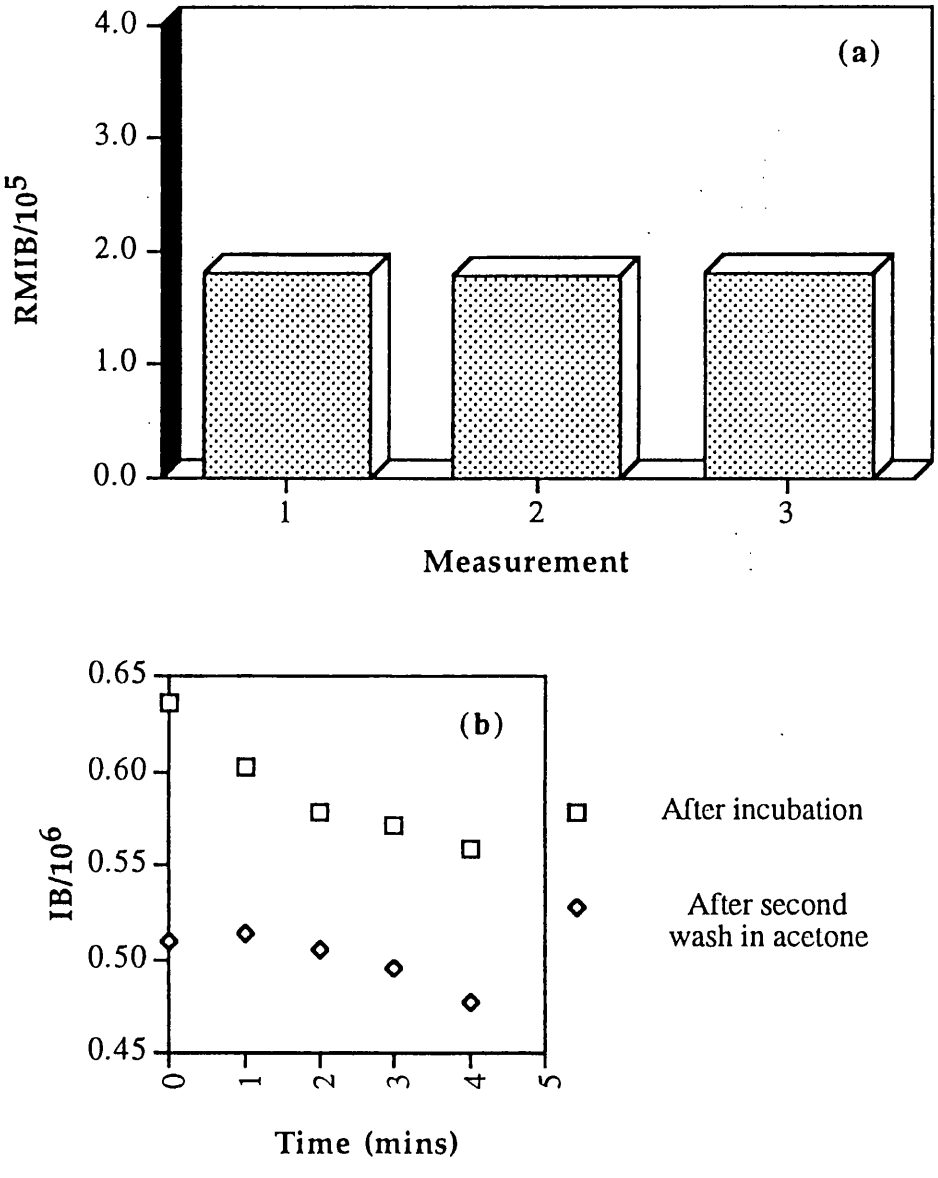

Figure 14.8. Fluorescence microscopy results for the 1 μg/ml FITC sample. (a) Relative Mean Integrated Brightness (RMIB) after incubation (1), one wash in acetone (2) and two washes in acetone (3). (b) 'Bleaching' curves, i.e. Integrated Brightness (IB) versus exposure time.

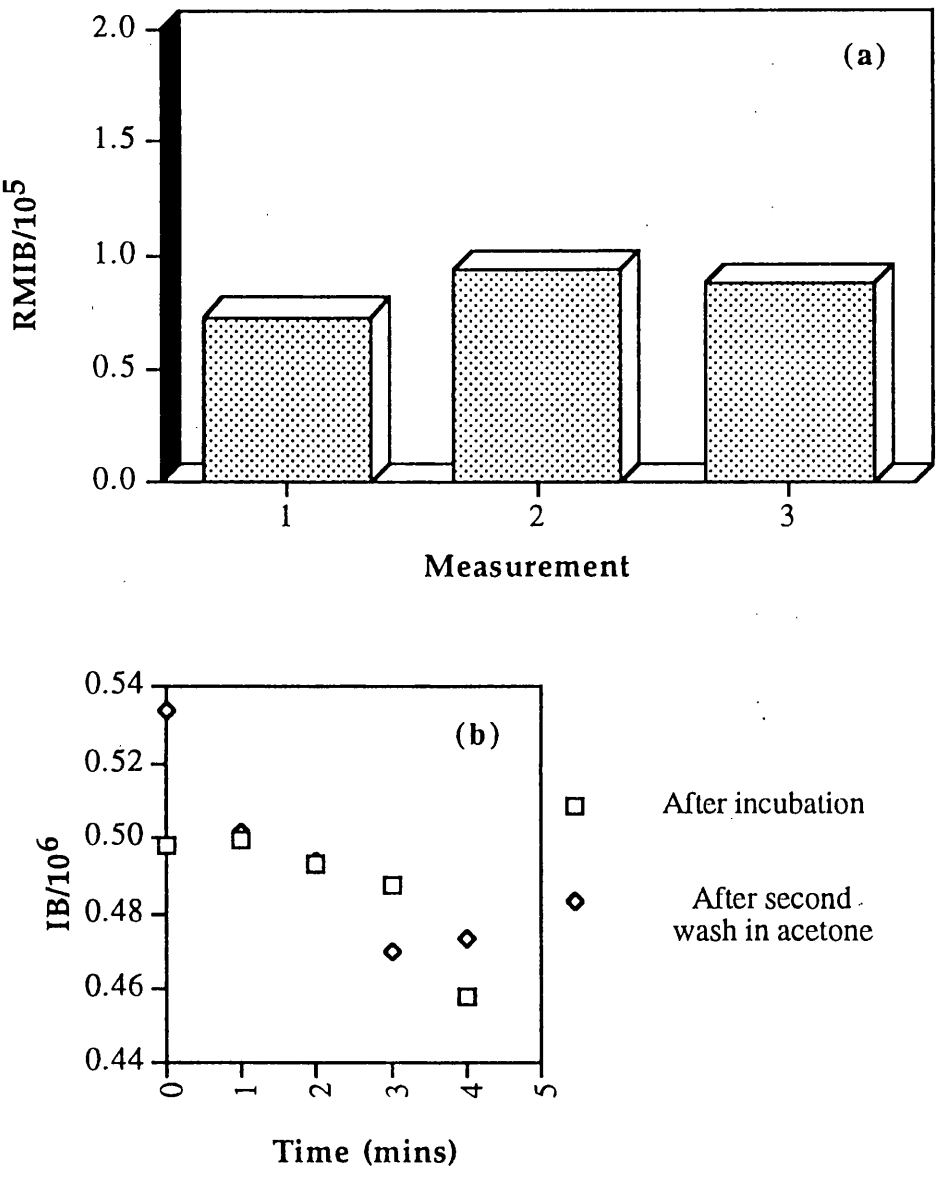

Figure 14.9. Fluorescence microscopy results for the 0.5 µg/ml FITC sample. (a) Relative Mean Integrated Brightness (RMIB) after incubation (1), one wash in acetone (2) and two washes in acetone (3). (b) 'Bleaching' curves, i.e. Integrated Brightness (IB) versus exposure time.

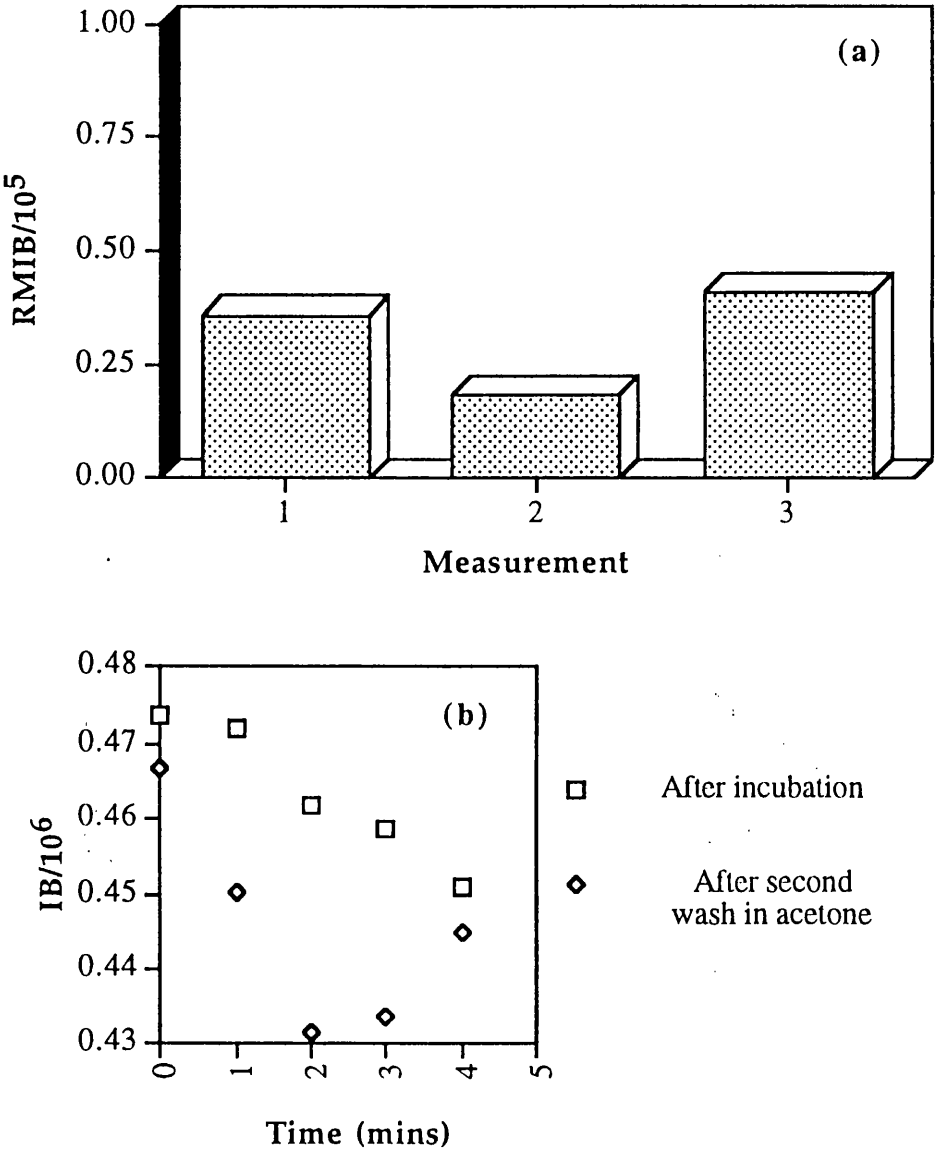

Figure 14.10. Fluorescence microscopy results for the 0.1 µg/ml FITC sample. (a) Relative Mean Integrated Brightness (RMIB) after incubation (1), one wash in acetone (2) and two washes in acetone (3). (b) 'Bleaching' curves, i.e. Integrated Brightness (IB) versus exposure time.

SAMPLE	Measurement	Mean Integrated Brightness	Standard Deviation	Relative Mean Integrated Brightness
Reference		433637	11083	0
200 µg/ml	After incubation	1318962	117991	885325
	After 1 wash in acetone	812589	6632	378952
	After 2 washes in acetone	758688	13327	325051
50 µg/ml	After incubation	1180461	447242	746824
	After 1 wash in acetone	724155	83207	290518
	After 2 washes in acetone	705205	29373	271568
10 µg/ml	After incubation	674992	10896	241355
	After 1 wash in acetone	641148	24422	207511
	After 2 washes in acetone	638670	10061	205033
5 µg/ml	After incubation	647607	11692	213970
	After 1 wash in acetone	602618	5343	168981
	After 2 washes in acetone	602650	11422	169013
1 µg/ml	After incubation	612993	15972	179356
	After 1 wash in acetone	610254	22918	176617
	After 2 washes in acetone	613858	11643	180221
0.5 µg/ml	After incubation	506584	9573	72947
	After 1 wash in acetone	526943	20718	93306
	After 2 washes in acetone	521077	25719	87440
0.1 µg/ml	After incubation	467683	18549	35846
	After 1 wash in acetone	451959	9207	18322
	After 2 washes in acetone	474357	8258	40720

Table 14.I. Fluorescence microscopy results for FITC molecules deposited on AEAPS/ITO.

after the second wash in acetone. The law becomes linear in both cases, even if with smaller accuracy, for samples incubated in 10 and 5 μg/ml FTIC solutions. It is still linear after the second wash in acetone for the 1 μg/ml sample and points are randomly distributed in the cases of the 500 and 100 ng/ml samples.

Finally, analysis of curves in figure 14.11 indicates a logarithmic dependence of the Relative Mean Integrated Brightness on the concentration of solutions used. For measurements taken after incubation the dependence is logarithmic only when the analysis is restricted to samples incubated in solutions with concentration up to 10 μg/ml.

14.3.2 HRSEM and STM Characterization of ITO Substrates

Figures 14.12 (a) and (b) show HRSEM images obtained on ITO films A and B, respectively. Figure 14.12 (a) shows a 'grain-like' structure with grain size ranging from about 100 Å, to about 400 Å. Figure 14.12 (b) shows that in absence of a SiO_2 adhesion-promoting layer, the ITO film reveals areas that are completely amorphous and areas characterized by micro-grains separated by well-defined boundaries. The morphology for the ITO substrates obtained from Siemens (sample C) (figure 14.12 (c)) shows a grain-like structure of different sizes and shapes.

The analysis of all three samples had to be fairly fast due to the effect of contamination on the samples' surface. In fact, vapors of hydrocarbon compounds present into the column of the SEM polymerize on the sample surface due to the electron bombardment and become permanent. Furthermore, since the samples are semiconductors, electrostatic charging up of the exposed area often make the image blur up. This effect was particularly severe for the ITO sample from Balzers deposited on glass and with a SiO_2 in between (sample A).

Figures 14.13 (a) and (b) show two STM images of ITO samples A and C respectively. Figure 14.13 (a) shows an island-like structure with largest grains being about 500 Å in size, consistent with the HRSEM results (see figure 14.12 (a)). The surface also shows to be highly corrugated. Figure 14.13 (b) reveals a very irregular morphology for sample C, with largest grains being about 200 Å in size.

14.3.3 AFM Characterization of Patterned ITO Samples

Figure 14.14 shows a 12 x 12 μm^2 AFM topographic image of pattern A. As clearly visible, the AEAPS molecules were successfully patterned. The difference in the pattern size between figure 14.14 (a) and (b) is an artefact due to the hysteresis of the piezoelectric tube. Figure 14.15 (a) and (b) show a zoom in across the pattern step. This image reveals that the AEAPS deposition method results in

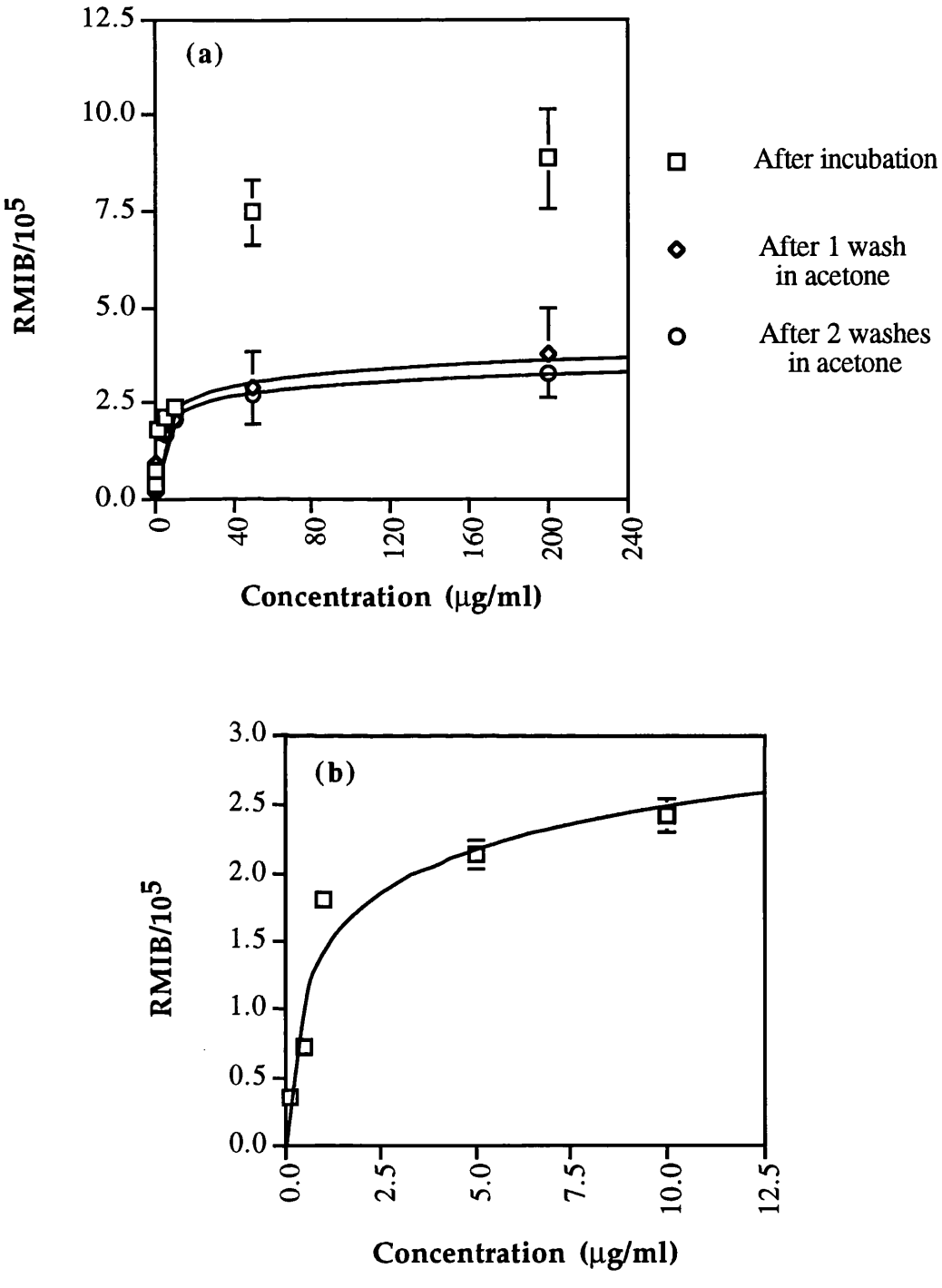

Figure 14.11. Fluorescence microscopy results. (a) Relative Mean Integrated Brightness as a function of FITC concentration after incubation, one and two washes in acetone. (b) RMIB data relative to measurements after incubation for FTIC concentration up to 10 μg/ml.

Figure 14.12 (following page). HRSEM images of ITO films. (a) Sample A (Balzers, with a SiO_2 adhesion-promoting layer). (b) Sample B (Balzers, no SiO_2 adhesion-promoting layer). (c) Sample C (Siemens). Images were obtained with a 10 kV (a) and 20 kV (b and c) electron beam.

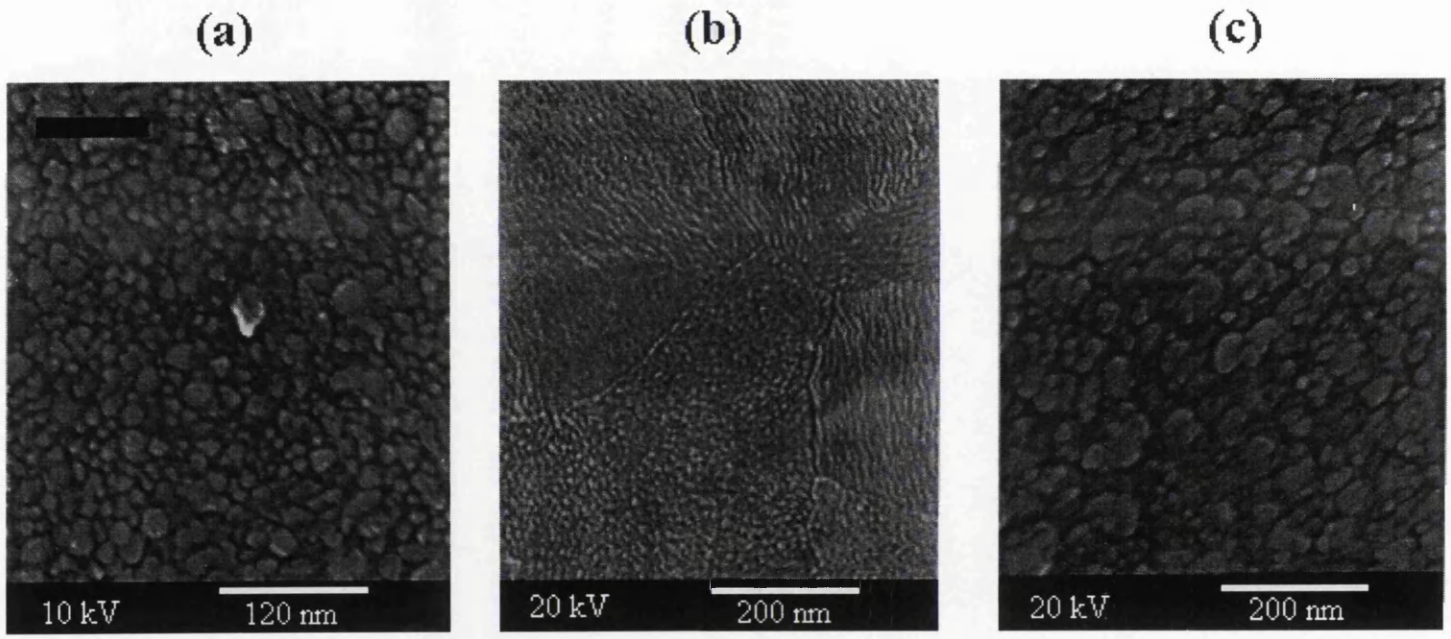
(a)
(b)
(c)
10 kV
120 nm
20 kV
200 nm
20 kV
200 nm

Figure 14.13 (following page). Constant current STM images for ITO samples A (a) and C (b). Image size=(a) 3000x3000 $Å^2$, (b) 2000x2000 $Å^2$. Black-to-white=80 Å. Tunneling current=0.1 nA; bias voltage=(a) 200 mV, (b) 300 mV.

(a)

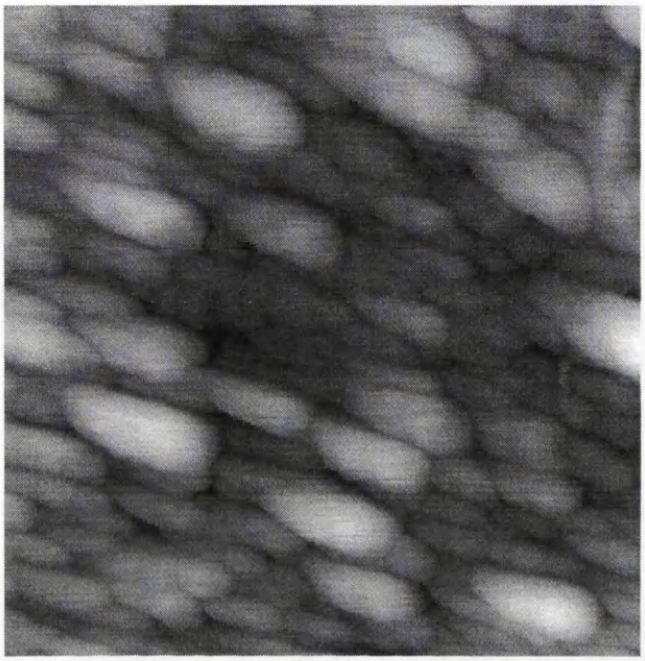

(b)

severe 3D-clustering of the molecules. The size of these clusters ranges from 100 to 150 nm. The pattern step height, as measured from AFM images, is about 20-30 nm. This result is consistent with the studies performed at a later time at LBNL. Formation of a polysiloxane network likely already occurs in solution due to the high percentage of water. Experiments performed at LBNL showed that a similar molecule, i.e. aminopropyltriethoxysilane (APS) can be successfully self-assembled on mica surface to form a monomolecular layer. However, even if the chemistry did not reveal to be the most appropriate in this case, the experiments clearly demonstrate the validity of the microfabrication method A (figure 14.2).

Figure 14.16 shows a topographic image obtained on pattern B. This image shows that AEAPS and BSA were successfully patterned, as of scheme B (figure 14.3). The height of the step was measured to be about 35 Å. This height is smaller that the height expected for BSA molecules, i.e. 54 Å. The discrepancy could be either the result of excessive pressure exerted by the AFM tip on the soft sample or an effect of the preparation method.

14.4 Conclusions

Results presented in this chapter show how chemistry and photolithography patterning technique can be combined to spatially define areas bearing different organic/biological functionalities on an appropriate substrate. Despite the aminosilane used in this study did not reveal to be the most appropriate, the technique is general enough to allow the use of more suitable molecules. If required, it should also be possible to increase the spatial density on the surface by using sub-micron lithographic techniques, such as electron-beam lithography. This would allow to decrease the size of the sensor on one side and increase its complexity on the other. One of the major challenges in such a task is the development of suitable immobilization methods, able to retain biomolecules functionality without sacrificing ligand-receptor specificity. Key to such development is the availability of appropriate sample analysis techniques at the atomic/molecular level. Ultra-high resolution techniques, such as scanning probe techniques, have already provided a great deal of data on organic materials and are helping chemists and material scientists to improve their samples preparation methods and develop new ones. The potential for new and greater improvements in the field of biosensors has never been greater.

Figure 14.14 (following page). Forward (a) and backward (b) AFM topographic images of pattern A (6 μm grating) taken at 0.5 nN. Image size: 12x12 μm^2. The brighter stripe corresponds to an AEAPS area. The step height is measured to be ~30 nm.

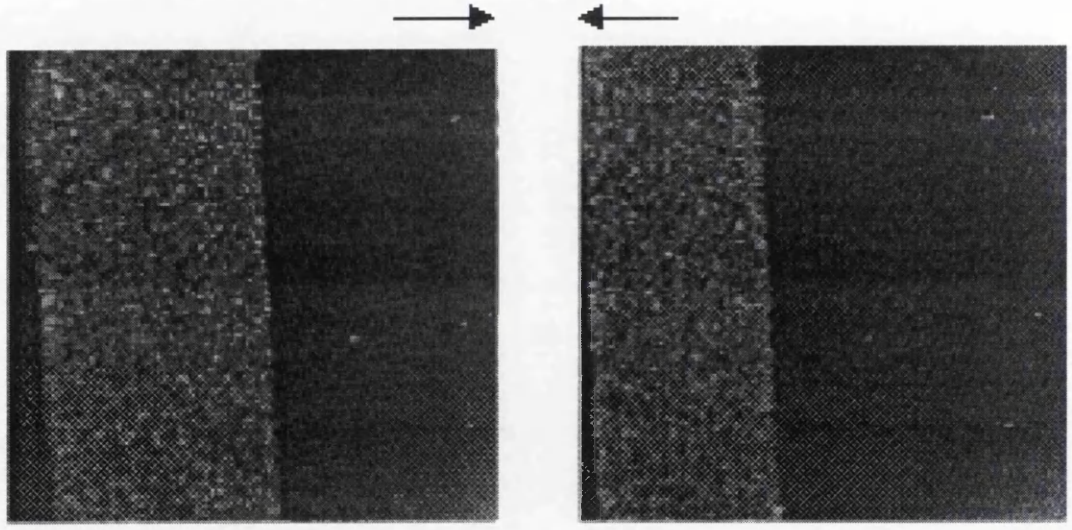

(a) (b)

Figure 14.15 (following page). Forward (a) backward (b) AFM topographic images across the AEAPS/ITO step shown in figure 14.13. Image size=1.2x1.2 μm^2.

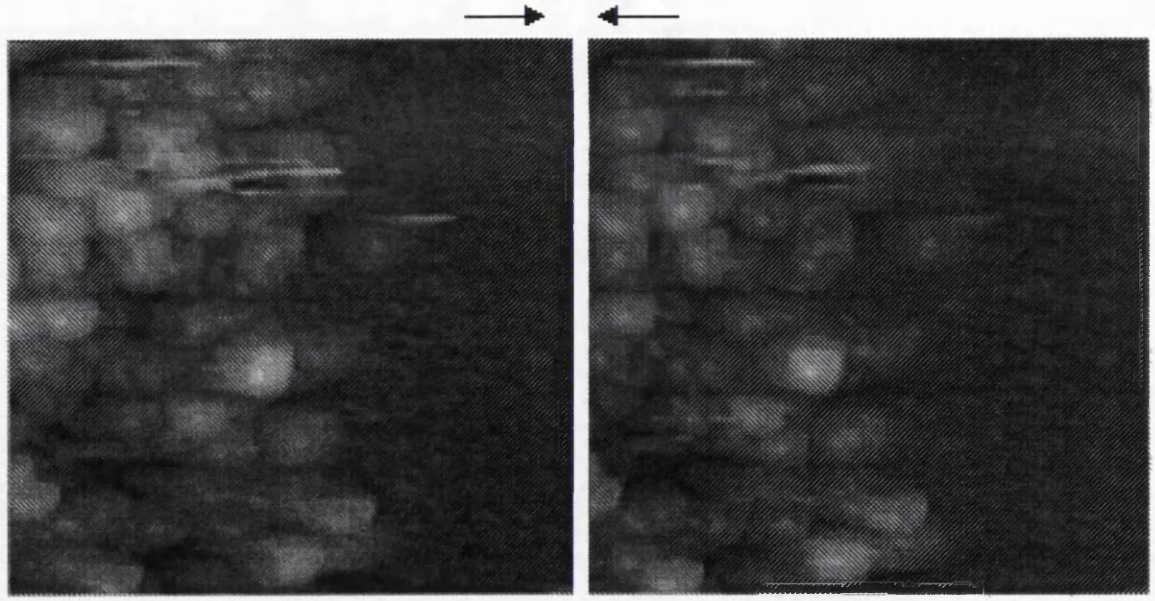

(a) (b)

Figure 14.16 (following page). Forward (a) and backward (b) AFM topographic image of pattern B. Image size=21x21 μm^2. The step is measured to be ~35 Å high.

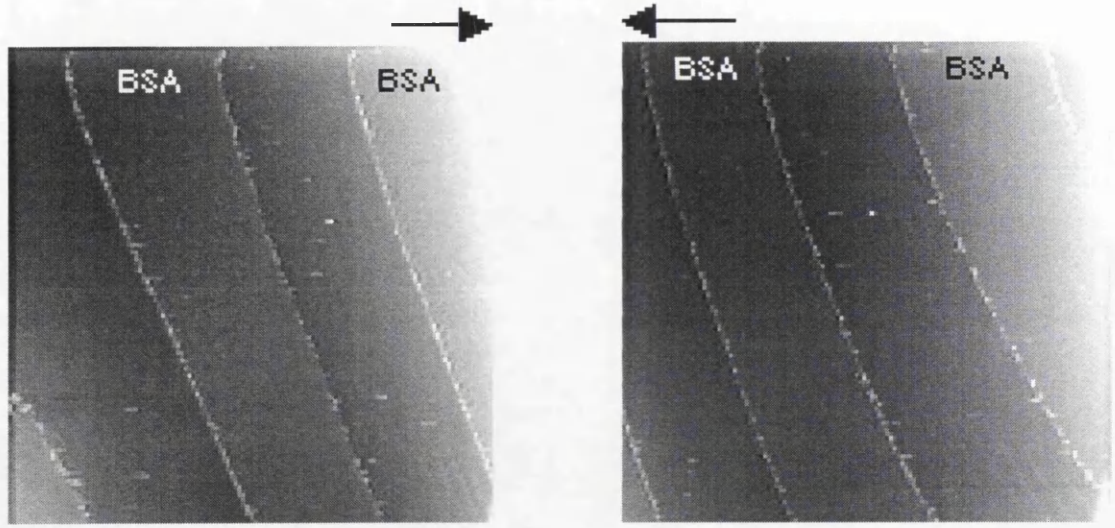

(a) (b)

References

[1] G. Binnig, H. Rhorer in *Trends in Physics*, J. Janta, J. Pantoflicek edts. (European Physical Society: The Hague, 1984).

[2] T. P. Beebe, T. E. Wilson, D. F. Ogletree, J. E. Katz, R. Balhorn, M. B. Salmeron, W. J. Siekhaus, *Science*, **243**, 370 (1989).

[3] P. G. Arscott, G. Lee, V. A. Bloomfield, D. F. Evans, *Nature*, **339**, 484 (1989).

[4] R. J. Driscoll, M. G. Youngquist, J. D. Baldeschwieler, *Nature*, **346**, 294 (1990).

[5] D. D. Dunlap, C. Bustamante, *Nature*, **342**, 204 (1989).

[6] G. Lee, P. G. Arscott, V. A. Bloomfield, D. F. Evans, *Science*, **244**, 475 (1989).

[7] M Salmeron, T. Beebe, J. Odriozola, T. Wilson, D. F. Ogletree, W. Siekhaus, *J. Vac. Sci. Technol. A*, **8**, 635 (1990).

[8] C. R. Clemmer, T. P. Beebe Jr., *Science*, **251**, 640 (1991).

[9] W. M. Heckl, G. Binnig, *Ultramicroscopy*, **42-44**, 1077 (1992).

[10] R. Tueta, M. Braguier, *Thin Solid Films*, **80**, 143 (1981).

[11] M. Hoheisel, A. Mitwalski, C. Mrotzek, *Physica Status Solidi A*, **123**, 461 (1991).

[12] J. Dutta, S. Ray, *Thin Solid Films*, **162**, 119 (1988).

[13] H. H. Weetall, *Immobilised Enzymes, Antigens, Antibodies, and Peptides. Preparation and Characterization* (Marcel Dekker Inc.: New York, 1975).

[14] E. P. Arnaud, *Ph. D. Thesis*, Department of Cell Biology, Glasgow University (UK), 1994.

[15] C. Frediani, M. Allegrini, C. Ascoli, P. Connolly, M. Labardi, G. Moores, E. P. Arnaud, *Nanotechnology*, **5**, 95 (1994).

[16] I. M. Watt, *The Principles and Practice of Electron Microscopy*, (Cambridge University Press: Cambridge, 1985).

Chapter 15

A Reference System for SPM Applications

15.1 Introduction

One of the difficulties most often encountered in many SPM studies is the inability to image the exact same area of the sample before and after some transformation of the surface has taken place. In the absence of a reference system on the surface, results are statistical data obtained at several locations on the surface. This approach clearly works best for surfaces that transform uniformly across the sample surface. In a few STM studies,[1, 2] researchers were able to maintain the position of the tip at a chosen location of the sample throughout several days by continuously compensating for thermal drift. This kind of procedure is complicated and very time consuming. More importantly, it is not always feasible since approaching the STM or AFM tip to the surface may disturb processes taking place at the surface itself.

In chapters 12 and 13 (figures 12.3 and 13.4) it was shown how important being able of imaging the exact same area of the samples can be to understand the dynamics of micron-scale processes. Such ability would be even more desirable at the sub-micron scale. Lithographic techniques can be used to define a pattern on a variety of surfaces. Such pattern definitions reach today the nanometer resolution, well within the scan range of any SPM instrument. When micron-scale features are of interest, photolithography can be used and pattern generation is fast and relatively inexpensive over the area of a standard SPM sample, i.e. 0.5x0.5-1 cm^2. Furthermore, optical microscopy can be used to choose a specific area of the sample. This was in fact the case of the thermochromism and affinochromism studies presented in chapters 12 and 13. Of course, the scan and in-plane offset ranges of the SPM piezo have to be at least as large as the smallest pattern feature. In other words, a pattern the smallest feature of which is 20 μm would be of no use with a 1 μm scan and offset ranges. Electron-beam lithography allows for pattern definition of features as small as 10 nm. Problems in this case arise since features of this size are not visible by optical microscopy. Furthermore, direct writing on a 1 cm^2 surface area can be time consuming and expensive. Therefore, a method that combines photo and e-beam lithographies would be best suited for SPM

applications.

During the initial stage of this PhD, work was carried out aimed at developing a process to define a pattern on substrates that could be used as a reference system for organic and/or biological SPM studies. At that time the author's attention was focussed on Au surfaces as an alternative substrate to oxidized surfaces, such as the ITO samples described in chapter 14, for biological SPM applications. Since the Glasgow's STM scan range was $0.5 \times 0.5\ \mu m^2$ and initial AFM studies of this project had been carried out in Pisa (Italy), the intention was to develop patterns that could be used for AFM studies in Italy and STM studies in Glasgow. The maximum scan size of the AFM in Pisa was $28 \times 28\ \mu m^2$ and that imposed limits on the pattern size. E-beam lithography was used.

The two types of patterns, A and B, were both fairly simple, that is grids of 50 nm wide lines enclosed by a frame or series of concentric frames, as schematically shown in figure 15.1 (pattern A) and 15.2 (pattern B). The lines and frame(s) were the regions written by the e-beam. Furthermore, to define an orientation, the pattern was made asymmetrical with respect to x and y. The grid serves as reference system, while the frames were designed to facilitate the identification of the patterned area by optical microscopy. That requires that the SPM system be equipped with an optical microscope.

15.2 Materials and Methods

15.2.1 Preparation of Au films

During the course of this project, Au films prepared in several different ways, such as evaporation, sputtering, and on different substrates, such as mica, glass and silicon, were characterized.[3] In chapter 7 the preparation and characterization of Au films on mica as performed at LBNL was discussed. For the studies presented in this chapter Au samples were prepared by e-beam evaporation (Plassys) on clean Si substrates, using a Ti layer to promote adhesion. While Au layers deposited in this way do not exhibit many flat areas, their preparation is fast and preparation conditions easy to reproduce. Requirements of surface flatness were not stringent for the experiments described here.

Au films were evaporated at a base pressure of 10^{-7} torr to a total thickness of 50 nm. The Ti layer was 15 nm thick.

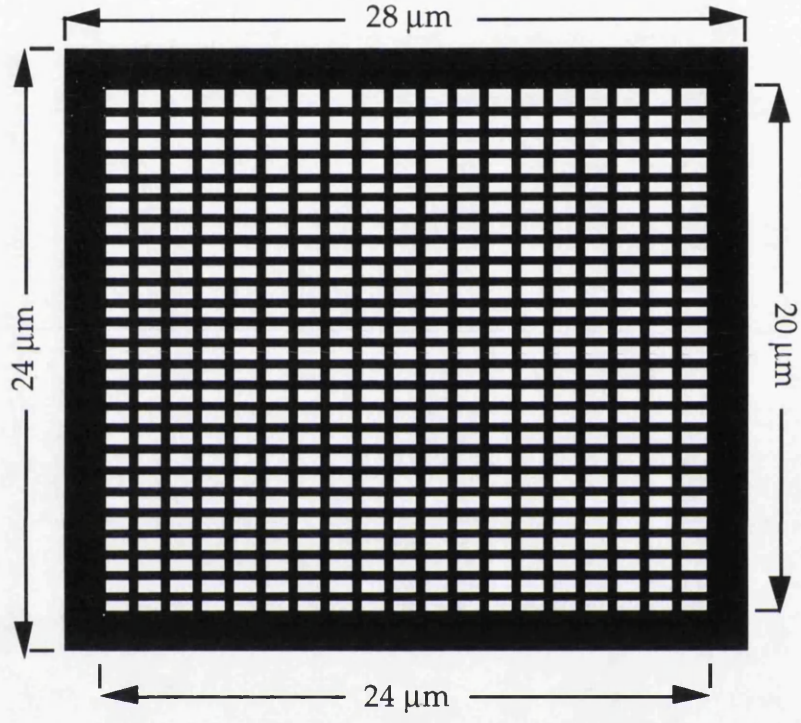

Figure 15.1. Schematic of pattern A. The black areas are those defined by the electron beam. Grid lines are 50 nm wide, the pitch, i.e. center-to-center spacing, is 0.4 µm and 0.35 µm in the horizontal and vertical directions, respectively.

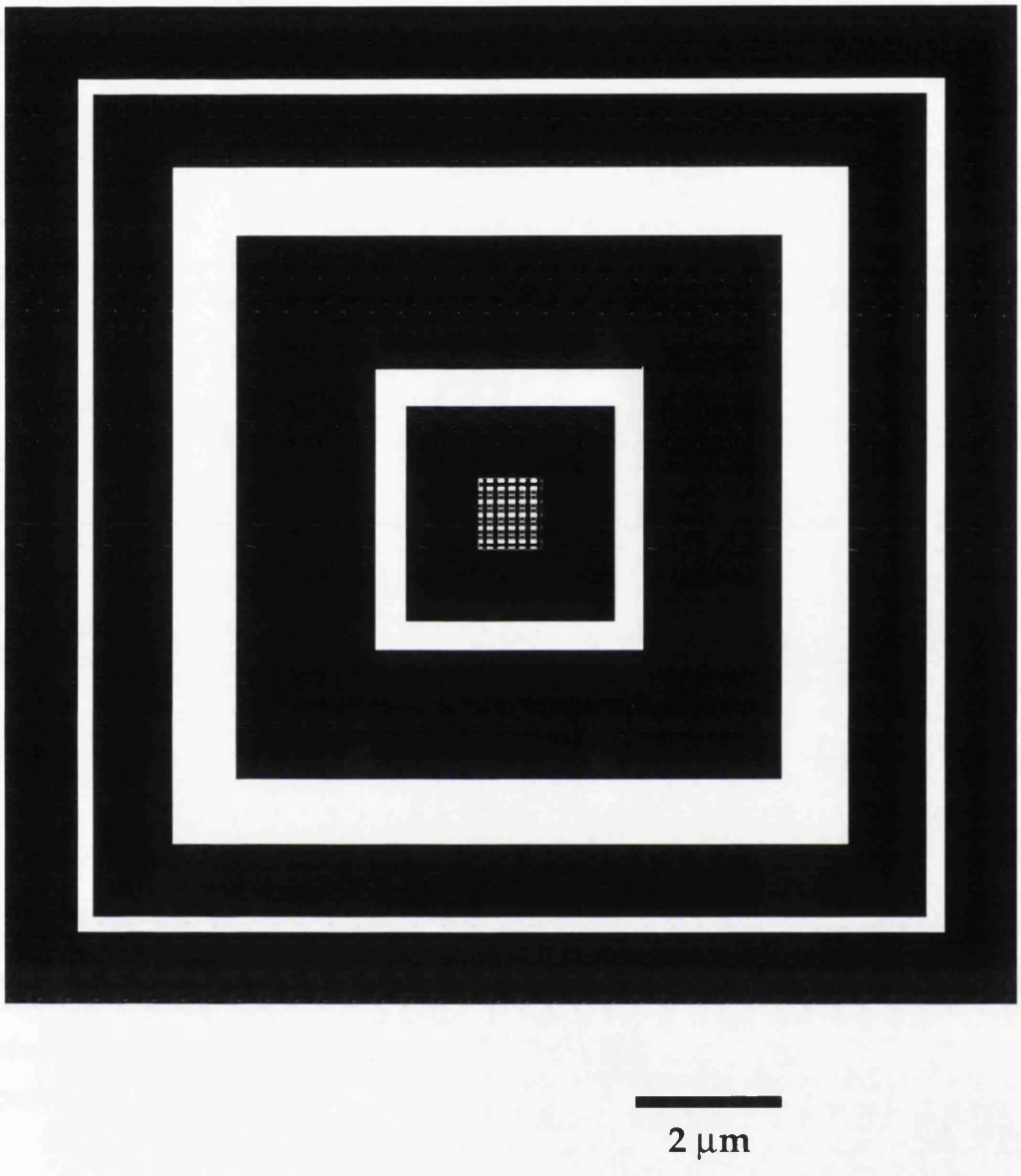

Figure 15.2. Schematic of pattern B. The black regions are those exposed to the electron beam. The pattern size is 14.8x14.6 μm^2. The inner grid is 1.4x1.2 μm^2. Grid lines are 50 nm wide; the pitch is 0.22 and 0.19 μm in the horizontal and vertical directions, respectively.

15.2.2 Pattern Definition on Au Films

Right after extraction from the evaporator, the Au films were spin coated with poly(methylmethacrylate) (PMMA) (4% BDH) at 5000 rpm for 1 minute to give a resist thickness of 50 nm. Samples were then baked at 180 ^{o}C for at least 4 hours. This preparation was carried in a Clean Room in the Ultra Small Structures Laboratory at the Department of Electronics, Glasgow University (UK).

Patterns were written using a Philips PSEM500 scanning electron microscope modified into an electron-beam lithography system.[4, 5, 6] For patterns definition an accelerating voltage of 50 kV and a beam spot of 160 Å were used for the electron beam. Exposure tests were performed and the optimal exposure dose was found by analyzing, after development, Au/Pd (150 Å) sputter coated samples by a Hitachi SEM S800.

Samples were developed in a mixture of 3:1 IPA:MIBK for 30 seconds at 23 ^{o}C, then rinsed in isopropyl alcohol (IPA) and blown dry in a stream of N_2. Samples were then Ar^+ etched in an Oxford Ion Beam Miller. The accelerating and beam voltage were 150 V and 400 V respectively. Samples were tilted ~8^{o} respect to the beam and the sample stage was rotated during etching. After etching, PMMA was removed and samples analyzed again by scanning electron microscopy. The pattern definition scheme is shown in figure 15.3.

15.3 Results and Discussion

An STM image of evaporated Au films on Si is shown in figure 15.4. As can be seen, the surface is fairly rough and very few flat islands can be found on the surface. More details about Au films characterization can be found in the author's second year PhD report.[3]

Figure 15.5 (a) shows a scanning electron microscopy micrograph of a patterned Au sample (pattern A shown in figure 15.1) sputter coated with a Au/Pd layer. The pattern is easily identified. The effect of contamination on regions previously analyzed is clearly visible on the top portion of figure 15.5 (a) as dark areas. Figure 15.5 (b) shows a sample following an Ar^+ sputtering of 90 seconds and an O_2 plasma ash of 1 minute. Usually a soak in warm acetone is sufficient to remove the resist, however in these experiments this procedure was not sufficient. This effect may be the consequence of the fixation of contamination onto the surface by the Ar^+ etch beam. The additional O_2 ash treatment effectively removes excess PMMA. It should be pointed out, however, that exposure to the O_2

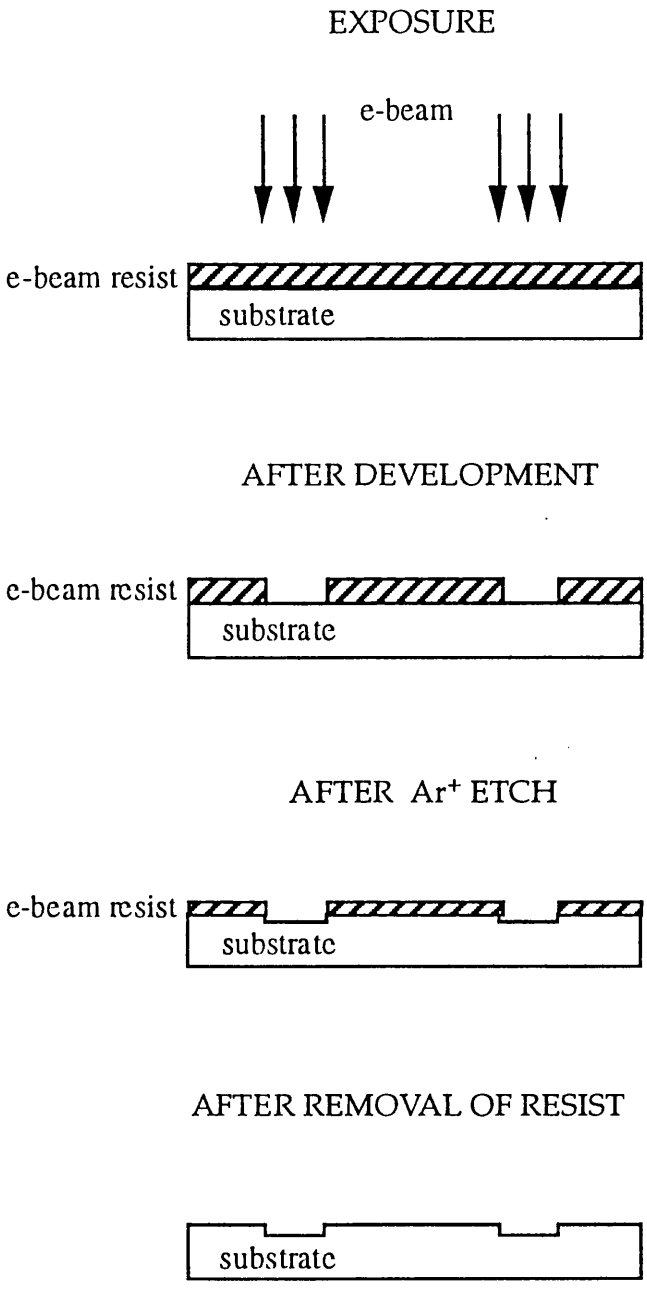

Figure 15.3. Schematic of pattern definition on gold substrate by electron-beam lithography and Ar^+ etch.

Figure 15.4 (following page). STM constant current image of a gold film on silicon obtained with a tungsten tip. Image size: 2000 x 2000 $Å^2$. Black-to-white: 106 Å. Tunneling current=0.1 nA, bias voltage=1 V.

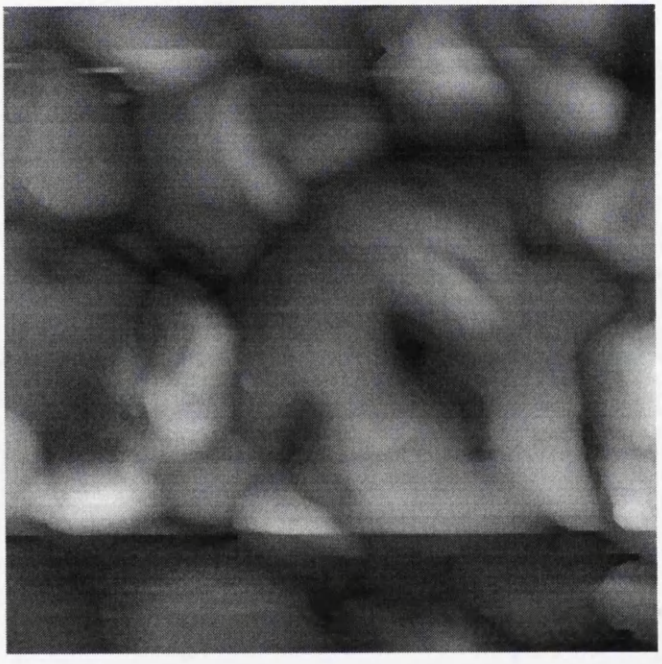

beam can roughen the surface, if prolonged. In cases where the morphology of the surface has to be preserved throughout the pattern definition process, this effect could represent a serious problem.

Figure 15.5 (c) shows a scanning electron micrograph for the pattern defined in figure 15.2. In this case too, the pattern is clearly defined on the surface.

Despite the successful development of a fabrication method, the patterns written on the Au substrates could not be imaged by AFM. Patterns could be identified by optical microscopy but only in dark illumination, not in bright field. This is likely due to the shallow depth of the etched grooves, so that even the presence of frames several microns wide did not enable easy localization of the pattern on the surface. The use of dark illumination enabled localization of pattern A (figure 15.1 and 15.5 (a)) by the AFM Italy. Attempts to image pattern B (figure 15.2 and 15.5 (c)) were made at LBNL, using the commercially available system described in chapter 4. Such attempts were unsuccessful too.

15.4 Conclusions

These preliminary results on the definition of nanometer sized patterns on gold substrates show that, while the task is feasible from the engineering point of view, the use of such patterns as reference system in nanometer scale SPM studies is not straightforward. The main difficulty lies in the fact that most SPM systems are not equipped with sophisticated enough optical microscopes for the initial identification of such patterns. In some cases, as for example for the home-built AFM used by the author at LBNL, the implementation of such optical systems is not feasible due to the head design.

One possible solution is to combine photolithography and electron-beam lithography for the pattern definition. For example, photolithography could be used to define a series of micrometer sized concentric frames, similar to those shown in figures 15.2 and 15.5 (c). The frames could be etched deep enough in the substrate to make the localization of the pattern possible with a standard stereo-optical microscope, such as those common in many SPM systems. Electron-beam lithography could then be employed to define a grid pattern in the center of the framed region. Such operations were not possible with the PSEM 500 system used by the author to define the patterns shown in this chapter, however they could be carried out by using an e-beam writer, such as that available at the Department of Electronics. By using this system, the grid pattern definition in the area of the

Figure 15.5 (following page). Scanning electron micrographs of patterns defined by electron-beam lithography on a gold film. (a) Pattern A, prior to Ar^+ etch and coated with a 150 Å Au/Pd layer. (b) Detail of pattern A after removal of e-beam resist by O_2 plasma ash. (c) Pattern B. All images were taken with a 30 kV electron beam by the secondary emission mode.

(a)

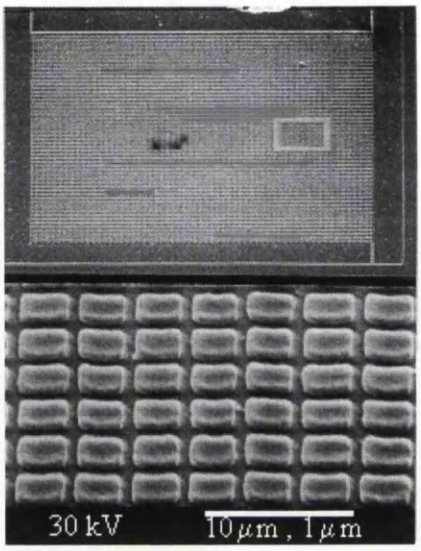

(b)

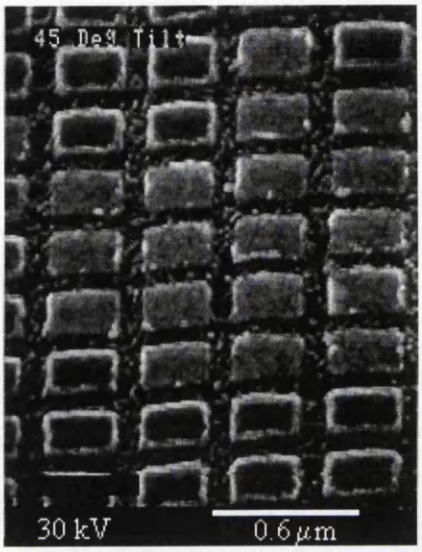

(c)

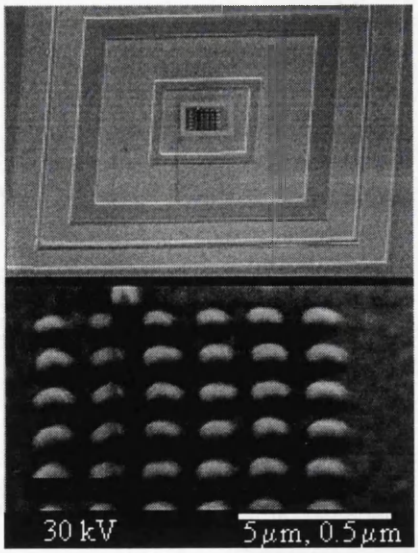

surface defined using photolithography would be straightforward and the pattern definition could be repeated easily multiple times over the substrate surface.

References

[1] G. E. Poirier, M. J. Tarlov, *J. Phys. Chem.*, **99**, 10966 (1995).

[2] B. J. McIntyre, Personal Communication.

[3] A. Lio, *Second Year PhD Report*, August 1993.

[4] S. A. Rishton, *PhD Thesis*, Glasgow University, 1984.

[5] W. S. Mackie, *PhD Thesis*, Glasgow University, 1984.

[6] C. E. Binnie, *PhD Thesis*, Glasgow University, 1985.

Chapter 16

Concluding Remarks

16.1 Summary of Experimental Results

The experimental results presented in this thesis have shown that AFM can provide very useful information on the structure and physical-chemical properties of organic interfaces and contribute to a fundamental understanding of a variety of molecular scale processes. Several fundamental issues and present limitations of atomic force microscopy are also discussed throughout this dissertation.

The first part of this thesis is dedicated to AFM studies of the nanometer-scale structural, frictional and mechanical properties of bare and chemically modified mica and Au(111) surfaces. Applications of polydiacetylene thin films for novel biosensor applications and as templates for mineralization studies were explored during the second part of this project. The third and final part further describes biosensor applications and presents preliminary results of experiments aimed at defining a reference system on a substrate for SPM applications by sub-micron lithography.

I.

- Initial experiments were performed on freshly cleaved mica and Au(111) films on mica (see chapter 7). These surfaces were used as substrates for the self-assembly of silane and thiol molecules and to calibrate the piezoelectric scanner in the x, y and z directions. Their atomic lattices are resolved in both topographic and lateral force images for a wide range of loads and with a variety of tips, from 'sharp' (tip radius: 200-400 Å) to 'blunt' (tip radius: 400-700 Å). Atomic 'stick-slip' is observed for the lateral force signal. Images of mica were often distorted as a result of a flake being dragged by the scanning tip. This observation implies that great caution is needed when using mica, or other layered materials, to calibrate the piezo scanner in x and y and the use of Au(111) surfaces is recommended instead. The 'atomic' corrugations of a few angstroms measured from atomic-level topographic images of mica and Au(111) (but also of organic materials) are not consistent with the picture of the tip

tracing contours of constant charge density. Possible contrast mechanisms are discussed: the first suggests that a convolution of atomic corrugations and compliance of the surface may be at the origin of the observed contrast, while the second proposes that the 'atomic' corrugations are simply the result of the component of the frictional force across the fast scan direction and instrumental artifacts or, in other words, an atomic force microscope operated in contact mode is in effect a frictional force microscope.

In relation to the studies performed on self-assembled monolayers, the behavior of both surfaces to the high pressures applied by the AFM tip was investigated and distinct responses were found for the two substrates. Mica, a layered and brittle material, is damaged in a layer-by-layer fashion, while gold responds elastically up to the maximum pressures applied, on the order of a few GPa. Also, it is proposed that the mica steps (10 Å high) that are created by the layer-by-layer wear of the surface be used to calibrate the scanner in z, rather than Au(111) monatomic steps (2.44 Å high).

- Self-assembled methyl and carboxylic acid terminated thiol monolayers were prepared on Au(111) and characterized by AFM in the (a) 'low' (up to a few hundred MPa) and (b) 'high' (few hundred MPa to few GPa) pressure regimes (see chapters 8 and 9).
  - ▲ At low values of the applied load and pressure the chains of alkylthiols monolayers (C_{n+1}) with an odd number of methylene groups $n \geq 7$ are observed to be in a hexagonal $\left(\sqrt{3}x\sqrt{3}\right)R30^{o}$ arrangement (see chapter 8).

    The methyl and possibly the topmost methylene groups are orientationally disordered at the pressures involved in these experiments, but the AFM images still reflect the long-range order of the main bodies of the alkyl chains. In contrast to diffraction techniques and STM, the c(4x2) superstructure is not observed. This result can be explained within the picture of the AFM tip being sensitive only to the stick-slip nature of friction and not to atomic corrugations. Interestingly, for the first time it was shown by AFM that also the chains of C_{11} alkylthiol monolayers (n=10) are in a $\left(\sqrt{3}x\sqrt{3}\right)R30^{o}$ arrangement as those of long chain thiols with an odd number of methylene groups. Low load AFM images of both short chain alkylthiols ($n \leq 5$) and COOH terminated C_{11} layers did not reveal any long-range order. These results may on one hand reflect the short-range order of these layers, but can be also the result of the tip disordering the layers, an effect that may be magnified with respect to the longer chain alkylthiols by the reduced stability and/or packing density of these layers.

▲ Investigations in the high pressure regime produced a number of significant new observations about the mechanical stability of long-chain alkylthiol monolayers and provided new insights on how energy is dissipated in these and other organic layers (see chapter 9). Two major effects could be observed. (a) As pressure increases above ~1.5 GPa, the AFM images of the C_{18} thiol lattice become increasingly disordered. This reduced degree of ordering in the chains is indicated by the progressive broadening of the Fourier peaks in the Fourier power spectra of the real-space images. Based on the energetics of these systems, it is proposed that the alkyl chains are 'melted' and disordered under the pressure applied by the AFM tip through creation of deep *gauche* defects, kinks etc. in the chains. (b) At a value of the pressure of ~2.3 GPa and below the elastic limit of gold, a transition from the $\left(\sqrt{3}x\sqrt{3}\right)R30^{o}$ thiol periodicity to the 1x1 periodicity of Au(111) is observed in the AFM images. Such transition is not abrupt and is reversible, that is the thiol periodicity is recovered upon decreasing the load. Although no visible permanent damage of the layers occurs, results indicate that the domain size in the molecular overlayer may be reduced. It is proposed that the thiol molecules are reversibly 'squeezed out' from under the tip while remaining in contact with the gold surface. Measurements of the tip height during the transition show that the tip-surface separation decreases by approximately the monolayer thickness, consistent with a displacement of the molecules in the tip-surface gap.

Further information on the molecular mechanisms that lead to the transition was obtained by measuring the frictional properties of the layers through the transition. These results show that the thiol layer is not reducing, but rather increasing the work done in moving the tip across the surface. The frictional force measured in successive scans at the same load near the transition increases before the transition: friction and energy dissipation increase as the degree of disorder in the chains increases. Once enough molecules are displaced for the stick-slip to be in registry with the gold lattice, friction decreases even though the load and tip-surface contact area have increased. In addition, the relative magnitude of the frictional forces measured by sharp tips and in absence of the transition (with 'blunt' tips) is consistent with an increase of the shear strength with pressure. This result is important since a theoretical model of friction explicitly predicts a dependence of the shear strength on the applied pressure as opposed to the adhesive model of friction, which predicts that the shear strength be independent of load. The observation of dependence upon one or the other is expected to be related to the value of the applied pressure and in this

respect AFM is unique in enabling one to access values of the pressure that are high enough for the two models to be tested.

- Self-assembled alkylsilane monolayers of different chain length were prepared on freshly cleaved mica. First, AFM was used to assess the effects of the preparation conditions and thermal annealing on the quality of the layers (see chapter 10). These experiments were performed because stability and quality of organic layers is most usually assessed only from macroscopic contact angle measurements and because, based on this type of measurements, it is commonly believed (but it has never been shown) that heating is necessary to produce stable and 'good quality' films. Molecular level structural AFM studies were also carried out (chapter 10).
  - ▲ Studies of the preparation methods produced a few significant new observations. (a) Monolayers of long-chain molecules (C_{18}) can be obtained if, after the self-assembly process, samples are sonicated for a long enough period of time. The sonication has the effect of removing clusters of polymerized molecules that are absorbed from solution. Such a procedure, however, is not appropriate for shorter chain molecules ($n \leq 12$) since the vibrations are enough to break the film apart. The contact angle measured on both flat (monolayers) and rough (monolayer+clusters) C_{18} silane layers is ~111-113^{o} proving that macroscopic wettability measurements are totally inadequate to assess the quality of these films. In addition, as it becomes increasingly difficult to form complete monolayers with decreasing chain length, contribution to the measured contact angle in these cases comes also from the substrate, a hydrophilic surface in these studies. (b) Heating C_{18} flat and rough alkylsilane films to temperatures from 50 to 130 ^{o}C showed that flat films (monolayers) are stable up to 110 ^{o}C and that beyond this temperature considerable disorder is created in the chains. When rough films are heated even to moderate temperatures (50 ^{o}C) the small clusters seen for the unannealed films coalesce to form larger and thicker ones. Contact angle measurements were once again unable to discriminate between the two types of layers. These results unequivocally show that molecular-level models of these films (and other organic films) cannot and must not be constructed solely from macroscopic measurements and that molecular-scale characterization is indispensable even for the relatively simple layers studied during the course of this PhD. AFM has the potential to contribute enormously toward the control of organic interfaces at the single-molecule level.

- ▲ The molecular level structure of alkylsilane SAMs (see chapter 10) was found to differ greatly from that of alkylthiol monolayers. Long-range order was not observed for long or short chains, although residual short-range order was revealed. These differences arise from the siloxane bonds existing between silane molecules, which produce considerable distortion in the chains.

- Armed with the knowledge of the molecular-level structure of thiol and silane monolayers, friction studies were carried out on both type of monolayers (see chapters 8 and 10). The structural information obtained on both types of layers is crucial to the understanding of their frictional properties.
  In order to understand the role of parameters such as chain length, headgroup-substrate interaction and long/short-range order of the chains in determining the frictional properties of organic layers, a comparative study of the frictional properties of alkylthiols and alkylsilanes monolayers as a function of chain length was performed. Since quantitative AFM and FFM measurements depend on the knowledge of the cantilever force constants and contact area, both of which could only be estimated in these studies, relative measurements conducted with the same tip were made. Also a freshly cleaved mica surface was used as a reference. For both type of films, the frictional forces are seen to depend on the number of methylene groups (n) in the alkyl chain. For the thiols, similar frictional properties are measured on layers with $n \geq 7$, while a greater variation with chain length is observed for the silane SAMs. The direct comparison between the two types of layers reveals a similar frictional behavior for C_{18} layers, indicating that long-range order does not lead to lower friction and that short-range order is the dominant characteristic. The frictional properties of thiol and silane monolayers having the same n, however, become increasingly different as the chain length of the molecules decreases, with the silane yielding higher frictional forces. The first important conclusion that can be made from these studies is that friction does not depend only on the chemical nature of the exposed groups, otherwise all chain lengths for all thiol and silane layers should have yielded similar friction values. It is proposed that the increase in friction seen with decreasing chain length and the short-chain silanes as compared to the thiols is due to poor packing and/or decreased packing density of the molecules. That favors the excitation of energy dissipating modes, such as *gauche* defects, bending around kinks, etc. that are quenched in the densely packed films, thus increasing friction.
  An additional contribution to friction from surface energy and adhesion can be identified when COOH terminated layers are compared to methyl terminated

ones. Interestingly, it was also observed that thiol monolayers increase the frictional forces measured on Au(111) films in air. This observation is attributed to the elastic response to pressure of a Au(111) surface in air and show that organic layers do not necessarily lubricate bare surfaces. A similar effect was observed for C_6 alkylsilanes and mica, while silanes with $n \geq 7$ yielded frictional forces lower than those of mica.

- Studies of the interaction of water with bare mica (see chapter 10) revealed that the adhesive properties of mica greatly depend on humidity. This adhesive force peaks around ambient humidity (typically 45-50% for these studies) and decreases for values at both low and high humidity. These results can be reconciled with previous scanning polarization microscopy and ellipsometry studies. The increase in the pull-off force up to ambient humidity is related to the formation and completion of the first monolayer of water on the mica surface. After that, liquid water multilayers form and the dependence of the pull-off force on RH can be understood in terms of capillary interaction and thermodynamics. Interestingly, during the course of these experiments the contrast in AFM/FFM images was seen to disappear in a reversible fashion for RH<20%, indicating that water plays an important role in the achievement of atomic-lattice resolution at ambient conditions.
  A markedly different behavior is seen for hydrophobized mica (that is C_{18} silane on mica). A weak dependence of the pull-off forces on RH is observed as likely due to the intercalation of water inside nanometer-sized defects present in C_{18} silane layers.

II.

- In relation to AFM studies of affinochromism and the blue-to-red color transition of thin films of sialic acid functionalized 10, 12 pentacosadiynoic acid, a systematic characterization of films prepared under different preparation conditions was carried out (see chapter 11). Based on these studies, optimum preparation conditions were determined. Blue Langmuir-Schaefer SAc/PCDA films were transferred from overcompressed multilayers, irradiated for 1 minute with UV light at the air-water interface, onto hydrophobic octadecyltriethoxysilane monolayers on mica. Red films can be obtained by irradiating the monomer molecules for 20 minutes. The Langmuir-Schaefer (or horizontal) method was used instead of the Langmuir-Blodgett method to expose the hydrophilic, biosensitive groups (the sialic acid groups) to the interface. The overcompression of the monomer molecules was necessary

since monolayers of the pure acid are not stable at the air-water interface and, as verified by AFM, monolayers cannot be transferred onto the substrate. The chromatic character of the LS films was readily visible to the naked eye (films really look blue or pink-red!) and easily characterized by visible absorption spectroscopy.

- ▲ Blue SAc/PCDA films consist of micron-sized domains separated by uncovered OTE areas. In each domain a stripe-like morphology on top of a nearly complete SAc/PCDA layer is present. The measured heights of the bottom layer and the stripes are consistent with SAc/PCDA trilayers tilted ~30° from the surface normal with the sialic acid groups lying flat on the PCDA surface. When imaged at higher magnification, the bottom SAc/PCDA layer is seen to consist of fine fibers that run parallel to one another and to the stripes. Important differences exist between the bottom SAc/PCDA layer and the stripes. The former is mechanically robust, as repeated scanning at low load does not produce any damage, while the stripes are laterally compressed and separated by the scanning tip. Comparison with monomeric films indicates that the increased mechanical stability of these films is the result of the polymerization process. At the molecular scale, the bottom layer reveals that a higher degree of order exist in the direction of the fibers. The value of the lattice constant measured along this direction is consistent with the intra-backbone periodicity measured for several PDAs by diffraction techniques. It can therefore be concluded that the direction of the fibers represents that of the polymer backbone. Random mismatch and misalignment of the hydrocarbon planes are instead observed between adjacent polymer chains. In this phase, the molecular arrangement of the side chains is determined by the spatial requirements imposed by the solid state polymerization of PDAs and are prohibited from assuming their planar (lowest energy) configuration.
- ▲ The addition of Cd^+ ions to the subphase had the expected effect of increasing the stability of the molecules and Cd-PCDA monolayers could be deposited successfully by the LB method on mica. At the molecular level, however, these films do not reveal a higher degree of order than the LS multilayers, as it may have been expected. While the molecules still appear to be regularly packed along the polymer backbone, neighboring polymer chains were randomly packed and the Cd^+ ions ultimately alter the long-range morphology of the layers.

- The red form of PDAs can be obtained as the result of a variety of perturbations. In these studies particular attention was given to affinochromic,

thermochromic layers and films transferred from molecules exposed to UV irradiation for a period of 20 minutes. Affinochromic layers are obtained after exposing blue SAc/PCDA LS films to the influenza virus, while thermochromic films are converted to the red phase by heat. While the three red phases are indistinguishable from visible absorption spectroscopy measurements, AFM reveals substantial differences.

- Red-phase films obtained by prolonged exposure to the UV light (see chapter 11) show a similar micron-scale morphology to that described for blue-phase films. Mechanical properties and molecular-level morphology of the bottom SAc/PCDA layer are identical to those observed for the blue-phase films. The mechanical stability of the stripes instead has increased and the chains are regularly packed in a hexagonal arrangement.
- Thermochromic layers obtained by heating blue-phase films to temperatures greater than 70 ^{o}C, show substantial transformations both at the micrometer and molecular level (see chapter 12). The domains of blue-phase films break parallel to the direction of the polymer backbone from breaks already existing in the blue-phase films and the newly formed polymer fibers are highly flexible. The SAc/PCDA chains untilt and re-arrange into a totally ordered, hexagonal conformation. Furthermore, the chains remain in such arrangement even at temperatures well beyond the thermochromic transition, an indication of the remarkable thermal stability of these layers.
- Affinochromic red phase films (see chapter 13) show that the influenza virus particles are primarily on top of the stripes of the blue-phase films, which now show a 'buckled' appearance. The bottom SAc/PCDA layer appear largely unchanged, suggesting that the sialic acid groups are accessible to the virus hemagglutinin only in the regions of the stripes.

The molecular-scale mechanisms of the blue-to-red color transition suggested by these observations are rather different for the three cases. The properties of the stripes of blue phase films may be the result of a reduced extent of polymer formation coming from these portions of the films being deeper into the water and hence further away from the UV source. When the monomer molecules are exposed to the UV light for a longer period of time, the higher mobility of the molecules of the stripes may favor the formation of well ordered structures in these regions. That in turn may cause strain on the polymer backbone and a decrease in the π-π bond overlap, giving origin to the blue-shift observed in the optical spectra. For the thermochromic effect, complementary FTIR measurements indicated that after the transition, the alkyl side chains bonds have more *trans* character compared to the blue-phase films, consistent with the re-arrangement observed by AFM. Such a re-arrangement of the side chains into

a lower energy configuration may again impose strain on the polymer backbone causing the changes in the optical spectra. Importantly, these results refute previous models based on visible absorption and FTIR spectroscopy studies of side chain entanglement and disorder as responsible for the thermochromic transition of these layers. Once again, these AFM results demonstrate on one hand the inadequacy of macroscopic methods in studying complex molecular-level processes and on the other that AFM is an extremely powerful tool for these kinds of studies. Finally, in the case of the affinochromic effect, AFM results suggest that the chromatic changes are brought by a disordering of the chains from the outside-in, in a similar way to the membrane fusion by the virus observed in natural systems.

- Polymeric Langmuir-Schaefer films of 10, 12 pentacosadiynoic acid were used also in an attempt to reproduce the unique conditions occurring in many living systems that lead to the absolute alignment of large numbers of inorganic crystals relative to the organic matrix (see chapter 13). The morphology of blue-phase PCDA films was observed by AFM to be indistinguishable from that of blue SAc/PCDA layers. Calcite crystallization on top of the PCDA template produced crystals that nucleated at the (012) face and were co-aligned with respect to the polymer backbone within a PCDA domain. At the same time the blue-to-red color transition was observed. Two key factors contribute to this unprecedented result of cooperativity at an organic-inorganic interface. Lattice match between calcite and the PCDA polymer backbone dominates along the *a* axis of calcite. Symmetry reduction in PCDA template (the chains are tilted) coupled with proper stereochemical match between the tilted carboxylates of the film and the carbonate of the crystals are responsible for the co-alignment of the calcite crystals. The color transition of the film from the blue to the red form suggest that the side chains of the PCDA matrix further re-organize upon crystallization most likely to optimize the specific stereochemistry of the carboxyl group.

III.

- Photolithography and silane chemistry were combined to spatially define areas bearing different organic/biological functionalities on indium tin oxide surfaces (see chapter 14). ITO surfaces were characterized by high-resolution scanning electron and scanning tunneling microscopies revealing a rough poly-crystalline surface. Amine terminated silane molecule were patterned on ITO and the patterns were characterized by AFM. Although the molecules were successfully

patterned, these layers, unlike the smooth silane overlayers described in chapter 10, appeared rather rough with severe 3D-clustering of the molecules. Although the cross-linking molecule used for these studies was not the most appropriate, the immobilization technique proposed is proven effective and general enough to be extended to more suitable molecules.

- Toward the aim of using gold films as substrates for organic/biological applications and be able to image the same area of the sample after some transformation has taken place, electron beam lithography was used to define nanometer-sized patterns on gold surfaces (see chapter 15). The results shown are only preliminary but outline some limitations of this method. In fact, while the presence of a nanometer-sized reference system on the surface is very desirable in many SPM experiments, the use of such patterns may be ultimately unpractical in most currently available SPM systems, because the patterns are very shallow and require the use of powerful optical microscopes operated in dark field illumination. Another serious problem lies in the need to sputter off, rather than wash away, the electron-beam resist since this process may significantly alter the substrate morphology. It is suggested that a combination of photolithography and electron-beam lithography be used for future developments of these or similar patterns.

16.2 Recommendations for Future Research Directions

Atomic force microscopy is still a relatively young technique and as such prospects for future work are enormous.

Much work can be and must be done to overcome present limitations of the technique. To date, major limitations of the technique lie in the fact that absolute measurements of forces are not possible in most cases, measurements of the force constants of the cantilevers and calibrations of the lateral force signal are not performed routinely and control of the tip is still lacking. The resolution of these fundamental issues is crucial to the assessment of the reproducibility of AFM results and its use as a nanotribology/nanomechanics tool. Clearly further work is indispensable. For example, the use of $SrTiO_3$ crystals has been proposed recently for measurements of the tip's profile. To date the method is best suited for tips with radius smaller than 500 Å. This limitation, however, is not intrinsic and can be removed by growing crystals with wider facets.

Other fundamental issues concern the understanding of the imaging/contrast mechanism in contact mode AFM. This knowledge is crucial to the understanding of the multitude of AFM images already reported in literature and the design of future AFM experiments. Experiments that can elucidate the full role of the frictional forces in atomic-lattice resolution images are encouraged. Of primary importance is the establishment of the variation, if any, of the measured 'atomic corrugations' with load. Extreme care is necessary however, since instrumental factors can also contribute to the observed corrugations. Also, if the AFM is a frictional force microscope, this should be true in air as well as in UHV, controlled atmospheres and liquid. Experiments conducted on the same surface (and possibly with the same tip) in a variety of environments are therefore recommended. The use of soft metal samples, such as gold, instead of layered materials, is suggested since the latter give origin to a variety of artifacts.

The use of AFM/FFM for nanotribology and nanomechanics studies of organic interfaces is still in its infancy. The results presented in the first part of this thesis represent the first systematic investigations aimed at understanding how different structural parameters affect the frictional properties and mechanical stability of organic layers. The prospects for future work in this field are exciting. The key is to decide on systems in which the AFM is likely to be able to provide a maximum amount of information. The results obtained on the methyl terminated C_{12} thiols and silanes suggest new experiments where purer chemicals are used. If purity is the not the relevant parameter, then one possibility is that the frictional properties observed for these layers are related to structural parameters of the

layers. In fact, it has been suggested that an n exists for which optimum order of these layers is achieved. Studies on carboxylic acid terminated thiol layers as a function of chain length are also recommended. Macroscopic studies of these films have indicated that layers with a number of methylene groups $n \geq 15$ are ordered. AFM could provide molecular-level structural information on one side and try to relate structural and frictional properties of the layers, in a way similar to that shown in this dissertation for methyl terminated thiols. Since, however, the COOH films are highly hydrophilic and become contaminated easily in air, experiments performed in controlled atmosphere are recommended. The studies can also be extended to OH terminated thiol molecules, molecules that contain fluorine atoms in the chains in place of hydrogen and also di-thiol molecules, that by having a sulphur atom at each end may go on the Au(111) surface in an inverted U-shape configuration and therefore directly expose methylene groups to the interface. The level of complexity may also be increased by using thiol-PDA molecules. In this case, added stability to the monolayer would perhaps come from the presence of the polymer backbone and the constraint imposed by the conjugated backbone on the aliphatic side chains may limit the way energy can be dissipated in these layers.

The natural extension of the pressure dependent investigation of the structural and frictional properties of octadecylthiol monolayers presented in this thesis would be studies of the transition, if any, as a function of chain length. Of particular interest would be experiments performed on chains with $n>17$, since these could elucidate whether a minimum n exists for the $\left(\sqrt{3}x\sqrt{3}\right)R30^{o}$ to (1x1) to occur. Studies on alkylthiols self-assembled on Au(11$\bar{1}$) single crystals are also recommended, since the presence and size of thiol domains on the surface may play a role in the transition. By increasing the size of the Au(111) terraces in going from Au(111) on mica to single crystals, the size of the thiol domains is likely to change too. In relation to these studies, MD simulations are also very much desirable to help elucidate the molecular-level mechanisms that lead to the transition.

Also, studies of the frictional properties of clean Au(111) films in UHV and of their dependence on the film thickness, if any, is suggested. These studies could help elucidate the role of the elastic properties of Au(111) films in determining the frictional behavior observed during this thesis work and also whether they depend on the thickness of the film, as it appears to be the case for a variety of solid lubricants.

Humidity dependent characterization of adhesive properties of bare chemically functionalized surface is only starting now. On one side the extreme sensitivity of the pull-off forces measured by AFM on the surface energy of the interface and penetration of water inside defects of the layers normally unresolved

in contact mode AFM imaging, opens the way to the use of the AFM as a sensitive hydrophilicity/hydrophobicity probe. On the other, such studies should help one answer fundamental questions on the interaction of water, or other liquids, with solid surfaces. It is recommended that the studies presented in this dissertation be extended also to measurements of friction as a function of humidity.

Further studies on colorimetric sensors incorporating functionalities other than sialic acid and their extension to other physical perturbations other than target binding are encouraged. Extension of the method toward the use of liposomes rather than LS films is already under way. To better understand the fundamental issues arisen during the course of this thesis work, a few experiments are suggested. For example, it was suggested that the observed frictional properties of LS SAc/PCDA and PCDA multilayers are influenced by contamination present in air. Experiments performed under water (after the contrast mechanism of friction under water is understood!) may help elucidate this point. Experiments performed in a liquid environment may also elucidate the nature of the filaments often present on the stripes of blue-phase films: if it is collapsed polymer material, as it is suggested, it may 'unfold' back in the liquid. Also, to ascertain whether the reduced mechanical stability of the stripes of blue-phase films is related to the extent of polymer formation in these regions (as suggested from the comparison with red polymer and monomer films), one may attempt to 'extract' the monomer from the polymer matrix by treating the blue films with a solvent in which the monomer is soluble (note that the polymer is insoluble in all solvents). Such experiments may also provide information on the mechanisms of the solvatochromic blue-to-red color transition.

As for the use of PDAs as templates for mineralization studies, the approach may be used for investigating, for example, fundamental properties of other oriented crystalline films. AFM experiments aiming at the study of the initial moments of the mineralization process may help elucidate further how the side chains of the PCDA templates re-orient upon mineralization and also whether nucleation of the calcite crystals starts at specific sites on the film.

The results presented in chapter 14 could be extended to different amine terminated molecules, such aminopropyltriethoxysilane (a 'simpler' version of the aminoethyl-aminopropyltrimethoxysilane molecules used in these studies) and more suitable preparation methods utilized. In the attempt to achieve a single-molecule control of the interface, sub-micron pattern definition methods may be developed.

Finally, it is suggested that the definition of a nanometer scale reference system for specific SPM applications be performed by combining photolithography and electron-beam lithography techniques on a large enough area of the sample to allow for easy optical identification of the patterned area. However, it should be kept in mind that such methods may alter significantly the morphology of the

interface and therefore make the use of such reference systems ultimately unpractical.